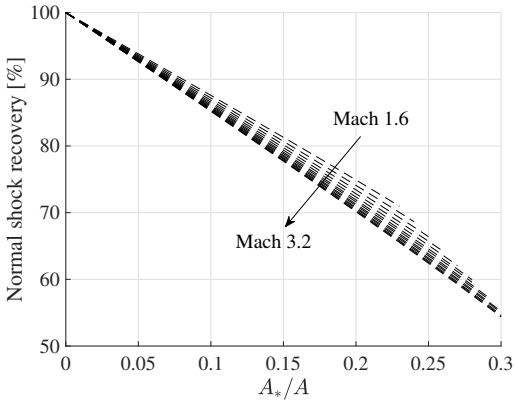

Figure 4.3: Percentage recovery of normal shock pressure rise for various confinement ratio A^*/A and bulk inflow Mach number M_0.

4.2.3 Smart one-dimensional model

Smart's model [116] is derived from the same flux-conserved approach with the addition of an equation for A_c representing the core flow area such that the mass flow rate $\dot{m} = \rho\, U\, A_c$. Figure 4.4 represents the control volume used in Smart's model to derive the conservation equations. Wall friction and heat losses are both accounted for. The derivation of the model equations (Eq. 4.11, 4.8, 4.9) are detailed in Smart [116]. Lastly, an additional equation for the local spatial pressure growth rate $\frac{dP}{dx}$ closes the system and allows forward integration in space. This equation can use any external model. The additional Eq. 4.9 describes the evolution of the core flow area ratio A_c/A, which has value 1 both at the foot and tail of the shock train. It marks the points of detachment/reattachment in Smart's analysis. This model, therefore, permits to determine both the pseudoshock length and the back pressure contrary to previously described models. Note that the first line of Eq. 4.9 contains the isentropic rate of change of A_c/A, while the second one adds wall friction forces to the analysis and the last one accounts for wall heath losses. This last one will be discarded in this chapter as all involved datasets assume adiabatic walls.

$$\frac{dM^2}{M^2} = -\left(1 + \frac{\gamma - 1}{2} M^2\right)\left[\left(\frac{2}{\gamma M^2}\frac{A}{A_c}\right)\frac{dP}{P} + \left(\frac{A}{A_c}\right)\frac{4C_f dx}{D_H} + \frac{dT_t}{T_t}\right] \tag{4.8}$$

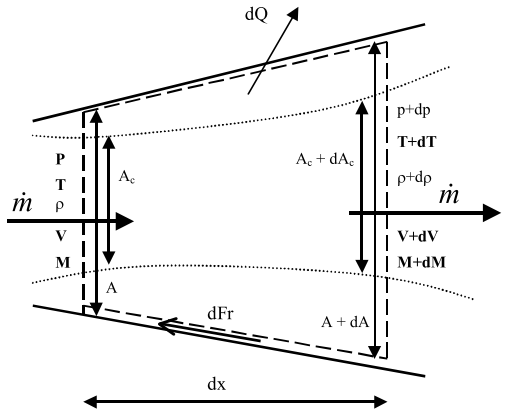

Figure 4.4: Control volume for the flux conserved analysis of Smart from [116].

$$\frac{d(A_c/A)}{A_c/A} = \left[\frac{1 - M^2[1 - \gamma(1 - A_c/A)]}{\gamma M^2 A_c/A}\right]\frac{dP}{P} + \left(\frac{1 + (\gamma - 1)M^2}{2A_c/A}\right)4C_f\frac{dx}{D_H} + \left(1 + \frac{\gamma - 1}{2}M^2\right)\frac{dT + t}{T_t} \tag{4.9}$$

The pressure closure chosen by Smart is Ortwerth's model [99] (Eq. 4.9). It consists of a linear correlation between the skin friction upstream of the recirculation bubble and the conversion rate of kinetic energy density q (Eq. 4.11) into pressure. This model relies on the observation that higher skin friction usually requires stronger adverse pressure gradients in order to detach the boundary layer, although a linear dependence is unclear due to data scattering [99]. Also such model cannot capture the roll-off in pressure profiles observed in low-Mach number shock train, as previously observed by Smart. It also fails to enforce consistency between pseudoshock length and pressure rise as seen in Fig. 4.5 for any given value of k. The next section will present the derivation of a new pressure growth rate closure equation.

$$\frac{dP}{dx} = q\frac{k_0}{D_H}C_{f0} \tag{4.10}$$

$$q = \frac{\rho V^2}{2} = \frac{1}{2}\gamma P M^2 \tag{4.11}$$

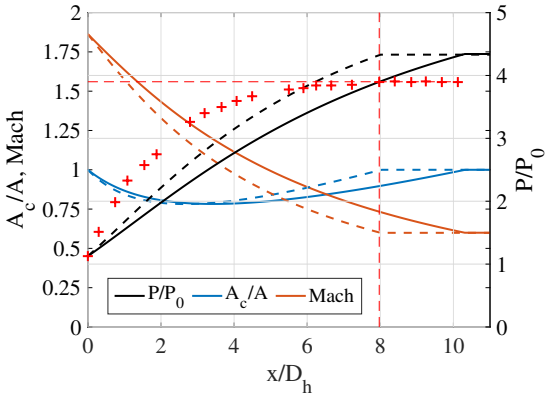

Figure 4.5: Original Smart model for the Mach 1.92 configuration [120] ($C_{f1D} = 0$) for (solid) $k_0 = 44.5$ and (dashed) $k_0 = 54.5$ matching the pseudoshock length.

4.3 Modified flux-conserved model

4.3.1 Improved pressure growth rate closure equation

As the pressure growth rate equation closes a set of analytically-derived conservation equations, it is responsible for the model inaccuracies described in Sec. 4.2.3. Orthwert's diffusion model consists of converting kinetic energy into internal energy at a linear rate. Based on the understanding of pseudoshock physics developed in Chap. III and present in the literature an improved model is derived to resolve the following features:

1. Normal pseudoshock pressure roll-off in the mixing region.

2. The abnormal strong importance of the upstream friction coefficient C_{f0} as opposed to the inlet confinement ratio in determining the pressure growth rate. As seen in Chap. III, the pseudoshock length varied almost linearly with the momentum thickness while C_{f0} remained constant at 0.00105.

3. The overshoot in pressure maximum recovery currently observed in the baseline model from Smart. This can be caused by the neglect of wall viscous losses, or by not accounting for the indirect path of energy conversion by dissipation of turbulent kinetic energy inside the core flow identified in Chap. III.

The corresponding modification to the baseline model are the following :

1. First, a pressure roll-off is obtained by changing the correlation constant k into a function of the local kinetic energy density $k(q)$. A reference Mach number where the transition between normal and oblique pseudoshocks occurs needs to be determined, as well as a proper transition function. The transition from a roll-off rate for normal pseudoshocks into a linear rate for oblique pseudoshocks is mostly a function of the Mach number, although close to the limit large confinement ratio can also play a role [52]. Based on Hunt *et al.* review of experimental datasets (see Fig.15 in [52]), the transition occurs between Mach 2.0 and Mach 2.5 except for one unusual case where the boundary layer is almost as thick as the channel half height ($\delta/h \approx 0.6$). The new function k needs therefore to be a function of both q and the flux-conserved Mach number M_1. $k(q, M_1)$ is presented in Eqns. 4.12, and equal to a ratio between q and q_0 to the power κ with an additive constant a. The purpose of a is to smooth the strength of the roll-off and relax the model stiffness. It will need to be calibrated just as the constant k_{ref}. Equation 4.13. The shape of the transition power $\kappa(M_1)$ (Eq. 4.13) was guessed from a qualitative observation of various datasets and found after some trial and error. Figure 4.6 shows how the roll-off function works once the parameters a,b,c,k_{ref},α,β and κ are calibrated (this will be the focus of the next section). The top left figure shows how κ changes for different Mach numbers, with red crosses corresponding to the cases presented in Tab. 4.1. The bottom left figure shows how $k(q)$ evolves throughout the pseudoshock (with $q/q(x = 0)$ decreasing) for various of M_1 ranging from normal to oblique pseudoshocks. The figure on the right presents the overall effect on some normalized pseudoshock profiles, with a sharper initial gradient compensated by a stronger roll-off for low Mach number (normal pseudoshocks) as opposed to a more linear pressure rise at high Mach numbers (oblique pseudoshocks).

$$k(q, M_1) = k_{ref} \times \left(a + \frac{q(x)}{q(x=0)} \right)^{\kappa} \Big/ \int_0^1 \left(a + \ y \right)^{\kappa} dy \tag{4.12}$$

$$\kappa = b \ (1 - tanh(c \ [M_{ref} - M_1])) \tag{4.13}$$

$$\frac{dP}{dx} = q \frac{k(q, M_1)}{D_H} C_{f0}^{\alpha} \ \sigma^{\beta} \tag{4.14}$$

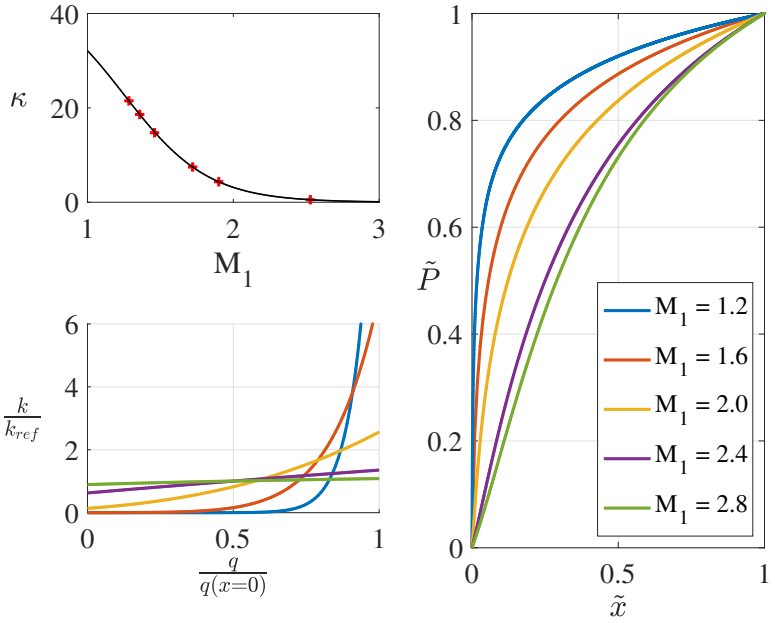

Figure 4.6: (Top left) Dependence of κ at pseudoshock foot ($q/q_1 = 1$) on flux-conserved Mach number M_1. (Bottom left) $k(q, M_1)$ dependence on local kinetic energy ratio $q/q(x = 0)$ and M_1. (Right) Normalized pseudoshock profiles for various M_1 using the new roll-off model.

2. The second modification to the original model is to replace the linear C_{f0} dependence of $\frac{dP}{dx}$ of Ortwert's model with the nonlinear term $C_{f0}^{\alpha}\sigma^{\beta}$ in Eq. 4.14. σ is the efficiency parameter derived from McLafferty's analysis. The reason for such modification is as follow. As seen in Chap. III, an increase in confinement ratio at constant Mach number and back pressure ratio leads to a longer pseudoshock by reducing the pressure growth rate of the successive centerline compression cells. This is mostly caused by the

shrinking of the normal-like section of the leading lambda shock. However, Smart's model closed with Ortwert's correlation does not replicate such dependence. Instead, a simple increase of A_* or A_θ causes a decrease of M_1 only, which results in a shortening of the pseudoshock and a reduction of back pressure. Therefore the dependence of pseudoshock pressure growth rate on initial confinement ratio is accounted for by the addition of σ^β where β is a positive unknown power which will be determined later but is expected to be close to 1.0 according to Fig. 3.11. The numerical study in Chap. III didn't cover a sufficiently large range of Mach and Reynolds number to precisely determine this dependence yet. As Ortwerth's correlation is modified, a power law α is added to the friction coefficient in the closure equation to counterbalance any effect C_{f0} and σ would duplicate. α will also be determined alongside β and expected to be inferior to 1.0. Note that α needs to be superior to zero to verify the asymptotic theoretical behavior of a standing normal shock when no boundary layer is present: *i.e.* an infinite pressure growth rate for an infinite C_{f0}.

3. Finally, neglecting friction and viscous losses lead the model pressure to naturally converge towards McLafferty's prediction. LDV measurements by Sugiyama [119] and DNS results from Chap. III on Mach 2.0 pseudoshocks revealed that the recirculation bubble (negative C_f region, considered friction-less in Smart's analysis) is localized in the close vicinity of the leading lambda-shock only, where the adverse pressure gradient is maximum. On the other hand, no large recirculation bubbles were observed in oblique pseudoshock where the adverse pressure gradient isn't sharper at the foot of the pseudoshock than at its tail (hence the linear pressure growth rate model). Additionally, the friction term accounts for turbulent/mean energy dissipation into internal energy by any other mean, such as the corner vortex pairing, and not just wall friction. Friction was therefore retained in the model in the form of Eq. 4.15 meant to account for all dissipative processes.

$$C_{f1} = d \ + \ e \times C_{f0} \tag{4.15}$$

4.3.2 Determination of model parameters

A set of $N_{par} = 9$ parameters [k_{ref},M_{ref},a,b,c,d,e,α,β] needs to be calibrated to ensure that the model can accurately capture the pressure rise for a wide range of operating conditions covering both ramjet and scramjet modes. It is important at this point to address the particular question of what quantities need to be optimized. While numerical simulations can provide exact flux-conserved profiles along the whole computational domain, available experimental data usually consist of wall pressure profiles. A wall pressure profile permits to identify both the pseudoshock length and final pressure rise. The final pressure rise obtained from the model is flux-conserved, and not necessarily equal to the wall pressure. However, as the flux-converged final pressure obtained from the model assumes a fully reattached flow, the outflow is a fully developed turbulent mixing region. According to classical boundary layer theory, the static pressure profile is therefore constant along the wall normal directions: the model can, therefore, use the wall PRR as a target PRR to calibrate the parameters.

Also, as flux-conserved profiles cannot be measured experimentally the wall pressure profile will be used as target profile to resolve the pressure growth roll-off. In the DNS of Fiévet *et al.* the difference between integrated pressure and wall profiles were minimal in the mixing region, but noticeable in the initial steeper rise. The integrated profiles contain more oscillations due to the centerline compression/expansion cells than the wall profiles. Using the wall pressure is also preferable since the model only resolve monotonic profiles.

The experimental and numerical datasets used to calibrate the new model are presented in Tab. 4.1. They will be referred to by their number throughout the chapter. The parameters are calculated through a minimization process of an error function using the genetic algorithm (GA) of Matlab Global Optimization Toolbox. A genetic algorithm permits to solve constrained problems by evolving populations of solution vectors using a selective process

Table 4.1: Pseudoshock flow conditions used to verify/calibrate the 1D model.

Case	Type	Size [mm]	M_0	P_0 [kPa]	C_{f0}	$\mathcal{A}_*$[%]	$\mathcal{A}_\theta$[%]	M_1	P_1 [kPa]
1	Exp. [98]	$\oslash$ 59.1	1.29	9.20	$3.73e^{-3}$	3.884	1.757	1.284	8.89
2	Exp. [98]	$\oslash$ 59.1	1.37	9.27	$3.65e^{-3}$	3.476	1.528	1.358	9.05
3	Exp. [98]	$\oslash$ 59.1	1.48	9.45	$3.73e^{-3}$	3.347	1.390	1.464	9.26
4	DNS [33]	57.2×69.8	1.91	17.35	$1.05e^{-3}$	19.99	6.335	1.721	16.01
5	Exp. [120]	50.8×20.3	1.92	104.9	$1.54e^{-3}$	5.768	1.932	1.86	103.1
6	Exp. [89]	19.1×9.5	2.83	16.83	$2.49e^{-3}$	16.55	3.801	2.53	16.78

resembling biological evolution. The population of solutions evolves continuously throughout the process. At each iteration, a set of current solutions are randomly selected and used as parents of a newly created generation of children solutions. As the process continues, generations converge towards the optimal solution as the least effective populations slowly decay. The error function $E_{\psi,\chi}$ is defined in Eq. 4.16 for a certain parameter population (or solution vector) ψ and a set of calibration cases χ. Additionally, solutions yielding a roll-off rate too far off (pseudoshock first and second quarters PRR error magnitudes are inferior to 20%) are arbitrarily discarded. Fig. 4.7 presents the evolution of the genetic algorithm for a typical run (computing time of several minutes on a single core).

$$E_{\psi,\chi} = \Sigma_\chi\left(\frac{PRR_{1D} - PRR}{PRR},\ \frac{L_{1D} - L}{L}\right) \tag{4.16}$$

Table 4.2 shows the error on pressure rise ratio PRR and pseudoshock length L when running the GA using different calibrating cases. More cases are progressively included in order to find a solution minimizing the error over the largest possible range of operating conditions. However, some of the cases are intentionally not used in the optimization process but will instead assess the model's accuracy a posteriori. The cases that will be used for calibration are cases 2, 4 and 6 only, while cases 1, 3 and 5 serve as witnesses. In Tab. 4.2 values labeled with a star represent cases where the pseudoshock length is within the 99% pressure rise locations (i.e. well within measurement error margins). It can be quite challenging to identify the exact location of the end of a pseudoshock and its length L due to the wall pressure roll-off in the mixing region. Indeed, 99% back pressure recovery L/D_h

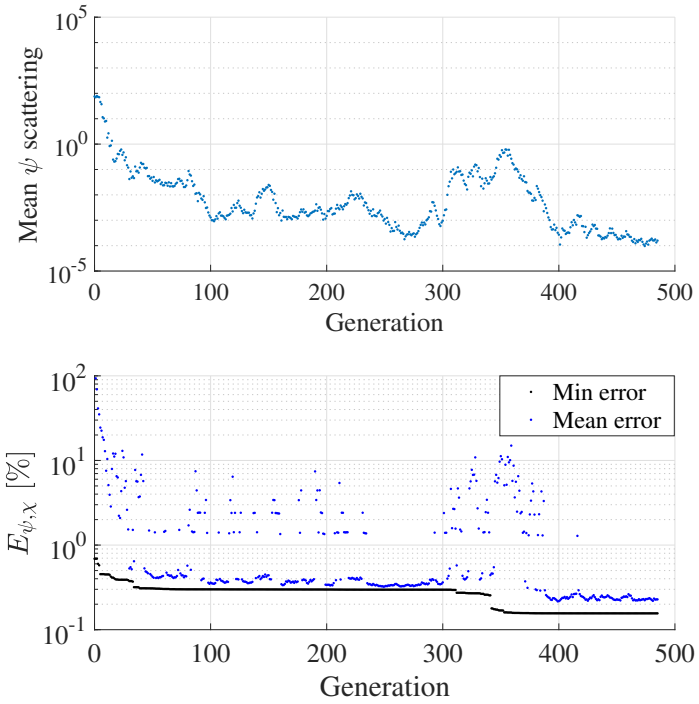

Figure 4.7: Example of the evolution of the error function $E_{\psi,\chi}$ during the genetic research of an optimal minimum.

margins are shown in brackets in Tab. 4.3, and are relatively important compared to the pseudoshock length. Overall, the $\mathcal{X} = [2,4,6]$ model is the most accurate as all pressure errors are around 1%, while all pseudoshock lengths are included in the 99% bounds or have an error of a few percents maximum. Interestingly, an optimization using all cases does not improve the solution further, suggesting that either pieces of physics are missing from the model or that some measurements used for calibration are inaccurate or ill-defined. Table 4.3 presents PRR solutions computed from a normal shock on the bulk flow conditions (PRR_{NS}), or using McLafferty's prediction (PRR_{McL}). The table entries of the current 1D model (PRR_{1D} and L_{1D}) contain the solutions obtained from the GA using $\mathcal{X} = [2,4,6]$. For this solution, the 6 cases pseudoshock profiles are plotted in Fig. 4.8. The model is found to correctly resolve the pseudoshock profiles for the witness cases (right side). This important result shows that a solution for cases 2,4 and 6 is a solution for cases 1, 3 and 5. This is a testimony to the model robustness. It can even be noticed that single-case calibrations are

already sufficient to correctly estimate all the PRR within a 5.3% error margin. A possible improvement to the model would be the replacement of the friction coefficient in Eq. 4.14 with a more complex and universal expression of the boundary layer capacity to withhold adverse pressure gradients. In general, friction coefficients are measured at the centerplane for the rectangular configurations, or computed from empirical correlations, and do not account for the low-speed corner flow dynamics.

Table 4.2: Model errors for different calibration cases.

Set χ used for model calibration	Back pressure rise error [%]						Pseudoshock length error [%]					
	1	2	3	4	5	6	1	2	3	4	5	6
Case 2	0.0	0.0	0.8	0.4	0.6	1.0	1.5	0.0	7.7*	1.2*	1.4*	10.5
Case 4	2.0	2.4	3.5	0.0	2.5	5.3	23.6	22.9	16.0	0.0*	2.8	9.3
Case 6	3.0	3.6	3.1	0.8	0.0	0.0	12.5	15.6	23.9	22.1	11.7*	0.0*
Cases 2, 4	2.2	2.3	1.3	0.3	1.9	3.6	1.0	0.3	5.9*	0.1	0.0*	0.2*
Cases 2, 6	1.2	1.5	2.6	6.3	3.4	3.0	1.3*	2.2*	8.4	13.2	1.3*	3.3*
Cases 4, 6	4.2	4.5	5.2	1.7	0.5	0.6	12.9	11.3	3.6	0.9*	3.5*	3.2
Cases 2, 4, 6	0.0	0.2	1.1	1.1	1.4	1.2	1.9	0.9	6.3*	0.6	0.8*	1.2
All cases	0.2	0.5	1.7	1.1	0.8	0.5	2.7	2.3	4.0*	4.9	3.6*	0.9

The optimized parameters for all the different model calibrations are presented in Tab. 4.4. Unfortunately, it appears that the solution vectors $\psi(\mathcal{X})$ do not converge as more cases are used for calibration. This raises the question of the validity of the solution vectors which were identified by a stochastic process. Rerunning them can result in different solutions, so another process should be used to quantify these solutions and identify an optimal set of

Table 4.3: Static pressure rise ratio (PRR) from pseudoshock foot to tail and pseudoshock length L using different models.

Case	PRR_{NS}	PRR_{McL}	PRR_{1D}	PRR	L_{1D}/D_h	L/D_h
1	1.77	1.67	1.54	1.55	0.836	[0.758 - 0.820]
2	2.02	1.94	1.72	1.72	1.213	[1.103 - 1.199]
3	2.39	2.29	2.00	2.03	1.669	[1.66 - 1.777]
4	4.09	3.03	2.63	2.66	8.772	8.723
5	4.13	3.99	3.47	3.47	6.207	[5.897 - 6.245]
6	9.18	7.28	6.05	6.03	7.271	[6.82 - 7.20]

Table 4.4: Model parameters for different calibration sets χ.

Calibration set χ	Model parameters obtained from genetic optimization algorithm								
	k_{ref}	M_{ref}	a	b	c	d	e	α	β
Case 2	103.6	1.170	0.604	23.50	1.664	3.703	$1.5e^{-3}$	1.034	1.644
Case 4	207.0	1.170	0.347	29.71	1.645	3.102	$2.3e^{-3}$	1.108	1.689
Case 6	96.5	1.159	1.787	35.26	1.84	2.954	$3.9e^{-3}$	0.987	1.646
Cases 2, 4	148.0	0.995	1.693	46.55	1.211	3.047	$2.3e^{-3}$	1.070	2.048
Cases 2, 6	152.2	1.055	0.781	31.97	1.380	3.551	$3.4e^{-3}$	1.111	1.644
Cases 4, 6	151.9	1.076	0.476	42.12	1.729	3.881	$1.7e^{-3}$	1.083	1.615
Cases 2, 4, 6	148.0	1.251	0.656	22.79	1.734	3.773	$1.3e^{-3}$	1.083	1.555
All cases	147.9	1.300	0.934	23.04	1.640	3.529	$2.2e^{-3}$	1.105	1.125

parameters which would converge as the number of cases used for calibration increase. This is the focus of the next section.

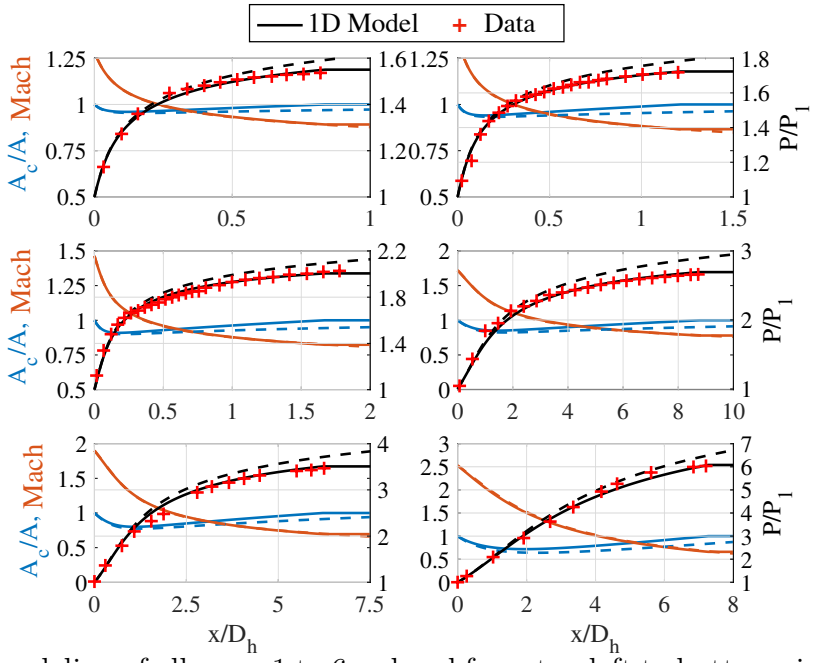

Figure 4.8: 1D modeling of all cases 1 to 6 ordered from top left to bottom right by increasing M_1, calibration set $\chi = [2,4,6]$. Dashed lines represent an inviscid simulation where $Cf_{1D} = 0$.

4.4 Bayesian optimization of the model parameters

The GA has proven that solution vectors yielding a model accuracy within error margin exist. Yet, in the practical case where this model would be used to predict a pseudoshock

profile for new flow conditions, one wonders which set of parameters should be selected. The non-convergence of the parameters renders this selective process impossible using the results from the previous section. Also, the GA was used to be optimized the model with datasets naturally including some margin of error. There are many possible sources of errors, including: pressure measurements uncertainty, identification of pseudoshock bounds in between microphone spatial step, error in evaluating the skin friction coefficient with external models, error in δ^* and θ measurements, negligence of corner effects (affecting the average skin friction, δ^* and θ distributions and confinement ratio), etc. Additionally, the model itself consists of a reduced-order description of a real pseudoshock and necessarily introduces simplifications inducing modeling errors. Lastly, the model is calibrated on the wall pressure profile which can contain traces of the strong compression/expansion waves in the shock train portion. Yet, the model pressure profile cannot resolve these details as it is monotonic. Therefore a relatively large margin of error should be attributed to each individual data point to loosely guide the optimum solution towards a smooth profile. All these concerns can be resolved by resorting to a Bayesian approach to infer the model's optimal set of parameters under these circumstances.

4.4.1 Bayesian inference

Bayesian inference is a statistical inference method which models all sources of uncertainty (including from lack of information) by attributing random variables (*i.e.* probability distribution functions) instead of fixed values to all parameters. It allows to continuously improve the optimization as more data becomes available by using the previous joint-distribution solution as the next initial guess. Bayesian inference procedures are as follows:

1. Build prior distributions for all N_{par} parameters based on any prior information on the model and its parameters. It corresponds to the probability of finding a solution vector ψ and is called Prob(ψ).

2. Define the model likelihood (an N_{par} dimensional joint-distribution) which evaluates

the likelihood of a solution vector ψ to describe the dataset $Data$, defined as Prob(Data,ψ)

3. Use Baye's theorem (Eq. 4.17) and a Markov chain Monte Carlo algorithm to sample the N_{par} posterior distributions Prob(ψ,Data):

$$Prob(\psi, Data) = \frac{Prob(Data, \psi) \times Prob(\psi)}{Prob(Data)} \tag{4.17}$$

4. If more data become available subsequently, the posterior distributions become the next priors and the process repeats.

An example of Bayesian inference of the posterior distribution is shown in Fig. 4.9. Note that the shapes need not be Gaussian. For complex posteriors, the maximum-a-posteriori (MAP) corresponds to the most probable solution which compromises both likelihood and accuracy. The posterior mean minimizes the squared error computed from the maximum likelihood estimate (see Sec. 4.4.3) while the posterior median minimizes the absolute error. Therefore, the posterior mean and median solutions trade likelihood for accuracy as they are further away from the estimated most probable "truth".

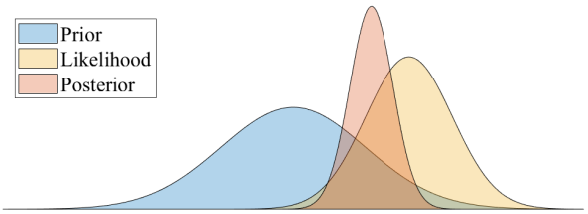

Figure 4.9: Illustration of a prior distribution combined with a likelihood distribution to obtain the posterior distribution.

4.4.2 Determination of the joint-prior distribution

The N_{par} priors are determined based on information currently known. In our case, the GA used in Sec. 4.3.2 has already identified several acceptable solutions ψ. The model calibrated with a set of parameters ψ is called $M(\psi)$. Figure 4.10 shows how the solutions

vectors Ψ obtained from the GA and shown in Tab. 4.4 are distributed. A simple Gaussian distribution fitted through these solutions can serve as a joint-prior for the Bayesian analysis. It contains preliminary information on the model parameters likely values. Note that the Gaussian fit gives a non-zero probability to obtain some negative values for coefficients which should remain position such as M_{ref}. It is not an issue as long as the corresponding model likelihood function tends towards zero for these values. Uniform priors over a range of credible values could be simply chosen, yet this would considerably slow the sampling process of the posterior as many unrealistic solution vectors would not immediately be discarded by the algorithm.

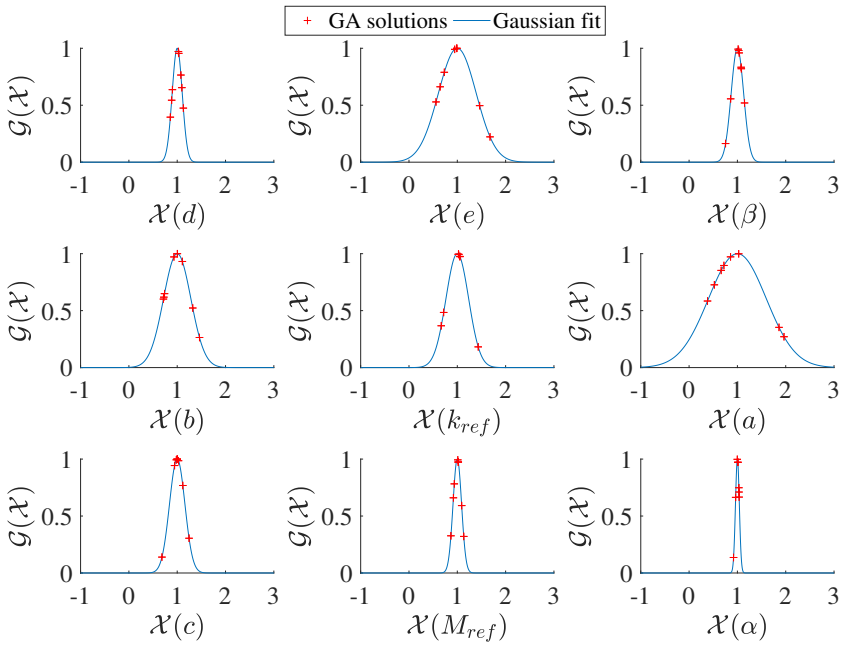

Figure 4.10: Solutions from the GA fitted by Gaussian distributions.

The priors standard deviations are called hyperparameters: they are the prior's parameters and are not being modified throughout the Bayesian inference process. The sensitivity of the posteriors on the priors standard deviations is investigated below in Sec. 4.4.4.3. Based on the results discussed below all the priors standard deviations were doubled compared to the values derived from the GA solutions presented in Fig. 4.10 for the remaining of the analysis.

4.4.3 Likelihood function and maximum likelihood estimate

The likelihood function brings information from the datasets into the Bayesian analysis. The process of computing the likelihood of a particular model defined by a solution ψ involves the computation of an error function just as in the GA process. Increasing the likelihood is equivalent to minimizing the error. Once this error is computed it is compared to its margin of error which has to be previously fixed.

The likelihood function corresponds to the term $\frac{Prob(Data,\psi)}{Prob(Data)}$ in Eq. 4.17. Let us decompose the whole $Data$ into all its components (all data points for example) $Data_i$ with their corresponding margins of errors σ_i. The model prediction of the data-element i (in our case, say pressure at location x_i) using solution vector ψ is called $Data_i^{M(\psi)}$. Defining the σ_i corresponds to evaluating the noise (or error) contained not only in the datasets but in the predicted value as well due to modeling errors. It can be difficult to evaluate both errors, and a common assumption [139] is to consider it iso-directional (zero mean), Gaussian and independent from all other data-element i. This consists in saying that the error cross-correlation matrix is diagonal. It can then be written that:

$$Prob(Data,\psi) = \prod_{i=1} Prob(Data_i,\psi) = \prod_{i=1} \frac{constant}{\sigma_i} \exp\left(- \frac{(Data_i - Data_i^{M(\psi)})^2}{2\sigma_i^2} \right) \tag{4.18}$$

which is then simply normalized by $Prob(Data)$ to form the likelihood function. The maximum likelihood estimate (MLE) is the solution which maximizes the likelihood, *i.e.* minimizes the error function. Note that the MAP is equal to the MLE when the priors are uniform, *i.e.* when it is unregularized.

It is convenient to manipulate the logarithm of the likelihood commonly called the log-likelihood throughout the Bayesian inference process. The loglikelihood is simply the sum of the negative normalized squared errors up to a constant which does not matter to the optimization. Note that this naturally permits to avoid the calculation of normalization

constant $Prob(Data)$.

Let us now define in detail what the error function will consists of. As explained in Sec. 4.3.2 three features need to be resolved by the model: the PRR, the pseudoshock length and the pressure profile roll-off. The error E_{case} was computed for all 6 cases (Tab. 4.1) as an average of the three errors on these three features called $E_{PRR,case}$, $E_{PSL,case}$ and $E_{ROL,case}$ respectively. $E_{PRR,case}$ is computed as the normalized squared error on the PRR:

$$E_{PRR,case}(\psi) = \frac{(PRR_{1D}^{M(\psi)} - PRR_{case})^2}{PRR_{case}^2}. \tag{4.19}$$

$E_{PSL,case}$ is computed as the squared error on the pseudoshock length:

$$E_{PSL,case}(\psi) = \frac{(PSL_{1D}^{M(\psi)} - PSL_{case})^2}{PSL_{case}^2}. \tag{4.20}$$

In sec. 4.3.2, $E_{ROL,case}$ was grossly accounted by the GA by discarding solutions too far off at either the first quarter or half pseudoshock length. With the Bayesian approach, every data point is involved in the calculation of the likelihood function and so $E_{ROL,case}$ is computed as the mean squared error over all the case's data points:

$$E_{ROL,case}(\psi) = \frac{1}{n(case)} \sum_{i}^{n(case)} \frac{(Data_{i,case}^{M(\psi)} - Data_{i,case})^2}{Data_{i,case}^2} \tag{4.21}$$

with $n(case)$ the number of data points per case.

As observed before, some data points located below a shock or an expansion wave can deviate from the overall monotonic pressure rise. This introduces an error as the model cannot resolve this feature, yet data resolving it is used. Additionally, pressure probes also have a measurement margin of error (typically below 1% for modern devices, here set at 1% considering old experimental data is also used). The precise location of the maximum pressure rise marking the end of the pseudoshock can also be determined with a margin of error based on half the experiment pressure probes spatial increment. Lastly, the data extraction process from old figures is imperfect and introduces error in both location and

magnitude. Note that the margin of error also measures the "weight" given to a particular error, so if the main objective is to obtain the correct PRR, one can choose to lower the σ for this error than the others. As the margin of error is defined as half the confidence interval usually based on a 99% confidence interval, the data noise standard deviation σ_i is about twice smaller for Gaussian noise. Based on this knowledge, we can only estimate the margin of errors for the different components by arbitrarily choosing the σ_i (express in [%]). The σ_{PRR} corresponding to all cases $E_{PRR,case}$ was set to 0.5%, the σ_{PSL} corresponding to all cases $E_{PSL,case}$ was set to 1.0%, and the σ_{ROL} corresponding to all cases $E_{ROL,case}$ was set to 10%. These arbitrary values were changed to $[\sigma_{PRR},\sigma_{PRR},\sigma_{PRR}]$ = [1.0,2.0,20.0]% showing little effect, and set equal to $[\sigma_{PRR},\sigma_{PRR},\sigma_{PRR}]$ = [1.0,1.0,1.0]% slightly worsened the accuracy of the model by forcing the solutions through "out-of-trend" data points.

The final expression of the error E used to compute the loglikelihood for a set of parameters ψ is:

$$E(\psi) = \sum_{case=1}^{6} \frac{1}{3}\left(\frac{(PSL_{1D}^{M(\psi)} - PSL_{case})^2}{PSL_{case}^2 2\sigma_{PSL}^2} + \frac{(PRR_{1D}^{M(\psi)} - PRR_{case})^2}{PRR_{case}^2 2\sigma_{PRR}^2} + \sum_{i}^{n(case)} \frac{(Data_{i,case}^{M(\psi)} - Data_{i,case})^2}{Data_{i,case}^2 2\sigma_{ROL}^2 n(case)} \right) \tag{4.22}$$

Note that if the squared differences are all linear functions of ψ, then the joint-likelihood is Gaussian and the posterior can be resolved analytically as the product between joint-prior and joint-likelihood. In our case, the error function is highly nonlinear and cannot be defined analytically. Therefore the class of the joint-posterior distribution is unknown. We need to resort to a stochastic sampling process in order to build it: a Markov chain Monte Carlo (MCMC) sampler.

4.4.4 Markov chain Monte Carlo sampling of the joint posterior distribution

4.4.4.1 Markov chain Monte Carlo sampling

A Markov chain Monte Carlo sampler is a stochastic algorithm which consists in constructing a sequential list, called the Markov chain, of walkers (elements) sampled from a probability distribution function. As a chain walks/samples through the probabilistic domain, it progressively increases its size. Eventually, all its walkers can approximate the distribution they were sampled from. The stochastic process is associated with the decision-making process of finding the successive walker. The probability distribution gradient serves as a primary factor as the walkers tend to avoid the low-probability regions, while the stochastic process permits to satisfy the "Markov property". This refers to the memoryless property of the chain: it ensures that the process of finding the next walker is not fully deterministic *i.e.* solely function of the previous walkers. Eventually, the Markov chain becomes decorrelated with its initial sequence.

Figure 4.11 shows a typical Markov chain built by sampling on the prior distributions projected on the (k_{ref},M_{ref}) parameters plan.

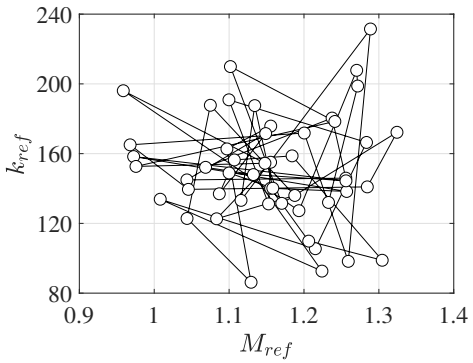

Figure 4.11: A fragment of a typical Markov chain sampling from the priors plotted on the (k_{ref}, M_{ref}) plane.

Native Matlab MCMC functions were first used for the Bayesian inference algorithm but were too slow. Instead, functions from the GWMCMC package from Aslak Grinsted are used throughout this chapter. The package source code relies on the work of Goodman and Weare [47] and Hogg [50]. A sanity check of the MCMC algorithm was performed on the

Gaussian priors, using 1000 independent chains composed of 10000 walkers each. As seen in Fig. 4.12 the Markov chains converge towards the correct result.

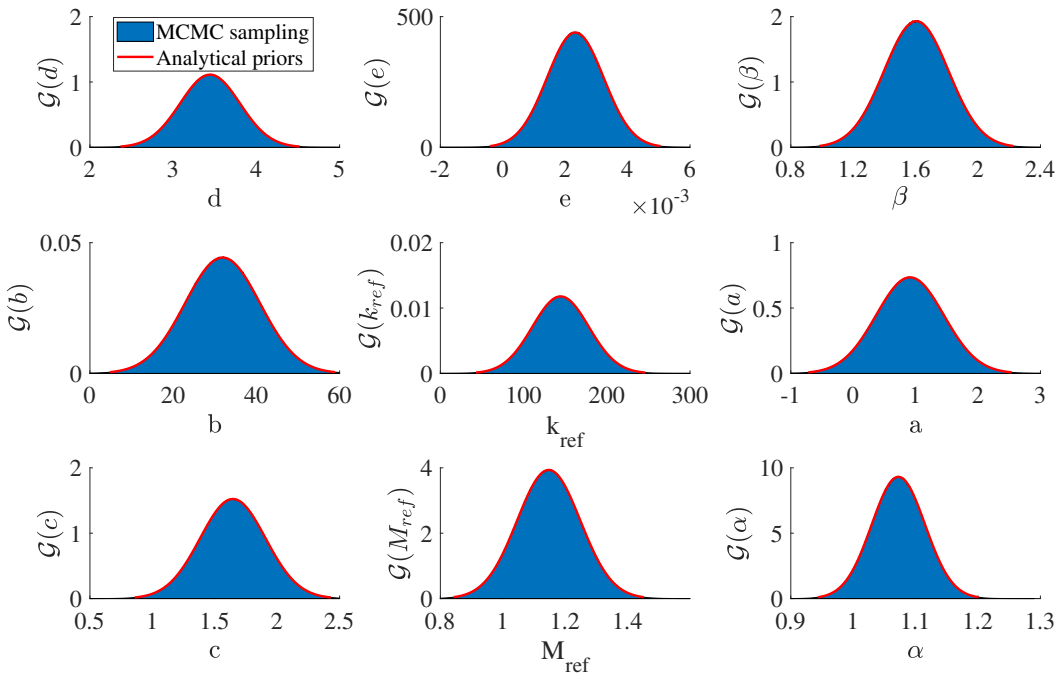

Figure 4.12: Reconstruction of the joint-prior distribution through MCMC sampling.

4.4.4.2 Sampling of the posterior distributions

In Sec. 4.4.4.1 we used the MCMC algorithm to sample from the priors. We now use the same method to sample from the joint-posterior distribution to construct it. By Baye's theorem (Eq. 4.17), drawing samples from the joint-posterior is equivalent to sampling from the product of the joint-likelihood with the joint-prior. By moving into the logarithmic space, this product simply becomes the sum of Eq. 4.22 with the "logprior". The logprior is the logarithm of the joint-prior 9^{th} dimension Gaussian. It is a simple sum of the 9 priors without the exponential up to a constant which does not matter to the MCMC sampler. The logarithm function is monotonic and does not change the optimization process.

The sampling of the joint-posterior was performed through 1000 independent Markov

chains composed of 20000 walkers each. This computation ran in parallel over 8 cores for about 8 hours. A typical sampling of the parameter k_{ref} over a fraction of a chain is shown in Fig. 4.13. Auto-correlations of all parameters averaged over the 1000 chains shown in Fig. 4.14 permit to validate the number of iterations chosen which ensures a large effective sample size. It is, in fact, necessary to run each chain long enough to ensure that the final values are uncorrelated with the starting positions. The starting positions are randomly spawned across the priors.

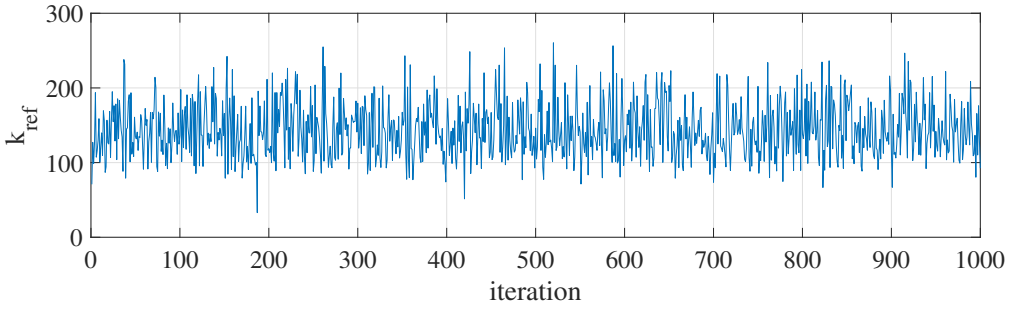

Figure 4.13: Sampling of parameter k_{ref} from a typical Markov chain.

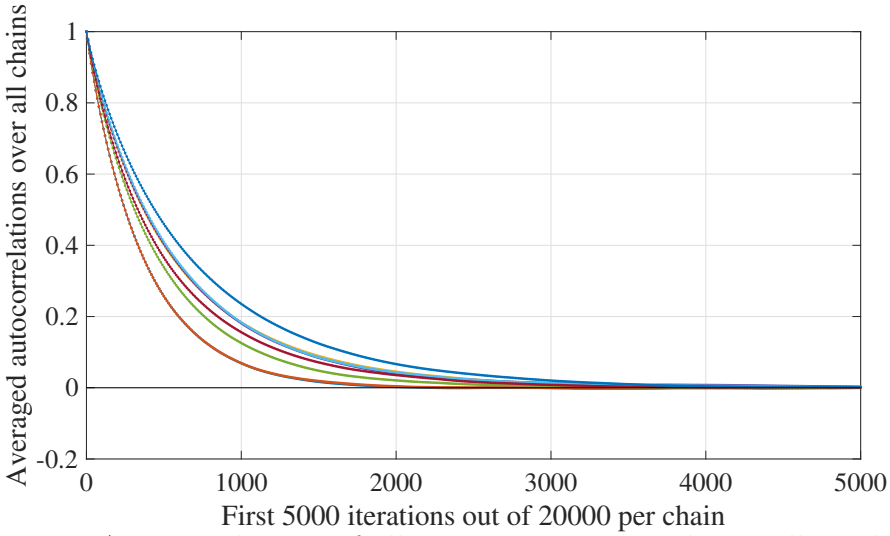

Figure 4.14: Autocorrelations of all parameters averaged over all Markov chains.

Figure 4.15 presents the posterior distributions for the 9 parameters, alongside the 9×9 cross-correlations forming together the joint-posterior. The cross-correlations between all parameters show that no parameter is completely independent *i.e.* a circular shape exists with the other 8 parameters. c can be considered the most independent parameter, while

d and e which characterize the amount of friction in the system appear to be related while independent of the other variables. A particularly strong correlation appears between k_{ref} and α which suggests that one variable could be modeled by the other.

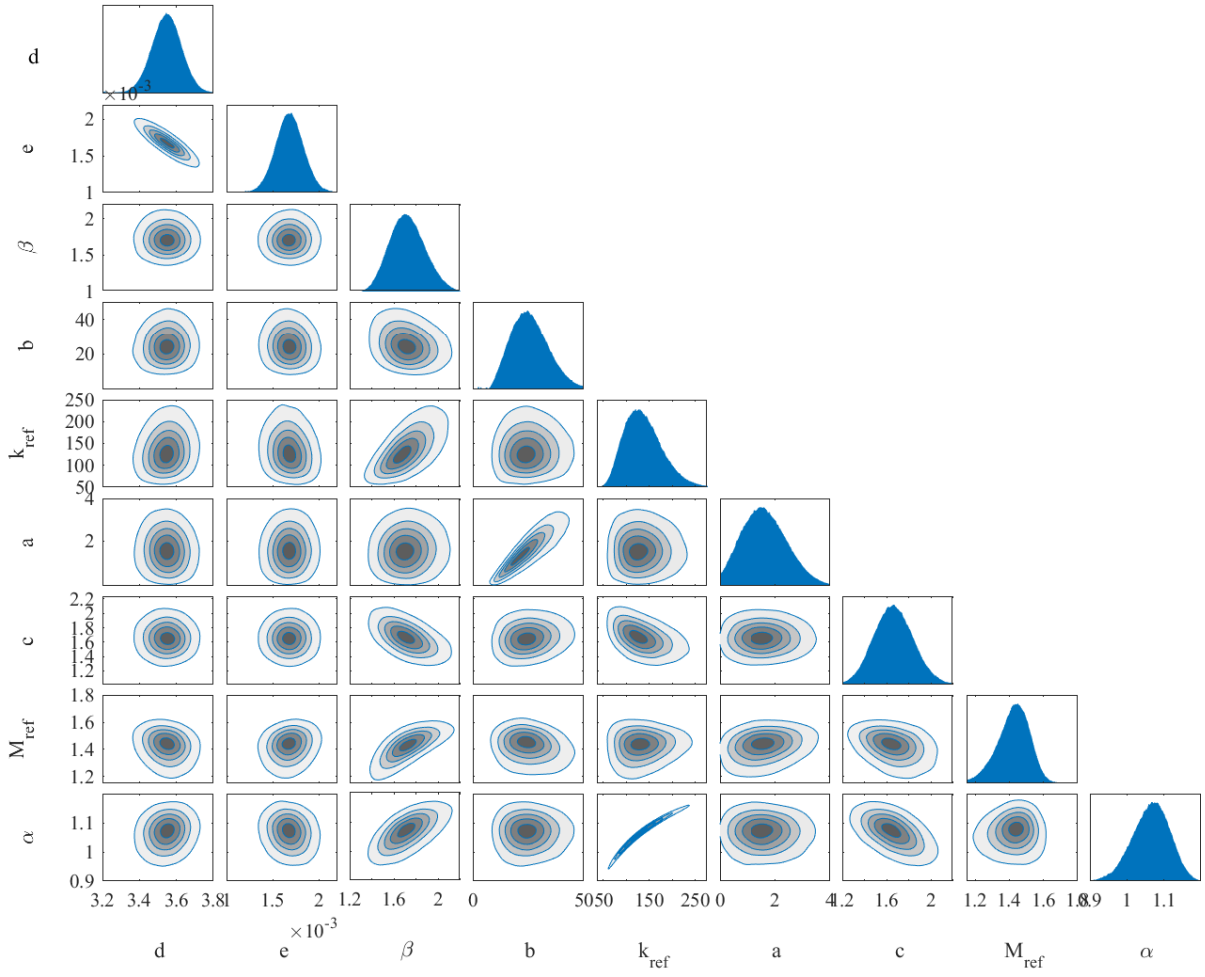

Figure 4.15: Posteriors distributions and cross-correlations between all the 9 parameters.

A comparison of the priors and posteriors for all parameters is shown in Fig. 4.16 highlighting the amount of information gained through the Bayesian analysis. Note that no posterior has the simple Gaussian shape of its corresponding prior.

Figure 4.17 shows the realization of many profiles obtained from 200 independent samples. The lines are black and transparent such that only large overlap regions are revealed. The most realized regions coincide with the least-squared error with the DNS dataset and agree

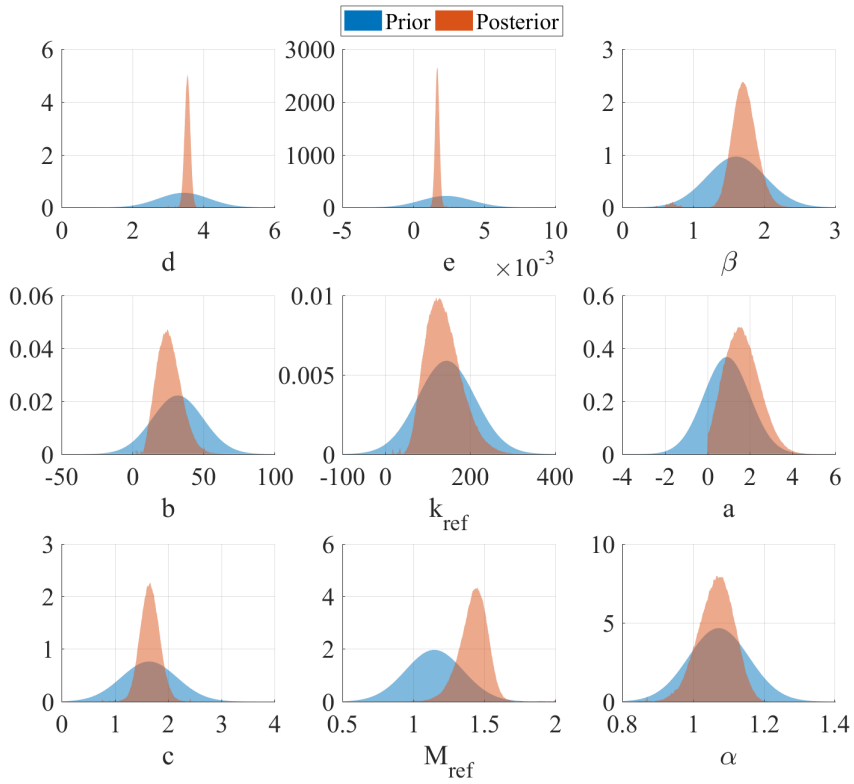

Figure 4.16: Prior and posterior distributions of the 9-parameters model.

Table 4.5: Model parameters derived from the posteriors distributions.

Posteriors	Error	k_{ref}	M_{ref}	a	b	c	d	e	α	β
MAP	0.92%	128.0	1.449	1.46	24.8	1.665	3.546	$1.70e^{-3}$	1.066	1.70
Median	0.57%	133.3	1.431	1.65	25.2	1.659	3.547	$1.68e^{-3}$	1.067	1.71
Mean	0.48%	137.5	1.424	1.64	25.9	1.660	3.544	$1.69e^{-3}$	1.064	1.71

to the dataset best. The mean solution is plotted in blue, and the original Smart model solution is also presented to highlight the improvements that have been made.

Finally, various solutions ϕ are identified from the joint-posterior which minimizes $E(\phi)$. It is reminded that these errors are summed over the 6 cases.

4.4.4.3 Sensitivity to hyperparameters

Choices were made to find priors based on prior information. Yet, running many more times the GA would surely result in different priors affecting the posteriors distributions. Running the MCMC algorithm choosing larger priors standard deviations permits not only

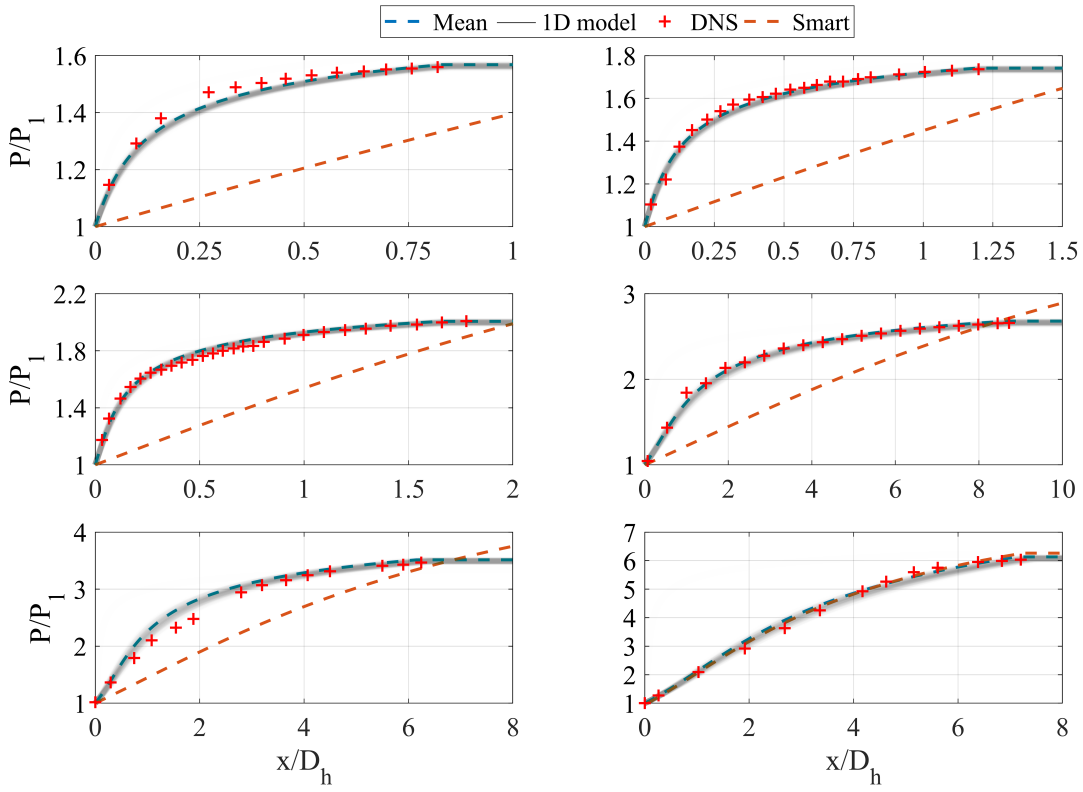

Figure 4.17: 1D model profiles obtained from 200 independent samples. The lines are transparent and the color is proportional to the number of overlapping.

to explore a larger parametric domain but to acknowledge the uncertainty on the lack of prior information. Hence a sensitivity analysis was performed on these hyperparameters.

Typical sensitivities of posterior distributions on their priors standard deviations are shown in Fig. 4.18 for 3 typical parameters. The distributions are converged for a doubled standard deviation, which is the values of the priors used in Sec. 4.4.4.2. Increasing the priors standard deviation means that we reduce our confidence in the GA results and allow more values to be considered in the Bayesian framework. Essentially, it relaxes the bounds of the plausibility of the parameters while still retaining some of the information obtained from the GA calculations. Note that the asymptotic profiles (standard deviation tends to infinity) would result in a flat prior. It would require many more chains to converged towards the posteriors and would discard the viable and accurate solutions found by the GA. In general, as the number of data points becomes large the dependence on the prior decreases [139].

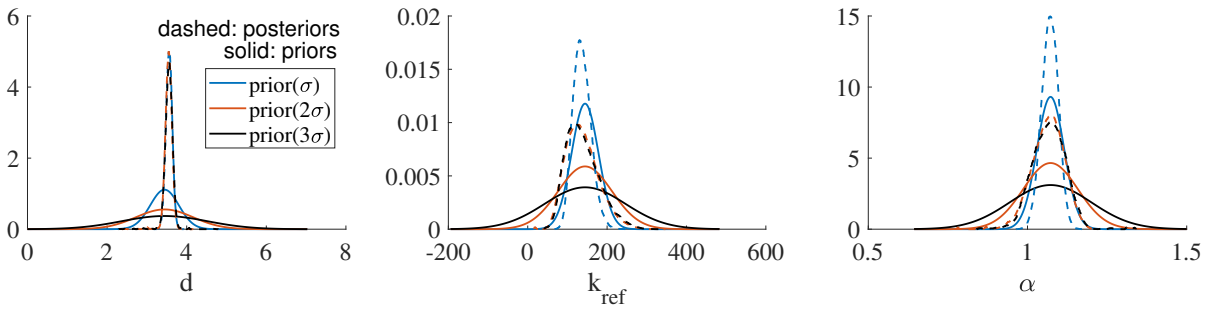

Figure 4.18: Impact of the priors standard deviations on the posterior distributions.

4.4.5 Model order reduction

The Bayesian analysis quantifies the parameters range of likelihood. It offers the opportunity to identify cross-correlations between parameters. It is then up to the user to make an active use of these and reduce the order of the model. This will necessarily reduce the volatility of the parameters and narrow all the posteriors. However, little information can be lost when the cross-correlation is very high. This is the case for parameters k_{ref} and α: the latter can be defined as a function of the first. This is shown in Fig. 4.19 where a polynomial function of k_{ref} can be fit and replace the ninth parameter, reducing the order of the model to 8.

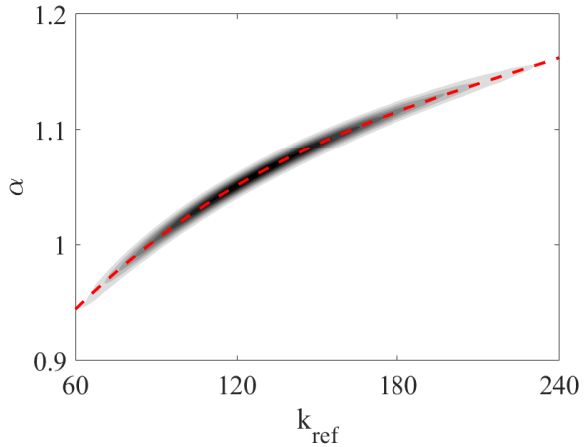

Figure 4.19: Cross-correlation between parameters k_{ref} and α with a fitting third order polynom.

Figure 4.20 shows the resulting new joint-posterior based on that compact model.The new

posteriors are compared with the priors and $N_{var} = 9$ posteriors in Fig. 4.21. Other cross-correlations were used to reduce the model to order 6 by using the weaker cross-correlations between parameters d and e and between b and a seen in Fig. 4.15. The resulting joint-posterior was essentially reduced to 6-dimension joint Dirac function on the minimum error values. Note that the error was still very low (below 1% just as in Tab. 4.5) but this would defeat the purpose of the Bayesian analysis which is to provide information over the widest range in parametric space.

Finally, another important information can be extracted from the current analysis. The error function used to define the likelihood can be instead be computed in every case separately. The 6 resulting joint-posteriors (one per case) are sampled from statistically independent datasets. These can then be plotted alongside some of the key characteristics of these cases such as their confinement ratio or their flux-conserved Mach number M_1. This is done in Fig. 4.22 which presents a 2D contour of the joint-posteriors for the 8-parameters model. The Y-axis represents the case M_1 and the X-axis the posterior distribution. The contours are linearly interpolated in between M_1 values. It can be noticed that contrary to the genetic algorithm results, the optimized solutions ψ are relatively constant. This analysis permits to offer a user, given a prominent inflow variable as the M_1 for instance, a set of parameters with an interval of confidence to use with the model. The MAP value offers a compromise between plausibility and accuracy while the mean values offer the highest accuracy. It is only possible to identify a set of parameter to model pseudoshocks which inflow properties are bounded by the cases used during this study (see Tab. 4.1). A Matlab script of the 1D model calibrated for case 4 is presented in Appendix B.

4.4.6 Notes and instructions to users

A reduced-order model for pseudoshocks based on the flux-conserved approach of Smart [116] was derived through data-driven optimization. A pressure growth rate, which serves as a closure equation, is constructed in light of new understanding of pseudoshock physics.

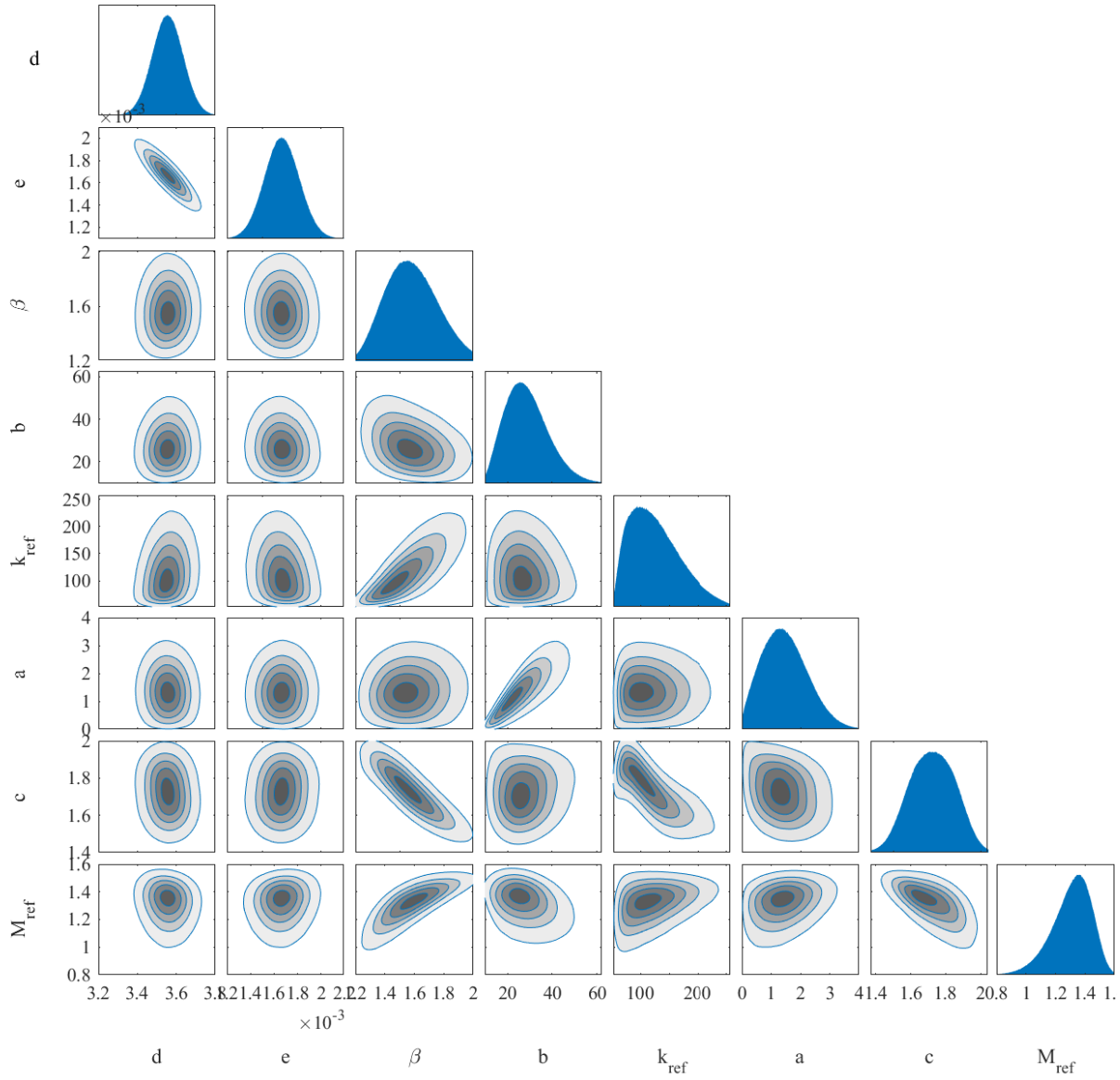

Figure 4.20: Posteriors distributions and cross-correlations between all the 8 parameters.

Once calibrated, the model is able to predict the pseudoshock length, pressure rise and wall pressure roll-off over a wide range of inflow conditions relevant to a dual-mode scramjet isolator. The model is sufficiently robust to estimate these metrics within a 2% error over the whole dataset when calibrated using only half the available statistically-independent data. While computationally inexpensive, this model requires a complete description of the

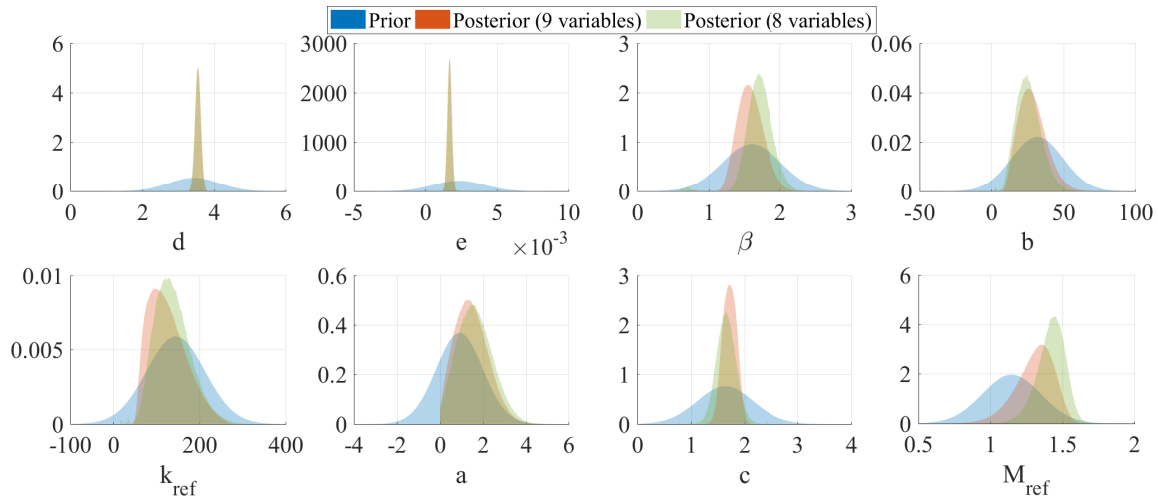

Figure 4.21: Prior and posterior distributions of the compact 8-parameters model compared with the $N_{var} = 9$ posteriors.

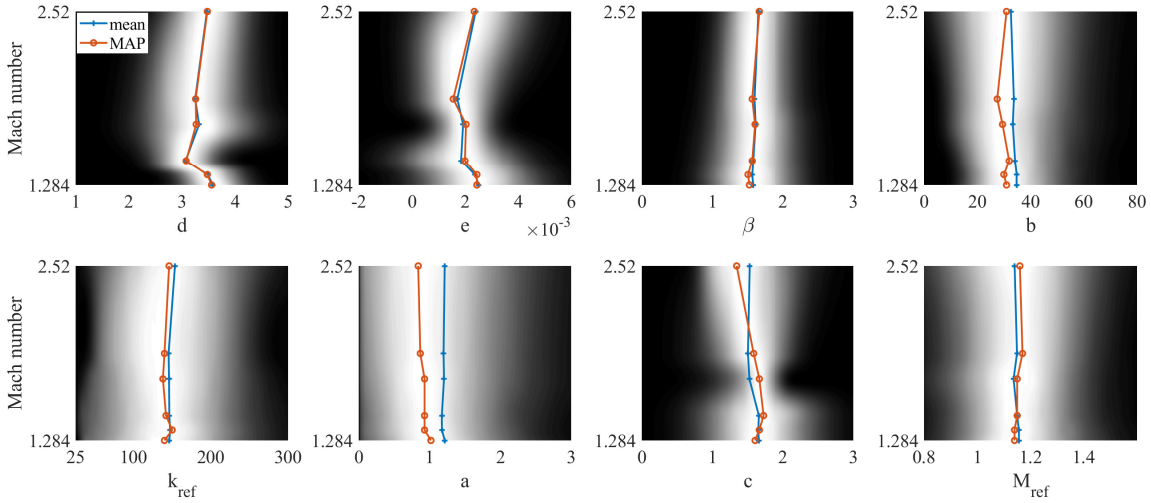

Figure 4.22: 8-parameters model posteriors calibrated on each case separately and plotted against the calibrating case's Mach number.

inlet flow. The model presented in this paper can be used by following these steps:

1. Locate the pseudoshock foot location. This position is located just upstream of the leading shock, where the wall pressure profile begins to rise due to the shock train.

2. Measure/calculate the bulk flow values at this location: P_0, T_0, M_0, $C_{f,0}$, $\mathcal{A}_*$, $\mathcal{A}_\theta$, and T_t.

3. Compute the flux-conserved state at the pseudoshock foot using Eqn. 4.3 - 4.7.

4. Find a set of model parameters either from:

   - Use the MAP solution determined from the whole dataset in Tab. 4.5. These coefficients should be the safest to use.
   - Interpolate in the M_1 space the 8 coefficients from Fig. 4.22 using either the MAP or mean lines. The 9^{th} coefficient, α, is defined as : $\alpha = 0.771004521308883 + 0.003574187209155\, k_{ref} - 0.000012561088603\, k_{ref}^2 + 0.000000018594761\, k_{ref}^3$. These coefficients could be more accurate than the previous solution, yet were derived from a unique experiment. 4.5.

5. Use the 1D script provided in the appendix B with updated coefficients and initial state.

4.5 Pseudoshock dynamic model

4.5.1 Summary of Chapter III findings

The pseudoshock response to inflow confinement ratio harmonic perturbations was studied in Chap. III. The motivation was to improve our understanding of pseudoshock response to inflow perturbations, as could happen during flight as was seen in Fig. 1.5 in Chap. I. The figure shows the time-signal of the angle of attack measured on the HyShot-II [117] during reentry when functioning in scramjet mode. Modeling the impact of such instabilities on the pseudoshock would help design robust isolators.

In particular, Sec. 3.4 showed the existence of a resonance between the pseudoshock foot and tail oscillation amplitudes. Two mechanics behind this phenomenon were identified and can be summarized as follow. First, the upstream perturbation propagates through the shock cells with a certain time-lag, affecting their sizes such that the shock train motion becomes similar to a spring. The centerline shock-to-shock interactions, therefore, resemble that of a

simple harmonic oscillator. Second, the trailing shocks would periodically weaken/strengthen when convecting downstream/upstream, *i.e.* the shocks pressure rise depends on the local flow relative velocity (Fig. 3.28). This causes the shock train trailing shocks to disappear periodically which drastically increase the apparent pseudoshock length oscillation. This phenomenon is referred to as the apparent Mach number effect, and the shock train is defined as being in a strong/weak state when convecting respectively upstream/downstream. Figure 4.23 shows some pressure snapshots at different phase ϕ revealing the variation of shock train (hence pseudoshock) length over a half-period.

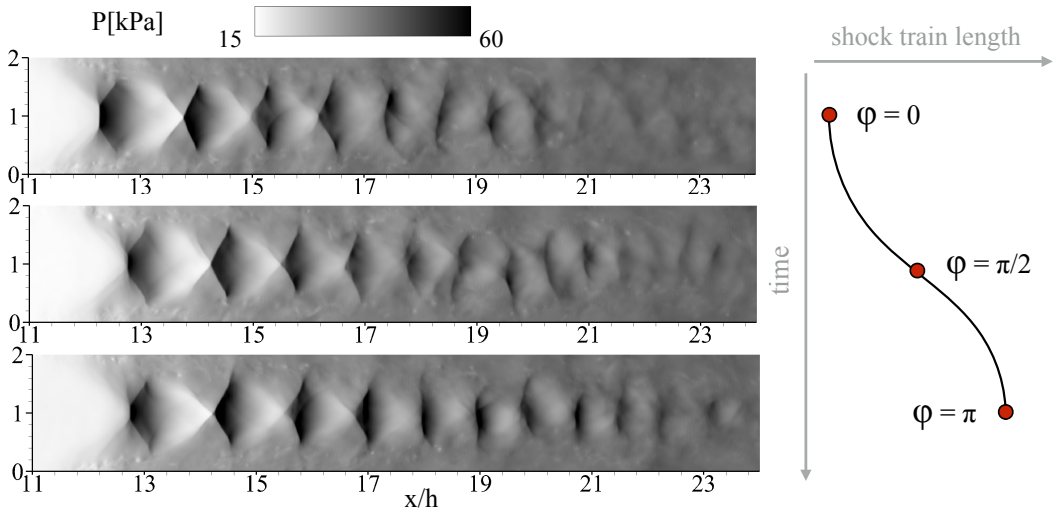

Figure 4.23: Static pressure snapshots of normal shock train DNS [33] during forced harmonic oscillation.

The impact of the shock train strong/weak state on the pseudoshock length is somehow counter-intuitive. The overall pressure rise occurs either through shock compressions (pressure strain rate source term) or in the boundary layer and mixing region (mean/turbulent kinetic energy dissipation source term). As the latter energy conversion process has a slower rate (Sec. 3.3), the same pressure rise caused by shock would occur over a larger distance through dissipation. As there always is a pressure increase in the mixing region due to the viscous deceleration of the flow, the shock train pressure rise is inferior to the pseudoshock PRR. Hence, when the shock train is in a weak state and provides a smaller pressure increase,

a longer mixing region is necessary to accommodate the same back pressure. The opposite is true, and a strong shock train typically results in a smaller mixing region and pseudoshock length. The sketch in Fig. 4.24 illustrates both strong and weak states.

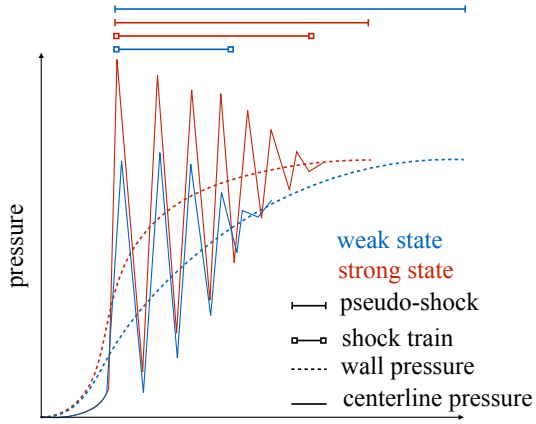

Figure 4.24: Sketch of centerline and wall pressure throughout pseudoshock in both strong and weak states.

4.5.2 Dynamic model objectives

The objective of this section is to model this resonance effect on pseudoshocks using the 1D model. As only case 4 (Tab. 4.1) is considered in this section, the optimal $\chi = 4$ calibration set parameters ψ shown in Fig. 4.22 is used. The following notations are introduced in this section. x_X is the time-varying X% pressure rise location measured from the inlet plane pressure ($P_{in} = 14.5$ kPa) to the outflow back pressure ($P_{out} = 46.2$ kPa). ϕ_X refer to the phase lag between the pseudoshock foot oscillation with the X% pressure rise location. Lastly, the oscillation amplitude at the exact excitation frequency (93 Hz) extracted from spectral decomposition is called $\mathcal{E}_X$.

4.5.2.1 Qualitative response

The oscillating pseudoshock datasets comprise one excitation frequency $f = 93$ Hz on a spatially-resolved grid, and several inflow oscillations at $f = [20, 60, 100, 200, 500, 1000]$ Hz on a coarse grid. Only the spatially-resolved case at 93 Hz is used to quantitatively calibrate

the dynamic model. The following qualitative observations could still be made from the coarse cases. At the lowest oscillation frequency (20 Hz), the shock train simply moved around without any apparent change to its inner structure. At intermediate frequencies (100Hz), the resonance phenomenon appeared at the end of the shock train while the first cell size remained approximately constant. At the highest frequency (1000 Hz) the shock train tail was standing while, most interestingly, the shock train first cells were now resonating. This suggests that the shock train cells possess different resonating frequencies.

The spring-like shock train structure is revealed by plotting isocontours of positive and negative streamwise pressure gradient. The shocks are shrinking in size while the local density and temperature keep increasing. Assuming a local harmonic oscillator response, the larger shock-to-shock distance would increase the time lag. Also, the local flow density and speed of sound are related to the acoustic impedance, which is increasing along the pseudoshock: this suggests fewer reactions to the highest frequencies hence a smaller resonance frequency. All these observations are consistent with those described in the previous paragraph.

4.5.2.2 Quantitative response

Fig. 4.26 (top) shows the static model pseudoshock compared to the DNS profile. $\mathcal{E}_X$ and ϕ_X were extracted from the DNS dataset in the PRR space, and are plotted along space in the bottom figure. Every cross represents a percent increment in PRR from 10 (foot) to 100% (tail). While the 1D model pseudoshock length equals the DNS pseudoshock length, their PRR profiles can slightly differ along the first D_h. Therefore the $\mathcal{E}_X$ and ϕ_X profiles are simply projected in space ($\mathcal{E}_x$ and ϕ_x) such that the 1D model can use the exact same profiles. Some oscillations due to the centerline shocks are present, and a monotonic approximated profile is defined. Resolving the approximated profiles of the phase lags and oscillation amplitudes is the quantitative objective of the dynamic model. Note that the approximated profiles for $\mathcal{E}_X$ and ϕ_X do not use the last 4 points corresponding to the last 4 percents (97 to

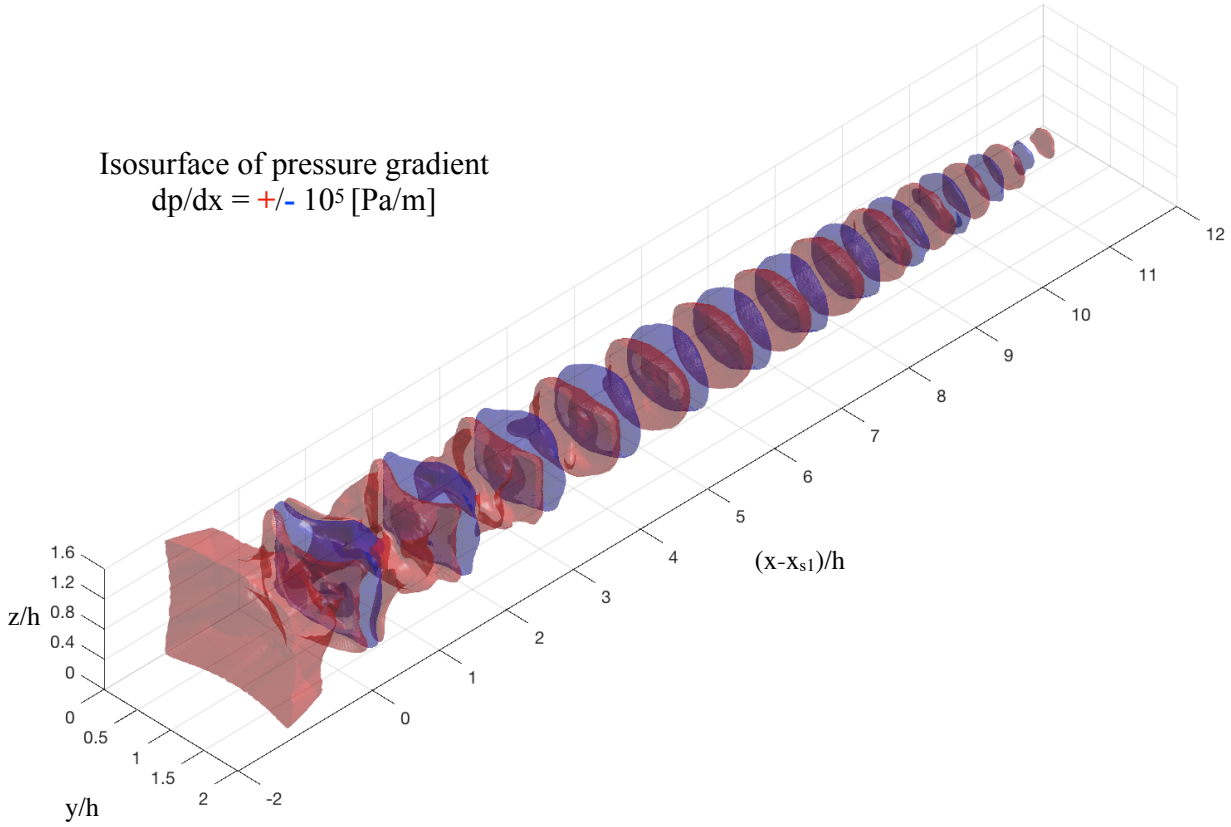

Figure 4.25: Isocontour of the static pressure gradient $\frac{\partial P}{\partial x}$ in the shock train region.

100% PRR). The reason they are discarded is due to their steeply decreasing signal-to-noise ratio shown in Fig. 4.27. It is postulated that this is due to the proximity of these points to the numerical back pressure. The fluctuating wall pressure signal, despite filtering, can sometimes not find a position corresponding to these PRR percents, especially in weak state. Hence the signals can suddenly jump in time which results in a higher signal-to-noise ratio and a collapse of the sinusoidal shape. This explains why ϕ_X converges towards zero for X% $>$ 96 (signals lose coherence), and why the oscillation amplitude decreases beyond 90%.

Fig. 4.26 (bottom) reveals a complex anharmonic response. The initial pseudoshock portion (the first 2 shock train cells) increase of phase lag with the foot, while the rest of the shock train increases the oscillation amplitude. The signals similarly start to lose coherence

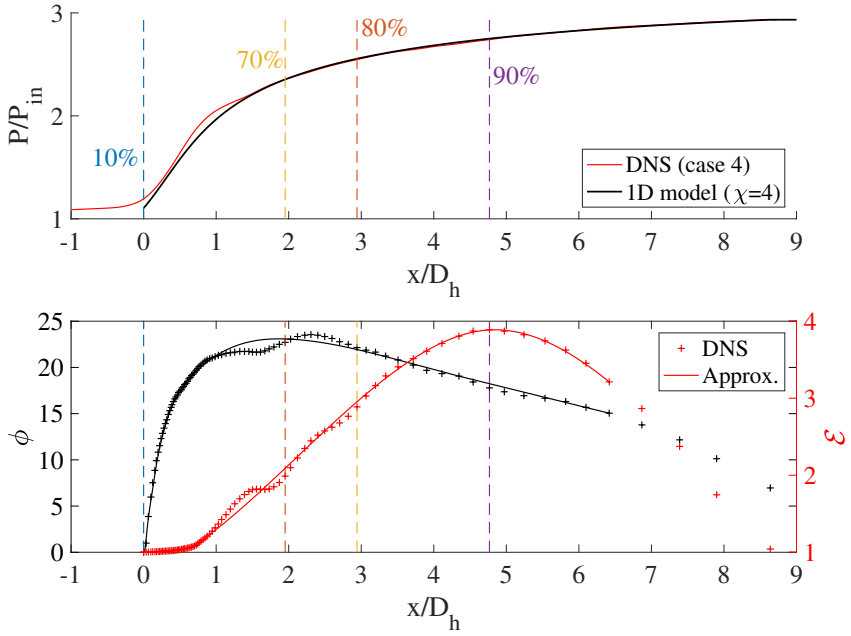

Figure 4.26: (Top) Comparison between DNS time-averaged wall static pressure and 1D model (calibration $\chi = 4$)profiles. (Bottom) Local oscillation amplitude $\mathcal{E}$ and phase lag with pseudoshock foot ϕ

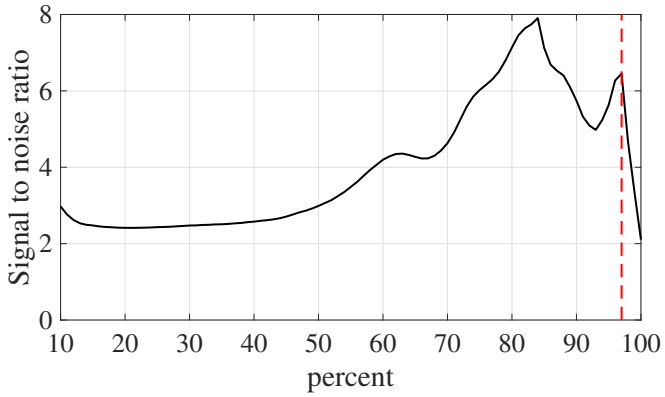

Figure 4.27: Local signal to noise ratio along the percentage pressure rise (100 is the pseudoshock tail) computed as the ratio between the first and second maximum values of the local oscillation amplitude spectra. The red line corresponds to 97% PRR.

in the mixing region and collapse near the computational domain outflow. This suggests a region of higher stiffness and resonance frequency at the pseudoshock foot, and a progressive decay: once again this is coherent to the qualitative observations made in Sec. 4.5.2.1.

4.5.2.3 Model input

In Chap. III, the resonance was revealed by wall pressure signals. Finding the precise end of the pseudoshock becomes impossible when looking at an instantaneous highly fluctuating pressure profile. The location of 80% PRR (x_{80}) was therefore arbitrarily chosen from the filtered wall pressure profile (monotonic as seen in Fig. 3.21 (left) or Fig. 4.28 (top)) to quantify the resonance response. This roughly corresponds to one-third of the pseudoshock length or half the shock train where the pressure growth rate is high enough to permit accurate measurements of oscillations amplitude and phase. Figure 4.28 shows on the top a typical instantaneous and filtered wall pressure profiles from which these signals are again extracted. These signals are plotted in the bottom left figure, alongside their respective amplitude single sided spectra ($\mathcal{SSA}$) in the bottom right. As we move further downstream throughout the pseudoshock, the oscillations start to deform from the inflow purely harmonic excitation signal. Turbulence and other modes get excited as seen in Fig. 4.28 (spectra are non-Dirac). Therefore, the peak amplitudes measured from their spectrum $\mathcal{E}_{10}$, $\mathcal{E}_{70}$ and $\mathcal{E}_{80}$ contain only a fraction, albeit dominating, of the whole signal energy. It was decided to extract this precise harmonic component of interest and discard the rest as noise to build the dynamic model. However, this reduces the energy of the signal by truncating non-93 Hz responses. This is an approximation as it is expected that turbulence and the shock train self-oscillations [52] would progressively diffuse the energy of the dominant harmonic to others. Yet modeling these effects is beyond the scope of the current model.

The DNS 10% pressure rise location signal x_{10} is also presented in Fig. 4.28. It is located in the small region upstream of the leading shock where pressure starts to increase due to diffusion throughout the subsonic boundary layer: it marks the start of the pseudoshock region. It is almost a purely harmonic 93 Hz signal x_{10} with $\mathcal{E}_{10} = max(\mathcal{SSA}(x_{10})) = 12.0$ mm. This suggests that the upstream turbulent boundary layer has efficiently transported the inflow perturbations with little spectral diffusion. It defines the foot oscillation $x_f = \mathcal{E}_f \cos(\omega t)$ $\mathcal{E}_f = max(\mathcal{SSA}(x_{10})) = 12.0$ mm for the remainder of the study: it is the input

of the dynamic 1D model. It is reminded that only 4 periods are included in the dataset, which is the maximum the expensive computational runtime could resolve. All data $\mathcal{E}_X$ and ϕ_X used to create the dynamic 1D model could be more accurately evaluated had many more periods be resolved in the simulation. Lastly, one of the perks of the 1D model is the exact definition of the end of the pseudoshock (where $A_c/A = 1$): it is therefore possible to define the tail oscillation signal $x_t = \mathcal{E}_t \cos(\omega t + \phi_t)$ where $\mathcal{E}_t$ is the oscillation amplitude at the tail of the pseudoshock (i.e. the wall back pressure rise location), and ϕ_t is the phase lag induced by the shock-to-shock interaction (as in a simple spring) up to the shock train tail.

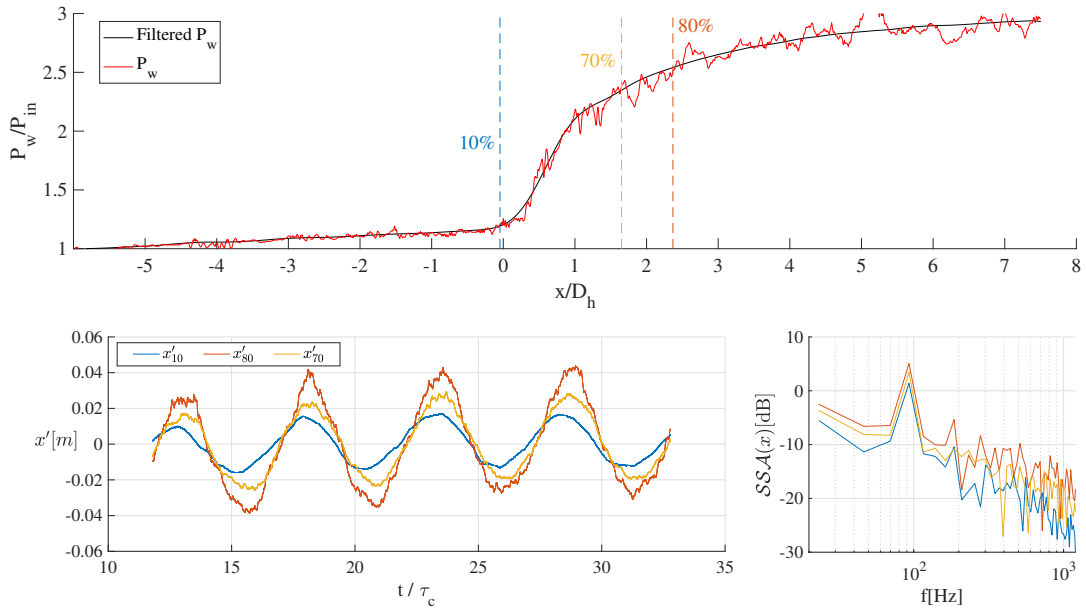

Figure 4.28: (Top) Typical instantaneous wall static pressure, filtering and pressure rise location signals extraction. (Bottom left) Time fluctuations of 10, 70 and 80% pressure rise locations from the oscillation simulation presented in Sec. 3.4.2 (Fig. 3.25) alongside (bottom right) their respective single-sided amplitude spectra in dB [ref = 1cm].

The model objectives are to resolve both the $\phi(x)$ and $\mathcal{E}(x)$ profiles and the qualitative observations when forcing the pseudoshock foot to oscillate at 93 Hz with a 12.0 mm amplitude. It is expected that resolving the quantitative observations will naturally result in a pseudoshock dynamic behavior in agreement with the qualitative observations.

4.5.3 Anharmonic oscillator model

4.5.3.1 Methodology

Now that the goals are set, the method used to adapt the static 1D model to account for inlet perturbations is presented. It is derived from the observation that the response is composed of both a forced driven locally harmonic (hence globally anharmonic) oscillator component and the apparent Mach number effect (Chap. III). These components will be calibrated based on the information presented in Sec. 4.5.2.1 and Sec. 4.5.2.2.

The apparent effect accounts for the relative flow speed between the shock and the flow when computing the real shock pressure rise. It is therefore necessary to first include the pseudoshock movement caused by the anharmonic component. The locally harmonic oscillator response is therefore quantified first. It will be referred to as the harmonic component despite its globally anharmonic nature. The oscillation signal for a particular location x is governed by the following equation:

$$\frac{\partial^2 x}{\partial t^2} + 2\xi(x)\omega_0(x)\ \frac{\partial x}{\partial t} + \omega_0(x)\ x = \omega_0^2(x)\ x_f, \tag{4.23}$$

where the harmonic oscillator component of the pseudoshock response is fully quantified by its local stiffness $\xi(x)$ and natural pulsation $\omega_0(x)$. The phase lag at every position along the pseudoshock ϕ and the oscillation amplitude are evaluated from Eqns. 4.24 and 4.25:

$$tan(\phi_{harm}(x)) = \frac{2\omega_0(x)\xi(x)\omega}{\omega^2 - \omega_0(x)^2}, \tag{4.24}$$

and

$$\mathcal{E}_{harm}(x) = \frac{\omega_0(x)^2\mathcal{E}_f}{\sqrt{(\omega^2 - \omega_0(x)^2)^2 + (2\xi(x)\omega_0(x))^2\omega^2}}. \tag{4.25}$$

The DNS dataset is used to find the pseudoshock $\xi(x)$ and $\omega_0(x)$ from $\phi(x)$ and $\mathcal{E}(x)$. However, we cannot directly use the measured phase lag and amplitude ratio. Indeed, these

measurements contain both the effect of the locally harmonic resonators and the apparent Mach effect. They cannot be used to close the harmonic oscillator system of equations as is usually done. Instead, we will assume certain profiles for (ξ,ω_0) for the time being, allowing us to fully resolve the pseudoshock response.

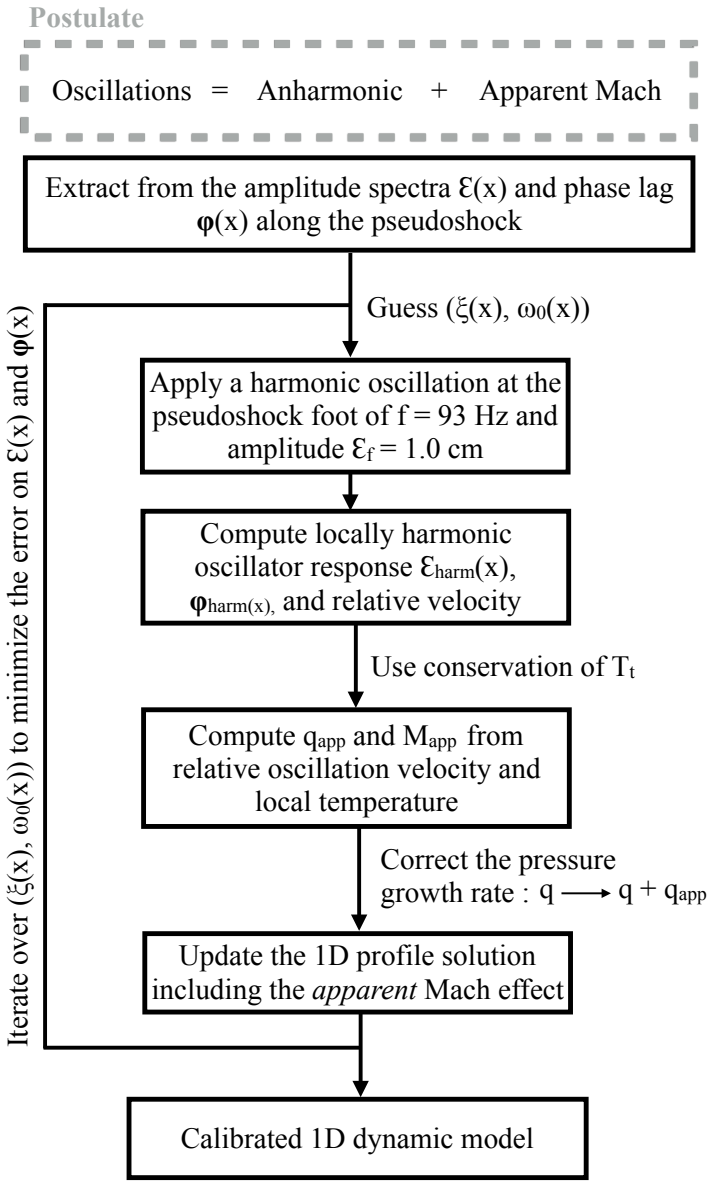

Figure 4.29: Schematic of the derivation of the dynamic model parameters.

The second step is to oscillate at 93 Hz and amplitude 12 mm the 1D model foot location x_f. Then, we can apply the harmonic oscillator solution determined in step 1 to compute

the oscillation amplitude $\mathcal{E}_{harm}(x)$ (necessarily inferior to $\mathcal{E}_X$ as the apparent Mach effect increases the amplitude) and phase lag $\phi_{harm}(x)$ along the pseudoshock. It is now possible to compute the local convecting velocity at every position along pseudoshock. The local apparent Mach number is defined as the local Mach number minus the relative Mach number.

The third step is to modify the 1D model local pressure growth rate based on the local convecting velocity. The apparent Mach effect on the local pressure growth rate must be quantified first. Figure3.28 showed how the shocks pressure rise increase when in a strong for $M_{app} > M$ and vice versa. Let us define $\tilde{P}_1$ the leading shock centerline pressure, and $\dot{P}_1$ obtained by using normal shock relations on the upstream apparent Mach number. The centerline shock convective velocity can easily be computed from the time-resolved dataset. However, it is difficult to identify the instantaneous flow velocity because of the three-dimensional turbulence intensity. Hence it is decided to use the averaged streamwise velocity right upstream of the leading shock. The sum of the bulk flow speed with the instantaneous relative velocity is used to compute the apparent Mach number and corresponding $\dot{P}_1$. Figure 4.30 presents the correlation between $\dot{P}_1$ and $\tilde{P}_1$. These profiles collapse well on the identity line despite the highly turbulent nature of the flow, with an average of 1.002 and a correlation coefficient of 0.87. This is remarkable as $\dot{P}_1$ is simply computed from the pre-shock time-averaged streamwise velocity and using normal shock relations, therefore assuming that the shock front is perfectly perpendicular at every timestep which is only true for time-averaged contours. This strongly suggests that the 1D model pressure growth rate closure equation can be modified to account for the apparent Mach number effect by simply replacing the kinetic energy q with the local apparent local kinetic energy $q_{app} = q - q_{rel}$ with q_{rel} being the relative speed kinetic energy in the streamwise direction.

The last step is to simply iterate on (ξ,ω_0) in order to minimize the error between $\mathcal{E}_{DNS}(x)$ and $\mathcal{E}_{1D}(x)$ along the pseudoshock.

Figure 4.29 summarizes the methodology used to derive the dynamic 1D anharmonic oscillator model. Fig. 4.31 shows how the apparent Mach effect affects the pseudoshock

length and back pressure recovery. The dashed lines correspond to the simple harmonic model alone, and the solid line represents the full anharmonic model. Note that the effect is consistent with the illustration of the weak/strong shock trains shown in Fig. 4.24 as the pseudoshock length increases when moving downstream ($M_{app} < M$) and vice versa. It is noticed that not only does this effect increases the oscillation amplitude of the pseudoshock length, but it makes the back pressure oscillates: the model also acts as a transfer function between pseudoshock instabilities and the outflow pressure signal.

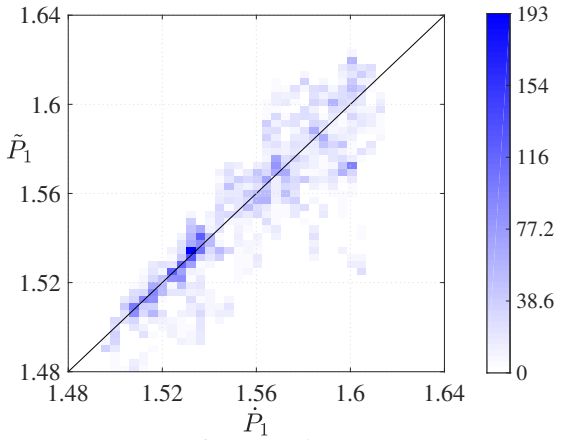

Figure 4.30: Correlations between $\dot{P}_1$ and $\tilde{P}_1$ from the DNS dataset of Fiévet *et al.* [33].

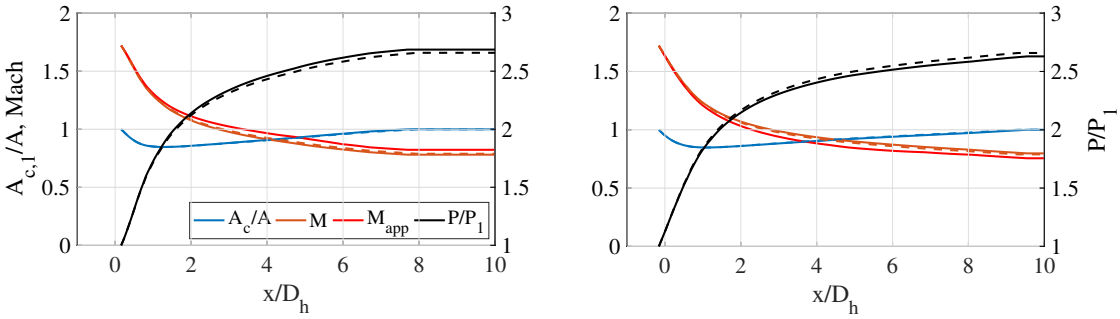

Figure 4.31: Illustration of the apparent Mach effect on the pseudoshock profile whence convecting upstream, *i.e.* in a strong state (left), or downstream, *i.e.* in a weak state (right).

4.5.3.2 Results

The iterative process was performed until a converged solution minimizing the errors of $\phi(x)$ and $\mathcal{E}(x)$ along the pseudoshock. The results are shown in Fig. 4.32 which compares the approximated target profiles for phase lag and oscillation amplitudes from the DNS and those obtained by the dynamic model. The corresponding local stiffnesses, characteristic and resonance frequencies are plotted in Fig. 4.33 from top to bottom respectively. The dynamic model, which is based on the postulate shown in Fig. 4.29 does verify the qualitative observations made from the coarse oscillation cases. The start of the pseudoshock does possess a higher resonance frequency which is consistent with both the spatially resolve 93 Hz oscillation case (the start of the pseudoshock increases the phase lag for minor amplitude gains) and the coarse grid cases. It is likely that the ξ and ω_0 locally depend on the shock train structure, the number and size of cells particularly. Therefore, this particular solution would probably be inaccurate for other Mach numbers configurations. Yet, the method itself would work once the harmonic oscillator component has been quantified. One could imagine an experiment where pressure transducers are used to measure the phase lag and oscillation amplitudes along the streamwise directions. Then, the same iterative process is shown in Fig. 4.29 could be performed. Finally, this model uses as input the physical oscillation of the pseudoshock foot location. It makes no assumption about the nature of the perturbations causing these oscillations. It can apply to inlet pressure waves, changes of Mach number of confinement ratio alike. However, the model would probably not be able to "reversibly" predict the shock train response to outflow perturbations.

The model has been calibrated for the dominant harmonic of the x_{10} oscillation. We can now feed the exact $x_f = x_{10}$ signal as an input with all its spectral components, and compare what the model gives with the exact measurements. This comparison is presented in Fig. 4.34 and shows how this simple model can reproduce most features presented in these turbulent signals. While resolving high-frequency noise is beyond the scope of this model, there appears to be an issue with the resolution of the very low frequencies. Indeed, looking back at

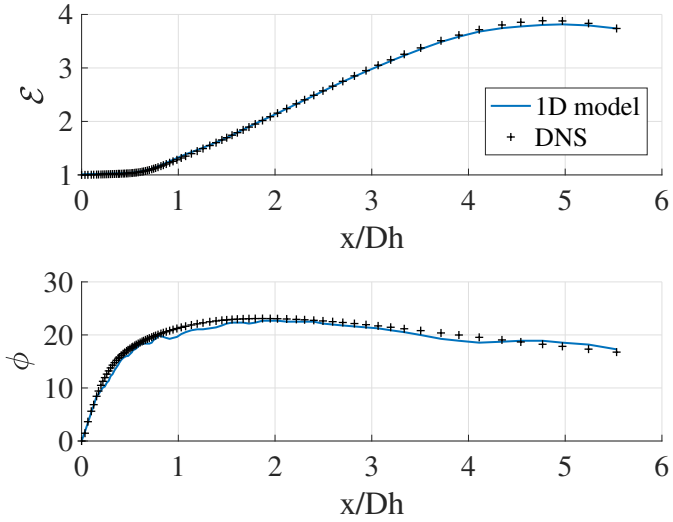

Figure 4.32: 1D model prediction of the x_{70} and x_{80} using $x_f = x_{10}$ as input signal.

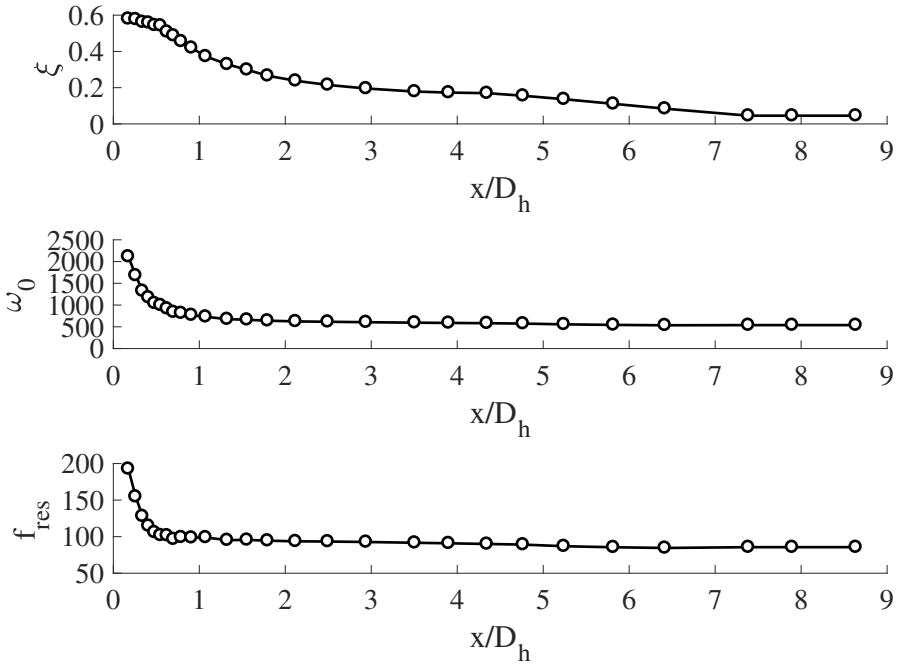

Figure 4.33: 1D model prediction of the x_{70} and x_{80} using $x_f = x_{10}$ as input signal.

the signals single-sided amplitude spectra in Fig. 4.28 it appears that the low frequencies amplitudes do keep increasing in amplitude which conflicts with the postulates the model is based upon. Indeed, for frequencies much lower than the resonance frequencies the amplitude should remain approximately constant. It is possible that these movements could be residue

from when the transient pseudoshock was still slowly adapting to the numerical back pressure and slowly moving towards its equilibrium position in the tunnel. Alternatively, it is possible that the oscillations interact with the back pressure and reflect back at a very low convective speed hence the low-frequency boost. Indeed, Wagner *et al.* observed [134] that upstream-traveling pressure waves from the outflow travel at an approximately 5% bulk flow speed. If so, these displacements would be polluting the spectral analysis.

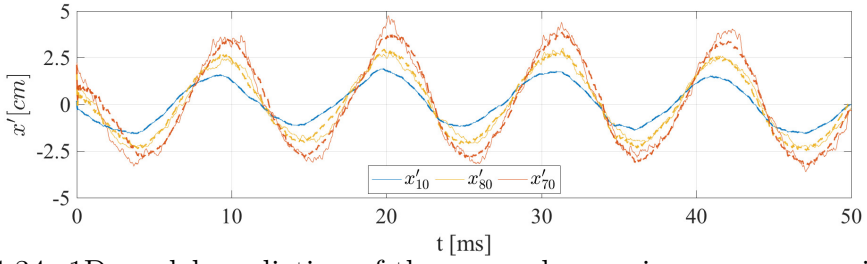

Figure 4.34: 1D model prediction of the x_{70} and x_{80} using $x_f = x_{10}$ as input signal.

4.5.4 Model transfer functions

The dynamic 1D model is now used to compute transfer function for a broad range of perturbations frequencies and amplitudes.

From a practical perspective, the pseudoshock length is usually defined as the distance over which an arbitrary pressure rise occurs, and it is therefore bounded by particular pressure values. Let us define $\mathcal{E}_{90-f}$ the distance of interest between the start of the pseudoshock and the location where the flux-conserved static pressure reaches 90% of what the static back pressure is. 1D and 2D Bode diagrams are presented in Fig. 4.35. The resonance phenomenon is caused by the harmonic component which decays exponentially past the resonance frequency. On the other hand, the apparent Mach becomes predominant for large relative velocities, *i.e.* for large frequencies and excitation amplitudes. This results in a strong nonlinearity along the input oscillation amplitude $\mathcal{E}_0$ space with potentially result in a catastrophically large resonating ratio.

Instead of computing the pseudoshock length based on a particular pressure rise threshold, we can simply define it as $x_{t-f} = x_t - x_f$ the distance between tail and foot. The

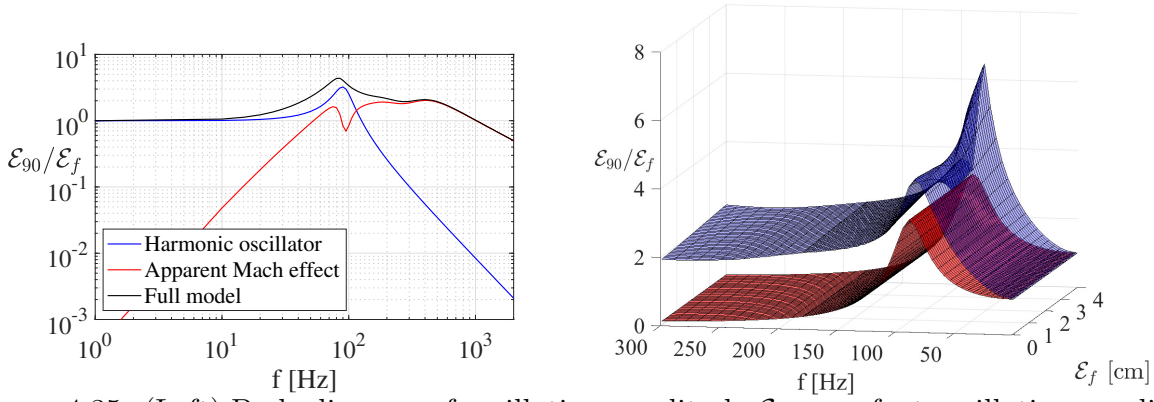

Figure 4.35: (Left) Bode diagram of oscillation amplitude $\mathcal{E}_{90}$ over foot oscillation amplitude $\mathcal{E}_0 = 12$ mm. (Right) Bode surface of oscillation amplitude $\mathcal{E}_{90}$ for the harmonic oscillator part (in red) and the full model (in blue) for various $\mathcal{E}_0$.

oscillation amplitude of x_{t-f} is called $\mathcal{E}_{t-f}$. Likewise, we can still define a $\mathcal{E}_{90-f}$ length which would be practically measurable. Their Bode diagram are shown in Fig. 4.36 (left) for $\mathcal{E}_0 = 12$ mm. This time, as frequency increases past resonance, the profiles converge to a similar limit close to 2% of the static pseudoshock length L. This limit is non-zero as the pseudoshock foot still oscillates at 12 mm. The figure on the right presents a Bode surface for varying excitation amplitudes of the ratio between pseudoshock oscillation amplitude over its static length.

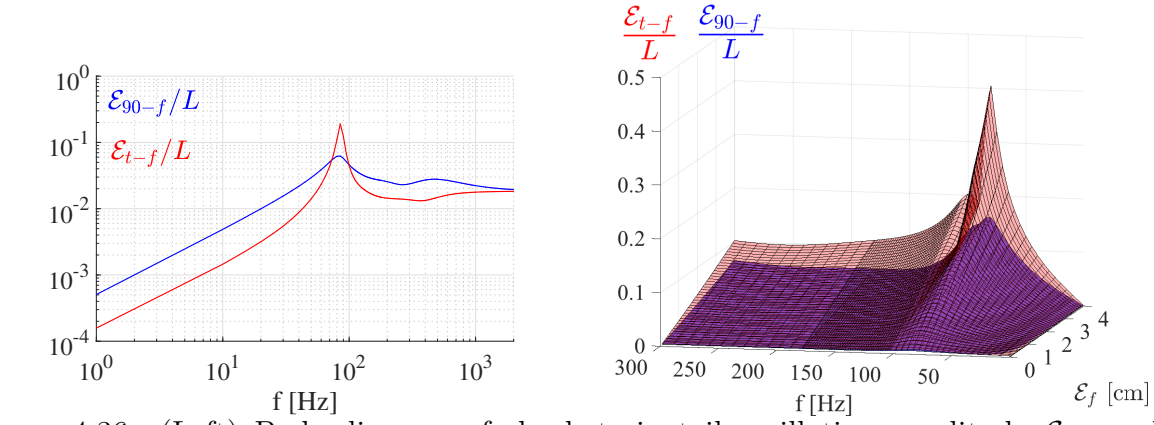

Figure 4.36: (Left) Bode diagram of shock train tail oscillation amplitude $\mathcal{E}_{100}$ and $\mathcal{E}_{80}$ over foot oscillation amplitude $\mathcal{E}_0$. (Right) Bode diagram of pseudoshock length oscillation amplitude $\mathcal{E}_{pst}$ over idle length L_{pst}.

As observed in Sec. 4.5.3.1 the pressure rise at the tail of the 1D pseudoshock is affected by the apparent Mach effect such that spatial oscillations will trigger back pressure oscillations.

A 2D Bode diagram of these oscillations of Back Pressure Ratio (BPR) referred to as $\mathcal{E}_{BPR}$ is plotted in Fig. 4.37. In this case, the increase of the perturbation amplitude $\mathcal{E}_f$ has a much strong effect on the final ratio $\mathcal{E}_{90-f}/\mathcal{E}_f$ for the same frequency compared to $\mathcal{E}_{t-f}/\mathcal{E}_f$. This is caused by the local convecting speed being proportional to the input amplitude.

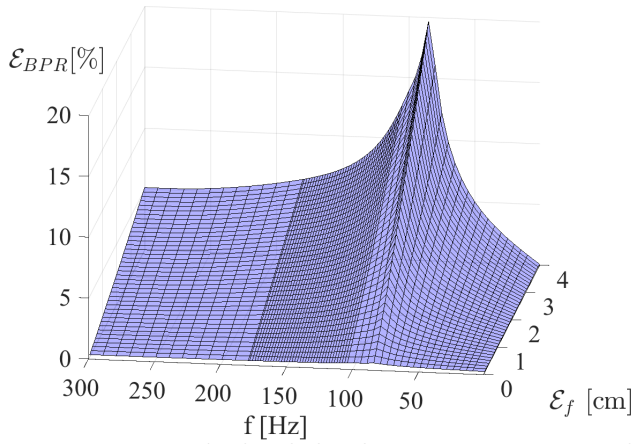

Figure 4.37: pseudoshock back pressure rise amplitude.

The most extreme case (4.0 cm foot oscillation amplitude at resonance frequency) could theoretically have such catastrophic effects on the shock train that it is unlikely the isolator/combustor equilibrium be sustainable.

4.5.5 Influence of low-pass filter

It appears that resonance can break down the shock train structure quite dramatically (Figs. 4.36 and 4.37). Fortunately, a low-pass response of the shock train foot was also identified in Chap. III: higher frequency inflow perturbation are damped and result in a lower leading shock amplitude oscillation. It was suggested that the low-frequency dynamic of the recirculation bubble located underneath the leading shock would stabilize its position. In fact, as the wall pressure distribution inside the bubble is homogeneous (see Fig. 3.9), the bubble could act as a large moving-averaging filter and damps the smallest wave-numbers. A more trivial explanation of the shock train foot low-pass response to any kind of inflow oscillation (Mach, pressure, confinement ratio) is as follows. The shock train oscillates between

two stable positions given by the inflow oscillation bounds. If the inflow oscillation timescale is superior to the time needed by the shock train to convect to either bound, then the leading shock amplitude is maximum. However, if the inflow oscillation timescale becomes inferior to the shock train accommodation timescale, then the leading shock's oscillation amplitude decreases. The DNS oscillations are constrained between two stable shock trains which leading shock are located at 10.5 and 41.9 cm from the inlet plane. Coarse grids simulation for frequencies 20, 60, 100, 200, 500 and 1000 Hz were carried out, and the shock train foot oscillation amplitudes were of 26.24, 7.98, 4.84, 3.39, 1.37 and 0.86 cm. A simple first-order low-pass filter $\mathcal{F}_{LP}$ can be constructed with a gain of 1 (determined from the conservation of energy: 0 Hz oscillation yields a ratio of 1) and accommodation timescale τ_0 as shown in Eq. 4.26. The cut-off frequency is estimated from the 20 Hz oscillation case (having an amplitude of 15 cm) compared to the half-distance between the steady bounds of 24 cm(see Fig. 3.9). The simulation dataset presents a decay of -10 dB/decade for the amplitude (i.e. -20 dB/decade for the power spectrum density) with a dB reference value of 1. A first-order filter appears to predict well the decay in amplitude of the foot oscillation at high frequencies as seen in Fig. 4.38.

$$\mathcal{F}_{LP}(i\omega) = \frac{1}{1 + \frac{i\omega\tau_0}{2\pi}} \tag{4.26}$$

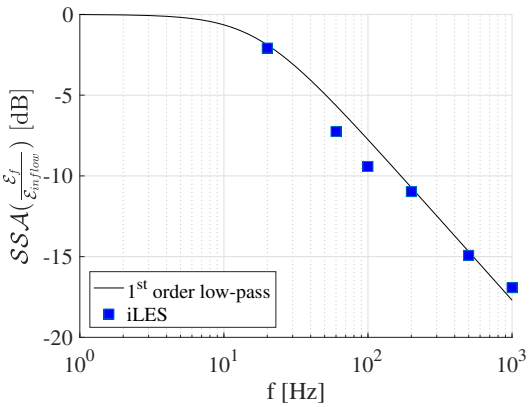

Figure 4.38: First order low-pass filter of cut-off frequency 17 Hz compared with the shock train foot amplitude oscillations from Fiévet *et al.*.

Adding the effect of the low pass preemptive filtering to the pseudoshock foot oscillation drastically alters the Bode diagrams shown in the Sec. 4.5.4. Bode surfaces showing the ratio between tail and inflow oscillation amplitudes (not foot) and BPR oscillations are shown in Fig. 4.39. The resulting Bode surfaces now correspond to the measured Bode diagram shown in Fig.3.22 showing a decaying amplitude in the high frequencies limit. As observed in Chap.III the low-pass filter plays a key stabilizing role. Isolators should be designed with the lowest possible cut-off frequency.

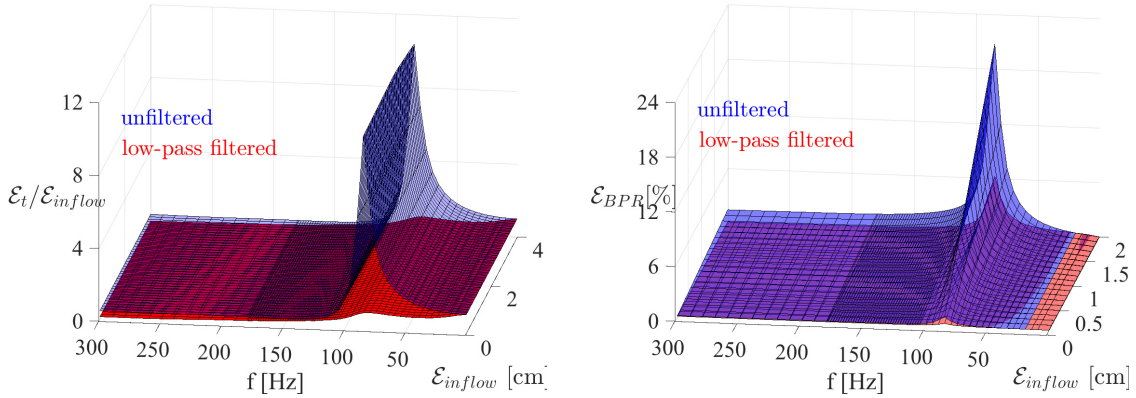

Figure 4.39: Ratio of shock train tail amplitude .

4.5.6 Pseudoshock sensitivity to broadband noise

It is possible to combine several harmonic excitations of different amplitude, frequency, and phase to observe the pseudoshock sensitivity to broadband perturbations. It is expected that occasional rogue waves (constructive interference) could sporadically disrupt the shock train, but that the overall effect would be to damp the apparent Mach effect by destructive interference. Additionally, the transfer function of the harmonic resonator component of the shock train will damp the high frequency and increase the magnitude of oscillations around the resonating frequency.

First, we observe the impact of inflow broadband perturbations (white noise) on the pseudoshock length. Then, the low-pass filter previously determined will be applied to this broadband perturbation resulting in red or Brownian noise. A harmonic oscillation of

frequency $f = f_r = 93$ Hz and amplitude 10 mm is used as the reference. The white and red noise signals amplitudes are re-scaled in order to have the same energy as the harmonic reference. For this particular input energy, the reference signal is expected to show the maximum pseudoshock length oscillation amplitude. The input signals of the shock train foot location x_t are presented in Fig. 4.40 alongside their single-sided amplitude spectrum. The output is the pseudoshock length L, *i.e.* the distance $x_t - x_f$, and is shown in Fig. 4.41. The noisy excitations are mostly filtered out while their resonating component and its spectral surrounding gained amplitude. This results in a much lower $\mathcal{E}_{\sqcup-\{}$ for those signals than for the pure harmonic excitation. The $\mathcal{SSA}$ also reveals that the resonance harmonics are excited.

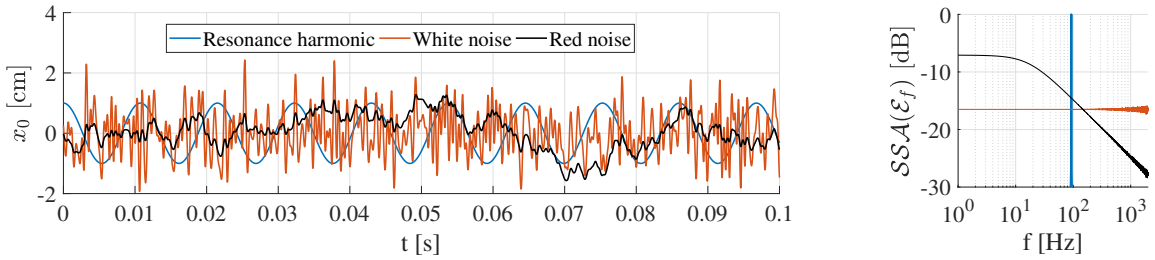

Figure 4.40: (Left) pseudoshock foot location $x_f(t)$ for various inflow excitations. (Right) Single-sided amplitude spectra of x_f in dB [ref = 1cm].

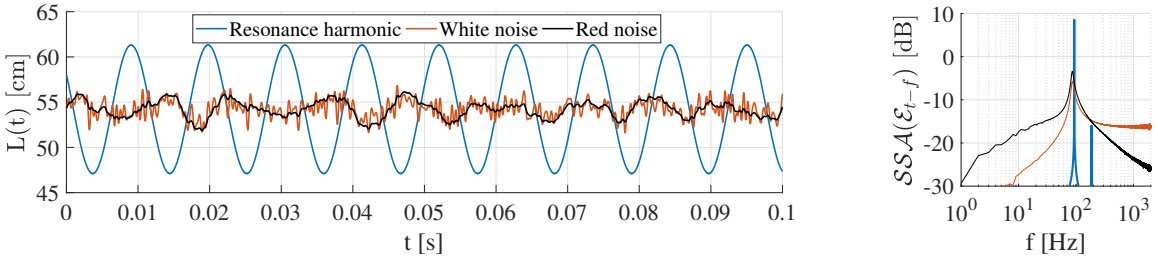

Figure 4.41: (Left) pseudoshock length L for varying foot location $x_f(t)$ presented in Fig. 4.40. (Right) Single-sided amplitude spectra of L in dB [ref = 1cm].

Figure 4.42 shows how this different noise affects the pseudoshock pressure rise. Again, the harmonic excitation results in a larger BPR oscillation amplitude than for the white and red noise excitations. Yet, an unstable pressure rise is attained in all cases. Shock train

spatial oscillations trigger the emission of pressure waves traveling through the post pseudoshock region: this means a time-varying thermodynamic state in the combustor. While a long isolator could contain the pseudoshock oscillations the issue of traveling back pressure waves remains. Indeed, the excitation of some spatial modes in the isolator results in the excitation of thermo-acoustic modes in the combustor, potentially affecting ignition. Should any of the combustor characteristic frequencies be similar to any of the harmonics of the pseudoshock resonance frequency, these pressure waves could trigger some instabilities downstream. A coupling of such isolator-combustor instabilities could lead to unstart through coupling of the isolator and combustor resonating modes, especially in ramjet mode where large subsonic boundary layer allow upstream acoustic feedback. Note that in order to use this model as a design tool, the dynamic model needs closure by expressing the local stiffness and resonance frequencies as a function of local quantities resolved by the static 1D model.

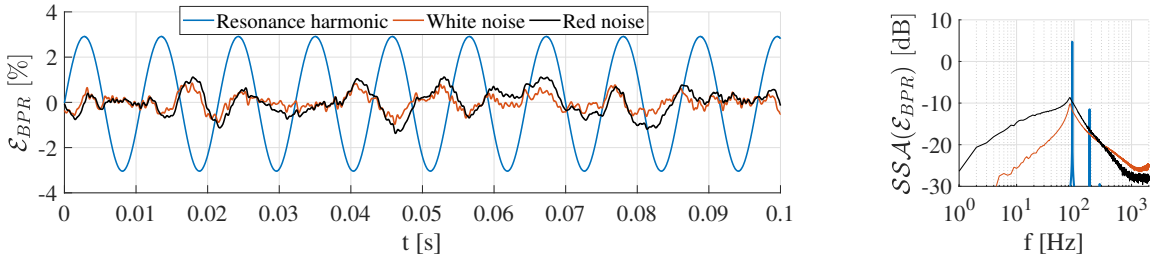

Figure 4.42: pseudoshock BPR for varying foot location $x_f(t)$ presented in Fig. 4.40.

4.6 Chapter conclusions

A 1D model for pseudoshock is built from a parametric optimization study and calibrated from various existing datasets. This static model is able to accurately predict the time-averaged pseudoshock roll-off profiles, lengths and pressure rise ratio over a broad range of flow conditions (Mach numbers, duct aspect ratio, Reynolds number, boundary layer confinement ratio). The model is then used to derive a dynamic anharmonic oscillator model

of pseudoshock sensitivity to inflow perturbations. A transfer function is determined which gives the oscillation of the pseudoshock tail, length and pressure rise ratio as a function of its foot oscillation. It is able to accurately predict the shock train dynamic observed from numerical simulations, including a certain resonance effect which could potentially disrupt the whole engine. This dynamic 1D model could, therefore, prove a valuable and unexpensive tool in designing DMSJ isolators and addressing the issue of engine unstart.

CHAPTER V

Effect of vibrational nonequilibrium on pseudoshocks

Numerical simulations of DMSJ engines often rely on the assumption of thermal equilibrium, where the internal modes of molecular motion are assumed to be in equilibrium. Similarly, isolator experiments usually run at low-enthalpy conditions where the flow vibrational energy mode is not activated. Hence, the effect of vibrational nonequilibrium on a pseudoshock have not been scrutinized yet. The nonequilibrium compressible flow solver presented in Chap. II is used to investigate the effect of nonequilibrium on the pseudoshock structure. A geometrical configuration as close as possible as the one used in Chap. III is intentionally used. It is found that nonequilibrium diminishes the pressure growth rate resulting in a longer pseudoshock. The outflow thermodynamic is noticeably affected and out-of-equilibrium. The effect of wall heat losses incidental to high-temperature internal flows is also studied and found to decrease the size of the recirculation bubbles. This results in a larger normal-like portion of the leading lambda-shock, hence a smaller pseudoshock. Lastly, the 1D model derived in the previous chapter is modified to account for these new results. Some of this work is included in Fiévet and Raman [35].

The chapter is organized as follows:

- Sec. 5.1 further discusses the motivations of this study.
- Sec. 5.2 details the flow configurations, solver and grid resolution.
- Sec. 5.3 studies the impact of wall heat losses on the pseudoshock.

- Sec. 5.4 studies the impact of vibrational nonequilibrium on the pseudoshock.
- Sec. 5.5 proposes modifications to the 1D model presented in Chap. IV to account for the high temperature effects presented in this chapter.

5.1 Motivation

As explained in Chap. I, the presence of large gradients is expected to trigger vibrational nonequilibrium in a scramjet isolator. Numerical simulations would be the ideal tool to fill this literature gap and quantify this physical phenomenon. Yet, to the best of the author's knowledge, all pseudoshock numerical simulations used either the calorically or thermally perfect gas thermal model. Its impact on pseudoshocks structure has never been investigated before, although theory shows it can potentially have a noticeable effect on the thermodynamic properties of the flow. As the airflow exiting the isolator enters the combustor, it is critical to correctly estimate its temperature, pressure, and mass flow rate. Failure to do so would result in misdesigning the isolator, increasing the risks of unstart.

A secondary consideration when dealing with high-enthalpy flows is to determine the thermal boundary conditions. It is common to assume adiabatic wall in the case the run covers a short time over which thermal exchanges with the wall are negligible. However, in the case of a steady stream possessing low-speed and recirculating areas close to the wall, heat losses can become relevant. In this case, a fixed wall temperature is chosen to compute the flux. A temperature of 300 K corresponding to ambient conditions is very often chosen in numerical simulations [76, 44, 19, 7]. The impact of this choice on pseudoshock structures is not well understood yet.

Vibrational nonequilibrium can be numerically resolved using the tools detailed and developed in Chap. II. The scope of this chapter is to use these tools to simulate the high-temperature equivalent configuration of the DNS presented in Chap. III. Both equilibrium and nonequilibrium thermodynamic solvers will be used to quantify the effects of vibrational

nonequilibrium and assess its relevance for DMSJ design. As the temperature is increased the impact of wall heat losses will also be quantified as two more simulations assuming either isothermal/adiabatic wall conditions will be performed. Finally, based on the new results modifications to the 1D model will be suggested and implemented to account for these high-temperature effects.

5.2 Numerical details

The numerical details relevant to the isothermal/adiabatic and equilibrium/nonequilibrium pseudoshock simulations are presented in this section.

5.2.1 Flow configurations

Three pseudoshock simulations are performed in this chapter. The first two use either adiabatic or isothermal wall with wall temperature $T_w = 300$K and assume a thermally perfect gas. The last one uses the same isothermal wall condition with vibrational nonequilibrium.

The compressible flow solver uses the same numerical schemes as presented in Sec. 3.1.2. It is coupled with the multi-temperature description of vibrational energy coupled with the Landau-Teller model and Millikan and White correlation to resolve the relaxation process as presented in Chap. II.

These simulations mimic an engine operating in ramjet mode: the post-pseudoshock flow is subsonic. The vehicle is set to fly at Mach 5.5 at 35 km altitude. Figure 5.1 presents the ramjet engine intake and isolator section which is the focus of the current analysis. This simple geometry is inspired by the HyShot-II experiment [117]. It represents a canonical configuration for a rectangular isolator, and the distance between the boundary layer bleed and the inlet plane of the computational domain is not specified. Instead, it is assumed that the flow at the inlet plane is at thermal equilibrium as if the distance was long enough to permit full relaxation of the vibrational energies of O_2 and N_2. This means that any vibrational nonequilibrium observed in the upcoming simulations is triggered by the shock

Table 5.1: Flow conditions in the model ramjet engine zones for a 35 km altitude flight.

Zone	P[kPa]	T[K]	Mach
1	0.9	240	5.5
2	6.5	627	3.0
A	27.5	1040	2.0
B	88.6	Unknown	<1

train itself. This is, therefore, the minimal amount of vibrational nonequilibrium observable in such engine, as there should realistically be a residual amount of nonequilibrium caused by the intakes 2 oblique shocks.

The same grid R2 as in Chap. III is used for these three simulations. Likewise, both the inflow bulk Mach number ($M_0 \approx 1.9$), inflow confinement ratio ($\mathcal{A}_* \approx 16\%$) and domain BPR (70% of a normal shock) are kept as close as possible to case B (see Tab. 3.2). Essentially, only two variables are changed: the inlet temperature and density. This ensures that the shock train structure remains similar. Table 5.1 presents the thermodynamic state of the airflow in the various zones of this model ramjet engine.

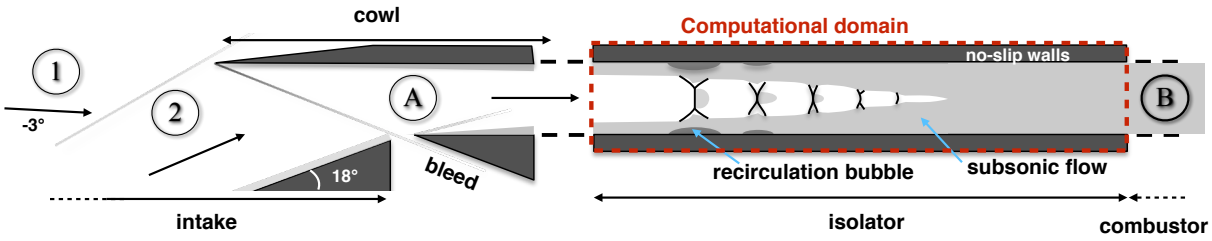

Figure 5.1: Sketch of ramjet engine inlet and isolator showing the DNS computational domain.

5.2.2 Inflow file

The same inflow is used at the computational domain inlet for the adiabatic, isothermal and isothermal with vibrational nonequilibrium.

The Van Driest transformed wall-normal velocity profiles of the inflow centerplane are shown in Fig. 5.2 and attest to the quality of the inflow. The wall unit y+ equals 21 μm. The Van-Driest transformed velocity profile matches the linear and logarithmic growth in

the inner/outer regions. Also, the Reynolds stresses profiles compares favorably with other supersonic turbulent boundary profiles from Martins [84] (Mach 2.32 and $Re_\theta = 4450$) and Bernardini *et al.* [9] (Mach 2.28 and $Re_\theta = 2500$). Note that as the high temperature naturally increases the viscosity, it was not artificially increased as in the CPG DNS to reach a DNS-like resolution. The inflow boundary layer thickness δ is equal to 12.3 mm. The momentum thickness $\theta = 0.70$ mm. The inflow Reynolds number Re_θ equals 2474.

This newer inflow was generated in three stages which differs from the previous chapter's cold inflow construction process. First, as in the former method, a uniform Mach 2.0 flow is initiated into same tunnel geometry albeit with streamwise periodic boundary conditions. Second, rather than sample the outlet plane once the boundary has grown to the target value (previous method) we sample the first onset of turbulence into an intermediary inflow file. Third, we feed this inflow file with some artificial randomness into the same tunnel with streamwise non-periodic and non-reflective boundary conditions. In this last stage, the tunnel has to be sufficiently long to let the turbulent boundary layer profiles grow to the target values. As the flow convects through that larger tunnel, the spatial resolution increases towards the main simulation target grid. The final inflow file is then sampled wherever in the tunnel the wall-normal velocity profiles are closest to the desired values. Note that this new method is computationally more expensive as it requires the generation of an intermediary inflow file. However, it permits to sample longer, decorrelated inflow files for the main simulation. The boundary layer height also remains rigorously constant throughout the inflow.

The flow-through time is estimated a posteriori from the mean centerline velocity to be of 0.97 and 0.84 from the equilibrium and nonequilibrium time-averaged solutions. The new inflow spawns over 2.5 ms, so almost three centerline flow-through times.

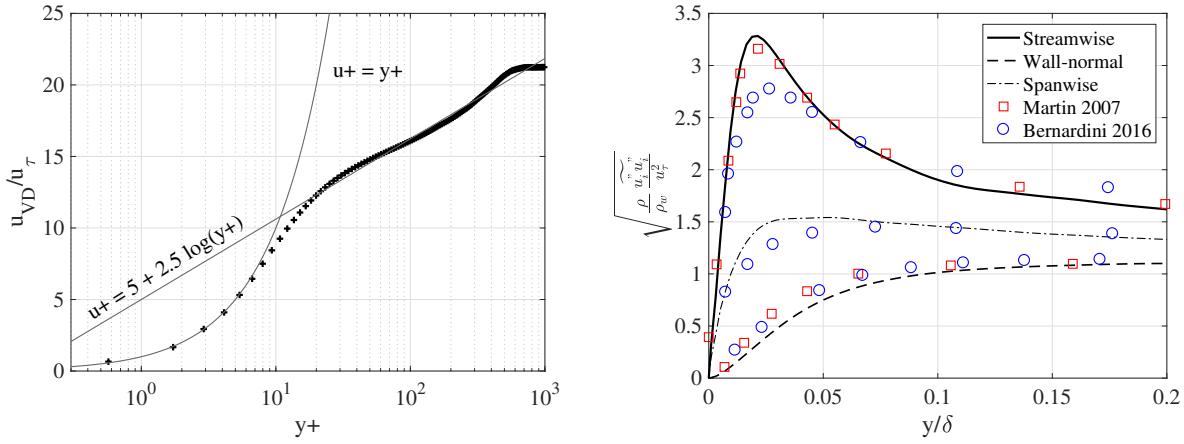

Figure 5.2: Time-averaged inflow boundary layer profiles of (left) the Van-Driest transformed streamwise velocity and (right) the Reynolds stresses.

Table 5.2: Different grid resolutions used for the shock train DNS.

Grid	N_x	N_y	N_z	$\Delta x+$	min $\Delta y+/\Delta z+$	max $\Delta y+/\Delta z+$	Cells <10y+
$R2+$	2048	320	256	20.1	0.99	20.6	5
$R3+$	3072	480	384	13.2	0.99	14.0	9

5.2.3 Simulations resolution

The parameters known to have the largest impact on the pseudoshock structure were kept constant from the previous CPG DNS. We therefore expect that a resolution close to the previously used R2 grid (see Tab. 3.1) is enough to resolve the shock train. The coarser grid R1 is not investigated at all. A grid with a resolution equivalent to R2 is called R2+. A finer grid referred to as R3+ with a similar resolution than the R3 grid is also used to properly verify grid convergence. While grids R2+ and R3+ possess the same number of grid points than R2 and R3, the resolution in wall unit is slightly different for two reasons. First, the stretching coefficient used to cluster the grid at the wall was slightly relaxed to barely reach a 1y+ resolution at the wall. This permits to slightly increase the centerline resolution. Second, the increased temperature has lowered the inflow Re_θ to 2474 such that there was no need to artificially increase the viscosity as was done before to obtain a tractable wall unit. The resolutions in terms of y+ for the high-temperature simulations are presented in Tab. 5.2.

The R2+ simulations all ran over 2.4 ms to ensure a proper convergence when constructing their time-average profiles. They used 8000 cores over 24 hours for the equilibrium and nonequilibrium models. The R3+ simulations all ran over 0.8 ms to ensure a proper convergence when constructing their time-average profiles. A CFL number of 0.9 was used yielding a typical timestep of 65 ns. They used 10000 cores over 48 hours for nonequilibrium case, half this amount for the equilibrium case. The adiabatic wall case was only run on grid R2+.

Figure. 5.3 shows time-averaged static pressure contours (from 40 to 120 kPa by increment of 10 kPa) and streamwise velocity (from 100 to 1000 m/s by increment of 100 m/s) in the Z-centerplane for both R2+ and R3+ grid for the nonequilibrium case. The time-averaged location of leading shock x_{s1} differed from 278 μm: only 0.8 % of a half-channel height. The complex pseudoshock structure is almost equally resolved by both grids which confirms that the R2+ grid is fine enough. The subsonic centerline pockets are equally spaced and of similar size. The boundary layer is also almost identically shaped. Overall, the convergence of the nonequilibrium pseudoshock structure is verified. It is expected that grid convergence on this most complex case induces grid convergence on the corresponding TPG simulations as well.

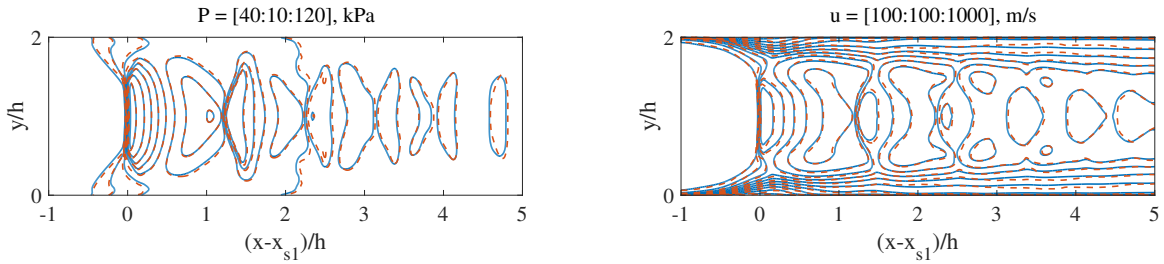

Figure 5.3: Z-centerplane time-averaged (left) static pressure and (right) streamwise velocity contours for the equilibrium isothermal wall simulation using either the R2+ (blue) and R3+ (red) grid.

Grid R2+ only will be used in Sec. 5.3 investigating the effect of wall heat loss. The finer grid R3+ is used throughout Sec. 5.4 which studies vibrational nonequilibrium. A qualitative view of the computational domain and pseudoshock (equilibrium and isothermal wall case) is presented in Fig. 5.4.

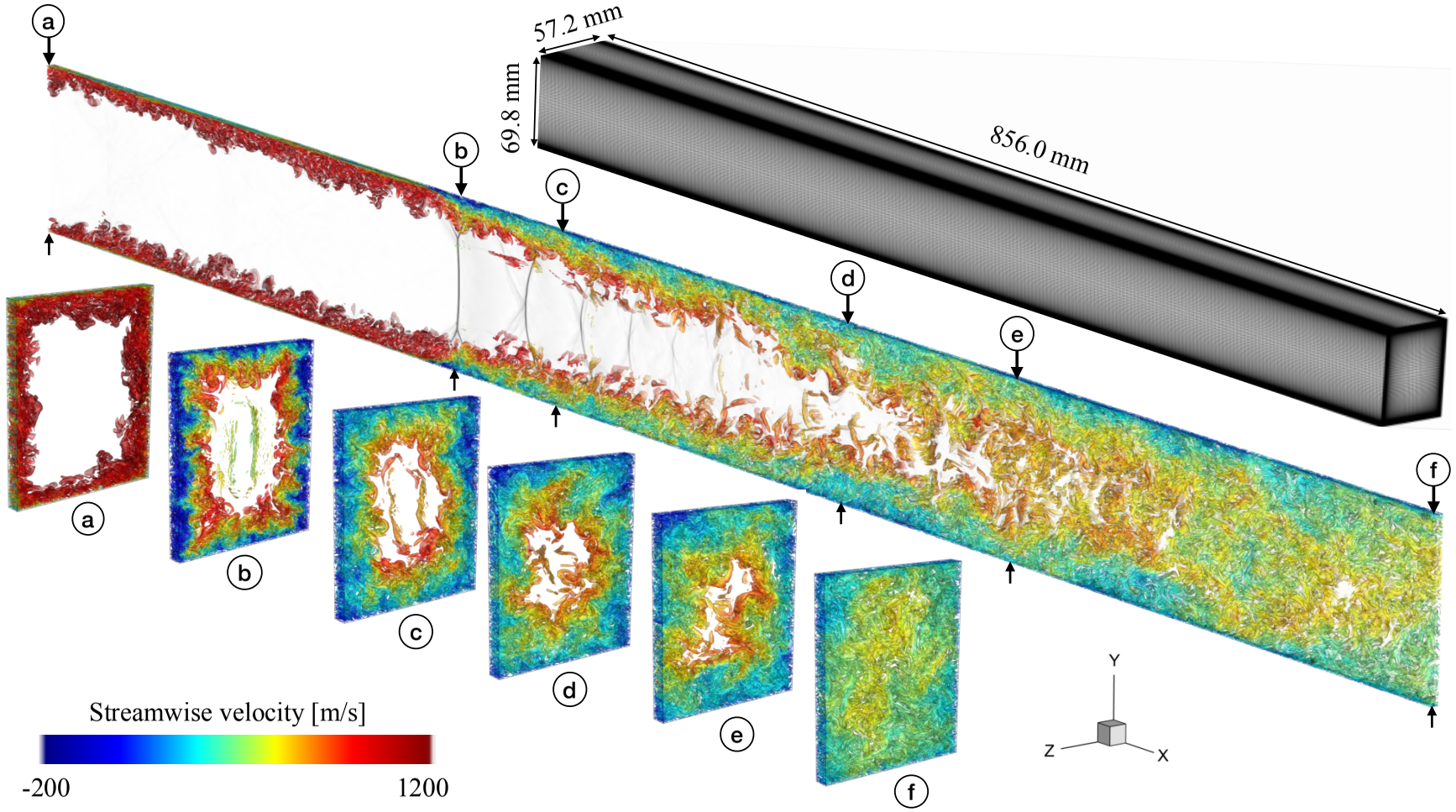

Figure 5.4: View of the computational grid (one cell out of 28 plotted) and isocontour of the second invariant of the velocity gradient tensor colored by streamwise velocity.

5.3 Impact of wall heat losses on pseudoshocks

The pseudoshock structure difference for either isothermal (T_w = 300 K) and adiabatic wall conditions is investigated in this section.

5.3.1 Centerplane 2D shock train structure

Figure 5.5 shows snapshots and time-averaged Mach contours of both isothermal and adiabatic simulations. The sonic isoline (Mach number equal to unity) is shown in black and reveals the strong difference in shock structures between these two cases. The centerline Mach number tends to drop below one faster than on the shock train edges creating a scissor-like shape in the isothermal case. The normal-like portion of the leading shock appears to be smaller in the adiabatic case. This results in noticeably smaller subsonic pockets and larger cell. This is precisely what was observed for larger inflow confinement ratio in Chap. III, yet here the inflow is identical. Larger lambda feet are observed in the adiabatic case which suggests that a larger recirculation bubble is present. By shrinking the normal-like portion the pseudoshock length would increases. The static pressure and streamwise velocity fields are also shown in Fig. 5.6. They are plotted in the leading shock reference frame and highlights the strong variation in shock cells sizes and numbers, resulting in different shock train length. These results are consistent with Kamali *et al.*[59] who observed that wall cooling reduced the cell sizes in a Mach 1.6 shock train.

5.3.2 3D shock train structure

The 3D time-averaged dataset is used to integrate the flux-conserved pressure, density, and temperature. These profiles are shown in Fig. 5.7 and are consistent with the previous observation on the pseudoshock structure. Its length varies from approximately 11 to 16 half-channel heights.

The amount of heat lost by the system as the flow convects through the channel can be computed from the flux-conserved total enthalpy profiles shown in Fig. 5.8. Note that this

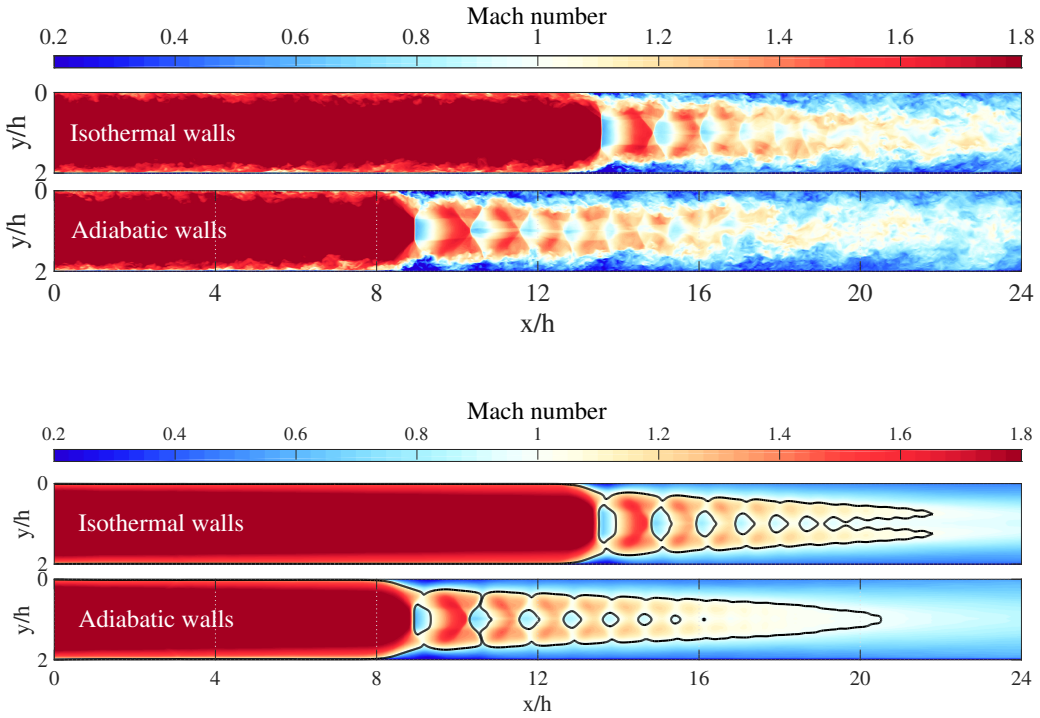

Figure 5.5: (Top) Instantaneous and (bottom) time-averaged contours of the Mach numbers for the (above) isothermal and (below) adiabatic simulations at the Z-centerplane.

value is computed a posteriori from time-averaged static temperature and velocity fields, which explains why oscillations are present at the unsteady shock locations. In theory, this value is supposed to remain constant for the adiabatic case, which is verified as the inlet and outlet total temperatures are equal. On the contrary, the isothermal wall simulation losses energy through wall heat losses which has the effect of decreasing its total temperature from approximately 1600 K (inlet) to 1450 K (outlet) along the channel.

The 3D sonic isocontours of both cases are shown in Fig. 5.9. The plot covers half the domain (up to half the spanwise domain) and cuts through the shock train. It can be seen that the differences between the subsonic cells locations/sizes increase further downstream. Yet, both simulations appear to possess a similar pre-pseudoshock sonic core (this is further quantified below).

Fig. 5.10 shows how bigger the bottom wall recirculation bubble is in the adiabatic case.

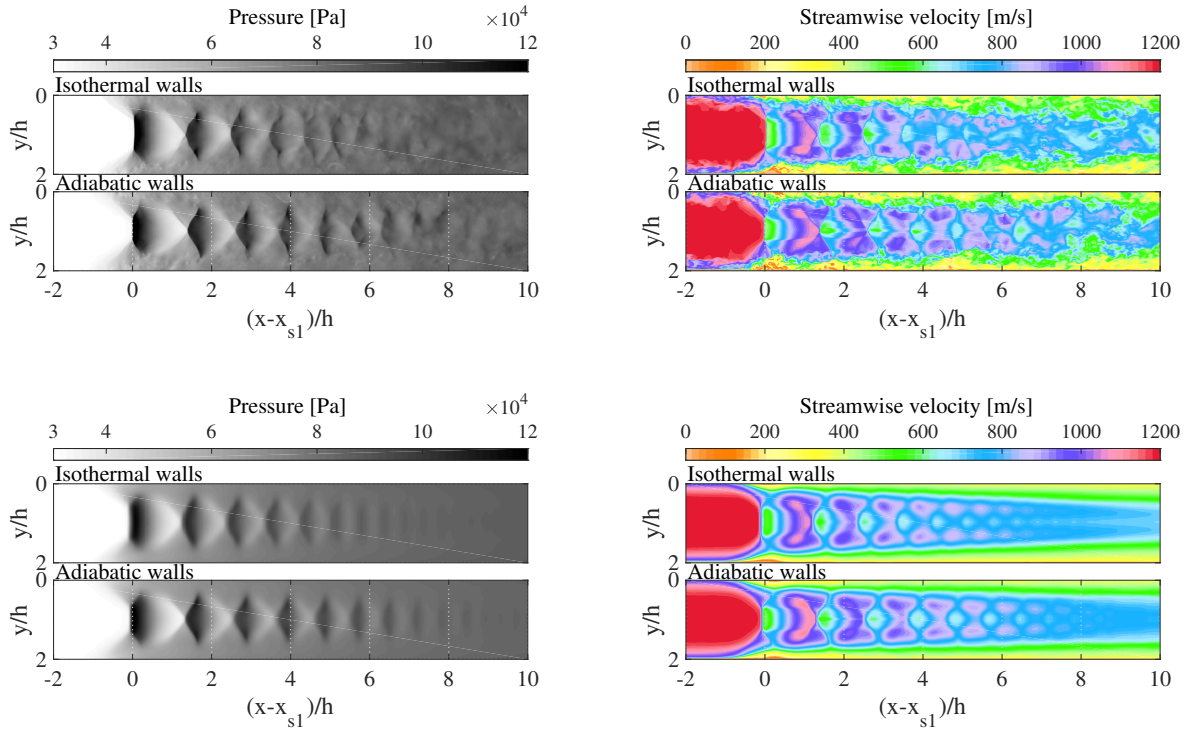

Figure 5.6: Z-centerplane (top) instantaneous and (bottom) time-averaged contours of the (left) static pressure [Pa] and (right) streamwise velocity [m/s]. In each pair the isothermal and adiabatic cases are respectively located above and below.

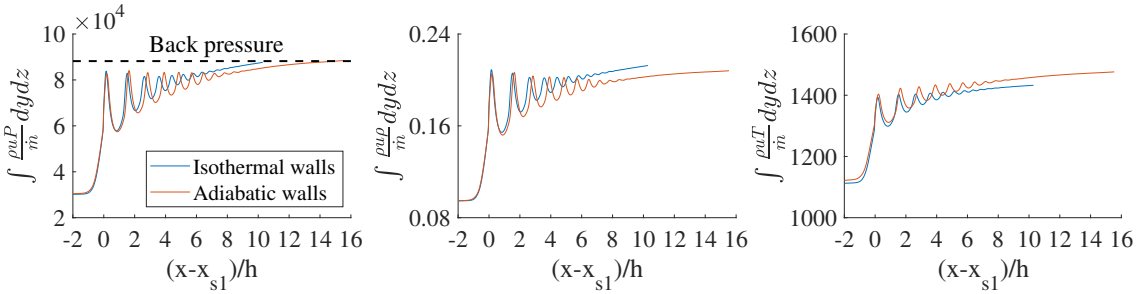

Figure 5.7: YZ Flux-conserved integrals of the static (left) pressure [Pa], (center) temperature [K] and (right) density [kg.m^{-3}] fields for both isothermal and adiabatic walls simulations.

This effect on the core flow is seen in Fig. 5.11 which presents the Y-centerplane streamlines. There is a larger detachment of the upstream boundary layer which shrinks the sonic core flow and the normal-like portion of the leading shock, just as in the Z-centerplane 2D contours shown in the previous section.

It is well known in boundary layer theory that a positive wall-normal static temperature

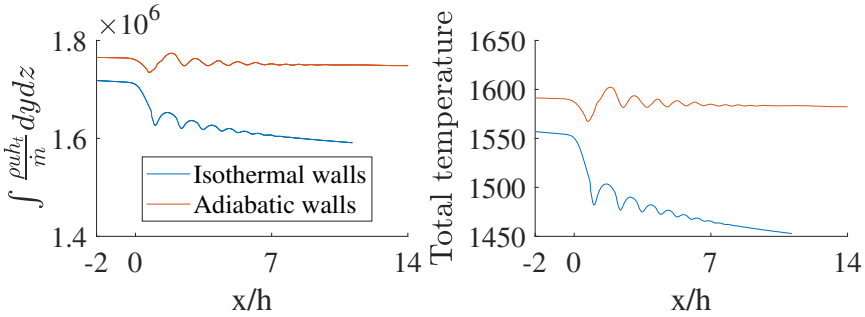

Figure 5.8: YZ Flux-conserved integrals of the (left) specific total enthalpy [J.kg^{-1}] and (right) total temperature [K] for both isothermal and adiabatic walls simulations.

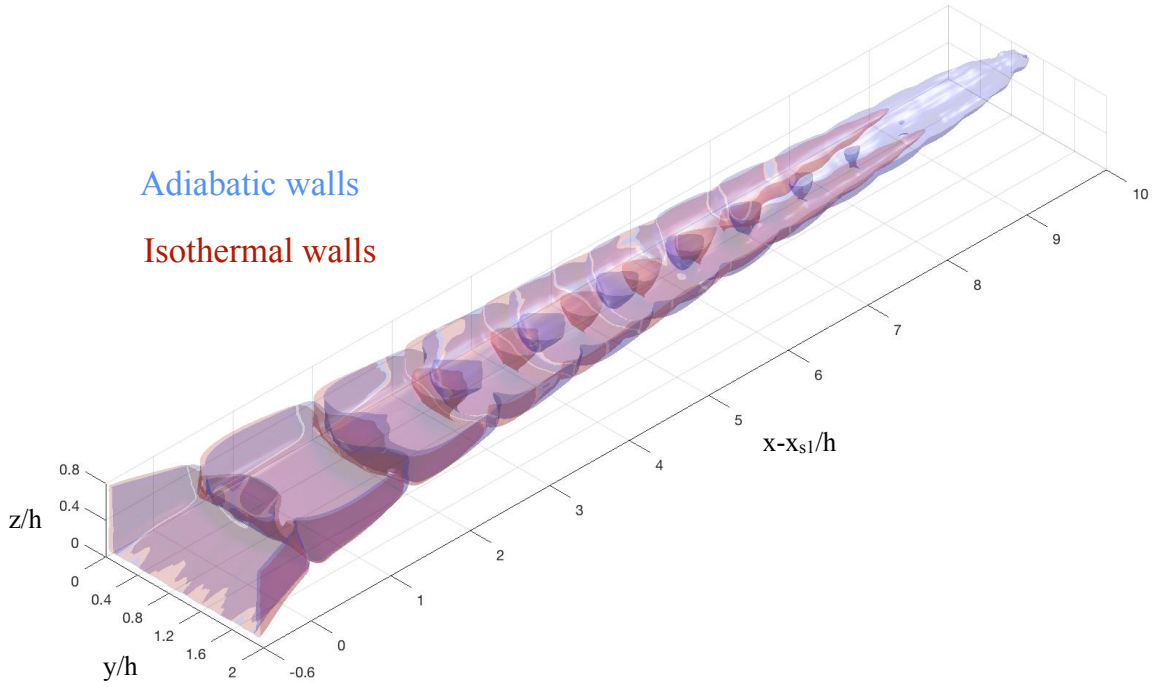

Figure 5.9: Mach = 1 isocontours for the adiabatic and isothermal walls cases.

profile (*i.e.* in the case of wall heat losses) has an effect equivalent to a negative streamwise pressure gradient: it helps prevent boundary layer separation [140]. Several recent DNS of STBLI [9, 142, 124, 132] have shown how wall heat losses affect the size of the recirculation bubble under the leading shock, and the bottom wall compression fan (which corresponds to the lambda foot in a normal shock train). Bernardini *et al.* and Volpiani *et al.* performed several DNS of STBLI (an oblique shock generated by an upper wedge impinges on a turbulent boundary layer) using various T_w ranging from half to twice the recovery temperature

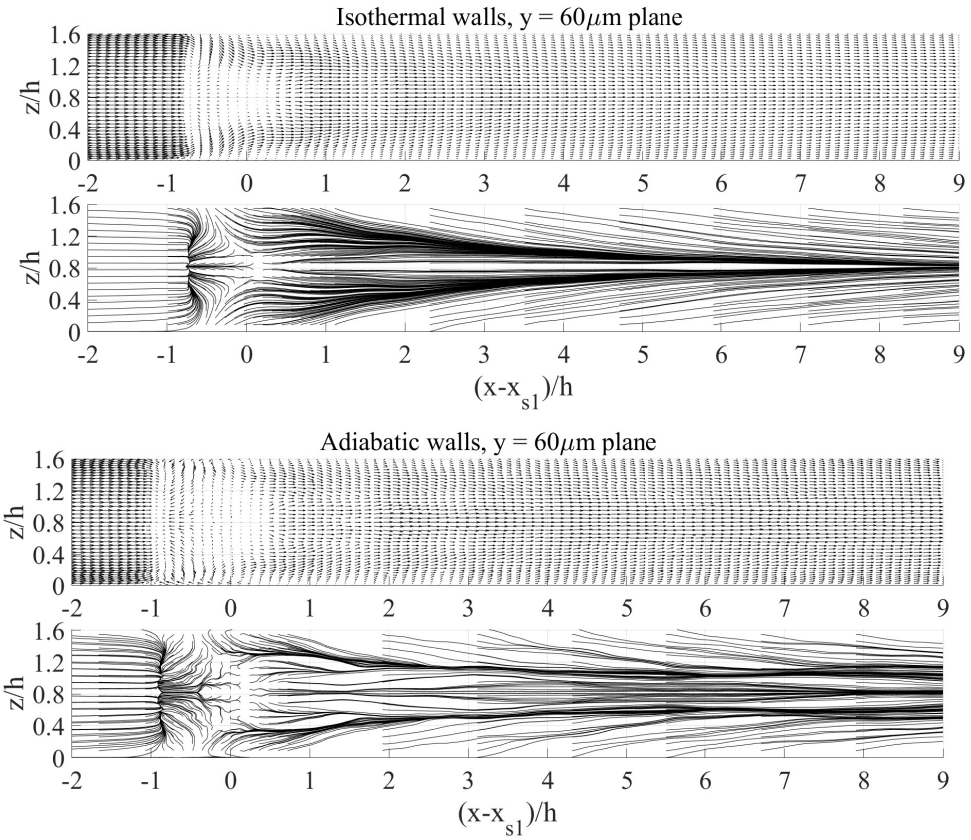

Figure 5.10: Velocity vectors and streamlines extracted from the y=60μm plane for (top) isothermal and (bottom) adiabatic walls cases.

T_r. Their result is particularly relevant to the present study as their inflow boundary layer Re_θ equals 2500 and their bulk inflow Mach number is equal to 2.28, which are both very close to the present case. They found that wall heat losses bring the upstream boundary layer sonic line closer to the wall than in the hot wall or adiabatic cases. Hence the subsonic turbulent streamwise-coherent structures present in all turbulent boundary layers depart further away from the wall. This would shift upstream the shock foot and increase the size of the recirculation bubble. Conversely, they found that the size of the recirculation bubble decreased for large heat losses, and increased when the wall was heated. Figure 5.12 shows how the impinging shock penetrates deeper in the turbulent boundary layer when the wall temperature is reduced. Notably Bernardini *et al.* concluded that the change in STBLI structure was not due to the heat losses around the separation point, but due to change in upstream boundary layer profile. Yet, the upstream boundary layer appears to have a similar

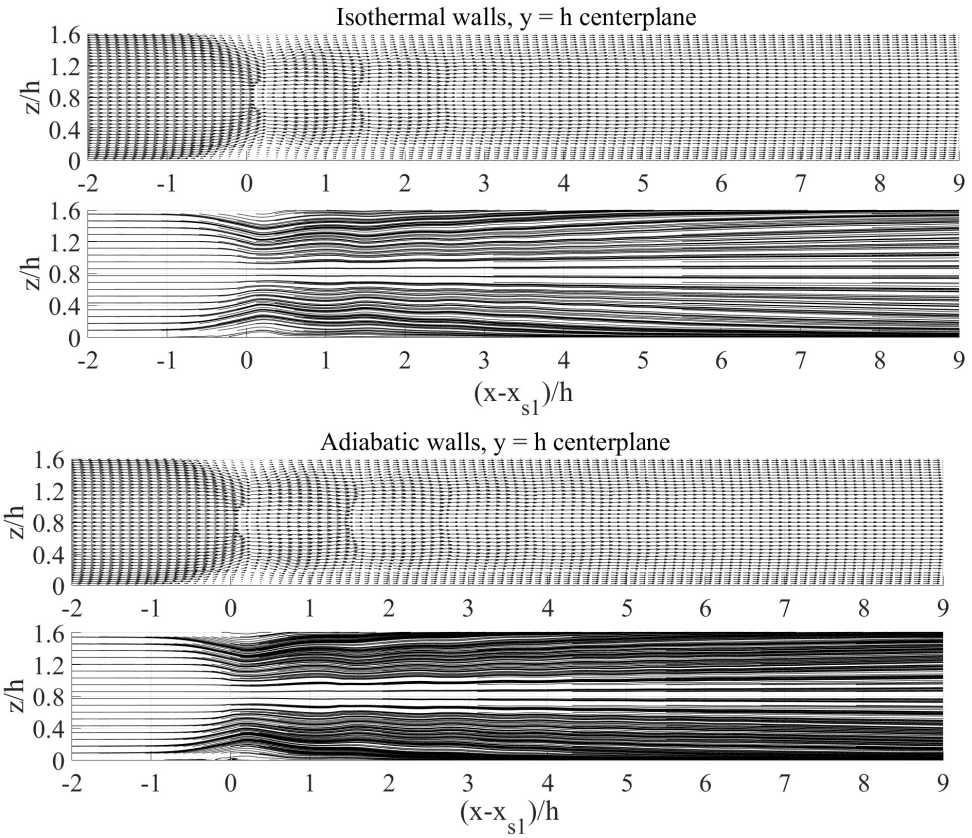

Figure 5.11: Velocity vectors and streamlines extracted from the y=1h plane for (top) isothermal and (bottom) adiabatic walls cases.

height for all cases. Additionally, they found that the friction coefficient upstream of the separation bubble was almost unchanged for all cases. Zhu *et al.* observed the same result in a ramp geometry. In the present study, the confinement ratios [$\mathcal{A}_*$,$\mathcal{A}_\theta$] are of [0.155,0.065] and [0.160,0.057] right upstream of the pseudoshock for the isothermal and adiabatic cases respectively. The bulk Mach numbers are between 1.89 and 1.88. These changes are too subtle to explain such a large difference with the correlations found in Chap. III. Hence the wall heat losses must have influenced another parameter which has not been considered yet.

Figure. 5.13 presents the non-streamwise instantaneous velocity fields for the isothermal case. Large streamwise-coherent structures alternatively positive/negative are observed upstream of the separation point, particularly in the w contours. These structures disappear after they pass the lambda foot (revealed by the strong v magnitudes). The interaction of these large-scale vortical structures with the lambda foot could play a relevant role in

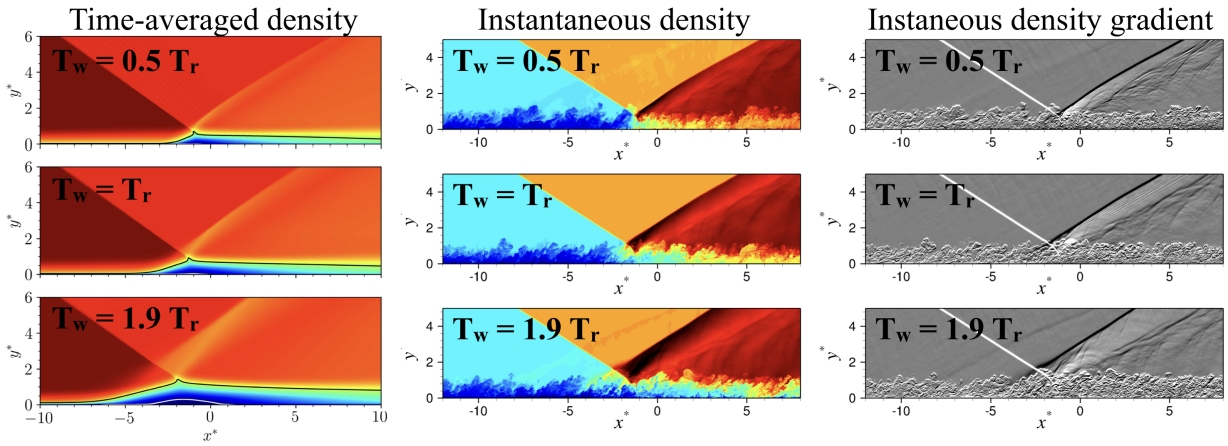

Figure 5.12: DNS of STBLI for various wall temperatured from Bernardini *et al.* [9] and Volpiani *et al.* [132].

determining the leading shock cell structure. The vortical skeleton of the pseudoshocks for both cases is extracted from the time-averaged 3D dataset and analyzed in the next section.

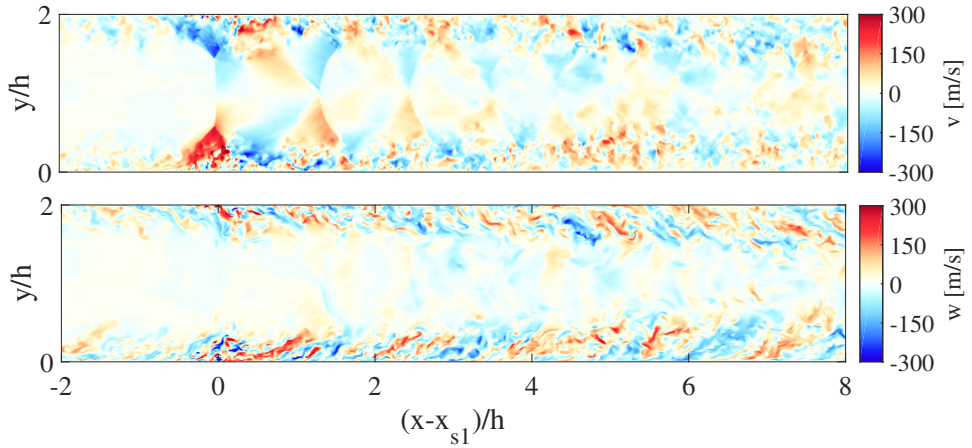

Figure 5.13: Z-centerplane snapshot of v (wall-normal) and w (spanwise) velocity vector components for the isothermal walls case.

5.3.3 Vortical structure

As explained in Sec. 5.3.2 the differences observed between the two cases seem to originate with the leading shock/cell characteristics. Boundary layer cooling likely affects the velocity profiles and the vortical structure. The vortical structure upstream of the shock train consists

of pairs of counter-rotating vortex in each corner of the channel shown in Fig. 5.14.

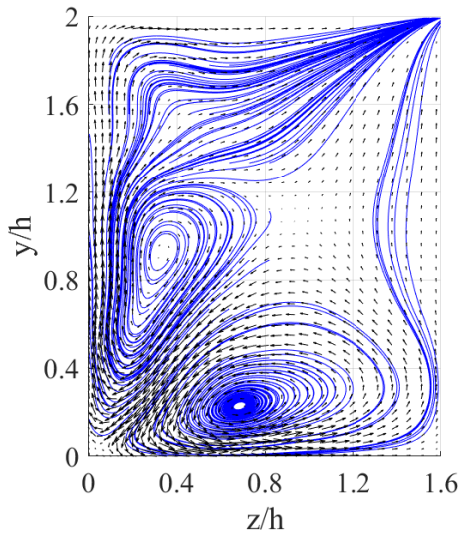

Figure 5.14: Velocity vectors (black) and streamlines (blue) extracted from the $x = x_{s1} - 0.1m$ plane for the adiabatic walls case.

In order to identify and quantify the differences in shock train vortical structures between both case, the rigid vorticity ω_r defined as the rigid-body component of the vortical field is extracted from the 3D time-averaged dataset using Triple Decomposition Method (TDM) Kolar *et al.* [67]. It permits to extract from the vortical fields the strain and shearing due to the shock waves and wall shear stresses. An illustration of such decomposition is given in Fig. 5.15. In the current analysis, the decomposition was performed in the Favre-averaged velocity field.

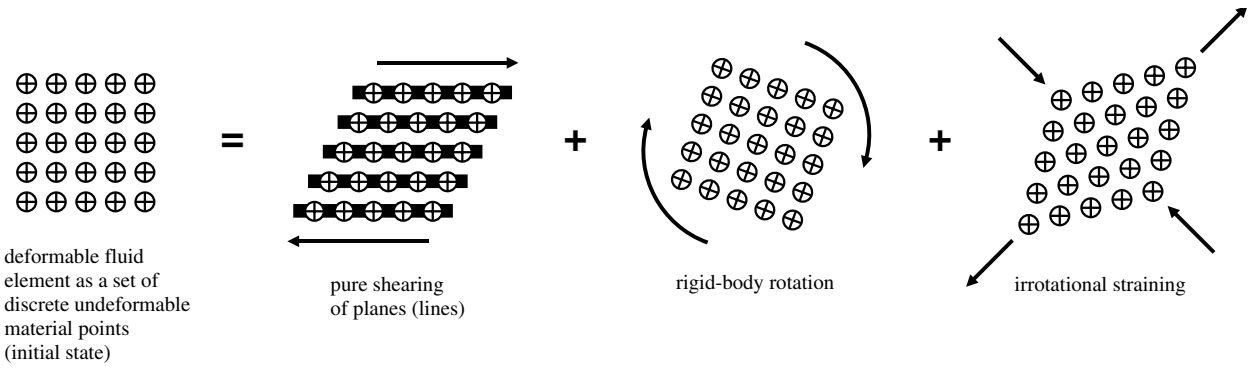

Figure 5.15: Vortical triple decomposition method process from Kolar et al. [67].

Such decomposition is shown in Figs. 5.16 where the top contour shows the vector velocity field in the Y-centerplane colored by vorticity ω_{XZ}. It is difficult to identify any vortex due to the high strain and shearing, but the TDM reveals the location of vortex pairs located in between every shock train cells (bottom contour).

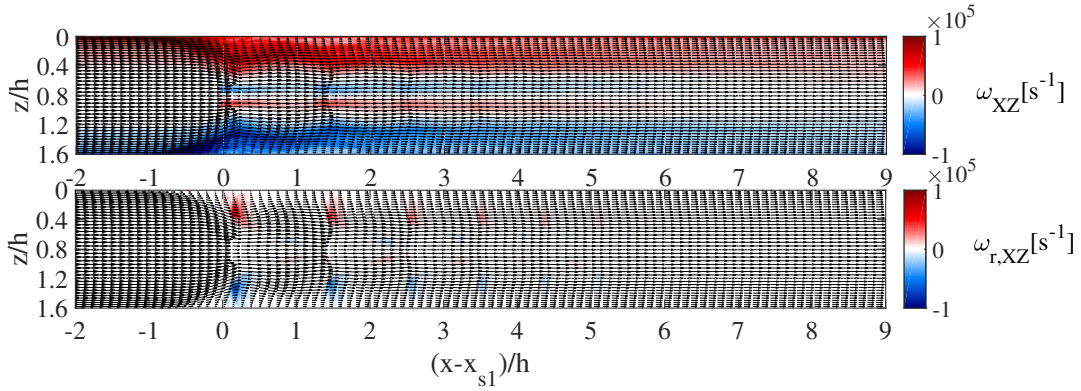

Figure 5.16: Velocity vectors extracted from the y=1h plane for the adiabatic walls case colored by (top) plane vorticity ω_{XZ} and (bottom) plane rigid body vorticity $\omega_{r,XZ}$.

The TDM is also used in the streamwise-normal plane YZ and is presented in Fig. 5.17 (first contour). In order to facilitate the analysis and construct a clean 3D shock train vortical skeleton the following method is used. First, an arbitrary threshold of 10^4 [s^{-1}] is chosen to plot the skeleton isocontours. Then, as seen in the second contour in Fig. 5.17 this threshold is used to define a mask value, or Boolean inside/out of all vortices. The next step consists in integrating $\omega_{r,XZ}$ inside every vortex that has been separately identified as in the third contour of Fig. 5.17. Lastly, a circle of area equal to the Boolean area is placed in every vortex core location. It is colored by $\int \omega_{r,XZ}$. Each vortex is now represented by a circle giving its size, colored by its strength, and centered on its core location as seen in the right contour in Fig. 5.17. The same process in the XZ plane is shown in Fig. 5.18 and shows how it presents a clear, quantified picture of the shock train vortical skeleton upon which the shocks cells are attached. The same operation is performed across all planes. The computation of all these fields took about 30h on a single core.

The whole shock train skeleton is then reconstructed in 3D slice by slice. A small spatial-average filter (less than h/100) is used to smooth its shape, plotted in Fig. 5.19. It reveals

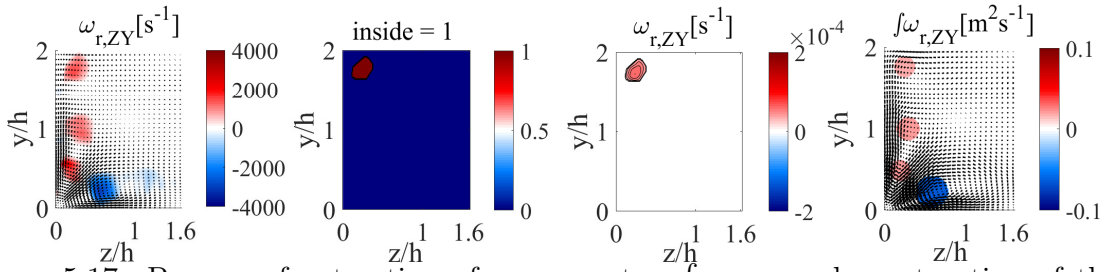

Figure 5.17: Process of extraction of every vortex $\int \omega_{r,XZ}$ and construction of the shock train vortical skeleton.

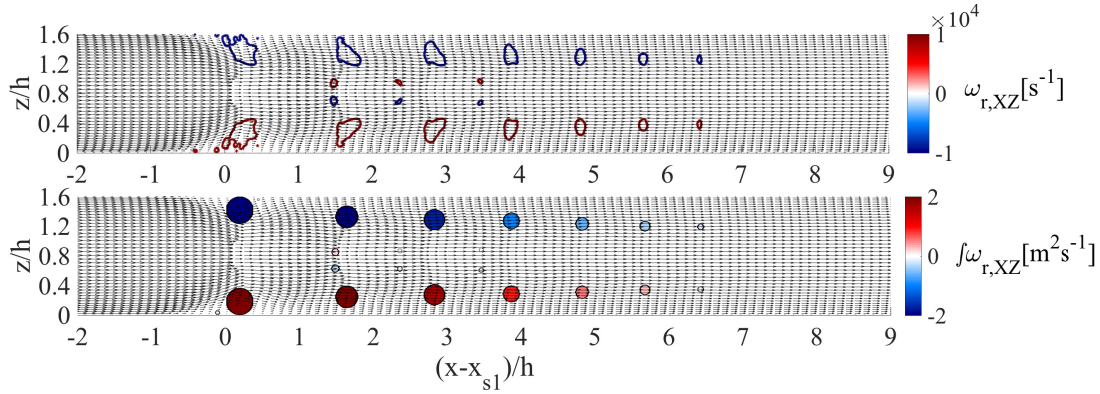

Figure 5.18: Velocity vectors extracted from the y=1h plane for the adiabatic walls case colored by (top) isocontours of $|\omega_{r,XZ}| = 10^4$ [s^{-1}] and (bottom) integrated $\omega_{r,XZ}$ within top contours limit and plotted as a circle centered on vortex core location.

how rigid vortex quartets are positioned in between cells as pillars, progressively weakening both in size and magnitude as the pressure rise ratio of each successive shock cell diminishes. We can deduce that they do not increase with the boundary layer height but with the cell size, *i.e.* with the adverse pressure gradient. The pre-pseudoshock streamwise vortices disappear when they reach the recirculation bubble. They reappear after the reattachment point. Their strength reduces each subsonic cell where the centerline pressure is large and tends to detach the boundary layer. However, contrary to the XY and XZ vortex quartets they do not weaken further downstream. In fact, they seem to reach a maximum size and strength once they reach the pseudoshock fully developed turbulent mixing region: this suggests they scale with the turbulent boundary layer height. Another pair of streamwise counter-rotating vortices re-appears at the center of the spanwise wall. They both strengthens right under each shock and weakens through the expansion waves. Their size appears to slowly decay through the shock train suggesting that they behave similarly than the XY and XZ vortex

quartets.

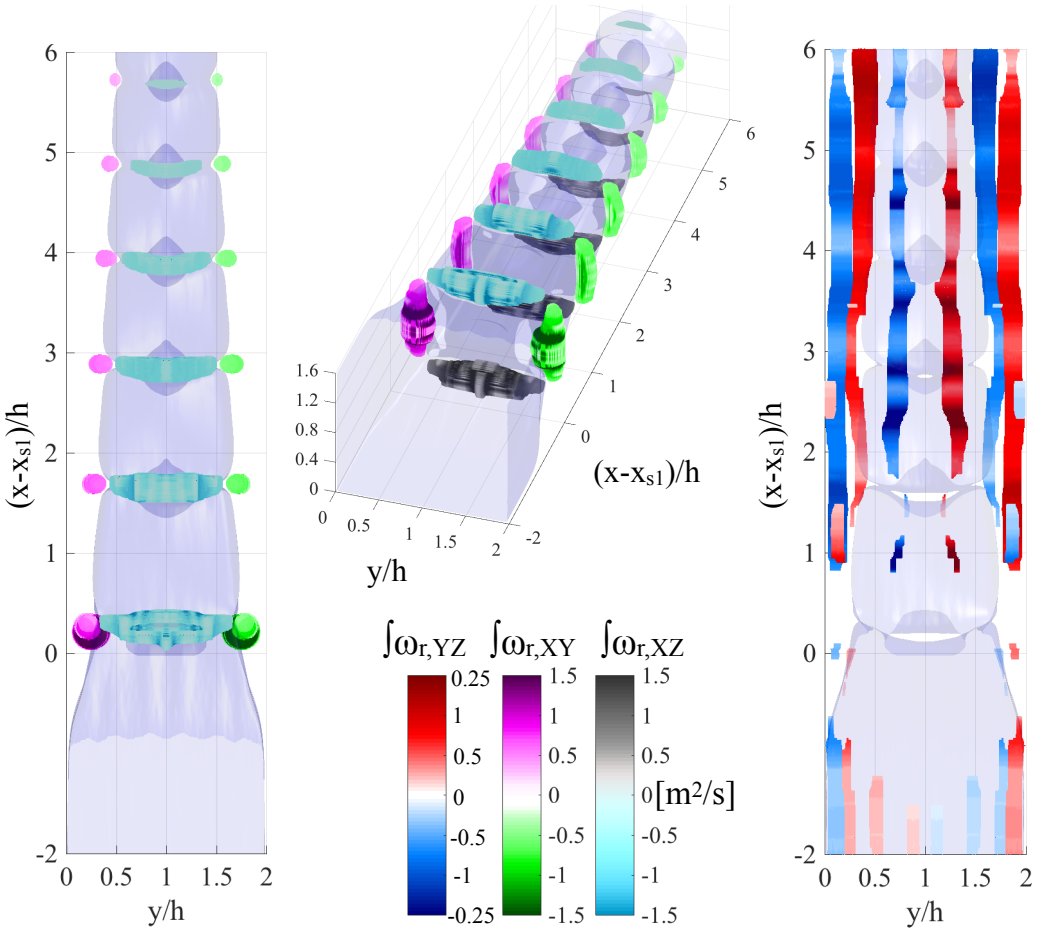

Figure 5.19: 3D vortical skeleton of the adiabatic walls case shock train.

The strengths of these rigid vortices are integrated and plotted with other quantities of interests in Fig. 5.20 for both isothermal and adiabatic walls cases. Such quantities are the wall and centerline pressure profiles (top right), and the sonic core ratio (top left). The upstream sonic ratio is higher for the cooled wall as observed by Bernardini *et al.* [9]. The upstream $\int \omega_{r,YZ}$ is stronger for the adiabatic case especially right upstream of the separation point. They also are much stronger under the first shocks which is consistent with the larger lambda feet observed in Fig. 5.5 for instance. Interestingly, all vortex quartets are consistently largely stronger for the adiabatic case (bottom right plots).

This analysis cannot determine whether the increased vortical activity is "responsible for"

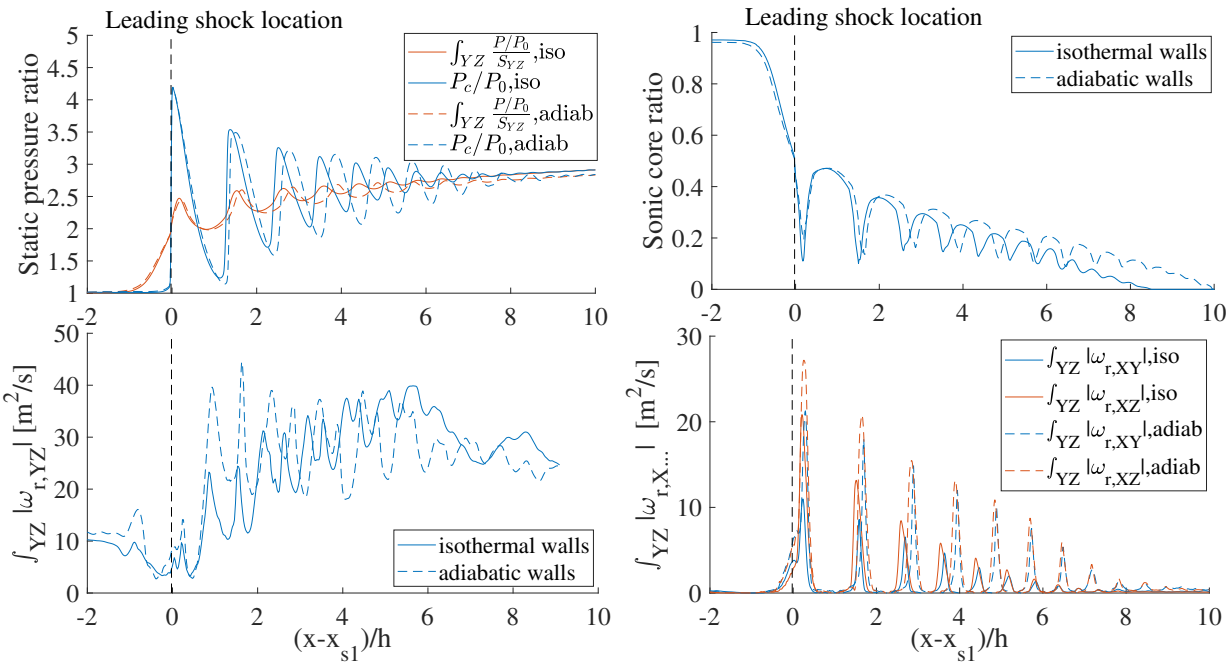

Figure 5.20: (Top left) Centerline and YZ-integrated static pressure profiles. (Top right) Sonic core area ratio. (Bottom left) YZ-integrals of rigid vortex $\omega_{r,YZ}$. (Bottom right) YZ-integrals of rigid vortices $\omega_{r,XY}$ and $\omega_{r,XZ}$. All profiles are plotted in the leading shock's reference frame and compare the (solid) isothermal and (dashed) adiabatic walls simulations.

or "a consequence of" the larger shock train cells in the adiabatic case. However, as observed by the STBLI DNS mentioned in the previous section [9, 142, 124, 132], the upstream velocity profiles determine how deep the shocks impinge into the turbulent boundary layer. In conclusion, it is proposed that the larger upstream vortices coupled with the smaller sonic core are responsible for the change in the leading lambda shock foot, hence the normal-like portion, hence the compression rate which determines the pseudoshock length.

5.4 Impact of vibrational nonequilibrium on pseudoshocks

The focus of this section is to quantify the impact of vibrational nonequilibrium on the pseudoshock structure. For the purpose of this discussion, the shock structure simulated using TPG assumption is referred to as the equilibrium calculation. Likewise, the simulation resolving the vibrational energy relaxation process is referred to as the nonequilibrium

solution.

5.4.1 Differences in shock train structures

Figure 5.21 shows instantaneous snapshots of Mach number for the equilibrium and nonequilibrium solutions. In the nonequilibrium case, the specific heat capacity ratio is computed from the vibrational temperature, which is then used to evaluate the local speed of sound. The first difference between the cases is in the location of the leading shock, which is positioned farther upstream in the nonequilibrium case. The leading λ-shock encounters a slightly thinner boundary layer since the near-wall subsonic region grows in size with streamwise distance within the isolator. To further understand the structural difference, sonic isosurfaces of both equilibrium and nonequilibrium cases are shown in Fig. 5.22 up to half the spanwise domain. Here, the leading edge of the shock train is taken as the origin in the streamwise direction. It is seen that the effect of vibrational nonequilibrium is quite minor on the sonic core length. However, the nonequilibrium case has slightly smaller cells, and this difference accumulates over the length of the domain leading to larger differences in the location of the sonic core downstream. Overall, the shock trains have the same scissor-shape sonic core, and the nonequilibrium case needs a longer post-shock train mixing region to accommodate the same numerical back pressure condition. The pseudoshock length varies from approximately 11 (equilibrium) to 16 (nonequilibrium) half-channel heights.

Static pressure and streamwise velocity fields are also shown in Fig. 5.23 in the leading shock's reference frame. It can be seen that the time-averaged fields are very similar to the instantaneous snapshots, indicating that the large-scale features of the flow are dominated by the shock train and the associated shock structures. Further, the shock train itself might exhibit low-frequency oscillatory motion [52, 33], but the spatial structure remains nearly unaltered as the entire shock train moves up or downstream in the isolator. Similar to Fig. 5.22, it is seen that the diamond-like cell formed by the leading shock is smaller in the nonequilibrium case compared to the equilibrium case. As a result, the shock train from the

nonequilibrium is shorter than that for the equilibrium case (even though the pseudoshock is longer for the nonequilibrium case).

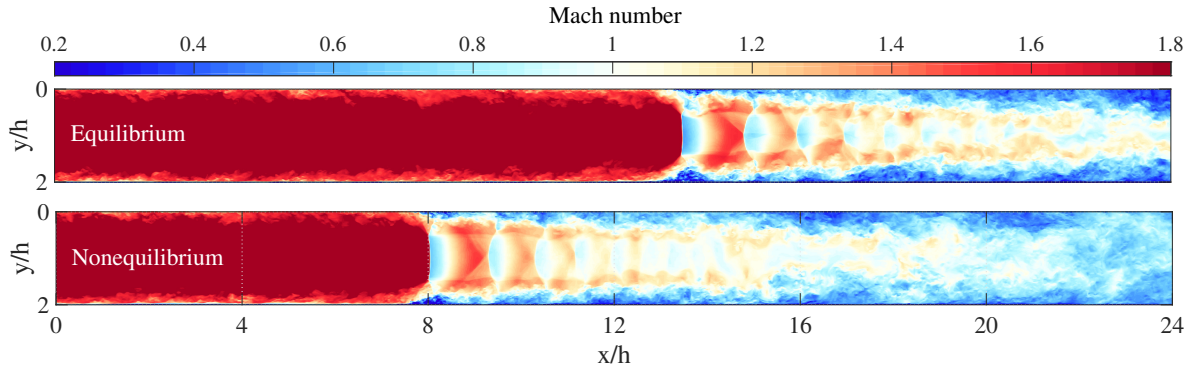

Figure 5.21: Instantaneous contour field of Mach number for the (top) equilibrium and (bottom) nonequilibrium simulations at the spanwise centerplane.

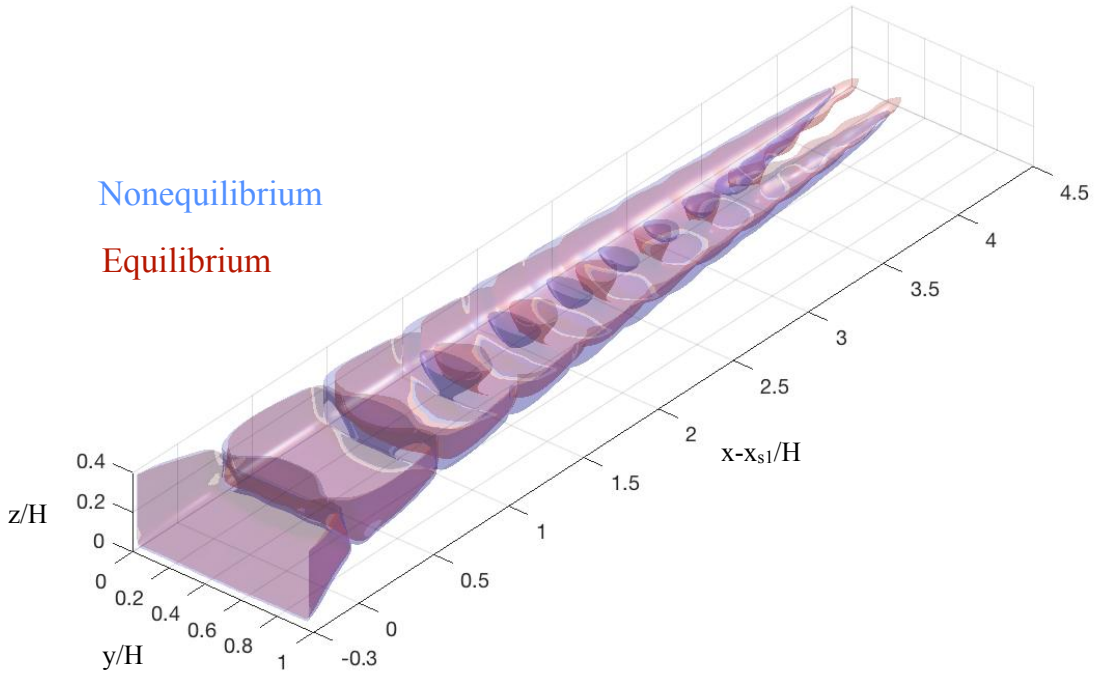

Figure 5.22: Isocontours of sonic condition for the equilibrium and nonequilibrium calculations.

5.4.2 Pseudoshock-triggered nonequilibrium

Figure 5.24 shows the distribution of nonequilibrium throughout the isolator section by comparing translational and vibrational temperatures. There are significant differences in

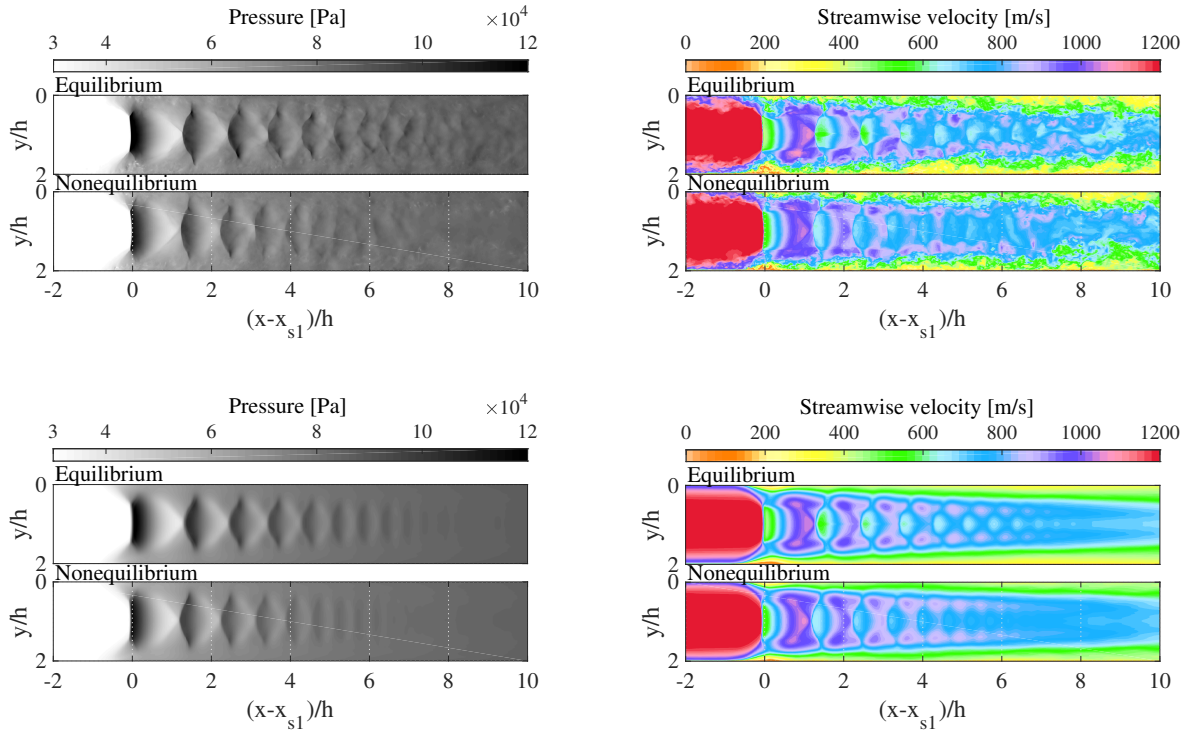

Figure 5.23: Spanwise centerplane (top) instantaneous and (bottom) time-averaged contours of the (left) static pressure and (right) streamwise velocity. For each figure, the top plot is the equilibrium solution while the bottom plot is the nonequilibrium solution.

the local temperatures. The instantaneous figures show that the translational temperatures after each compression shock reaches a high value, where the mechanical compression raises the internal energy of the fluid. Since O_2 relaxes faster than N_2, its vibrational temperature remains close to the translation temperature, albeit with a delayed reaction to temperature T changes. For instance, in the post-compression region (for each cell), the translational temperature drops considerably as the fluid expands, but the O_2 vibrational temperature exhibits lower variation as it relaxes towards the varying translational temperature. Very significantly, N_2 does not equilibrate at all in the computational domain, leading to a nitrogen distribution that is underpopulated at higher vibrational energies. The increase in N_2 temperature occurs mainly in the low-velocity near-wall region, where the higher translational temperature lowers the relaxation time scale [90]. These features are more prominently observed in the difference plots shown in Fig. 5.25. As discussed above, the expansion region

behind each λ-shock leads to a state with a higher vibrational temperature of O_2. As a result, the O_2 population is alternately underpopulated and overpopulated throughout the isolator. As the strength of the shocks decreases with downstream distance, O_2 is able to relax much faster, although these changes have a negligible impact on N_2 relaxation.

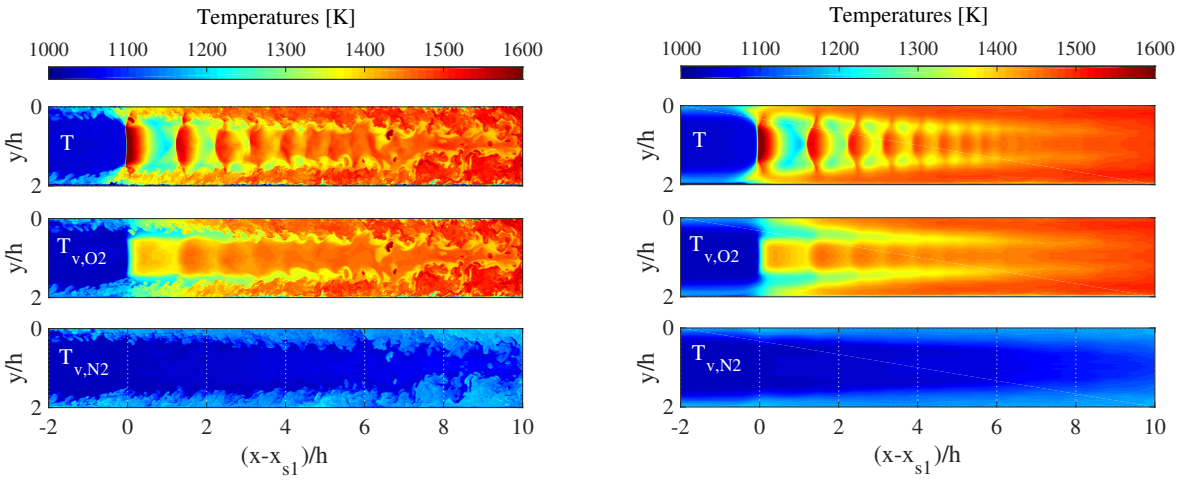

Figure 5.24: Spanwise centerplane (left) instantaneous and (right) time-averaged contours of the (top) static temperature T (center) O_2 vibrational temperature T_{v,O_2} and (bottom) N_2 vibrational temperature T_{v,N_2}.

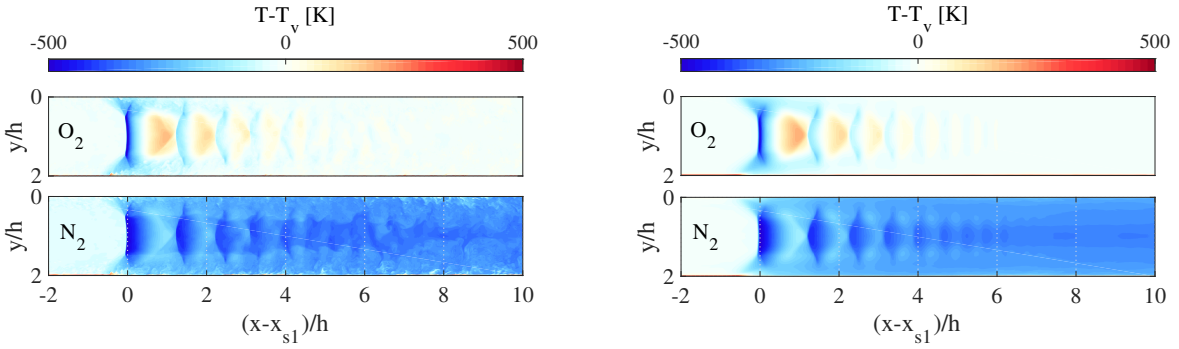

Figure 5.25: Spanwise centerplane (left) instantaneous and (right) time-averaged contours of the difference between static temperature T and (top) O_2 vibrational temperature T_{v,O_2} and (bottom) N_2 vibrational temperature T_{v,N_2}.

In order to understand the energy partition, the ratios between the local vibrational energy of a species and its energy at equilibrium, computed from the translational temper-

ature, are shown in Fig. 5.26. Further, the area-averaged streamwise variation in this ratio is also shown. It is seen that the ratio shows over and under-population for O_2 along the centerline, consistent with the observations in Fig. 5.25. However, the area-averaged value shows that both O_2 and N_2 remain vibrationally cold, but O_2 relaxes approximately midway through the pseudoshock. This is mainly due to the fact that even though the expansion regions occupy a larger cross-section, the density in this region is lower compared to the region between the low-speed near-wall flow and the core flow. As a result, the population at any cross-section along the isolator remains at lower vibrational temperature. This result would be particularly useful for developing one-dimensional isolator models [116], but remains outside the scope of the current work.

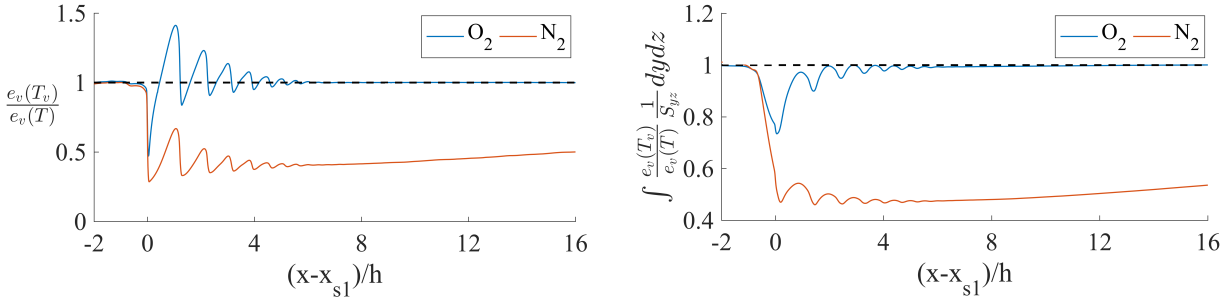

Figure 5.26: (Left) Centerline and (right) area-integrated ratios between the vibrational energies and their local equilibrium values evaluated from T.

5.4.3 Effect of nonequilibrium on the pseudoshock location and length

The differences in pseudoshock structure between the equilibrium and nonequilibrium case were discussed in Sec. 5.4.1. One general conclusion is that nonequilibrium, in an area-averaged sense, stores some of the kinetic energy in the translational and rotational mode. Figure 1.14 showed that when cold nonequilibrium ($T_v < T$) is present, the higher energy content of the translational/rotational modes leads to a slight reduction in the static pressure. In this section, the effect of these two observations on the pseudoshock location and length is discussed.

The 3D time-averaged dataset is now used to compute the cross-sectional integrals of

pressure, density, and temperature along the streamline direction. The flux-conserved integrals of the TRE e_{tr}, the vibrational energy $e_v = Y_{O_2} e_{v,O_2} + Y_{N_2} e_{v,N_2}$ and the mean kinetic energy K are also computed. These profiles are shown in Fig. 5.27. Logically, it appears that nonequilibrium impacts the pseudoshock pressure, density and temperature profiles very similarly than for a normal shock (see Fig. 1.14), which is very intuitive as per pseudoshock definition: a fraction of a normal shock pressure rise occurring over space. The flow is essentially vibrationally under-excited, mostly due to the slow relaxation of N_2 molecules, which causes a significant 90 K difference in outflow temperatures. Likewise, the integrated density equals 0.0893 kg.m^{-3} at the inflow plane, and 0.2127 and 0.2033 kg.m^{-3} for the outflow equilibrium and nonequilibrium cases respectively.

Also, the pseudoshock length noticeably varies from approximately 11 to 16 half-channel heights as observed in Sec. 5.4.1. It is shown in the canonical case in Fig. 1.14 that such cold nonequilibrium decreases the rate of conversion of kinetic into internal enthalpy. Similarly, the pseudoshock integrated pressure plot (top right in Fig. 5.27) reveals that the shock-triggered pressure growth rate is indeed hampered by cold nonequilibrium. Hence, while the equilibrium pseudoshock only needs 11 half-channel heights to rise up to the outlet numerical back pressure, the nonequilibrium pseudoshock is still 2.489 kPa short at the same length. Since the shock-based pressure rise is weaker in the nonequilibrium case, a longer post-shock train turbulent mixing region is needed where pressure will grow up 2.489 kPa through both viscosity and relaxation of e_{v,N_2}. It was computed that pressure gain in the extra region through relaxation of e_{v,N_2} only accounted for 0.277 kPa. This suggests that it is essentially pointless to design isolators long enough to let N_2 naturally relax by the combustor, as Fig. 5.26 showed. Note that 2.489 kPa is only a small fraction of the isolator inlet/outlet gradient: it represents a 5.1% pressure rise defect only. Yet, the pressure growth rate in the post-shock train region through viscous dissipation is weaker than through the shock train [85]. Hence, this modest 5.1% pressure rise defect results in an extra 5 channel half-height: this corresponds to a 45% pseudoshock length increase. The pseudoshock can only find this

extra space by shifting upstream, as observed in Fig. 5.21.

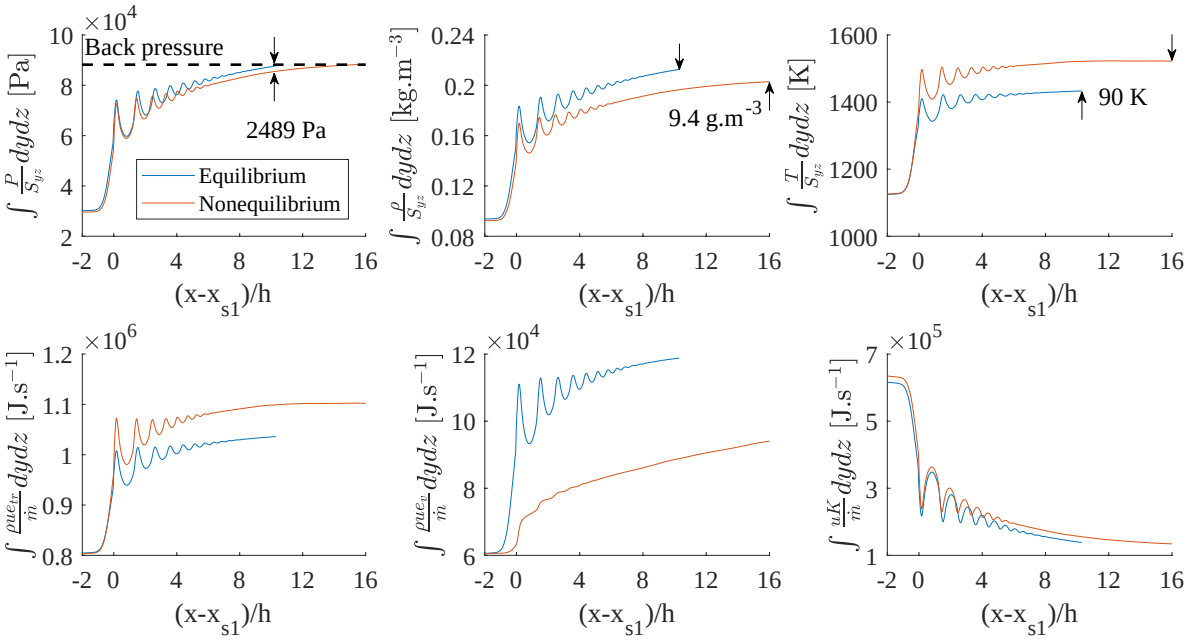

Figure 5.27: (Top) Area integrals of (left) pressure, (center) density and (right) temperature. (Bottom) Flux-conserved integrals of (left) TRE, (center) vibrational energy and (right) mean kinetic energy.

Finally, the various energies flux at the inflow and outflow planes are presented in Tab. 5.3 for both cases. It summarizes how the bulk energy conversion process is affected by nonequilibrium. For both cases, the time-averaged mass flow rate $\dot{m}$ is constant at 0.405 kg.s^{-1}. The sum of the fluxes is not constant due to wall heat losses. Note that Fiévet *et. al* studied the same configuration with adiabatic walls [36] and observed a similarly longer nonequilibrium pseudoshock. As seen in Tab. 5.3, vibrational energy accounts for 7.2% of the internal energy flux before the pseudoshock, for 10.2% at the equilibrium outflow plane and for 7.8% at the nonequilibrium outflow plane. Overall, the defect in N_2 vibrational energy flux is only of 12.8 kJ.s^{-1}, *i.e.* less than 3% of the internal energy flux. Yet, it is sufficient to drastically affect the thermodynamic state and the pseudoshock as seen throughout Sec. 5.4.

While these variations are small, they have profound consequences on the location of

Table 5.3: Inflow and outflow energies fluxes [kJ.s^{-1}] for both equilibrium and nonequilibrium pseudoshocks.

Zone	Mean kinetic	Translational+Rotational	Vibrational(O_2)	Vibrational(N_2)
Inflow - both	258.73	313.45	8.59	15.66
Outflow - Eq.	56.12	420.06	14.25	33.52
Outflow - Noneq.	53.68	445.98	17.06	20.77

shock structures and their impact on downstream processes. Due to the lower pressure in the nonequilibrium case, the pseudoshock is longer in order for the static pressure to reach the imposed back pressure. This distance to reach the backpressure is controlled only by the relaxation time for N_2, which is large compared to the flow through time. To accommodate this longer pseudoshock, the shock train has to move upstream. Hence, even though the pressure differences are minor, the relaxation rate is small enough that a large variation in shock location is observed. Further, even at the end of the isolator, the N_2 population has not reached equilibrium.

To quantitatively assess this specific impact of nonequilibrium, it is useful to use the equilibrated state defined in Sec. 2.3.2. As a reminder, the equilibrated temperature T^* is defined as the equilibrium temperature obtained from the local sum of internal energies. Similarly, P^* is defined as the pressure corresponding to T^* assuming ideal gas law and local fluid composition. Figure 5.28 shows the area-averaged integral of the equilibrated static pressure P^* with the same pressure plots presented in Fig. 5.27 (top left). $\int P^*$ and $\int P_{eq}$ profiles collapse remarkably well, with only minor shifts due to small changes in shock locations. These two profiles reach the numerical back pressure at the same distance from their leading shocks, indicating that the extra length of the nonequilibrium pseudoshock is indeed solely caused by the residual nonequilibrium due to N_2. The net pressure defect due to this nonequilibrium is also shown in Fig. 5.28. At the end of the isolator, there is still almost 3000 Pa of pressure defect. In other words, if equilibrium is reached, this net pressure increase will be observed as the local static pressure in the domain. This is a potential stability issue for DMSJ. Since relaxation can be accelerated by the presence of water vapor [34], which is the product of combustion downstream, there could a sudden

increase in pressure that can adversely affect the stability of the propulsion system, leading to engine unstart [73].

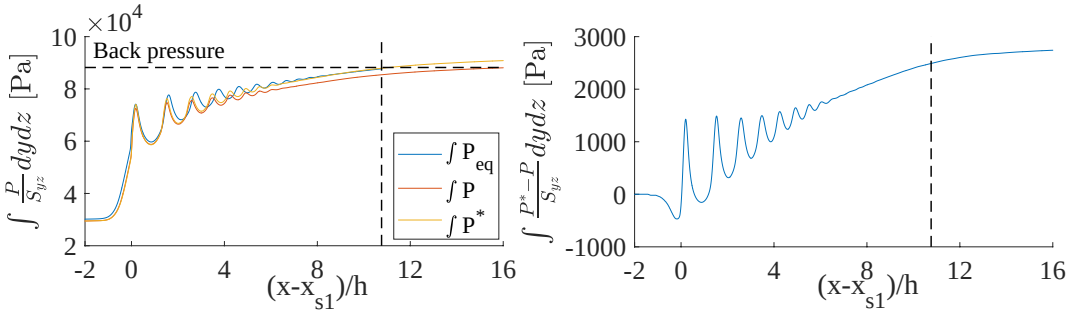

Figure 5.28: (Left) Area-integrated profiles for static pressures from equilibrium case (P_{eq}), nonequilibrium case (P) and nonequilibrium-converted value (P^*). (Right) Area-integrated pressure defect.

It is important to recognize that these important effects on isolator flows were caused by marginal changes in distribution of the internal energy between modes (see Tab. 5.3). Hence a 2.4% difference in excitation of vibrational energy resulted in this 45% increase of pseudoshock length. Figure 5.29 presents on the left the percentage of internal energy stored in vibrational modes for air at different temperatures. The right figures shows for different flight speed the percentage of internal energy stored in vibrational modes for a ramjet flying at 35 km altitude and recovering 70% of a normal shock temperature. A flight speed of Mach 4.2 is enough to place 2.4% of the internal energy inside vibrational modes, resulting in the same amount of nonequilibrium computed from the current pseudoshock simulations. If we place the threshold of relevance of vibrational nonequilibrium at one symbolic percent, then the limit is placed at Mach 3.6. However, at lower altitude, the atmospheric temperature would increase, lowering the flight Mach limit.

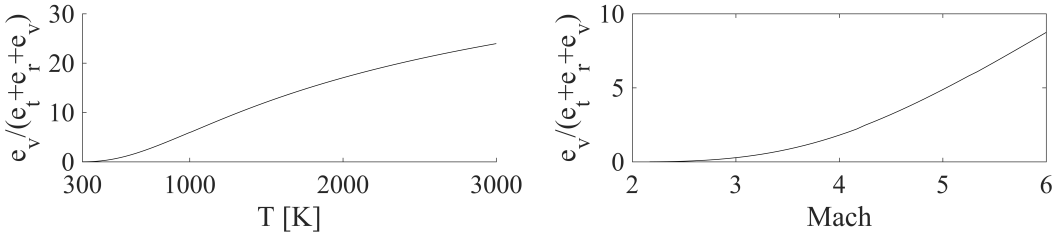

Figure 5.29: (Left) Percentage of internal energy stored in vibrational mode for air. (Right) Percentage of internal energy stored in vibrational mode for air for a ramjet flight at altitude 35 km, assuming a temperature recovery of 70% of a normal shock.

5.5 Implementation of high-temperature effects in the 1D model

5.5.1 Reformulation of the model using real-gas effect

The results presented in Sec. 5.3 and Sec. 5.4 are now used to improve the pseudoshock model derived in Chap. IV. First, the model equations must be reformulated to account for the nonlinearity between energy and temperature. Retaining the Mach number squared as a variable proved impossible due to the apparition of an implicit equation when trying to reduced the velocity and thermal variables into one. The model's equations are therefore simply derived from the 1D conservation equation with the addition of the ideal gas law and the same pressure-kinetic energy equation modeling its growth rate derived through Bayesian analysis in the previous chapter. As for the previous CPG model, the current kinetic energy is used to compute k_q and the closure equation used to evaluate the new dP. Then du and dh are computed instead of dM, note that the heat losses rate $\dot{q}$ now need to be evaluated. The new equations simply are :

$$dP = k_q C f_0^{\alpha} \sigma^{\beta} \frac{1}{2} \rho u^2 \frac{dx}{D_h}, \tag{5.1}$$

$$du = -\frac{dp + 4qCf_1 \frac{dx}{D_h}}{\rho u \frac{A_c}{A}}, \tag{5.2}$$

and

$$dh = -udu + \dot{q}. \tag{5.3}$$

Then, ChemKin is called to evaluate the temperature corresponding to the new internal enthalpy. It is simply done through a linear interpolation of an enthalpy-temperature bijection previously generated. The ideal gas law is used to update density and the new kinetic energy is computed: everything is ready for the next iteration.

5.5.2 1D modeling of the isothermal and adiabatic pseudoshocks

The new 1D model adapted for TPG gas is then used on the normal shock train equilibrium isothermal and adiabatic walls simulations. As the pressure growth rate equation was calibrated on CPG adiabatic datasets, there is no guarantee that it would retain its accuracy on a TPG pseudoshock with/without heat losses. Note that the impact of heat losses is analytically accounted by the model ($\dot{q}$). A smoothed heat loss profile, extracted directly from the DNS integrated total enthalpy profiles shown in Fig. 5.8, is used. The amount of heat lost by the end of the pseudoshock is therefore identical. This way, the validity of the CPG pressure growth rate closure is properly evaluated for TPG pseudoshocks. In general, heat losses could simply be modeled using a Reynolds analogy for instance as Smart suggested or a more sophisticated model, but this is beyond the scope of the present work. The results are shown in Fig. 5.30. It appears that the model evaluates correctly the pseudoshock length and pressure rise for the adiabatic case, while it largely overestimates the isothermal case length. This suggests that the CPG/TPG assumption matters little in defining the pressure growth rate. It also means that accounting for the wall heat losses throughout the pseudoshock is not enough to model the isothermal case. This is coherent with the conclusions of Sec. 5.3.

Figure 5.31 hints at what changes the pressure growth rate equation needs to better match the isothermal wall cases. The left figure correlates the first cell size (defined as the distance between the first 2 centerline subsonic zones) with the pseudoshock length (defined here as the distance between the leading shock location to the maximum wall pressure value).

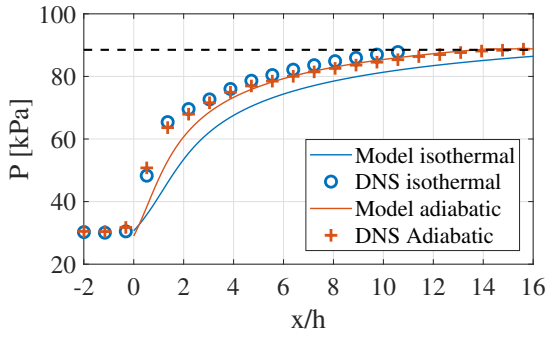

Figure 5.30: Comparison of the isothermal and adiabatic walls simulation with the modified 1D model.

It shows how vibrational nonequilibrium tends to further increase the pseudoshock length compared to the trend obtained from CPG DNS in Chap. III. The pressure rise ratio (70% of a normal shock), the centerline inlet Mach number (inflows initiated at uniform Mach number of 2.0) and the full geometry are kept identical for all these cases. The figure on the right shows the correlation between the first cell size and the length of the sonic core (distance between the leading shock and the last sonic streamwise location). As the correlation holds regardless of the use of adiabatic or isothermal wall boundary conditions we can deduce that the first cell size is a robust indicator of the shock train size. And the first cell size depends on the normal-like portion of the leading shock, as shown by the CPG simulations. Hence, we can deduce that the real impact of heat losses are upstream of the shock train, not throughout its region. This is once again coherent with the conclusions of Sec. 5.3. Therefore, there must be a difference in upstream conditions between both cases which triggers a longer first cell increasing the pseudoshock length. This is evidence that the model needs to be fixed through the pressure growth rate closure equation by a single coefficient, function of a new upstream condition function of upstream heat losses.

As explained in section 5.3, the inflow is identical and generated from an adiabatic channel. The wall heat losses from the inlet to the $x = x_{s1} - 2h$ position have resulted in a loss of 50 K in total temperature (see Fig. 5.8). The conditions used for the 1D model are shown in Tab. 5.4. Note that the boundary layer thickness and displacement thickness ratio $\mathcal{A}_*$ are roughly equal, and therefore are poor indicators of these boundary layer profiles

Table 5.4: Isothermal and adiabatic wall cases conditions for the 1D model.

Case	M_0	P_0 [kPa]	T_0 [K]	C_{f0}	$\mathcal{A}_*[\%]$	$\mathcal{A}_\theta[\%]$	M_1	P_1 [kPa]	T_1 [K]
Isothermal	1.89	32.15	1046	$0.75e^{-3}$	15.48	6.51	1.78	30.68	1023
Adiabatic	1.88	33.38	1048	$1.51e^{-3}$	16.04	5.77	1.83	29.01	1002

changes. The main differences are the halved skin friction coefficient and a 16% bigger $\mathcal{A}_\theta$. Such changes are going to affect the pressure growth rate closure equation by reducing both the efficiency σ and Cf_0 which are both taken at the power α and β, resulting in a slower rise rate. Yet, the opposite happens which show the inadequacy of the current closure equation to account for the weakening of the vortical structure. Still, Fig. 5.31 suggests some form of correlation and therefore a new formula could be designed to replace the $Cf_0^\alpha\sigma^\beta$ term which was already identified as being the weak part of the model in Chap. IV). Note that it is still relevant to retain the skin friction coefficient to a positive power to ensure the asymptotic behavior of a standing normal shock in case of an infinite shear stress. The results of Sec. 5.3 suggest that a parameter quantifying the upstream vortical activity (such as the strength of $\int \omega_{r,YZ}$) would be a pertinent choice. Unfortunately, more data on high-temperature shock trains would be necessary to accurately derive a new formula without simply find a situational correction.

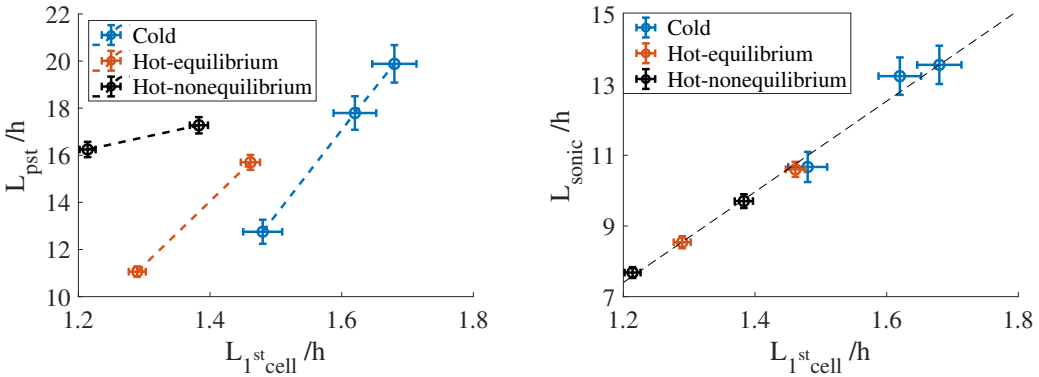

Figure 5.31: Correlation between the first shock train cell size and (left) the pseudoshock length or (right) the sonic core length for all the NST simulations.

To conclude, the pressure growth rate equation needs to be revisited to include the proportionality resulting from the correlation shown in Fig. 5.31. A coefficient function of

the upstream vortical activity (and possibly other variables) would permit to account for the larger pseudoshock pressure growth rate for cooled walls. The current coefficients $Cf_0^\alpha\sigma^\beta$ have the opposite effect due to the skin friction decreasing as wall viscosity decreases with the wall temperature.

5.5.3 1D modeling of the vibrational energies relaxation process

The current model works for adiabatic TPG pseudoshocks. it remains to assess its capacity in resolving vibrational nonequilibrium. Admitting that the adjustments to the heat loss model just discussed could be implemented, the pressure growth rate closure equation is simply adjusted up to a constant to match the correct pseudoshock length of the nonequilibrium case. Note that this does not guarantee that the model can correctly estimate the pressure rise. The 1D model is then adapted to resolve nonequilibrium. As the closure equation was derived to match equilibrium physics, it cannot be directly used to forward march in space the nonequilibrium flux-conserved temperature, pressure, velocity and density. Indeed, we know from Fig. 5.26 that the bulk flow remains vibrationally under-excited throughout the pseudoshock, which causes a pressure rise lag seen in Figs. 5.27 and. 5.28. However, the pressure growth rate closure equation gives a rate of change proportional to the local kinetic energy. And, as shown in Fig. 1.14, the kinetic energy is slightly increased by cold nonequilibrium to the delay in the conversion of kinetic energy into internal energy. Hence, naively using the current pressure growth rate model where $\frac{\partial P}{\partial x} \propto K$ on the nonequilibrium value would result in an opposite trend: a shorter pseudoshock. The correct way of accounting for nonequilibrium using the 1D model is to resolve at every iteration the state $\cdot^*$, *i.e.* the equilibrated thermodynamic quantities, and use these to compute the local pressure rise. Vibrational energies are updated using Landau-Teller model with Millikan-White relaxation timescales computed from the nonequilibrium temperature and pressure. Then, both source terms are used to update the next iteration. The steps are summarized as follows for a typical iteration:

1. The equilibrated thermodynamic state $\cdot^*$ is computed.

2. The dP^*, du^* and dh^* are computed as shown in Eqs. (5.1)-(5.3) from the equilibrated values P^*, q^*, ρ^*, u^*, h^* and A_c^*.

3. The vibrational energies source terms de_{v,O_2} and de_{v,N_2} are computed using the LTMW model with T, P, e_{v,O_2} and e_{v,N_2}.

4. The equilibrated state variables and new vibrational energies are separately updated using the source terms computed in the two previous steps.

5. Conservation of energy is used to find the new equivalent T, which gives the current step dT.

6. Having computed dT, the conservation of mass, momentum and energy and ideal gas law are used to evaluate dP, du and dh.

7. P, u and h are updated from these gradients, and the new area ratio and kinetic energy are computed.

However, the validity of the Landau-Teller linear relaxation model on 1D flux-conserved quantities needs to be assessed. Indeed, the relaxation model used so far consists in a division between the gradient of $e_v(T_v)$ and $e_v(T)$ and the relaxation timescale, which is inversely proportional to the local pressure and temperature to the power 1.5. The resulting nonlinearity is, therefore, an issue to a 1D approach as further explained. As seen in the 2D contours presented in Figs. 5.23 and 5.25 the areas of larger vibrational energy gradients coincide with the largest pressure areas: they are located along the centerline shocks. By definition, a 1D approach would not only smooth these gradients but the local pressure and temperature are also going to be much lower as being surface-averaged (and never reach a normal shock-like rise as locally observed along the shock train centerline). It is therefore anticipated that using the relaxation model on 1D flux-conserved values leads to an under-estimation of the vibrational energies source terms. In an effort to prove this point, the

Landau-Teller linear relaxation model is now used to compute relaxation source terms from the DNS flux-conserved quantities. They are then compared to the exact flux-conserved source terms locally computed from the time-averaged 3D dataset. The energy source terms are plotted on the top figure of Fig. 5.32, and appears to be relatively similar for O_2 which is a quick relaxing species. On the other hand, N_2 relaxation process heavily relies on the local gradient since its relaxation timescales are orders of magnitude larger than O_2's, and its relaxation source terms computed from flux-conserved quantities are under-estimated compared the exact values obtained from the DNS. The bottom figure shows the exact flux-conserved vibrational energies (solid lines) compared to the profiles obtained by forward integration of the 1D source terms from the top figures (dashed lines). As expected a slower relaxation occurs for N_2, and if the residence time was much lower than the local O_2 vibrational relaxation time the same issue would appear for that species too. A simple solution would, therefore, be to increase P and T used in the Millikan-White correlation of the relaxation time to account for the large portion of high P and T along the shock train cells. Likewise, the local equilibrium vibrational energies used to compute the local gradient could be evaluated with that artificially higher T.

Nonetheless, the current model with correction for nonequilibrium is used to predict the flux-conserved profiles for ρ, P, T and u of the simulation. It is important to start from the correct e_{v,O_2} and e_{v,N_2} since the objective is to assess the validity of the parallel equilibrated computation approach to resolve 1D vibrational nonequilibrium. Therefore the model's initial state 1 is determined by the exact flux-conserved quantities integrated from the 3D time-averaged dataset instead of using the simpler technique presented in Sec. 4.2.2. The results are present in Fig. 5.33 and show excellent comparison, notably in final amplitudes. It was decided to use the exact heat loss rate computed from the simulation. The vibrational energies profiles are shown in Fig. 5.34 and the expected slower relaxation occurs. Note that this results in less than 7000 J.kg^{-1} defect for e_{v,N_2} which represents only 0.3% of the internal energy: the impact on ρ, P, T and u is negligible.

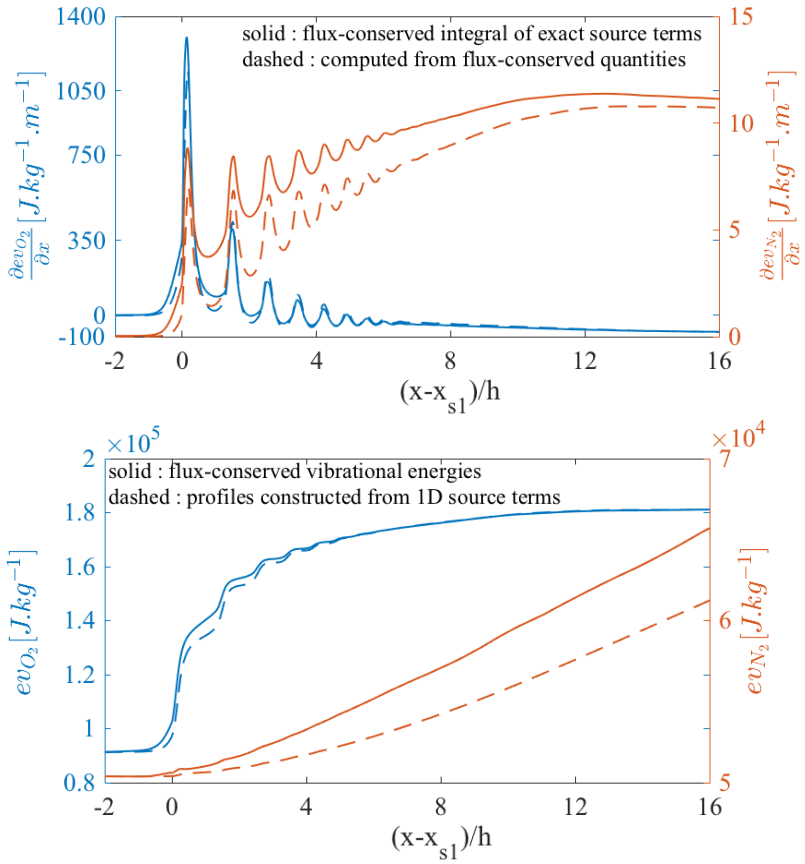

Figure 5.32: (Top) Landau-Teller relaxation source term for the vibrational energies of O_2 and N_2 YZ-integrated from (solid) the DNS or (dashed) computed from flux-conserved quantities. (Bottom) Flux-conserved vibrational energies of O_2 andN_2 compared with profiles reconstructed from source terms computed from flux-conserved quantities.

To conclude, the 1D model was adapted to account for vibrational nonequilibrium. Yet, it is unable to correctly predict the effect of upstream wall heat losses due to its strong dependence on the skin friction which is a crude indicator of a turbulent boundary layer profile vortical activity. In order to improve the model accuracy, it is necessary to include a corrective model on top of the $Cf_0^{\alpha}\sigma^{\beta}$ term. More datasets with various amount of wall heat losses would be needed to perform a Bayesian-regression to calibrate that enhanced model. CFD would be the perfect tool to generate such datasets as it would permit to accurately compute wall heat losses throughout the pseudoshock and, as importantly, upstream. It is possible to use the 1D model to resolve the flux-conserved vibrational relaxation process. The pressure growth rate equation used the local equilibrated state variables, while the

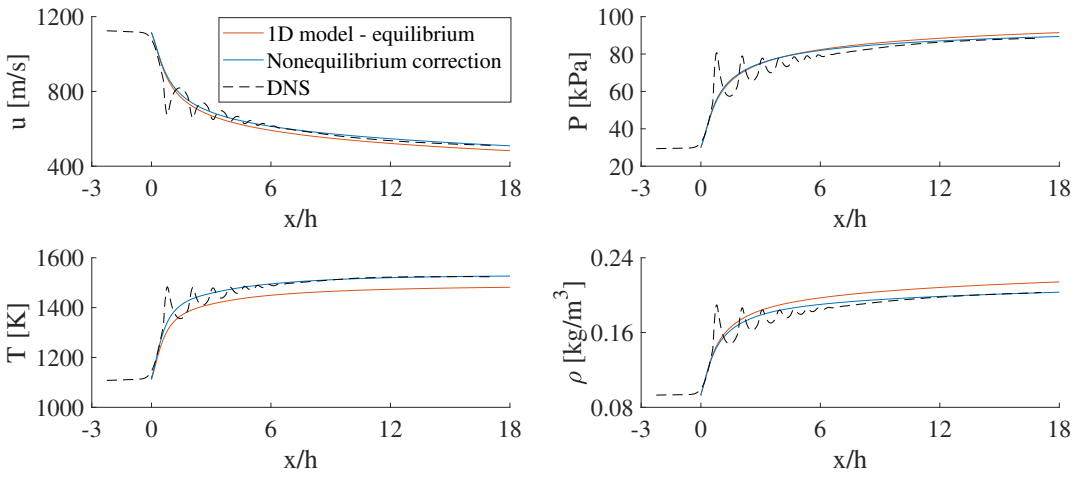

Figure 5.33: Flux-conserved (top left) velocity, (top right) static pressure, (bottom left) temperature and (bottom right) density profiles of the DNS compared with results obtained from the 1D model corrected with a vibrational relaxation model.

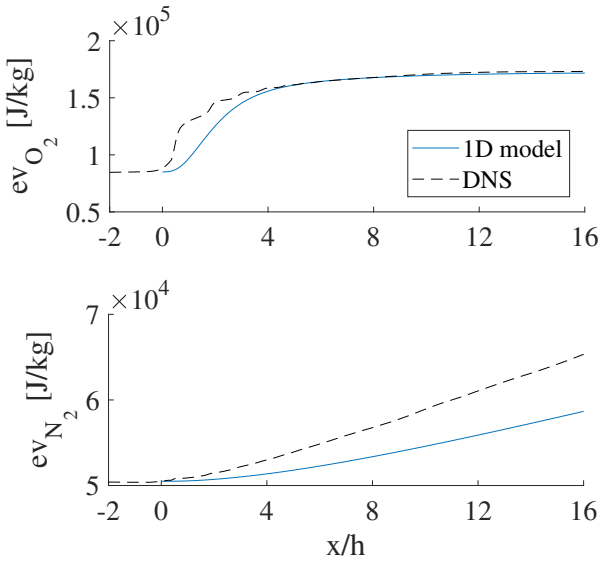

Figure 5.34: Flux-conserved of flux-conserved (top) e_{v,O_2} and (bottom) e_{v,N_2} obtained from direct integration of the DNS or from the 1D model.

flux-conserved vibrational energies were evolved with the LTMW model. However, the flux-conserved approach under-estimates the overall relaxation rates. Yet, it appears that the simple process described in this chapter works to a certain extent: the flux-conserved profiles and final states are correctly predicted provided the wall heat loss is resolved, and the corrections suggested are computationally cheap. This approach, therefore, verifies the great

conservation principles. While these two issues can appear to be serious for now, future datasets will help overcome these through Bayesian-regression and the current work could serve as a baseline.

5.6 Chapter conclusions

A set of high-temperature pseudoshock simulations have been carried out, which corresponds to realistic high-altitude hypersonic flight conditions. The impact of wall heat losses has been studied, and was shown to decrease the strength of vortices present in the turbulent boundary layer. As a result, the boundary layer was found to be more resistant to adverse pressure gradient and separate less. The shrinking of the recirculation bubble resulted in larger shocks inside the shock train, which increased the pressure growth rate. To conclude, increasing wall heat losses was found to reduce the pseudoshock length.

The effect of vibrational nonequilibrium on pseudoshocks were investigated using the nonequilibrium compressible reacting flow solver presented in Chap. II. As the flow convects through the shock train the vibrational energies of O_2 and N_2 fall out of equilibrium. While oxygen relaxes fast enough to reach equilibrium by the shock train tail, N_2 molecules are still vibrationally under-excited. This causes a weaker pressure growth rate along the pseudoshock, which results in an increased length in order to accommodate the same numerical back pressure than in the equilibrium simulation. The pressure defect through shock-induced compression is compensated by a larger post-shock train mixing region. Viscous dissipation amounts for the majority of the extra pressure generated to compensate vibrational nonequilibrium. The outflow possesses a static temperature 90 K smaller than the TPG case, a 5% smaller density, and has a N_2 vibrational temperature 300 K smaller than the translational temperature. Incidentally, this means that whenever the flow will be brought back to thermal equilibrium in the combustor through heat release, N_2 relaxation will further increase the pressure by an additional 3000 Pa currently trapped out of the N_2 under-excited vibrational energy. It was estimated that vibrational nonequilibrium effects become non-negligible for

flight Mach superior to 3.6 at 35 km altitude. This essentially suggests that DMSJ should always consider resolving the relaxation process of the vibrational energy.

Lastly, the 1D model derived in Chap. IV was modified to include the high-temperature effects discussed in this chapter. It appears that a sub-model for the integrated relaxation timescale is needed. The flux-conserved approach was shown to be suited to describe the relaxation process nonetheless.

CHAPTER VI

Impact of vibrational nonequilibrium in ignition in dual-mode scramjet engines

The impact of vibrational nonequilibrium on the combustor region is studied in this chapter using the DNS approach. Two models of ramjet and scramjet engines are simulated using either equilibrium/nonequilibrium thermodynamics and the modified reaction rates defined in chapter II. In some cases, ignition delay can lead to loss of propulsive thrust, as is observed in the ramjet configuration. In scramjet configuration, however, a complex bow-shock and horseshoe-like structure forms at the injector porthole. A combined effect of H_2-recirculation bubble with a succession of shock and expansion waves results in faster radicals H and O formations which enhances the ignition process. Lastly, a comparison with experimental data shows a closer match when resolving nonequilibrium. Some of this work was published in Fiévet *et al.* [39].

The chapter is organized as follows:

- Sec. 6.1 further discusses the motivations of this study.
- Sec. 6.2 presents the simulation and results in ramjet mode.
- Sec. 6.3 presents the simulation and results in scramjet mode.
- Sec. 6.4 presents the simulation of a scramjet experiment and a comparison between wall pressure profiles.

6.1 Motivation

Chemical reactions were shown in Chap. II to be highly sensitive to the vibrational energy of the reactants. In a rather simplified picture, chemical reactions require that molecules overcome the activation energy barrier, which is more probable for molecules with higher vibrational energy. Similarly, any region of the flow that contains molecules with lower-than equilibrium vibrational energy will likely exhibit lower reaction rates. Since compression shocks tend to create the latter situation, i.e. the post-compression vibrational distributions are initially frozen at the conditions prior to the shock, it is expected that chemical reactions will be suppressed by these conditions. Indeed, in the DNS of Koo *et al.*, [72], the presence of such a vibrational nonequilibrium in a jet flow led to a delay in flame stabilization and increase in flame lift-off height.

However, this view of the thermal nonequilibrium effect is very simplified in a DMSJ context. First, for a constant total energy, any reduction in vibrational energy implies that the translational (and rotational) energies are larger than the equilibrium values, as was shown in Sec. 2.3.2. For instance, in the chain-propagating reaction $H_2 + OH \rightarrow H + H_2O$, it was shown that OH vibrational nonequilibrium only had a marginal effect on the reaction rate. In other words, the reaction dynamics are insensitive to the vibrational energy of the OH molecules and depend more on the translational energy to create the products.

Second, in scramjet engines, the flow field near the fuel porthole is very complex as illustrated by the schematic from Ben-Yakar [4] presented in Fig. 6.1. The interaction between the airflow and the fuel jet forms recirculation bubbles, a bow shock (triggering cold vibrational nonequilibrium through compression) and an expansion wave (triggering hot vibrational nonequilibrium). Another expansion wave forms inside the fuel stream which is usually slightly under-expanded to prevent any backflow in the injector.

Such near-injector combustion physics has been widely studied in the past. Ben-Yakar *et al.* [4] studied the mixing process using Schlieren imaging, revealing the formation of large-scale eddies in the shear layer shown in Fig. 6.1. Gamba and Mungal [45] localized

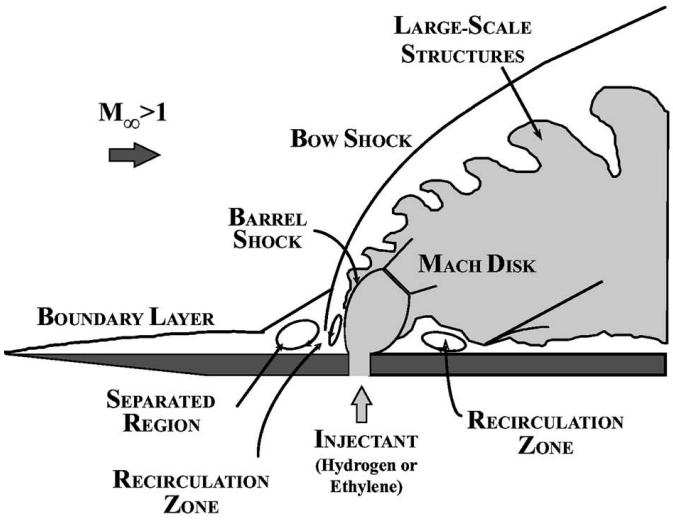

Figure 6.1: Flow structure schematic at the fuel porthole from Ben-Yakar [4].

the flame front by using OH*-chemiluminescence imaging. They showed that there exists an intensely burning region located at the bow-shock foot, right in front of the impinging jet. Also, they revealed that chemical activity decreased inside the expansion region. Last, they observed the presence of radical OH in the upstream recirculation bubble, which suggests that fuel can, at least intermittently, recirculate upstream and react within this pocket. Finally, computational studies using LES [61, 137] proved to be able to resolve this complex region and evaluate the flame lift-off. They observed the large-scale vorticity in the shear layer and the intermittent fuel upstream recirculation as well.

In the present study, the fuel stream is choked and under-expanded at the injector porthole. It is expected to trigger an expansion wave as observed by Ben-Yakar [4] as the jet pressure adjusts to the lower combustor pressure. Unlike compression shocks, the vibrational energy post-expansion is higher than the equilibrium value. Further, fuel-airflow mixing can also be the source of nonequilibrium as demonstrated in Sec. 2.2.4. Consequently, ignition is expected to occur within a region where the reactants are not at equilibrium. The flow structure will also play an important role in determining the impact of nonequilibrium on chemical reactions.

Third, and perhaps less important, is the effect of nonequilibrium on the bulk properties

of the fluid. Again, considering a constant energy flow, an increase in translational energy will increase the viscosity of the flow, which will reduce the turbulent mixing of the fluids. In the DNS study of Koo *et al.* [72], it was found that the change in heat release location delayed the increase in viscosity due to temperature increase, leading to slightly improved mixing. Hence, the bulk property variations represent a competing effect, where nonequilibrium and the resultant delayed ignition might increase turbulent mixing (in comparison to equilibrium).

With this background, the objective of this chapter is to determine the effect of nonequilibrium in DMSJ combustors. To this end, the nonequilibrium solver is used to simulate two combustor configurations: the first in ramjet mode, the second in scramjet mode. These combustors essentially consist in jet and subsonic/supersonic crossflow configurations, with an airflow thermodynamic state corresponding to a 35 km altitude flight at Mach numbers 5.0 and 9.0 respectively (same altitude as in Chap. V). Both equilibrium and nonequilibrium models will be used, the equilibrium simulations serving as test cases. First, the ramjet mode will be studied. It will simply consist in an extension of the isolator studied in the previous chapter. The scramjet mode will be simulated using the HyShot-II [103] experiment as a model. This configuration has been the focus of many previous numerical studies using RANS or LES computations assuming thermodynamic equilibrium chemistry in the combustor [60, 55, 19, 75, 104, 66, 15, 93, 7].

Lastly, a simulation of the HEG experiment [48] mimicking the HyShot-II 28 km hypersonic flight will be performed with both equilibrium and nonequilibrium model to compare our results with a real-life configuration.

6.2 Ramjet mode

The ramjet-like mode simulations presented in this section consist of a simple extension of the computational domain presented in Chap. V. The outflow of both equilibrium and nonequilibrium simulations (for isothermal walls condition) were sampled to generate inflow files for both cases. A H_2 injector was added to the bottom wall, at center and 3 cm from

the inlet plane. This configuration permits to study how nonequilibrium affects ignition in a canonical subsonic jet and crossflow configuration. However, this configuration is not based on any real ramjet design contrary to the following scramjet simulations. Hence, the analysis presented in this section provides a qualitative view of the problem [1]. Still, some of results and metrics that will be presented will be useful in assessing the effect of nonequilibrium in the HyShot configuration in the next section.

6.2.1 Numerical details

Figure 6.2 presents a 3D snapshot of the ramjet-like configuration for the (top) equilibrium and (bottom) nonequilibrium cases. The length L of the domain has been shortened to $L = 25$ cm compared to Chap. V. The grid resolution in the YZ plane matches the resolution of grid R2+ presented in Tab. 5.2 while 1000 cells were used along the X-direction, decreasing the $\delta x+$ to 11.8. The inflow is a fully developed 3D turbulent boundary layer as seen in the last YZ slice in Fig. 5.4. The inflow thermodynamic state comprises the final values extracted from Fig. 5.27's plots and are presented in Tab. 6.1 for convenience. The mass flow rates are both equal to 0.405 kg.s^{-1}.

Table 6.1: Ramjet inflow thermodynamic states for the equilibrium and nonequilibrium cases extracted from Fig. 5.27 and Tab. 5.3.

Inflow	$\int P$ [Pa]	$\int T$ [T]	$\int \rho$ [kg.m^{-3}]	$\int \dot{m} e_{v,\mathrm{O}_2}$ [kJ.s-1]	$\int \dot{m} e_{v,\mathrm{N}_2}$ [kJ.s-1]
Equilibrium	$8.8e^4$	1433	0.2127	14.25	33.52
Nonequilibrium	$8.8e^4$	1523	0.2033	17.06	20.77

The injector is located at 3 cm from the inlet plane, in the Z-centerplane and Y-bottom wall, and it has a diameter D_j of 0.5 cm. The H_2 injector is treated as a Dirichlet boundary condition: all the ghost cells included inside its circular cross-section are updated at every timestep with the fuel flow values. The injector is choked (Mach number equal unity) and is injected vertically at a velocity of 1200 m.s^{-1}, a pressure of 1 atmosphere (101.3 kPa) and a temperature of 250 K. This corresponds to a total temperature of 300 K, which was

[1] Further, no grid convergence was run on this simulation.

chosen to match the isothermal wall temperature. The fuel tank total pressure equals 192 kPa. The fuel mass flow rate equals 2.32 g.s^{-1} resulting in a fuel-oxidizer equivalence ratio of 0.24. The total pressure was chosen to avoid under-expanding the fuel and the appearance of a strong expansion wave at the bottom wall. The fuel porthole diameter was chosen small enough to ensure a large L/D_j ratio ensuring that the domain was long enough to capture the ignition process. These conditions resulted in a lean mixture, as is the case in DMSJ [76]: an equivalent ratio over 0.4-0.5 puts the engine at unstart risk due to both mass and thermal choking. The simulations both ran until the flame and mass flow rate stabilized. Then, it ran over 60 hours on 8400 cores, covering a total time of 3 ms. Statistics were sampled over a total of 6 flow-through times based on the smallest YZ-integrated velocity across the computational domain.

In both cases, fuel-air mixing appears to be very turbulent. A small recirculation bubble is present in front of the injector, and a large one appears right behind the injector as well. Ignition occurs slightly downstream and is re-attached to the fuel jet by the large recirculation zone. Hence, the flame front is attached to this zone. The temperature rises up to 2600 K in both cases, and most of the fuel has been consumed by the outlet plane.

6.2.2 Presence of nonequilibrium

Figure 6.3 presents on the left a snapshot of the Z-centerplane temperatures fields T, T_{v,O_2}, T_{v,H_2} and T_{v,N_2}, for the nonequilibrium case from top to bottom. The x-axis origin is placed at the center of the fuel porthole. The corresponding time-averaged contours are shown on the right. The flow coming from the isolator is known to be out of equilibrium (see Tab. 5.3) with a vibrationally under-excited N_2 population while O_2 is mostly at equilibrium. A pink dashed line indicates the local stoechiometric line based on the reaction $\mathrm{H}_2 + \frac{1}{2}\ \mathrm{H}_2 \rightarrow \mathrm{H}_2\mathrm{O}$. It appears that the presence of combustion and production of $\mathrm{H}_2\mathrm{O}$ contributes to quench nonequilibrium: N_2 barely relaxes in the cold regions while it quickly relaxes in the flame front. This appears clearly in Fig. 6.4 which shows the local gradient with the

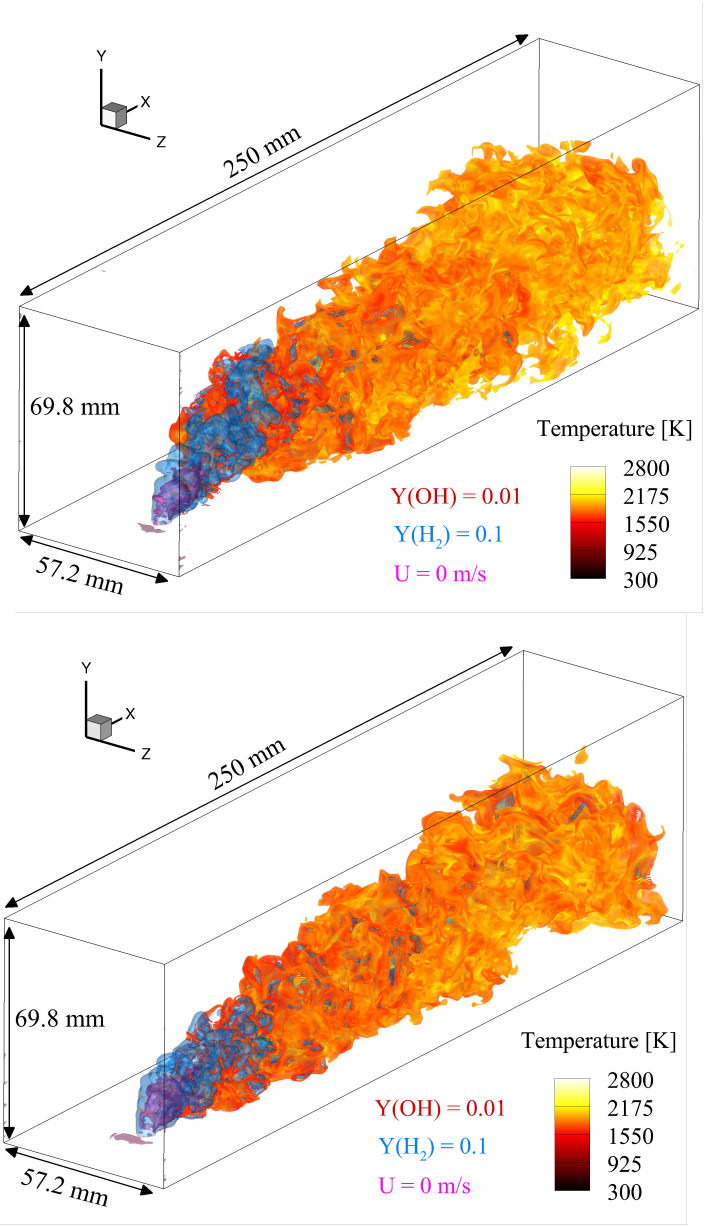

Figure 6.2: Snapshot of the ramjet-like configuration for the (top) equilibrium and (bottom) nonequilibrium cases.

translational temperature T. T_{v,N_2} is closer to T in the flame. Several other observations can be made from Fig. 6.4. First, there appears to be a $T - T_{v,\mathrm{O}_2}$ gradient at the inlet, while the isolator outflow O_2 species was at equilibrium. This was caused by an interpolation error in evaluating T_{v,O_2} from the inflow file e_{v,O_2}, causing an $\approx$ -30 K defect to occur at the inlet plane. Still, this corresponds to less than 0.1% of the internal energy flux, hence this error can reasonably be neglected. The green dashed line corresponds to each species's

mass fraction 0.000001 isoline. It can be seen that the H_2 coming from the under-expanded jet flow is vibrationally hot due to the expansion process. However, as it mixes with the hotter coflow, T_{v,H_2} becomes smaller than the translational temperature. In Sec. 2.2.4, the vibrational energy of N_2 was coming from both side of the shear layer. If the relaxation source term were to be arbitrarily set to zero, the energy would linearly mix as the inert scalar Z_{mix}. However, if a species comes from only one side of the shear layer, the vibrational energy would remain skewed towards the value of its inflow stream. This was experimentally observed by Reising *et al.* [112] in a mixing layer between cold Argon and hot Nitrogen. Here, the same mixing rule occurs as H_2 becomes vibrationally cold in the mixing layer. Indeed, it appears clearly that $T_{v,H_2} < T$ outside of the bent jet potential core. Conversely, O_2, coming from the hot airflow, is not vibrationally cold in the mixing layer. In fact, it appears to be several hundred Kelvin hotter than the fuel jet at the shear layer start. This results in a stoichiometric line crossing zones of vibrationally cold H_2 and vibrationally hot O_2, which can potentially alter ignition as seen in Fig. 2.23.

6.2.3 Impact on reaction rates

To better understand the coupling between nonequilibrium and chemistry, Fig. 6.5 presents realizations of (T,T_{v,O_2}) across the computational domain. The realizations are colored by (left) efficiency function $\phi_{F1} - 1$ from -1 to 3, (middle) heat released rate $\dot{q}$ [J.m^{-3}.s^{-1}] and (right) radical O production [kg.m^{-3}.s^{-1}].

The first figure on the left simply shows that there are many realizations far from equilibrium. The second figure shows that the reacting zone is overwhelmingly characterized by vibrationally hot O_2, which coincides with the exothermic region. A small endothermic region is located at the hottest locations where the T_{v,O_2} is slightly inferior to T and T ¿ 1800 K and closer to its peak temperature. This corresponds to a thin reacting region in the large separation bubble where the entering O_2 is colder than the hot burning pocket. Also, the fresh stream of O_2 dissociates through reaction $O_2 + H \longrightarrow OH + O$ as it enters

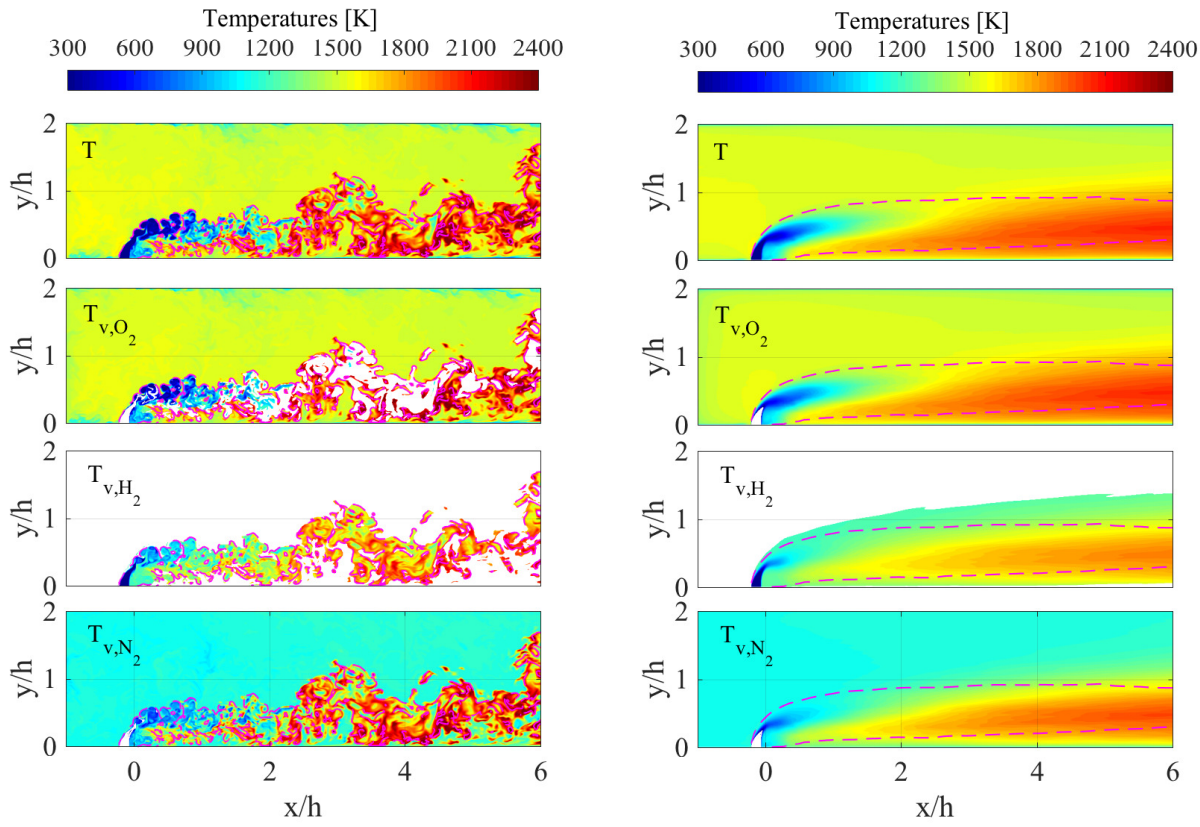

Figure 6.3: (Left) Snapshot of the of the Z-centerplane temperatures fields T, T_{v,O_2}, T_{v,H_2} and T_{v,N_2} from top to bottom. (Right) Corresponding time-averaged contours. The dashed pink line indicates local stoichiometric mixing.

this hot, burning, recirculation zone. The C-V coupling in Eq. 2.13 therefore decreases e_{v,O_2} (hence T_{v,O_2}). As a reminder, the vibrational energy of a reactant species slightly decreases during a reaction as explained in Sec. 2.2.1. Indeed, as seen in the right figure of Fig. 6.5, the negative $\dot{q}$ region corresponds to the region of radical O net production. Conversely, the exothermic region corresponds to the radical O depletion region. These negative $T_{v,\mathrm{O}_2} - T$ realizations are observed in the recirculation zone and where the airflow decelerates when interacting with the impinging jet. This instantaneously creates cold nonequilibrium through compressibility as observed in Sec. 2.2.4.

It is useful to consider the indicator $\frac{k_{Fi,qct}(T,T_v)}{k_{Fi,eq}(T^*)} - 1$ [%] for the i-th forward reaction Fi to understand if a reaction is fastened by nonequilibrium. The numerator is the local

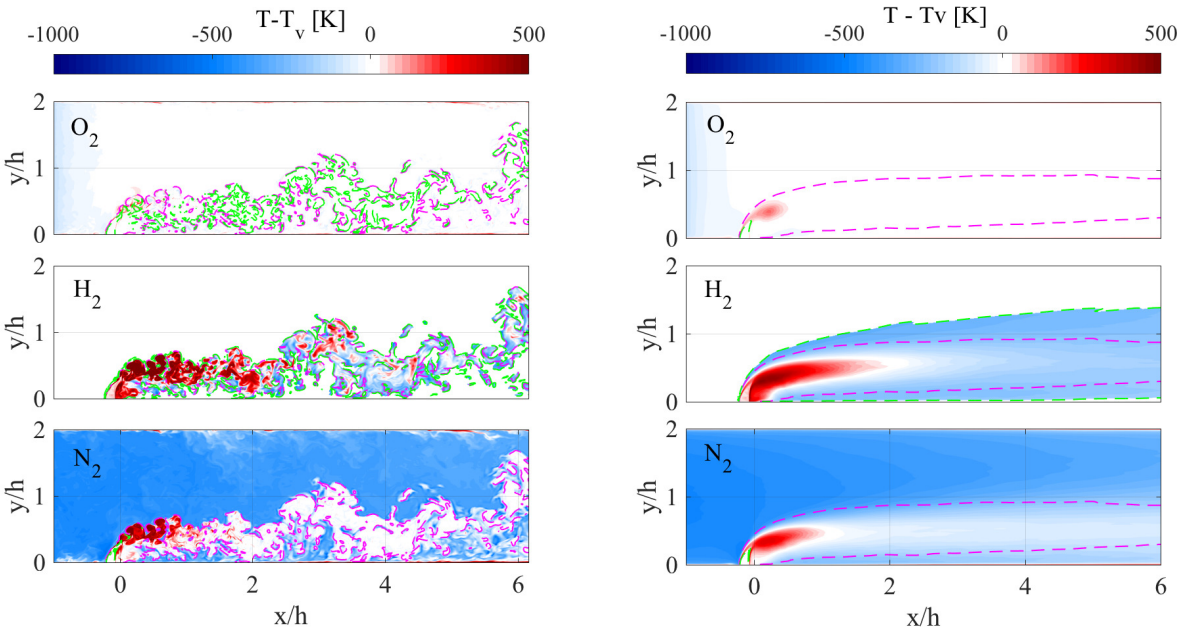

Figure 6.4: (Left) Snapshot of the difference between the local translational temperature and species (top) T_{v,O_2}, (middle) T_{v,H_2} and (bottom) T_{v,N_2} on the Z-centerplane. (Right) Corresponding time-averaged contours. The dashed pink line indicates local stoichiometric mixing while the green line marks the presence threshold of species mass fraction superior to 0.00001.

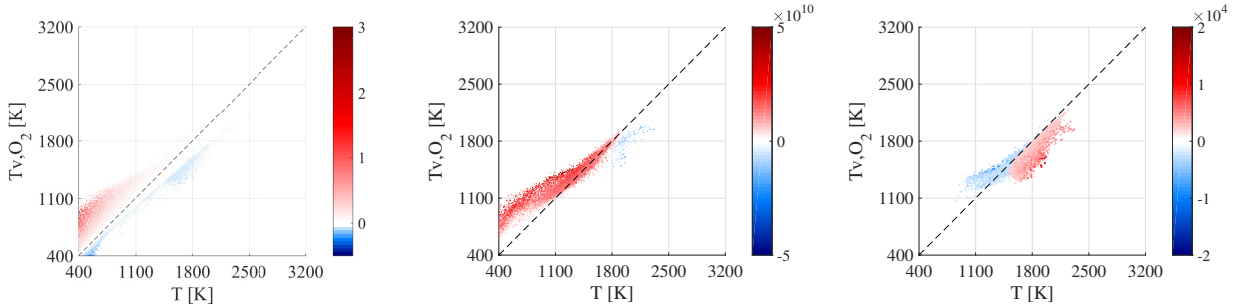

Figure 6.5: Realizations of T and T_{v,O_2} colored by (left) efficiency function $\phi_{F1} - 1$ from -1 to 3, (middle) heat released rate $\dot{q}$ [J.m^{-3}.s^{-1}] and (right) radical O production [kg.m^{-3}.s^{-1}].

nonequilibrium rate $k_{Fi,qct}(T, T_v)$ and the denominator is the reaction rate computed from the equilibrated state $k_{Fi,eq}(T^*)$. This indicator will be referred as the "reaction efficiency ratio".

Figure 6.6 shows the scattering of the full chain branching reaction rates (i.e. the rates times their reactant mole concentrations) against the corresponding reactants vibrational

temperature ratio. The plots are colored by the local reaction efficiency ratio in percentage. A value of 0 means that the local rates are identical to their respective equilibrated values, a negative value means that the equilibrated solutions would have higher reaction rates and a positive value that it would be lower. The first chain reaction has a pre-exponential coefficient of 0, hence only the efficiency function $\varphi_{F1}(T, T_{v,\mathrm{O}_2})$ matters, which explains the easy separation: negative values for $T_{v,\mathrm{O}_2} < T$, and positive values for $T_{v,\mathrm{O}_2} > T$. The second figure corresponds to reaction F2 and possesses essentially two zones: a negative one in the bottom right and a positive for the higher rates. The overlapping of these regions prevent from assessing which one dominates, but in general, the amplitudes of the efficiency ratio (in %) are modest for reaction F2 which is responsible for radical H formation. The right figure shows that $T_{v,\mathrm{OH}}$ is always lower than T in the reaction zone (F3 is responsible for H_2O formation). This occurs as OH is present in areas where T increases through heat release: $T_{v,\mathrm{OH}}$ trails behind as it relaxes. Also, the $C - V$ coupling term in Eq. 2.13 means that combustion decreases the overall vibrational energy of the reacting species as explained in Sec. 2.2.1. The F3 efficiency function is relatively insensitive to $T_{v,\mathrm{OH}}$ (see Fig. 2.19), but not to T_{v,H_2}. Reaction F3's pre-exponential factor equals 1.51, which appears to be insufficient to counter-balance the impact of the vibrationally cold H_2 on the reaction rate which is slightly damped by nonequilibrium.

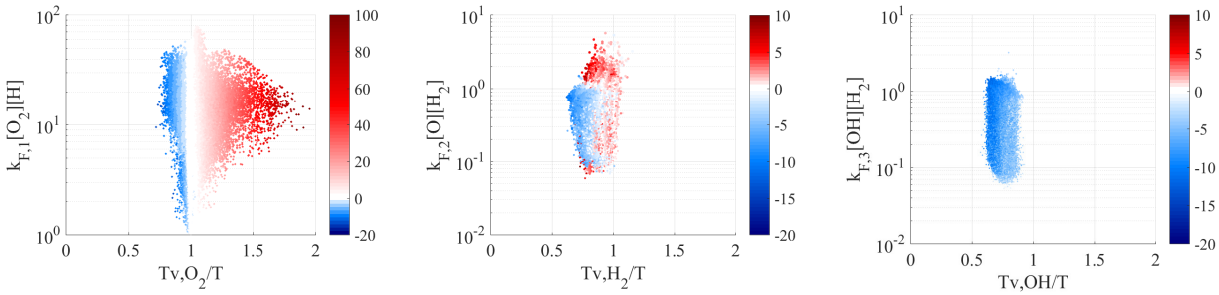

Figure 6.6: Realizations of (left) $k_{F,1}[\mathrm{O}_2][\mathrm{H}]$ with $\frac{T_{v,\mathrm{O}_2}}{T}$, (middle) $k_{F,2}[\mathrm{H}_2][\mathrm{O}]$ with $\frac{T_{v,\mathrm{H}_2}}{T}$, and (right) $k_{F,3}[\mathrm{OH}][\mathrm{H}_2]$ with $\frac{T_{v,\mathrm{OH}}}{T}$, colored by their respective reaction rates ratios in percentage.

In order to have a better picture of the location of these increased/decreased kinetic zones throughout the flame, these scatter plots are spatially distributed along the 3 physical

axes in Fig. 6.7. The dots are slightly transparent and are size proportionally to the local full reaction rates. They are colored by the reactions efficiency ratio. The complex flame front consists of turbulent flame sheets and very fine filament-like structures. Radical O production is locally enhanced by nonequilibrium when vibrationally hot O_2 encounters radical H. H_2 dissociation starts upstream as seen in the middle figure. It is enhanced as H_2 vibrational temperature is initially close to its total temperature (300 K) and is therefore cold throughout the mixing layer. As seen in Fig. 2.22 this results in an increased F2 reaction rate as N_2 is also coincidentally vibrationally cold. However, further downstream, the first two reactions which are the main sources of radicals become either neutral (F1) or damped (F2). This can be attributed to the excitation of the H_2 and N_2 population due to H_{20} quenching which brings it to equilibrium. N_2, therefore, becomes a "useless" thermal sponge. As for the bottom figure for reaction F3, the reaction rates are decreased by nonequilibrium as explained in the previous paragraph.

6.2.4 Comparison between equilibrium/nonequilibrium cases

The equilibrium and nonequilibrium simulations can also be directly compared. Figure 6.8 presents scatter plots of the chain branching full reaction rates weighted by the cell size for (top) $O_2 + H \rightarrow O + OH$, (middle) $H_2 + O \rightarrow H + OH$ and (bottom) $OH + H_2 \rightarrow H_2O + H$ along the streamwise direction X. The comparison is consistent with the analysis of the rates efficiency ratio: the first radical-forming reactions are initially higher in the nonequilibrium case, they then become smaller than the equilibrium case. Overall, the third reaction is always smaller at nonequilibrium.

The overall influence of nonequilibrium is quantified by integrating along the cross-sectional area the metrics presented in Figs. 6.7 and 6.8. The top plots in Fig. 6.9 presents on the top the YZ-integration of the reaction efficiency ratio weighted by the reactants mole fractions. This weight ensures that the areas of stronger reactions have more influence. It represents the integral view of Fig. 6.7. A value above unity means that the flow is locally

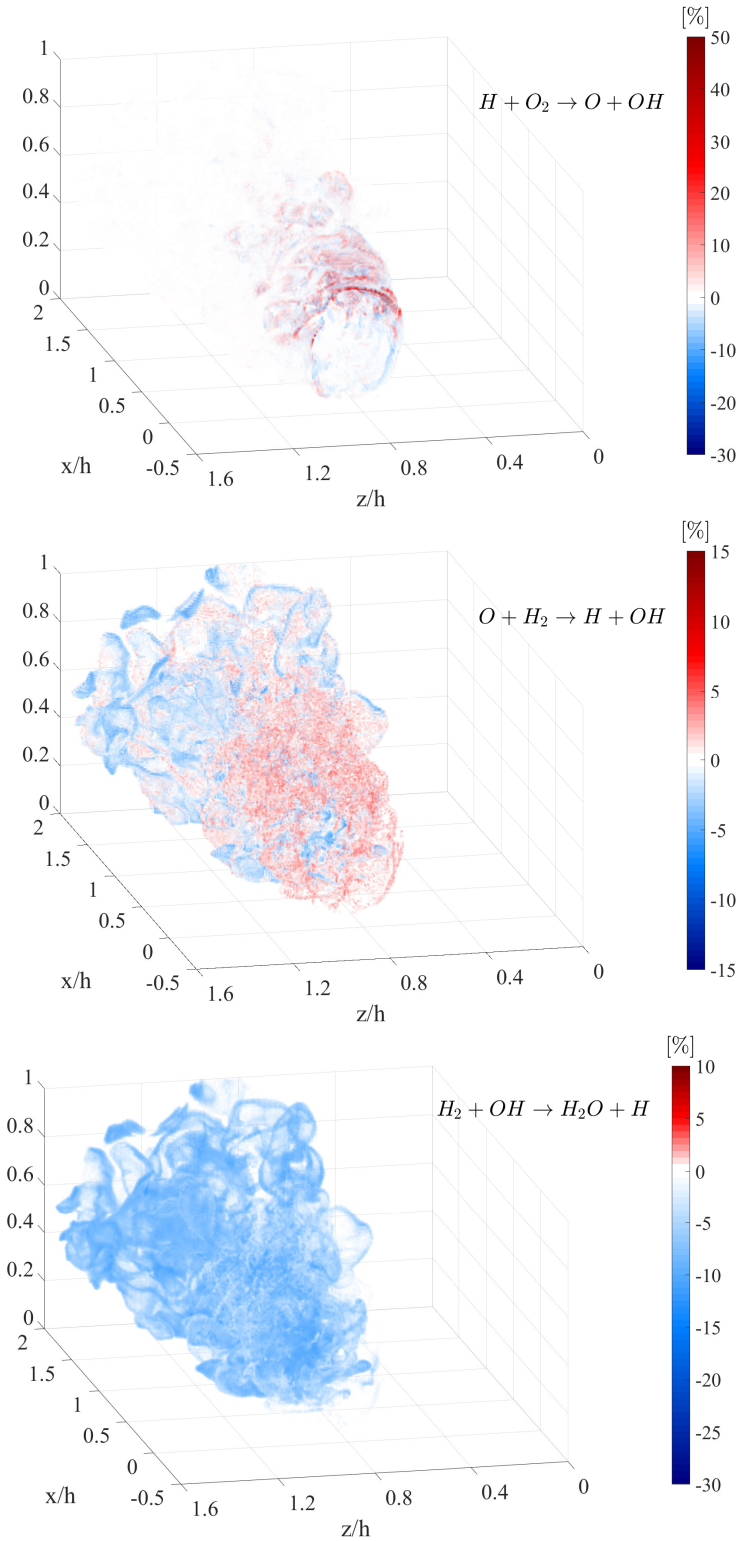

Figure 6.7: Scattering in the physical space XYZ of the reaction rates $k_{Fi,qct}[X_i]$ colored by the same efficiency ratio $\frac{k_{Fi,qct}(T,T_v)}{k_{Fi,eq}(T^*)} - 1$ [%] plotted in Fig. 6.6 for (top) $O_2 + H \rightarrow O + OH$, (middle) $H_2 + O \rightarrow H + OH$ and (bottom) $OH + H_2 \rightarrow H_2O + H$.

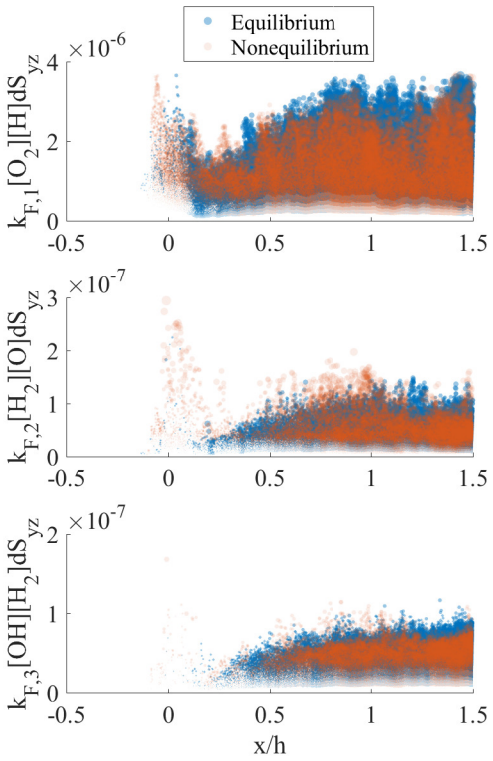

Figure 6.8: Scatter plots of the chain branching reaction rates times reactants concentrations [mol.cm^{-1}.s^{-1}] for (top) $O_2 + H \rightarrow O + OH$, (middle) $H_2 + O \rightarrow H + OH$ and (bottom) $OH + H_2 \rightarrow H_2O + H$ along the streamwise direction X.

reacting faster than if it was suddenly brought to equilibrium.

The bottom figure presents the YZ-integrals of Fig. 6.8 for the three chain reactions. Each reaction is normalized by its maximum value in the nonequilibrium case over the x = [-0.5h 1.5h] domain where ignition happens. The equilibrium integrals, also normalized by the same value, are plotted in dashed lines. The comparison confirms that there exists a small region from -0.1 h to 0.4 h where nonequilibrium increases the first two rates.

Finally, Fig. 6.10 shows the crossflow plane YZ integral of (left) water vapor mass $\rho Y(H_2O)$ [kg.m^{-1}] and (right) fuel mass $\rho Y(H_2)$ [kg.m^{-1}] for the equilibrium and nonequilibrium simulations. These observations are consistent with the previous analysis: there appears to initially be a faster combustion in the nonequilibrium case, which is swiftly inverted by the first 0.4 h. Beyond this inversion point, the equilibrium case seems to have a higher burning efficiency.

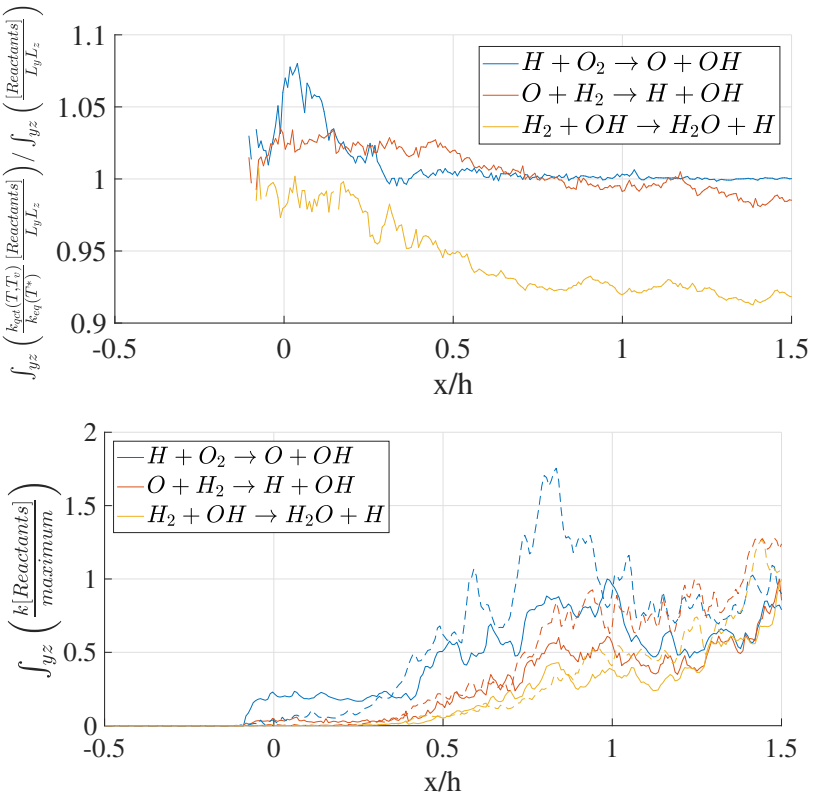

Figure 6.9: (Top) YZ integration of the reaction rates efficiency ratio weighted by the reactants mole fractions. (Bottom) YZ plane integration of the chain branching reaction rates shown in Fig. 6.8 (solid: nonequilibrium case, dashed: equilibrium case)

Overall, the differences are modest in this configuration. This can be attributed to several factors. First, the amount of inflow nonequilibrium is relatively low: less than 3% of the internal energy is affected as noted in the conclusion of Chap. V. Also, O_2 is at equilibrium by the injector location. Second, the speed is subsonic: the residence time will be much lower in scramjet mode which will increase nonequilibrium. Third, a large recirculation region forms behind the impinging jet, which pins the flame front in both cases.

6.3 Scramjet mode

In this section, two DNS of the HyShot-II configuration are carried. A presentation of some numerical details is given first. Then, the airflow-fuel interaction zone is studied. The differences between the equilibrium and nonequilibrium solutions are then presented. Finally, these difference are explain by investigating the impact of nonequilibrium on the

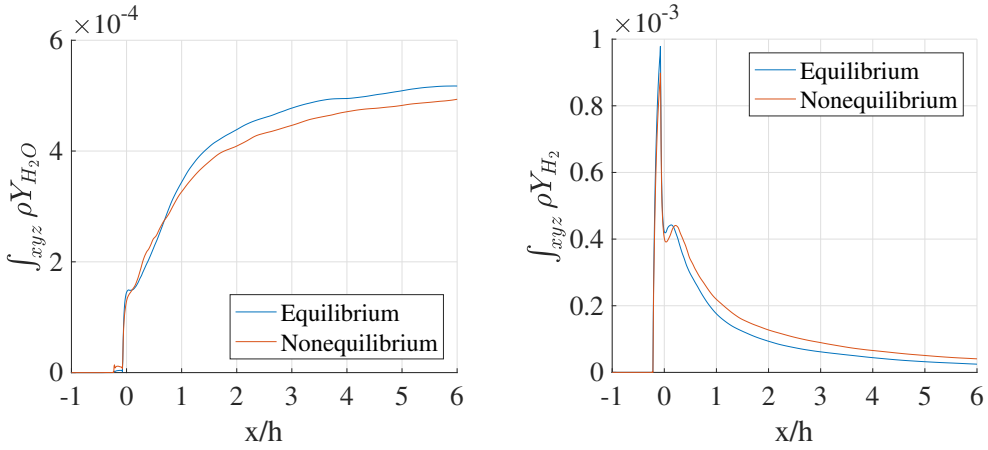

Figure 6.10: YZ integral of (left) water vapor mass $\rho Y(H_2O)$ and (right) fuel mass $\rho Y(H_2)$ [kg.m^{-1}].

ignition process.

6.3.1 Numerical details

6.3.1.1 Simulation configuration

The geometry is identical to the HyShot-II experiment [117], albeit only one injector out of fourth is included in the domain. The isolator and combustor heights are of 9.8 mm. The spanwise boundaries are treated periodically. The injector has a diameter of 2 mm and is centered along the 2cm-long periodic spanwise direction which corresponds to the distance between injectors. This is a common way of simulating the HyShot-II configuration [75, 19, 60]. The walls are modeled as isothermal at 300 K.

The far-field and flight conditions kept changing and were not steady throughout the flight-test experiment, mostly due to changes of altitude or oscillation of angle of attack [117]. This renders a direct comparison with the original dataset difficult. Hence, a steady realistic flight condition using the same altitude (35 km) than the previous ramjet isolator and combustor simulations is chosen for the sake of consistency. For both the ramjet isolator and combustor simulations, the flight conditions were given by Tab. 5.1 based, already, on a HyShot-II like configuration 5.1. The scramjet mode uses a higher flight Mach number of 9.0 (instead of 5.0) and an angle of attack of -1 degree (instead of -3). Figure 6.11

presents the configuration of the scramjet simulation. The air mass flow rate in the isolator is around 80 g.s^{-1} at $\approx$ Mach 2.5. The fuel mass flow rate equals 0.4 g.s^{-1}, which yields an equivalence ratio of 0.2. An inflow was generated with a simple turbulent boundary layer which height was estimated by running a RANS of the intake using FLUENT and a k-ω model. Little effort was spent in ensuring a perfectly resolved boundary layer since its fate is to be vacuumed into the shock bleed. The bleed primary purpose is to prevent the oblique shock to enter the isolator and disrupt the mass flow rate. Initially, a simpler version of this geometry without the bleed was simulated [34]. The shock would hit the bottom wall and separate the flow, forming a large recirculation bubble on the ramp. As the oblique shock moved due to the incoming turbulence and due to the dynamics of the boundary layer, part of the recirculation bubble would occasionally enter the isolator, slightly blocking the flow. This would intermittently increase the adverse pressure gradient and further separate the upstream boundary layer: the bubble would grow. It would slowly grow up to a certain point where flow blockage triggers unstart. In less than a few hundreds of microsecond, a normal shock would form at the isolator inlet and quickly convect upstream until it attaches to the inlet plane, unstarting this engine.

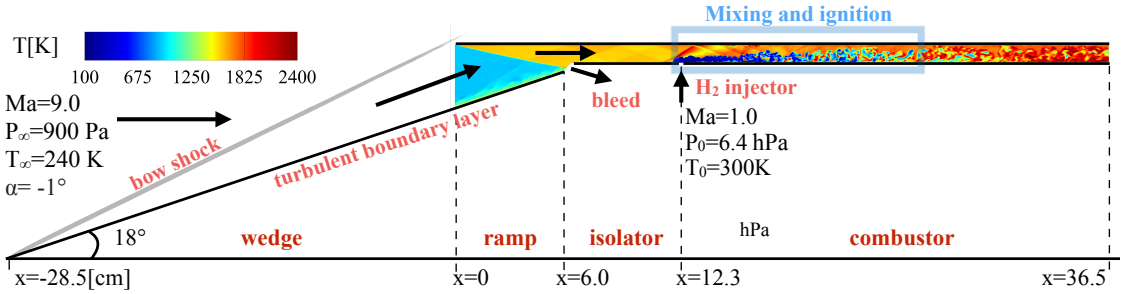

Figure 6.11: Configuration the scramjet simulation based on the HyShot experiment.

Figure 6.12 shows the operating scramjet engine for the equilibrium case. Isocontours of radical OH reveals a lifted turbulent flame. The horseshoe shape forming upstream of the fuel porthole will be discussed later.

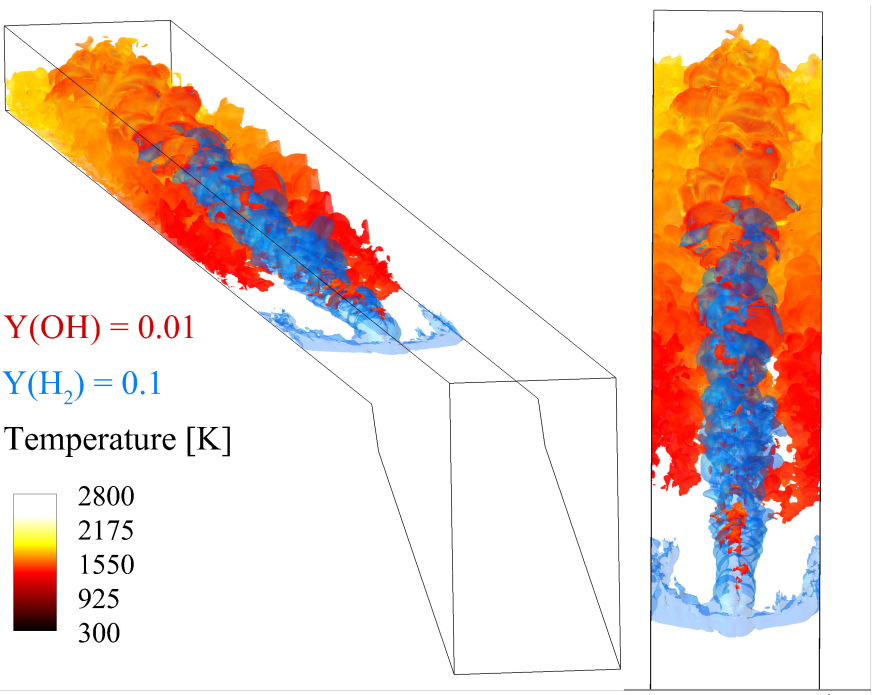

Figure 6.12: Illustration of the scramjet lifted supersonic turbulent flame (equilibrium case).

6.3.1.2 Grid convergence

A grid of $(n_x, n_y, n_z) = (3072, 192, 192)$ nodes is used to discretize the domain. The grid spacing is uniform in the streamwise and spanwise direction, while the grid is clustered closer to the wall in the wall-normal direction. The resolution in wall unit has a range of $\Delta_x = 12y^+$, $\Delta_z = 10y^+$ and $\Delta_y = [0.7 : 12]y^+$ for a y^+ unit estimated at $10\,\mu$m based on a previous calculation of the HyShot isolator [34].

Numerical convergence is verified by simulating additional coarser grids. The coarsest grid has $(n_x, n_y, n_z) = (1024, 64, 64)$ and the medium grid has $(n_x, n_y, n_z) = (2048, 128, 128)$ grid points. Figure 6.13 shows on the left figure the wall-normal profiles in the isolator (at $x = 0.1$ m) of static temperature and total energy. It is seen that the medium grid, which is used here for all discussions of the results, is already sufficiently well-resolved to capture the trends seen on the finest grid. The figure on the right presents the YZ integration of water vapor mass for the same resolutions showing the grid appropriately resolves the combustion process. The x-axis origin is placed at the fuel porthole center. The stairway-like profiles are caused by an oblique shock train developing through the combustor due to thermal

choking [76, 75] and will be discussed later. Static pressure contours of the combustor are presented for all grids in Fig. 6.14, illustrating the capacity of the intermediate resolution grid to capture the complex shock wave system and accurately resolve the jet and cross-flow interaction. The finest grid is used from this point.

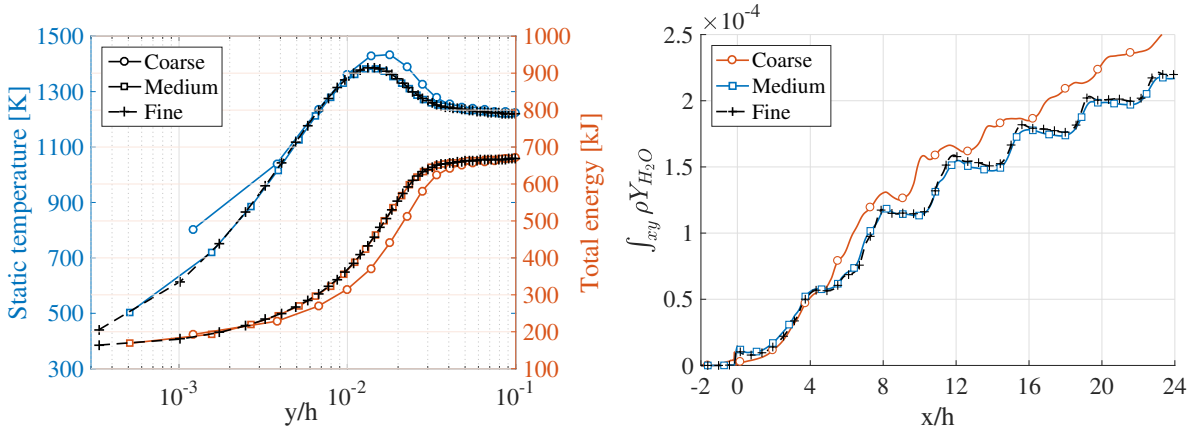

Figure 6.13: (Left) Wall-normal total energy and translational temperature profiles in the isolator for different grid resolutions. (Right) XY-integration of water vapor mass $\rho Y(H_2O)$ [kg.m^{-1}] for the same resolutions

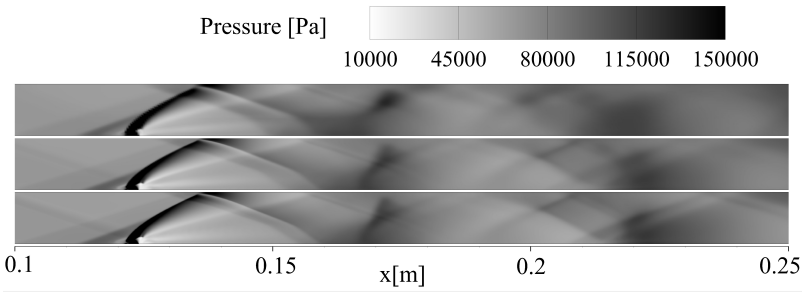

Figure 6.14: Static pressure contours of the combustor for coarse, medium and fine grid resolutions from top to bottom.

No turbulent combustion model is used, which can be problematic if the combustion lengthscales are smaller than the minimum grid size. The Damköhler number Da is a dimensionless number that measures the relative importance of gas-phase kinetics versus molecular mass transport. If Da is much greater than 1, then a reaction is fast relative to transport and a subgrid model is recommended; if it is less than 1, then transport processes occur on a shorter timescale than the chemical process. Figure 6.15 shows the Da number

defined as the ratio between the chemical timescale (defined as the inverse of the fastest species concentration rate-of-change) and the convective residence timescale (defined from the cell size and local flow velocity). As the values are mostly below unity, and given that grid refinement does not further improve the amount of H_2O formed along the streamwise direction, it can be argued that the ignition process is well resolved.

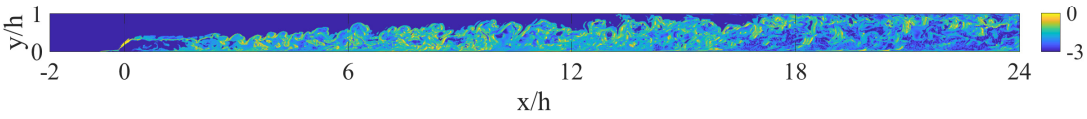

Figure 6.15: Damköhler number snapshots throughout the combustor plotted in log10 scale.

6.3.2 Combustor flow

The ignition region is particularly complex in scramjet mode, due to the interaction between the supersonic airflow and the impinging fuel stream.

6.3.2.1 Fuel-filled horseshoe

Figure 6.16 presents the ignition region for the nonequilibrium case. A bow-shock forms in the supersonic duct due to the blockage caused by the fuel injection scheme. It creates a large pressure gradient region in front of the impinging jet. This adverse pressure gradient creates a large recirculation bubble filled with H_2, where it can heat up and react. The hottest region of the computational domain is located right behind the bow-shock with temperatures occasionally reaching over 3200 K: this is an area of high-production rates of radicals. These observations are coherent with the Schlieren imaging of Ben-Yakar [4] and the OH^*-chemiluminescence measurements from Gamba and Mungal [45].

Figure 6.17 highlights some of the structures discussed in Fig. 6.1 inside the simulation. A large recirculation bubble inside the horseshoe structure is observed on the time-averaged solution (green isocontour). Likewise, a large expansion wave is present right behind the bow-shock (yellow isocontour).

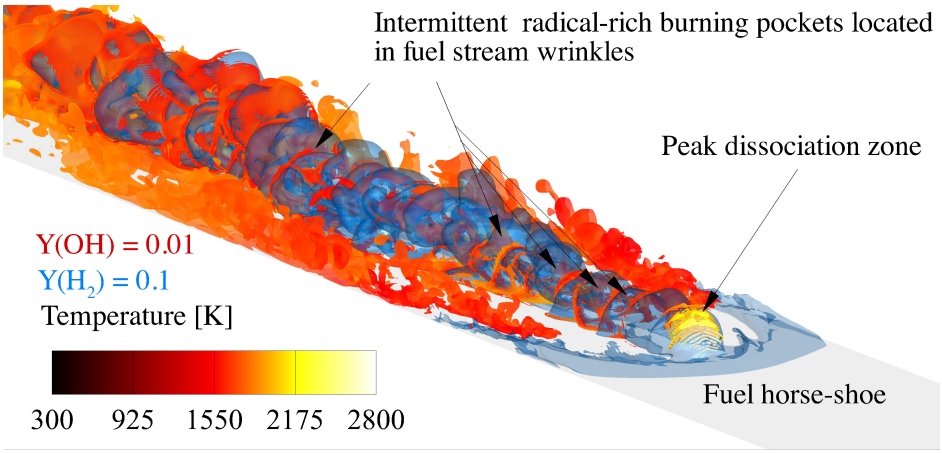

Figure 6.16: Supersonic wrinkled flame structure.

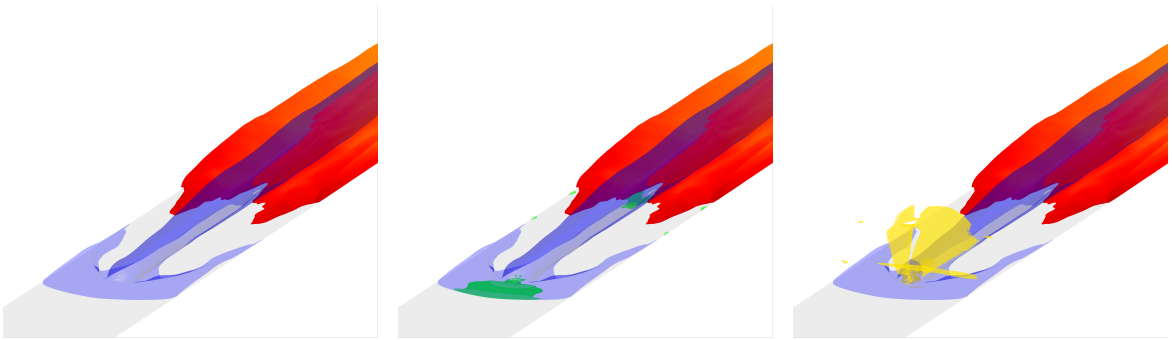

Figure 6.17: (Left) Time-averaged isocontours of $Y(OH) = 0.01$ (red) and $Y(H_2) = 0.1$ (blue). (Middle) Isocontour of $U = 0$ (green) added. (Right) Isocontour of arbitrary pressure gradient (yellow) highlighting expansion wave front.

The effect of the horseshoe on radical H spatial distribution is an important difference with the simpler ramjet-like configuration presented in Sec. 6.2. Indeed, H is created as the cold H_2 emanating from the jet recirculates upstream. Inside this pocket, H_2 can partly relax and dissociate. This permits to seed the shear layer with radical H and start up the first chain-branching reaction earlier than in ramjet mode. A marginal concentration of H from dissociation is enough to initiate the chain-reactions F1 and F2, which will then form all the radicals H, O and OH needed.

6.3.2.2 Flame wrinkling and burning pockets

In Fig. 6.1, large-scale eddies form in the shear layer. Their size depends on the jet Strouhal number [4], hence on its characteristic frequency. These eddies form flame "wrin-

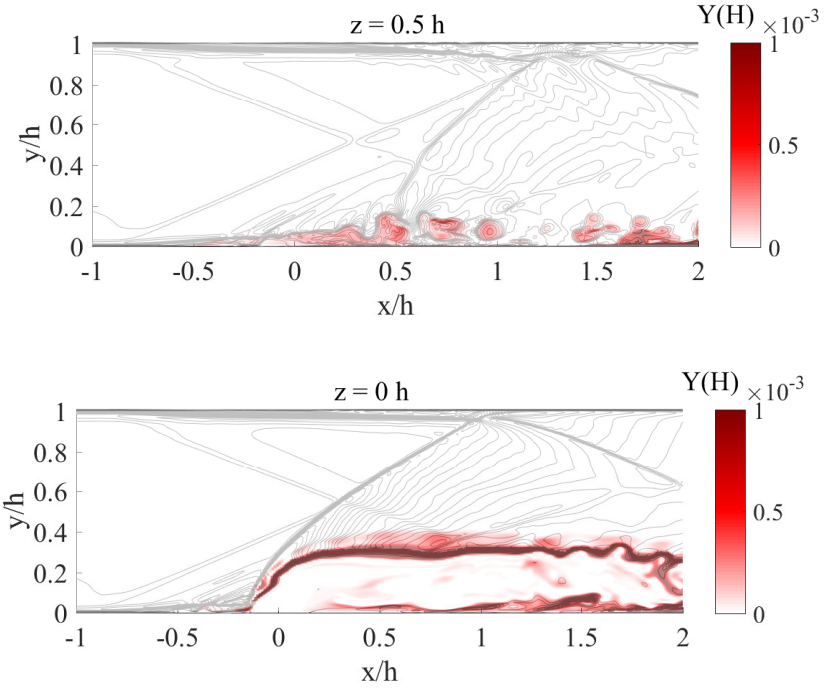

Figure 6.18: Z-slices showing contours of static temperature (gray) colored by H mass fractions.

kles", which are also present in the DNS as seen in Fig. 6.19.

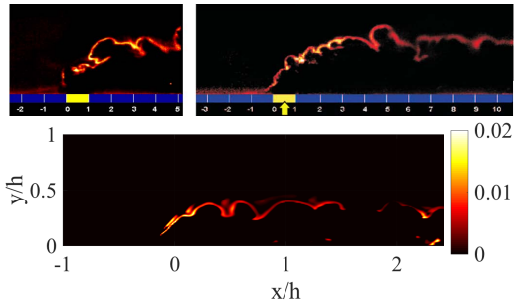

Figure 6.19: Comparison between (top) PLIF contours from Ben-Yakar *et al.* [4] and the (bottom) simulation $Y(OH)$.

As seen in Fig. 6.16, intermittent radical-rich pockets are located inside these wrinkles. The intermittency of the radical-rich burning pocket can be quantified by integrating the production rate of radicals H, O and of heat release $\dot{q}$ over a small region located around the start of the O_2-H_2 mixing layer (in the injector vicinity). The time-signals of these integrals are presented in Fig. 6.20 (top) normalized by their respective maximum value. The productions of radicals are highly synchronized, and their spectral analysis reveal the same

dominant harmonics: 193, 322 and 708 kHz by decreasing magnitudes, which are on the order of the jet characteristic frequency estimated as $v_jet/D_j = 600$ kHz. The heat release history is highly correlated to the radicals H and O bulk production rate, with correlation coefficients of 0.85 and 0.81 respectively. They also share the same dominant harmonics. Figure 6.20 (bottom) shows an instantaneous snapshot of the radical richness indicator defined as the product of H, O and OH mass fractions normalized by the maximal value over time. The convective speed of the pockets was computed around 1800 m.s^{-1}. The wavelengths corresponding to the harmonics characterizes well the regular spatial intermittency in between these radical-rich pockets: $\approx$ 2.5 mm (h/4) in between structures. Overall, the following explanation is proposed. As the jet interacts with the bow-shock, its penetration distance is unsteady. When the jet pushes against the bow-shock, the local pressure and temperature increase, leading to an increased radical production rate. When the jet is pushed towards the wall, the bow shock angle becomes shallower and provides a smaller compression rate, hence smaller radical production rates.

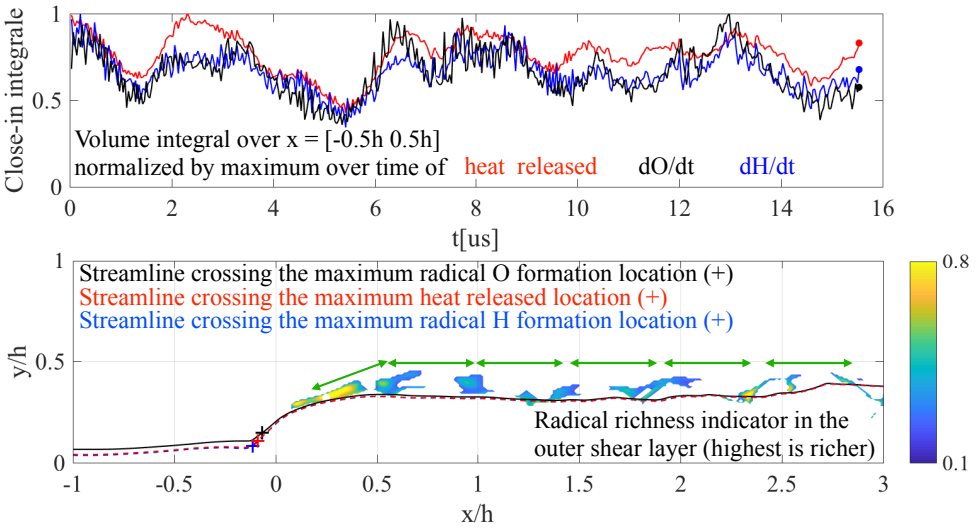

Figure 6.20: (Top) Time history of production rate of radicals H, O and OH in the injector vicinity. (Bottom) Indicator of radical richness.

6.3.2.3 Thermal shock train

Pressure rises in the combustor through heat release and thermal-choking. Additionally, the impinging jet creates a bow shock which introduces several oblique shocks reflecting on the bottom and top wall. As a result, shock structures develop throughout the combustor forming a thermal shock train (TST). The joint experimental-computational studies of Larsson *et al.* and Laurence *et al.* [76, 75] on the HyShot combustor showed that increasing the fuel equivalence ratio would increase thermal choking and push the TST upstream. At low equivalence ratio, the pressure gradually rises at an almost constant rate, as an OST. However, at high equivalence ratio (superior to 0.4-0.5 [76]), the pressure growth rate increases and resembles that of an NST. When this occurs, this adverse pressure gradient can unstart the engine. A TST is also observed in the present simulation. Figure 6.21 shows a centerplane snapshot of the static pressure field. A standing leading shock marks the start of the TST.

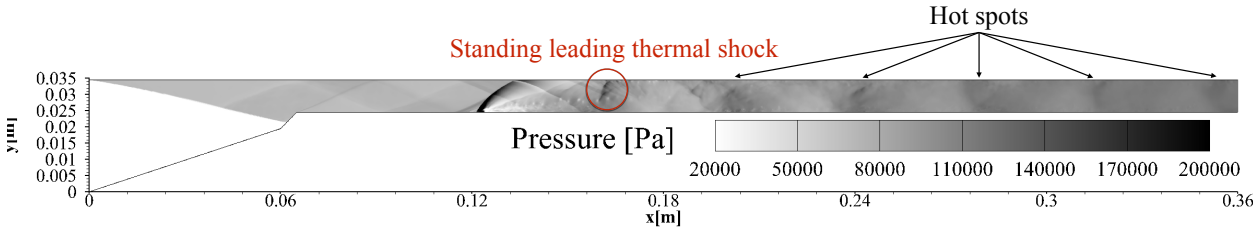

Figure 6.21: Centerplane time-averaged contour of static pressure P in [Pa].

Figure 6.22 shows the (top) instantaneous and (bottom) time-averaged centerplane heat release rate $\dot{q}$ [J.m^{-3}.s^{-1}]. The heat release rate increases wherever the TST's compression waves crosses the fuel stream. The local increase in pressure fastens reaction rates. This explains why the $\int_{xy} \rho Y(\mathrm{H_2O})$ in Fig. 6.13 (right) has a stairway-like shape. The convergence of the shock structures also appear clearly in Fig. 6.14.

The stoichiometric line is plotted in dashed red in Fig. 6.22, in a similar fashion than in Fig. 6.3. The horseshoe causes it to move upstream of the injector.

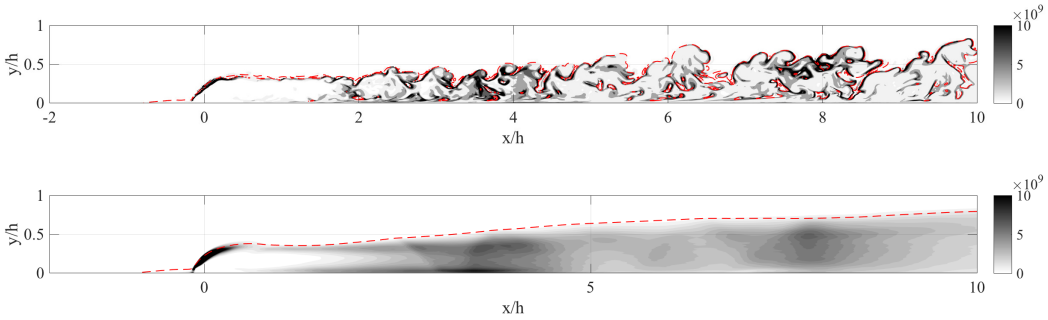

Figure 6.22: Centerplane (top) instantaneous and (bottom) time-averaged contours of heat release rate $\dot{q}$ [J.m^{-3}.s^{-1}]. The red dotted line marks the stoichiometric layer.

6.3.3 Comparison between equilibrium and nonequilibrium flame structures

6.3.3.1 Flame lift-off

The supersonic flame structure of the equilibrium and nonequilibrium cases are compared in Fig. 6.23. While both cases present the same macroscopic features described in Sec. 6.3.2, the difference in flame lift-off is striking. It is clearly seen in Figs. 6.24 and 6.25 which respectively show instantaneous and time-averaged contours of water vapor mass fraction $Y(H_2O)$ for both cases. In general, ignition in the region right behind the bow shock ($x \in [03h]$) is both stronger and steady in the nonequilibrium case. However, ignition only intermittently occurs in this area for the equilibrium case. Indeed, some scattered pockets of H_2O are present in the top contour in Fig. 6.24. This area corresponds to the initial mixing layer between the fuel and oxidizer which is crossed by the bow-shock expansion wave. It is known that expansion waves tend to extinguish flames as they brutally drop the gas temperature and density. However, they also trigger hot nonequilibrium: it could be that the resulting over-excitation of the reactants vibrational energy permits to sustain this drop in density and temperature.

Figure 6.26 presents how the ignition delay impacts the fuel burning rate. The left plots present the Z-centerplane integration of water vapor mass, and the right plot the 3D integral. The left plot shows that the TST is shifted due to the delay in ignition, hence in thermal choking. The right plots show that the profiles end up collapsing. This is caused by both

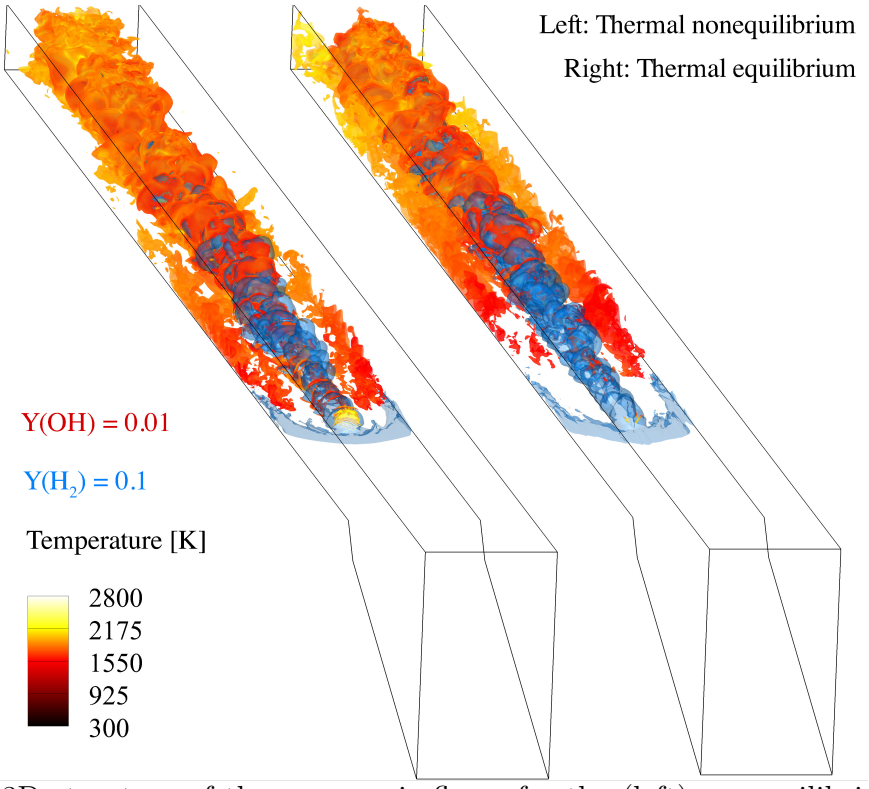

Figure 6.23: 3D structure of the supersonic flame for the (left) nonequilibrium and (right) equilibrium.

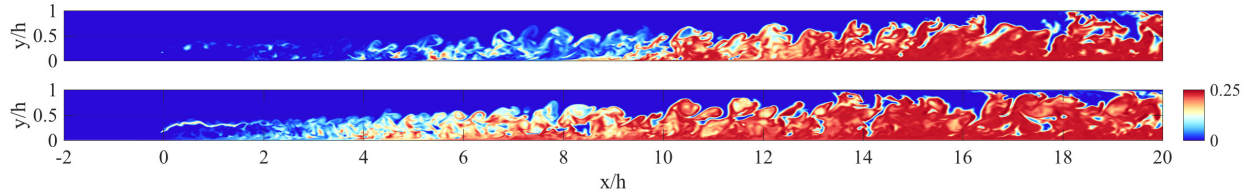

Figure 6.24: Instantaneous contours of water vapor mass fraction $Y(H_2O)$ of the (top) equilibrium and (bottom) nonequilibrium simulations.

the faster depletion of fuel in the nonequilibrium case, and also by the vibrational relaxation of the reactants as heavy molecules like H_2O or H_2O_2 appear. These molecules fasten the V-T relaxation rates. The stairway-like profile is observable when integrating along the Z-centerplane, not on the full 3D space. The difference in flame lift-off measures about 4 channel heights and the equilibrium case burning rate has caught up by the combustor outlet, 20 channel heights further downstream.

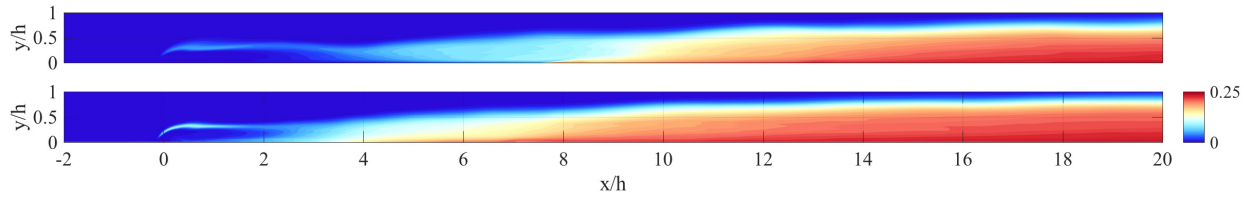

Figure 6.25: Time-averaged contours of water vapor mass fraction $Y(H_2O)$ of the (top) equilibrium and (bottom) nonequilibrium simulations.

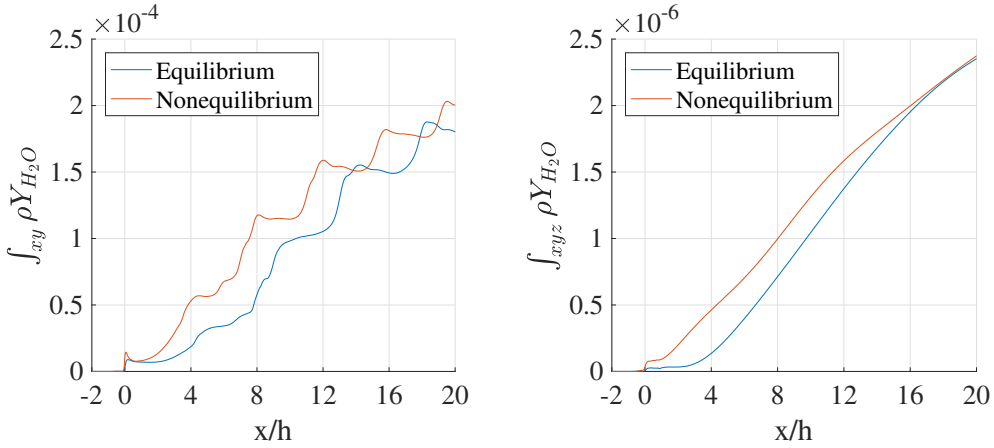

Figure 6.26: (Left) 2D-YZ and (right) 3D-XYZ integral of water vapor mass $\rho Y(H_2O)$ ([kg.m^{-1}] and [kg] respectively).

6.3.3.2 Presence of nonequilibrium in the combustor

In Sec. 6.2, nonequilibrium appeared due to mixing between the hot airflow and the cold fuel stream. The airflow N_2 vibrational energy was under-excited, while O_2 was at equilibrium. In scramjet mode, both the incoming O_2 and N_2 are vibrationally cold. Furthermore, the bow-shock followed by its expansion wave and the TST are going to trigger cold and hot nonequilibrium in the ignition region.

Figure 6.27 presents snapshots of the Z-centerplane temperatures fields T, $T_{v,\mathrm{O_2}}$ and $T_{v,\mathrm{H_2}}$ from top to bottom. The static pressure approaches one atmosphere only after the injector-triggered bow-shock, while the Mach number remains as high as 2.5. In the ramp and isolator sections, the local vibrational energy transfer rate from the over-excited translational and rotational internal energy modes to the vibrational mode is much smaller than the local

resident time. For instance, the pressure is barely of a tenth of an atmosphere in the ramp section (before the bleed). T_v contours do not permit to localize the oblique shock at all. O_2 has partially relaxed inside the isolator and reacts to the bow-shock where the pressure becomes sufficiently high to let it relax to equilibrium. It then becomes vibrationally over-excited inside the expansion region. T_{v,N_2} does not react to the crossing of the bow-shock. By the combustor outlet, O_2 has fully equilibrated while N_2 is at equilibrium inside the flame, and still vibrationally cold near the top wall.

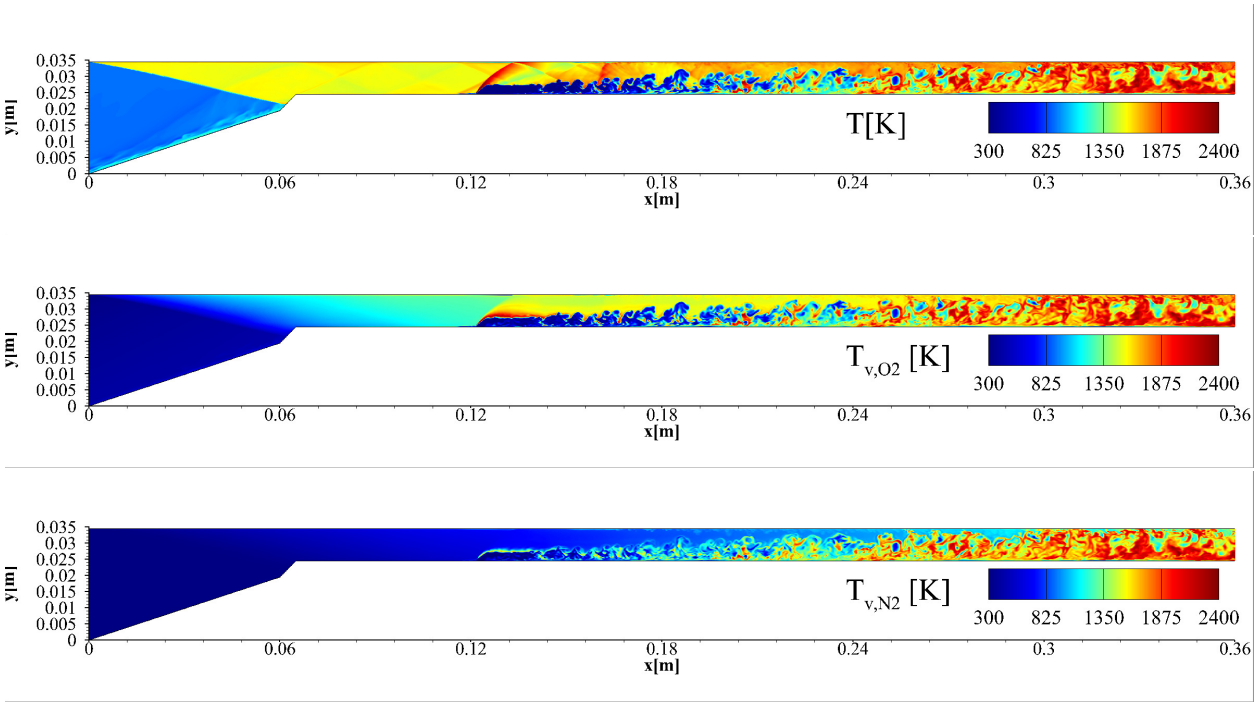

Figure 6.27: Snapshot of the Z-centerplane temperatures fields T, T_{v,O_2} and T_{v,H_2} from top to bottom over the whole computational domain.

Figure 6.28 gives the centerline T, T_{v,O_2} and T_{v,H_2} profiles for both equilibrium and nonequilibrium simulations. As in the nonequilibrium pseudoshock simulation, the compression stage over-excites the TRE compared to the vibrational energies. The initial vehicle intake shock brings the flow centerline temperatures up to 910 and 885 for the nonequilibrium and equilibrium cases respectively. The cowl shock (which ends into the bleeds) further increases these temperatures up to 1560 and 1350 K. Hence, a difference of 210 K results from these compressions, mostly due to T_{v,N_2} barely reaching 600 K by the combustor. It is

reminded that in Chap. V the isolator inflow was assumed at equilibrium in order to assess the minimal effects of vibrational nonequilibrium on the pseudoshock: the inflow T_{v,N_2} was around 1000 K.

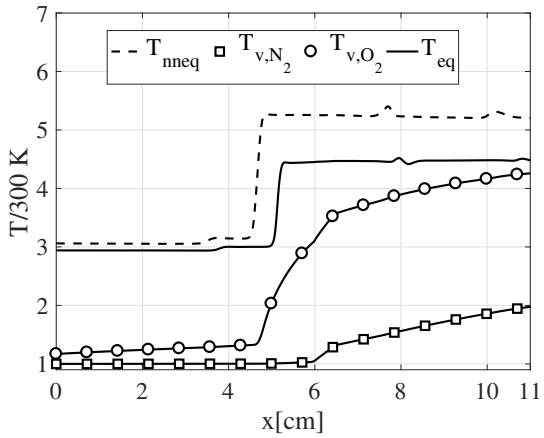

Figure 6.28: Centerline temperatures profiles for both simulations. T_{nneq} and T_{eq} are the translational temperature on the nonequilibrium and equilibrium simulations respectively.

As previously mentioned, the vibrational energies react differently when crossing the bow-shock. Figure 6.29 presents centerplane snapshots of vibrational temperatures and difference with the local translational temperature zoomed in the ignition region $x \in [-210]h$. In both figures, the green dashed line corresponds to the species α arbitrary "presence" threshold set to $Y(\alpha) = 1e^{-6}$. The pink dashed line shows the stoechiometric line. The corresponding time-averaged contours are shown in Fig. 6.30. The expansion region is clearly identified by the temperature time-averaged contour (top), and is located in between 0 and 2 channel heights from the injector porthole. At the bow-shock foot, the time-averaged temperature and pressure reach their maximal values across the domain ($\approx$ 2800 K and 250 kPa) while the flow slows down, and even interacts with the recirculation bubble. Hence, O_2 and N_2 relax much faster than anywhere else: right above the injector porthole T_{v,O_2} and T_{v,O_2} approximately reach 2400 and 1500 K. Consequently, the following expansion creates a region where $T_{v,\mathrm{O}_2} > T$, while $T_{v,\mathrm{H}_2} < T$ and even $T_{v,\mathrm{N}_2} < T$ as seen in the bottom contours in Fig. 6.30. Such conditions were shown to enhance ignition in Fig. 2.23, and in this case the stoechiometric line crosses through this region.

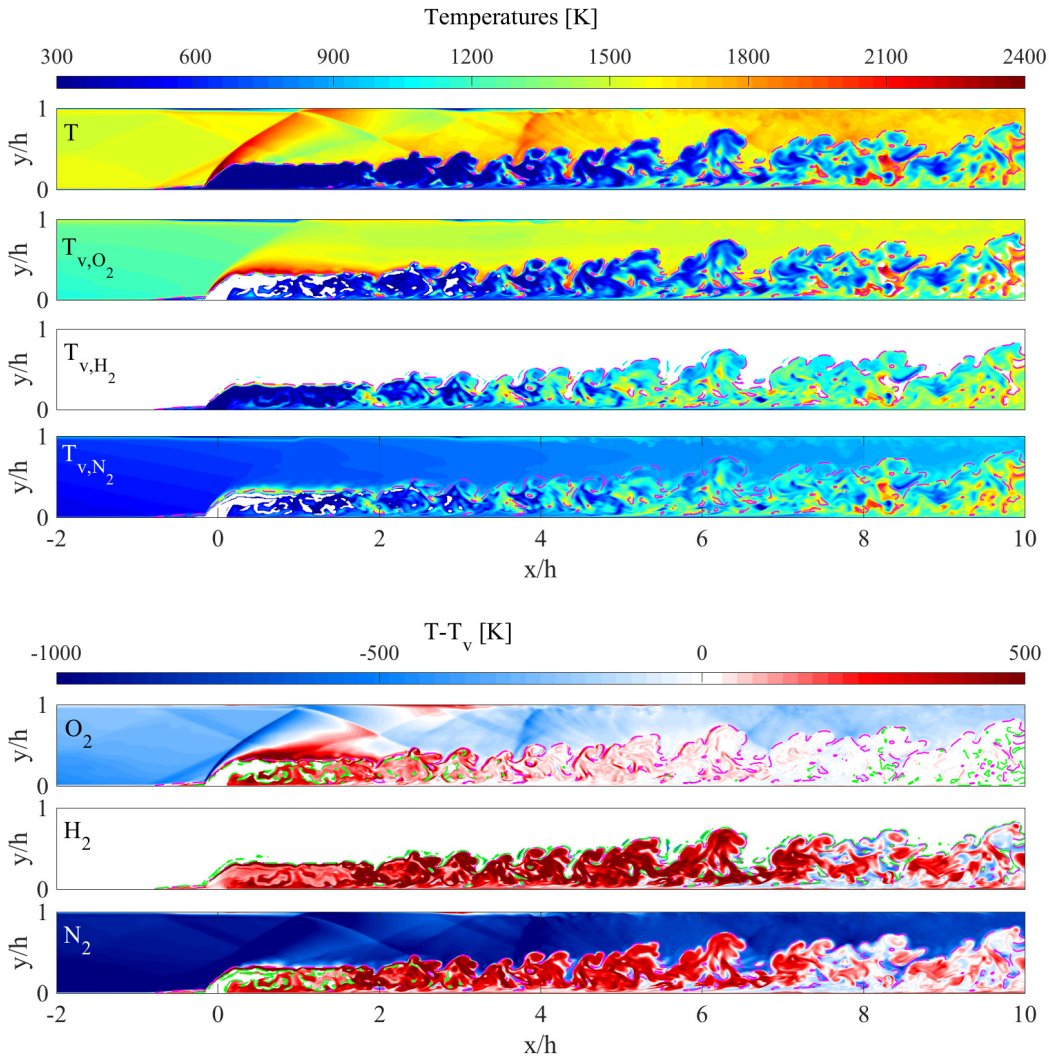

Figure 6.29: Centerplane snapshots of vibrational temperature and difference with the local translational temperature. The dashed pink line indicates local stoichiometric mixing while the green line marks the presence threshold of species mass fraction superior to 0.00001.

6.3.3.3 Effect of nonequilibrium on ignition

The diluter and reactant species were shown to exhibit significant nonequilibrium in the ignition region. As the ratios T_v/T deviate from unity, the reactions efficiency factors also do so. Figure 6.31 presents (top) instantaneous and (bottom) time-averaged contours of the product of all forward chain branching reaction efficiency functions $\phi_{F1} \times \phi_{F2} \times \phi_{F3}$. Pockets of radicals are also drawn with isoline of (red) $Y(H) = 0.004$ and (blue) $Y(O) = 0.004$ to ignition areas. Zero-streamwise velocity isoline is also shown in green. Note that the

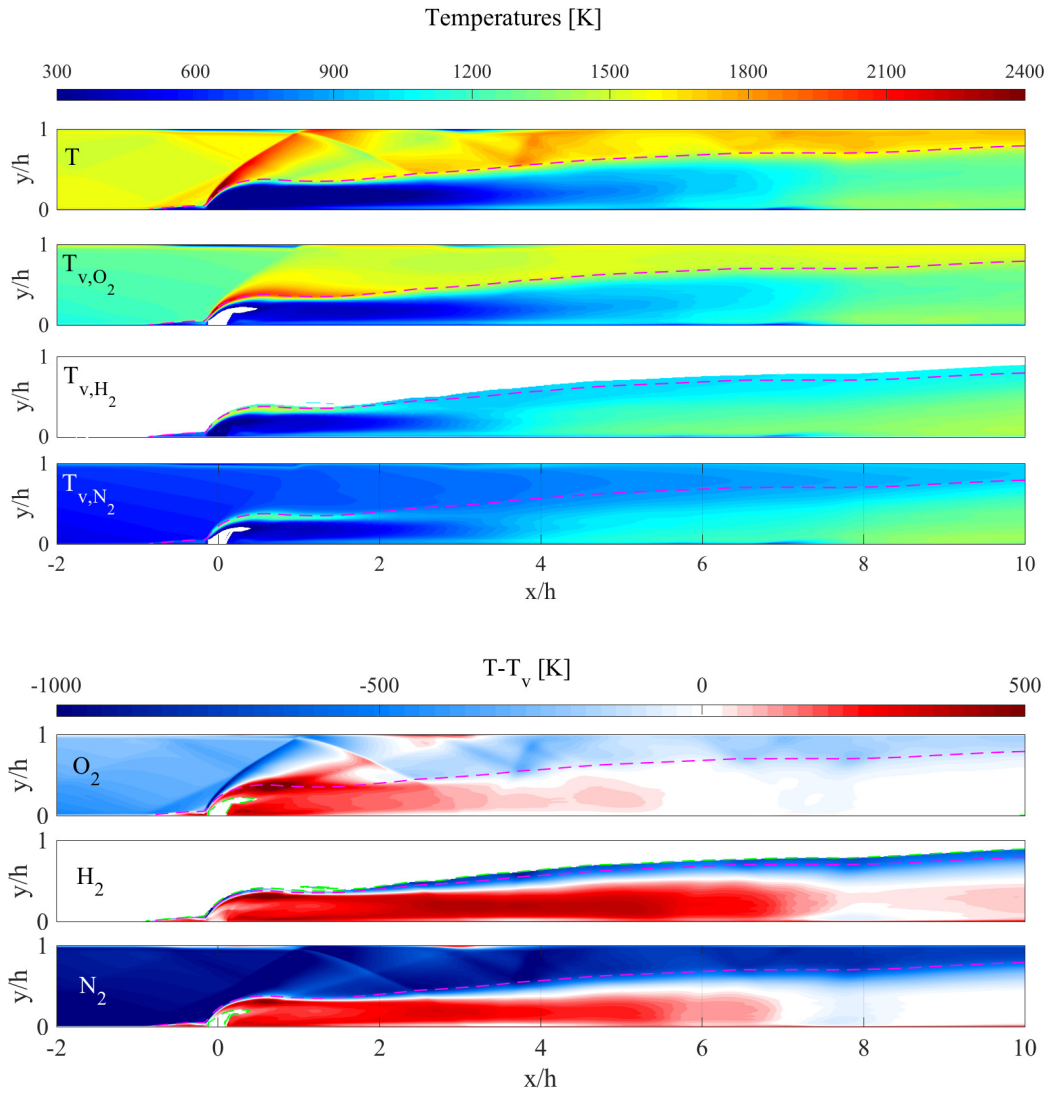

Figure 6.30: Centerplane time-averaged contours of vibrational temperature and difference with the local translational temperature. The dashed pink line indicates local stoichiometric mixing while the green line marks the presence threshold of species mass fraction superior to 0.00001.

ignition region is connected to the tip of the recirculation bubble. Overall, the ignition region coincides with high efficiencies areas, especially in the first 6 channel heights where the product $\phi_{F1} \times \phi_{F2} \times \phi_{F3}$ often increase beyond 10. It is therefore expected that the equilibrium simulation under-estimate the production rate of radicals, which would delay ignition. Interestingly, the product $\phi_{F1} \times \phi_{F2} \times \phi_{F3}$ reaches high values in a very thin layer in the mixing layer where ignition occurs ($x \in [02]h$). This could transform the flame front

by “encouraging” combustion along this thin layer.

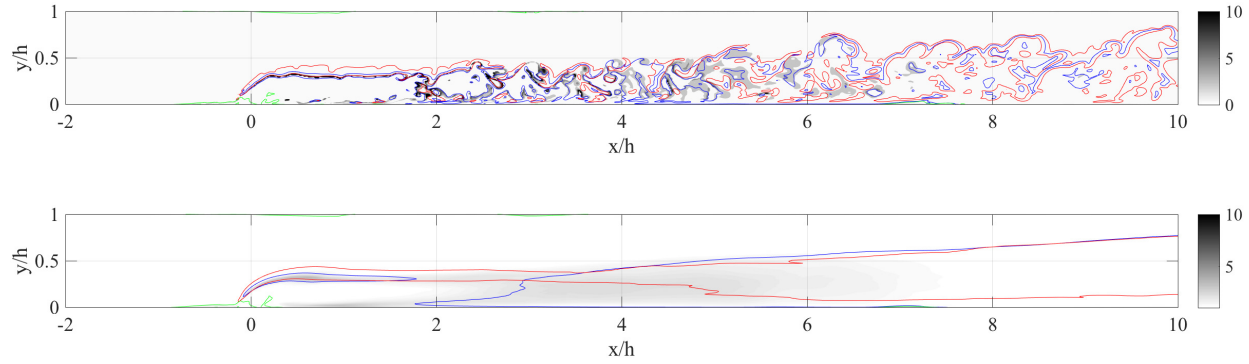

Figure 6.31: (top) instantaneous and (bottom) time-averaged contours of the product of all forward chain branching reaction efficiency functions $\phi_{F1} \times \phi_{F2} \times \phi_{F3}$. Pockets of radicals are also drawn with isoline of (red) $Y(H) = 0.004$ and (blue) $Y(O) = 0.004$. Zero-streamwise velocity isoline are shown in green.

Figure 6.32 presents centerplane time-averaged contours of radicals (top two) O and (bottom two) H mass fractions for the (first) nonequilibrium and (second) equilibrium simulations. As expected the population of radicals is higher in the nonequilibrium case. Also, it appears to be more concentrated along the layer of high $\phi_{F1} \times \phi_{F2} \times \phi_{F3}$. Notably, the production of radical H downstream in the vibrationally cold fuel jet post-potential core area, *i.e.* where element O coming from the airflow is present, is considerably enhanced.

Figure 6.33 presents centerplane time-averaged contours of species (top left) H, (top right) O, (bottom left) OH, (bottom right) H_2O production/depletion rate in [kg.m^{-3}.s^{-1}]. The region right above the injector porthole was identified as the region of maximum pressure and temperature. It is not surprising to see that it incidentally is the region of peak radical-production. The “reserve” of radicals OH then depletes as H_2O is produced in the mixing layer through $OH + H_2 \rightarrow H_2O + H$. Both radicals O and OH populations seem to not be rising beyond that very localized production region, while H still has a net production rate. Therefore, we can deduce that reaction F1 $H + O_2 \rightarrow OH + O$ limits the kinetic of ignition. This is a known result of H_2/O_2 combustion [94]. In the context of the present study, we can conclude that the positive efficiency ratio of reaction F1, thanks to $T_{v,O_2} > T$, greatly

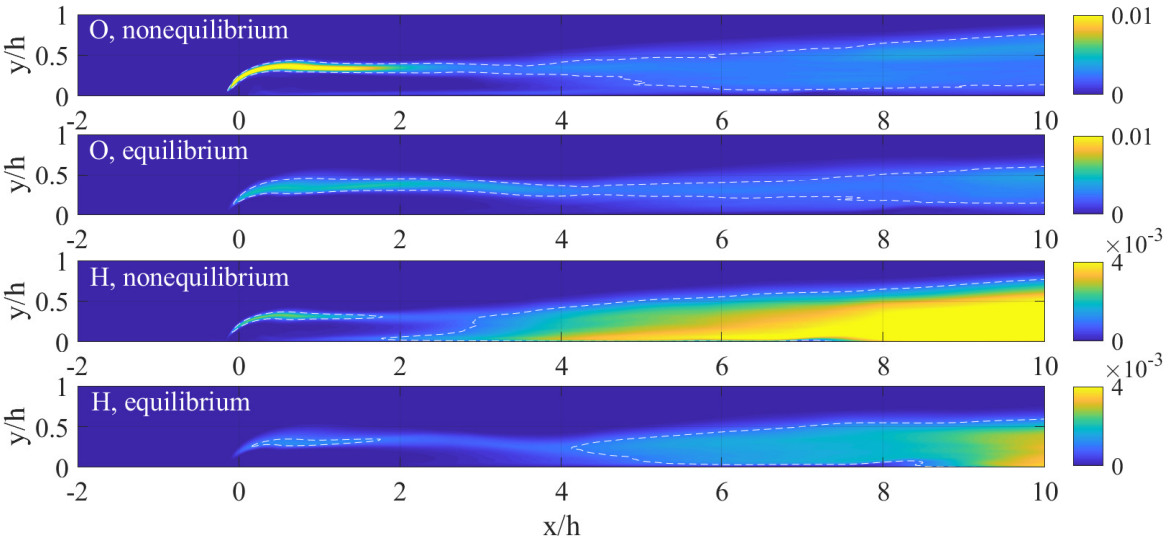

Figure 6.32: Centerplane time-averaged contours of radicals (top two) O and (bottom two) H mass fractions for the (first) nonequilibrium and (second) equilibrium simulations. The white dashed line corresponds to one-tenth of the colormap maximum.

contributes to the faster ignition of the nonequilibrium case.

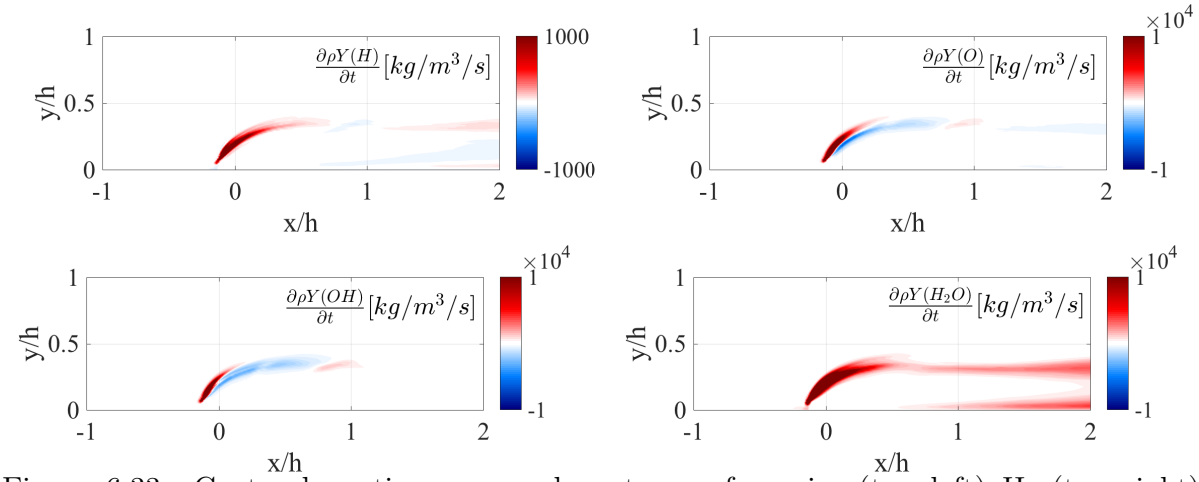

Figure 6.33: Centerplane time-averaged contours of species (top left) H, (top right) O, (bottom left) OH, (bottom right) H_2O production/depletion rate in [kg.m^{-3}.s^{-1}].

Figure 6.34 presents realizations of (T,T_{v,O_2}) across the ignition region defined as $x \in [-12]$ channel heights around the fuel porthole. The correlation are colored by (left) efficiency function ϕ_{F1}, (middle) heat released rate $\dot{q}$ [J.m^{-3}.s^{-1}] and (right) radical O produc-

tion [kg.m^{-3}.s^{-1}]. The shapes of these distributions is similar to Fig. 6.5, as some of the mechanism observed in ramjet-mode are still present. For instance, the bulk of the O_2 flow is vibrationally hot in the fuel mixing layer, while H_2 is conversely cold. Hence, combustion and heat release occur at $T_{v,O_2} > T$. This is further exacerbated as the ignition region crosses the expansion waves resulting in positive $T_{v,O_2} - T$ gradients. As observed in Fig. 6.16, the maximum temperature region is located right behind the bow-shock, in an area where the sudden compression creates a cold nonequilibrium region $T_{v,O_2} < T$. It coincides with a peak O production rate region as shown in Fig. 6.33. In Fig. 6.34 these realization appear clearly in the top right corner below the identity line in the second and third plots. In the third plot, the expanded burning shear layer is an exothermic and O-depletion region: it corresponds to the blue zone in the top right plot of Fig. 6.33. Overall, it appears that both the compression and expansion stage of the bow-shock play a critical role in the ignition process as little combustion occurs around the identity line in these correlation plots.

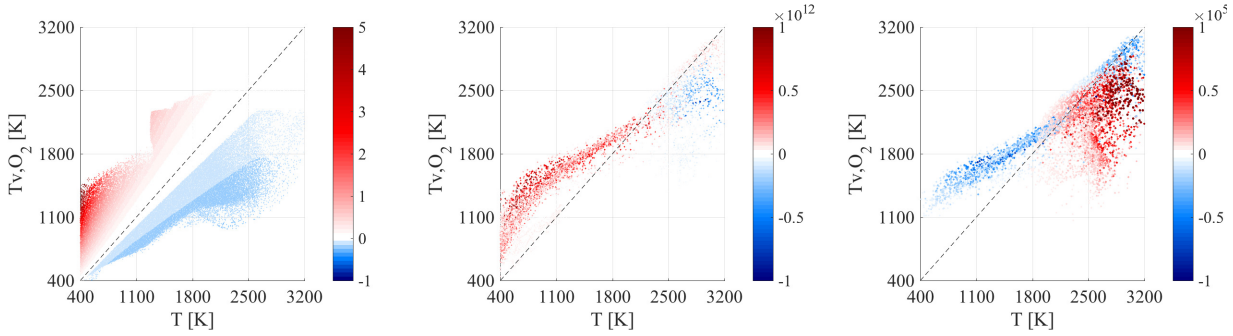

Figure 6.34: Realizations of T and T_{v,O_2} in the ignition region colored by (left) efficiency function ϕ_{F1}, (middle) heat released rate $\dot{q}$ [J.m^{-3}.s^{-1}] and (right) radical O production [kg.m^{-3}.s^{-1}].

Figure 6.35 presents realizations of (T,T_{v,O_2}) across the combustion region corresponding to the rest of the domain: $x > 2h$ from the fuel porthole. The correlations are again colored by (left) efficiency function ϕ_{F1}, (middle) $\dot{q}$ [J.m^{-3}.s^{-1}] and (right) radical O production [kg.m^{-3}.s^{-1}]. Unsurprisingly, the flow has equilibrated further downstream and combustion occurs around the identity line. The red area in the bottom left on the center plot corresponds to the vibrationally hot O_2 mixing with the cold jet near the bottom wall (using an isothermal

condition with $T_w = 300$ K). The production of radicals still tends to occur at the flame front where combustion increases T through heat release and T_{v,O_2} decreases through CVCV exchange.

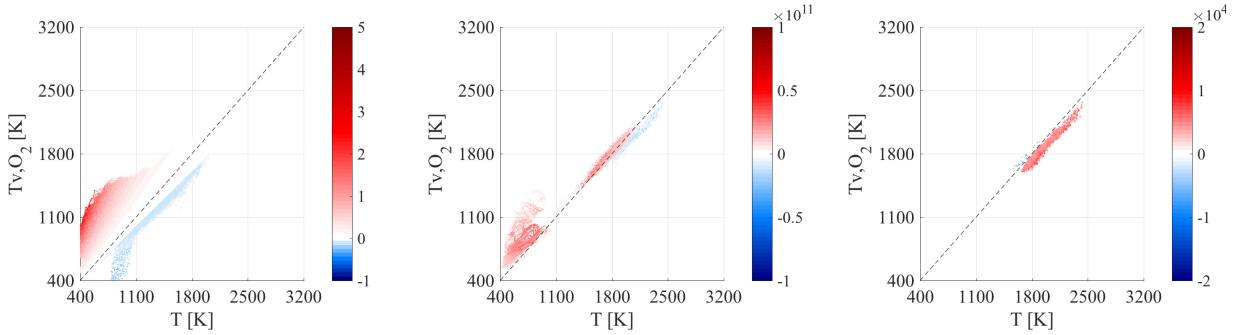

Figure 6.35: Realizations of T and T_{v,O_2} in the downstream region colored by (left) efficiency function ϕ_{F1}, (middle) heat released rate $\dot{q}$ [J.m^{-3}.s^{-1}] and (right) radical O production [kg.m^{-3}.s^{-1}].

Figure 6.36 shows the scattering of the full chain branching reaction rates (i.e. the rates times the reactant mole concentrations) against the corresponding reactants vibrational temperature ratio. The plots are colored by the local reaction efficiency ratio defined as $\frac{k_{Fi,qct}(T,T_v)}{k_{Fi,eq}(T^*)} - 1$ in percentage, in the same fashion as Fig. 6.6. The first plot is unsurprisingly similar to the first plot shown in Fig. 6.6, albeit with a stronger variation of the x-axis distribution caused by the compression/expansion structures. On the other hand, the expansion throughout the ignition region permits to populated the $T_{v,\mathrm{H}_2}/T > 1$ and $T_{v,\mathrm{OH}}/T > 1$ sides. Hence, the second and third reactions are also increased in these regions thanks to nonequilibrium as opposed to the ramjet mode. In general, the third reaction is less impacted by nonequilibrium with most relative errors within $\pm 5\%$.

Figure 6.37 presents on the physical space XYZ the scattering shown in Fig. 6.36 for (top) $\mathrm{O}_2 + \mathrm{H} \rightarrow \mathrm{O} + \mathrm{OH}$, (center) $\mathrm{H}_2 + \mathrm{O} \rightarrow \mathrm{H} + \mathrm{OH}$ and (bottom) $\mathrm{OH} + \mathrm{H}_2 \rightarrow \mathrm{H}_2\mathrm{O} + \mathrm{H}$.. The third reaction plot reveals an overall slightly negative value by a few percents, and no particular structure appears. The horseshoe structure is a place of increased reaction rates F1, which increases the amount of radical O. It is followed, in the sense of the flow, by the bow-shock compression stage. In this zone, the radicals O released upstream now interact

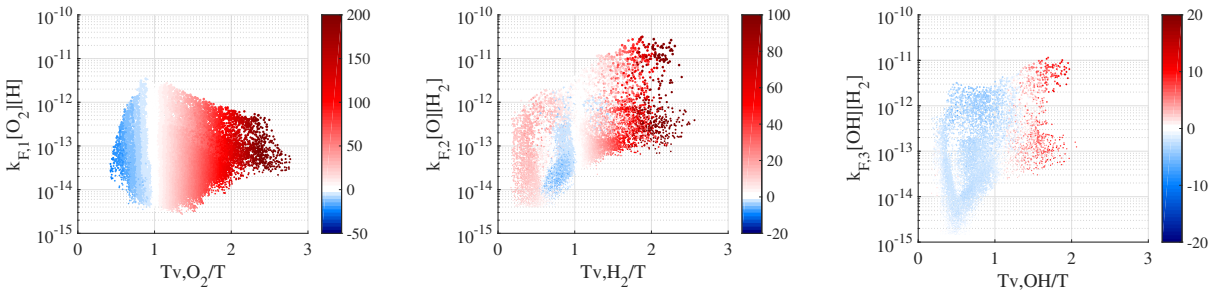

Figure 6.36: Realizations of (left) $k_{F,1}[\mathrm{O}_2][\mathrm{H}]$ with $\frac{T_{v,\mathrm{O}_2}}{T}$, (middle) $k_{F,2}[\mathrm{H}_2][\mathrm{O}]$ with $\frac{T_{v,\mathrm{H}_2}}{T}$, and (right) $k_{F,3}[\mathrm{OH}][\mathrm{H}_2]$ with $\frac{T_{v,\mathrm{OH}}}{T}$, colored by their respective reaction rates ratios in percentage.

with H_2 to create radicals H through reaction F2 which is increased by nonequilibrium. As a result, a larger amount of radicals is formed early on in the nonequilibrium simulation. The downstream radical-rich expanded zone also presents higher reactions rates for both F1 and F2. On the other hand, nonequilibrium tends to slightly reduce the rates in the "wake" region. This appears clearly when plotting the product of the efficiency ratios $\frac{k_{F1,qct}(T,T_{v,\mathrm{O}_2})}{k_{F1,eq}(T^*)} \times \frac{k_{F2,qct}(T,T_{v,\mathrm{H}_2})}{k_{F2,eq}(T^*)} \times \frac{k_{F3,qct}(T,T_{v,\mathrm{H}_2},T_{v,\mathrm{OH}})}{k_{F3,eq}(T^*)} - 1$ over YZ slices (normal to the streamwise direction). This contour is shown in Fig. 6.37 for various streamwise locations $x \in [0, 0.5, 1.0, 1.5, 2.0]$, along with equivalence ratio contours equals to [0.5, 1.0, 1.5] times the stoechiometric value. The fuel-rich size of the shear layer is where nonequilibrium considerably enhance ignition, as opposed to the wake region. Finally, the integral of the ratios presented in Fig. 6.36 weighted by the local reactant concentrations is plotted in Fig. 6.39, as was done in Fig. 6.9 (top). These profiles are yet another indicator in the integrated sense of the effect of nonequilibrium on the ignition process. Note that the third reaction is relatively unaffected.

Instead of quantifying the effect of nonequilibrium over the whole domain, the same analysis can be conducted along streamlines crossing through the reacting zones. Figure 6.40 shows the streamline passing through the maximum heat release location on the time-averaged solution. The contour on the right shows the time-averaged streamwise velocity and reveals the expansion wave inside the fuel stream. Figure 6.41 presents the temperatures and chain reactions efficiency ratio along this streamline. The streamline crosses the bow shock at around $x = -0.2h$, before entering the expansion wave. It can be noted that the low-speed high-

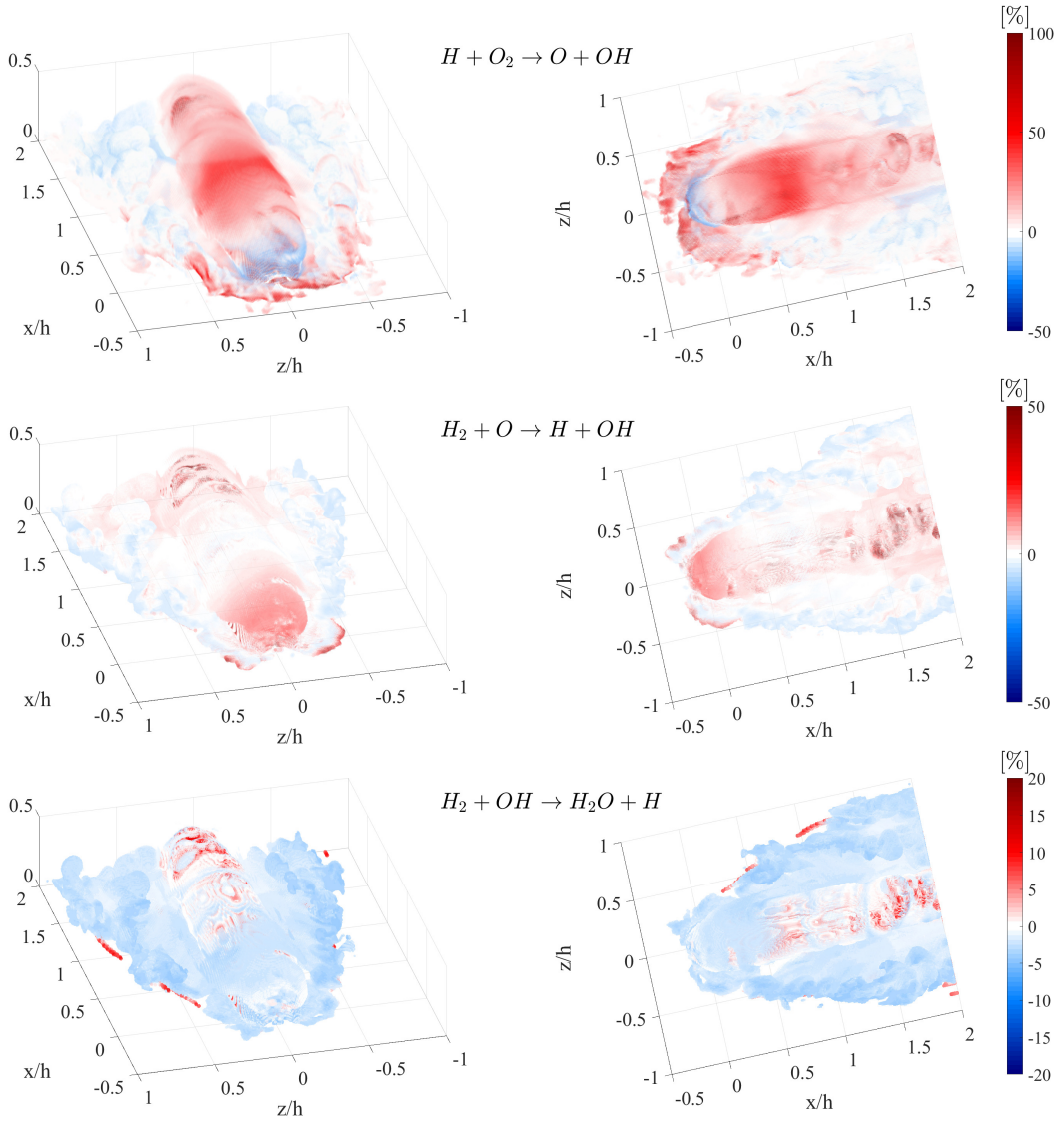

Figure 6.37: Scattering in the physical space XYZ of the reaction rates efficiencies $\frac{k_{Fi,qct}(T,T_v)}{k_{Fi,eq}(T^*)} - 1$ [%] plotted in Fig. 6.36 for (top) $O_2 + H \rightarrow O + OH$, (center) $H_2 + O \rightarrow H + OH$ and (bottom) $OH + H_2 \rightarrow H_2O + H$.

temperature area right behind the shock permits to relax all the vibrational temperatures by about 300 K. Throughout the expansion wave, the vibrational temperature ratios are above unity, just like the efficiency ratios for reactions F1 and F2. As noted earlier, that the third reaction efficiency ratio stays around unity. The efficiency ratio uses the local temperature T^* to evaluate the equilibrated reaction rate. Yet, this temperature depends on the amount of heat that has been released upstream through combustion. Since the efficiency ratios are

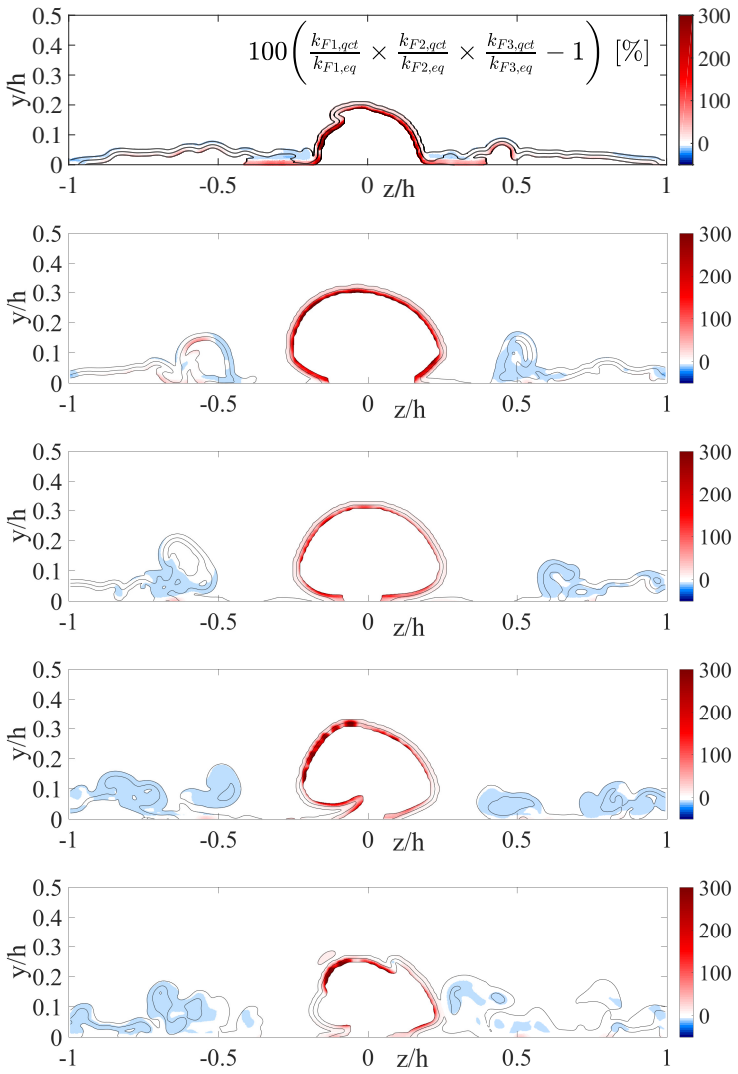

Figure 6.38: YZ-contours of mixture fraction around the stoechiometric line (0.5, 1 and 1.5) colored by the products of the three efficiency ratios of the forwards chain reactions rates shown in Fig. 6.37. The product of efficiency ratios are shown in percentage departure from -50 to +300 %.

mostly positive in the ignition zone, T^* progressively deviates and over-estimates what the local temperature would have been if the whole domain was brought to equilibrium. Hence, this indicator does not account for this "snowball-like" effect and under-estimates the effect of nonequilibrium on the rates.

This section's findings can be summarized as follows. First, the main difference with the ramjet-like mode is the appearance of a bow-shock in front of the impinging jet. As a result of the adverse pressure gradient, a fuel-rich recirculation bubble forms upstream of

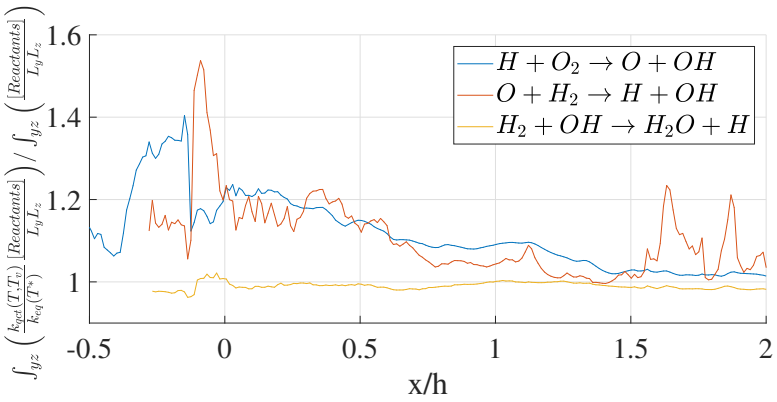

Figure 6.39: YZ integration of the reaction rates efficiency ratio weighted by the reactants mole fractions along the streamwise direction X for the three chain branching reactions.

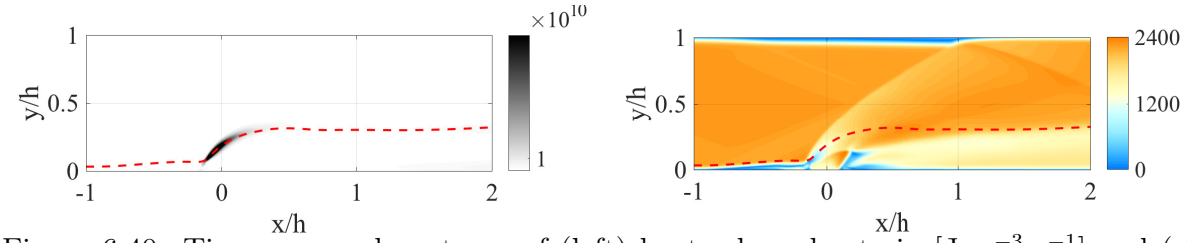

Figure 6.40: Time-averaged contours of (left) heat released rate in [J.m^{-3}.s^{-1}] and (right) streamwise velocity with streamline of maximum heat released rate in dashed red line.

the injector. Inside this bubble, vibrationally cold H_2 can relax, heat and dissociate: the release of radicals H starts up the chain reactions earlier (in a streamwise sense) than for the subsonic flame case. At the bow-shock, the translational temperature is higher in the nonequilibrium case due to compression: this fastens chain branching reaction rate F2 and only marginally slows down F1. Inside this hot low-speed region, species vibrational energies relax fast. Then, the flow enters the expansion wave. The expansion wave crosses the whole mixing layer for the first 2 channel heights from the fuel porthole. The species temperatures increase the reaction rate and sustain ignition, contrary to the equilibrium case where the expansion wave tends to extinguish the flame.

6.4 HEG-XIII experiment

In this last section, two simulations using either the nonequilibrium or equilibrium solver will be performed based on the HEG-XIII experiment from Hanneman *et al.* [48]. The

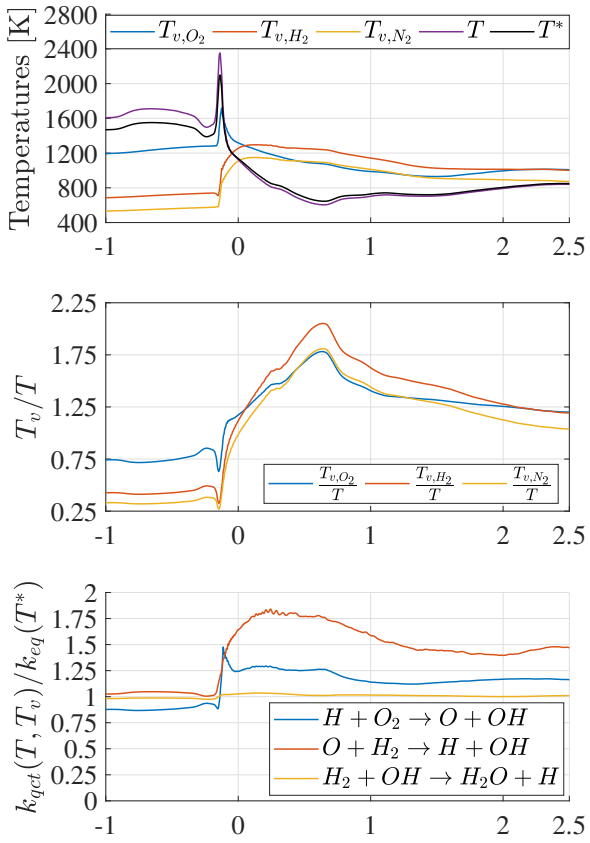

Figure 6.41: Profiles of (top) temperatures, (center) temperature ratios and (bottom) reaction ratio between nonequilibrium and equilibrated thermal state along the streamline presented in Fig. 6.40.

scope of this comparative study is to verify that the nonequilibrium simulation matches the experimental data better than the equilibrium simulation. This experiment is also based on the HyShot-II configuration and the far-field conditions mimic a 28 km altitude flight at Mach 7.37. As mentioned in Chap. V, Hanneman *et al.* did verify that their far-field inflow was at thermodynamic equilibrium: it is, therefore, the only experimental data we can safely use in this comparative study.

Figure 6.42 shows the computational domain and a typical snapshot of the current simulation. This time, it was decided to include the vehicle wedge inside the computational domain. A very coarse grid was used along the wedge and ramp sections, which prevented

the boundary layer to transition from laminar to turbulent. This is irrelevant as this boundary layer is swallowed by the bleed. Inside the duct, various resolutions were used to verify the grid convergence. The finest grid has $(n_x,n_y,n_z) = (4303,256,256)$, which is higher than in the previous section as pressure, hence density, is twice higher at 28 km than at 35 km. Grid convergence is verified in Fig. 6.43.

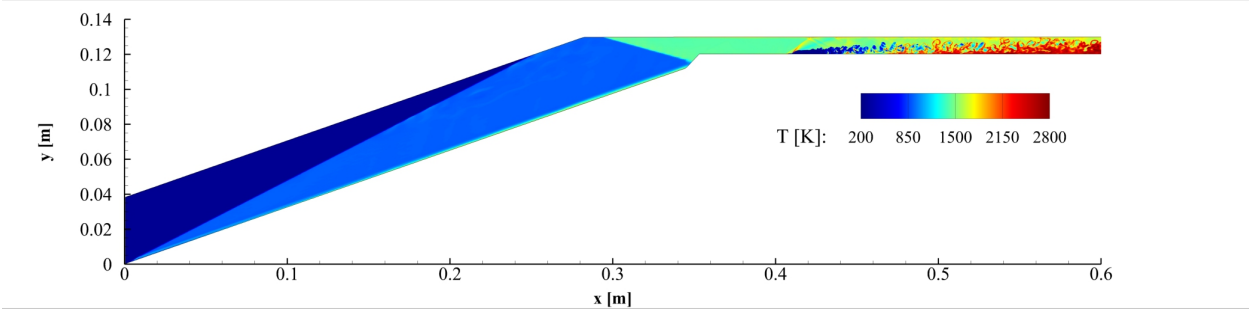

Figure 6.42: Computational domain of the numerical simulation of the HEG-XIII experiment.

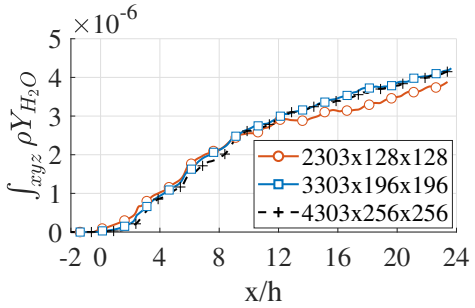

Figure 6.43: Time-averaged YZ integration of water vapor mass $\rho Y(H_2O)$ [kg.m^{-1}] for various grid refinement simulations of the HEG-XIII experiment.

Figure 6.44 shows the comparison of the time-averaged 3D flame structures for both equilibrium and nonequilibrium simulations of the HEG-XIII experiment. The fastest ignition of the nonequilibrium flame observed in the previous section still occurs.

Finally, Fig. 6.46 presents a comparison between the experiment and the simulations of the (top) bottom and (bottom) upper static pressure wall profiles for a fuel-equivalence ratio of 0.28. The nonequilibrium profiles match the experimental data better than the equilibrium case. First, the correlation coefficients between the experiment and the equilibrium/nonequilibrium cases are respectively of 0.61/0.66 and 0.63/0.93 for the top and bottom

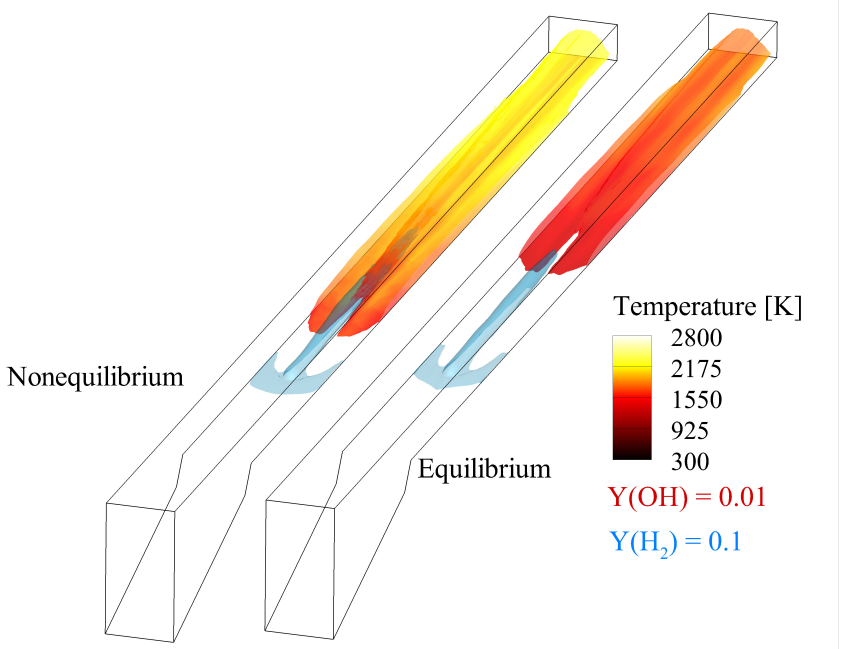

Figure 6.44: Time-averaged 3D flame structures for both equilibrium and nonequilibrium simulations of the HEG-XIII experiment.

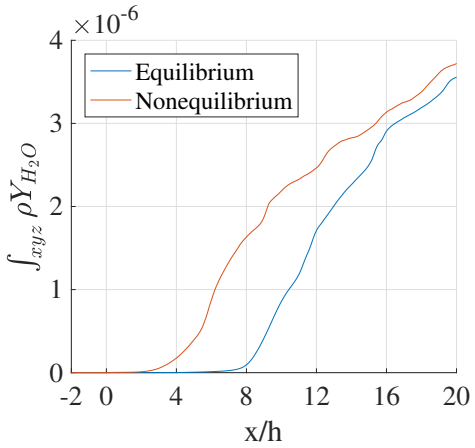

Figure 6.45: 3D-XYZ integral of water vapor mass $\rho Y(H_2O)$ [kg].

walls respectively. Also, the mean squared error are of 0.0238/0.000848 and 0.0255/0.0037 for the top and bottom walls respectively. Further downstream, the simulation appears to under-estimate the pressure growth. It is postulated that this lower pressure rise is caused by the use of spanwise periodic boundary conditions: in the experiment, wall-confinement helps the pressure rise through both friction and flow-blockage caused by the side-wall boundary layer growth. Also, the CVCV model used for some secondary reactions involving HO_2 and H_2O_2 tends to reduce the rates of reactions converting these species into H_2O and other

radicals. Yet, the locations of the expansion and compression waves appear to match really well, even if the pressure amplitudes are slightly off. For instance, the small bump formed by the last 3 pressure probes in the top wall is captured by the nonequilibrium simulation. Last, the comparison between these case is particularly good considering that a variation of 5% of the equivalence ratio can drastically affect the pressure profiles [48, 76].

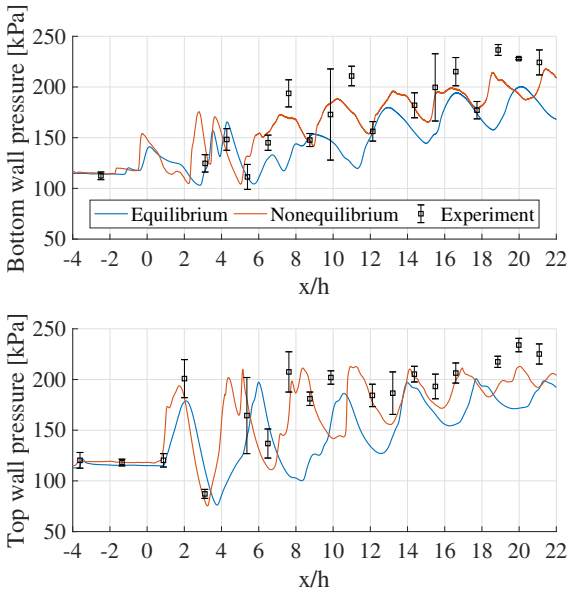

Figure 6.46: Comparison between the experiment and the simulations of the (top) upper and (bottom) bottom static pressure wall profiles.

6.5 Chapter conclusions

In this chapter, the effects of vibrational nonequilibrium on DMSJ were investigated using the nonequilibrium compressible reacting flow solver presented in Chap. II. Due to the presence of compression/expansion waves and the mixing between cold fuel and hot oxidizer, the reactants species interact at nonequilibrium. The rates of the reactions governing the ignition process are affected, which modifies the flame structure and burning efficiency. This is more flagrant in the supersonic flame case where a higher degree of nonequilibrium is present. Such configuration corresponds to a combustor operating in scramjet mode. The complex interactions between the fuel stream and the airflow results in the subsequent occur-

rence of both compression and expansion zones, hence trigger both cold and hot vibrational nonequilibrium. Overall, ignition is enhanced thanks to the release of more radicals H, O and OH throughout the mixing layer. The mixing layer is crossed by an expansion wave which extinguishes the flame in the equilibrium case, while the high T_v/T ratio sustains combustion in the nonequilibrium case.

Finally, the results obtained in this study permit to highlight a few interesting points relevant to scramjet design. First, in both ramjet and scramjet modes, it is preferable to keep the N_2 vibrational energy as low as possible. Not only does this allow to over-excite the translational and rotational modes of all species, but it also increases the vibrational energy of any other fast-relaxing species such as O_2. In scramjet mode, the flow speed is so high that O_2 might not have reached equilibrium by the combustor. If it had, its vibrational temperature would be even higher throughout the mixing layer, hence production of O would be more efficient. The fuel injection scheme could also be designed to favor the size of the horseshoe-like structure which was shown to enhance ignition. Also, the expansion wave contributed to enhancing ignition: it would perhaps be interesting to inject the fuel in a diverging duct. To conclude, the effects of vibrational nonequilibrium on ignition permit to explore new design concepts and radical farming mechanisms.

CHAPTER VII

Conclusions and future work

The work performed for this dissertation aimed at improving our understanding of some of the underlying physics in DMSJ engines as part of a broad effort to address the issue of unstart. To this end, highly-detailed numerical simulations of DMSJ engines components were performed. Large computational resources, in the millions of processor-hours, were utilized to generate this diverse collection of numerical datasets.

Four types of numerical simulations were carried out, each of them pertaining to DMSJ propulsion. First, DNS of cold isolator flows based on the experiment of Hunt *et al.*[52] were performed in order to study the pseudoshock's sensitivity to variations of inflow confinement ratio. Second, DNS of pseudoshocks at realistic flight conditions, *i.e.* with total temperatures high enough to excite the molecular vibrational energy modes, were carried. They allowed studying the effect of wall heat loss and vibrational nonequilibrium on the isolator shock structure. Third, numerical simulations of DMSJ combustor flows were performed in both ramjet and scramjet mode in order to investigate the effects of vibrational nonequilibrium on the ignition process. *Ab. initio* reaction rates accounting for vibrational nonequilibrium were derived for these calculations. Fourth, DNS of high-temperature free shear flows using a state-specific description of the vibrational energy state distribution were carried out to study the coupling between vibrational nonequilibrium and turbulent mixing in a compressible environment.

The results and conclusions drawn from these numerical studies can be summarized as follows:

Simulations of low enthalpy isolators: DNS of pseudoshocks based on the experiment of Hunt *et al.*[52] were performed. Three inflow files were generated from auxiliary DNS using different confinement ratio. The turbulent inflow momentum thickness measured at $z = 0$ bottom wall ranged from 43 to 86 μm. All inflow turbulent boundary layer velocity profiles correctly captured the inner (linear growth) and outer (logarithmic growth) regions. These three inflows were used to generate three different isolator flow solutions.

1. The DNS appropriately reproduced the main features of a normal shock train comprising lambda-shocks, diamond cells located in the core flow composed of compression and expansion waves, and a subsonic outflow. Notably, the wall pressure profile compared favorably well with the experimental data from Hunt *et al.* for the case matching the experiment's inflow confinement ratio.

2. When the inflow confinement ratio increased, the pseusodoshock's cells were contracted around the centerline. Notably, this shrank the normal-like portions of the lambda-shocks, which progressively converted the normal shock train into an oblique shock train. Since the normal-like portion of the lambda-shock decelerates the flow more efficiently than its oblique feet, the pseudoshock pressure growth rate decreased throughout the pseudoshock when the inflow confinement ratio increases. Hence, the pseudoshock length increased in order to match the same pressure rise and was pushed further upstream. This increase was found to scale almost linearly with the inflow Re_θ.

3. Variations in time of the inflow confinement ratio forced the shocks to oscillate at the same frequency. The pseudoshock response depended on the excitation frequency. Too low of a frequency simply displaced the pseudoshock in between the two stable locations

of the inlet confinement oscillation bounds. Too high of a frequency caused the pseudoshock to stand still, as the perturbation timescale became smaller than its reaction timescale: the isolator acts as a low-pass filter in this sense. Interestingly, a resonance frequency was discovered in between where the pseudoshock tail oscillates at a much higher amplitude than its foot. This was shown to be caused by the periodic weakening/strengthening of the compression waves when traveling downstream/upstream, *i.e.* when the flow relative velocity to the shock fronts would decrease/increase. As a result, the length of the pressure rise region was drastically affected, which can potentially have catastrophic results on the scramjet compression stage. The low-pass and resonance responses define the pseudoshock as an anharmonic oscillator.

4. The energy conversion process was quantified throughout the pseudoshock. Logically, it showed that the pressure work through shock compression was responsible for most of the conversion of kinetic into internal enthalpy. Notably, the analysis revealed that a slower and indirect conversion path exists where the mean kinetic energy first converts into turbulent kinetic energy, which later dissipates into internal enthalpy.

5. A pseudoshock pressure growth rate model was derived in light of these new findings. was calibrated using a Bayesian approach to datasets from diverse configurations. The end result is a 1D model which can accurately predict the pseudoshock wall pressure rise, roll-off rate and length over a wide range of inflow conditions pertaining to both ramjet and scramjet operational modes.

6. This pressure growth rate model was embedded into a flux-conserved 1D modeling for pseudoshocks, which was then calibrated using Bayesian inference. The end result is a reduced-order model for isolator flows that accurately estimates the pseudoshock length and pressure rise over a wide operational range pertaining to both ramjet and scramjet modes.

7. The 1D model was then converted into an anharmonic oscillator which was calibrated

to match the phase lag and oscillation amplitude measured from the forced-oscillation DNS. This dynamic model was subsequently found to reproduce the main features of the DNS filtered wall pressure signals, and serve as a real transfer function between isolator inflow and outflow time-resolved signals.

Simulations of high enthalpy isolators: Several DNS computations of the isolator configuration discussed above were then performed but with higher inflow enthalpy. The two sets of simulations (low and high enthalpy configurations) share the same bulk inflow Mach number ($M = 2.0$), isolator pressure rise ratio (70% of a normal shock rise) and inflow confinement ratio ($\mathcal{A}^* = 16\%$). The main differences are a change of inflow density and temperature to mimic realistic high-altitude hypersonic flight conditions (flight speed of Mach 5.5 at 35 km altitude). This resulted in a temperature range across the domain ranging from 300 to 1650 K, which is high enough to populate higher vibrational energy levels. Three DNS computations were performed. The first two assumed equilibrium thermodynamics with either isothermal (300 K) or adiabatic wall boundary conditions. The third DNS resolved vibrational nonequilibrium and used a 300 K isothermal wall boundary condition. The relaxation process of species vibrational energies was resolved using a multi-temperature model coupled with the compressible flow solver.

1. The vortical skeleton of a normal shock train was revealed by applying a triple decomposition method to the 3D Favre-averaged datasets on the equilibrium solutions. The decomposition revealed that pairs of counter-rotating vortices are located in each corner of the duct, upstream of the pseudoshock. These vortices disappeared where the boundary layer separates under the leading lambda-shock due to the strong adverse pressure gradient. Contrary to the common assumption, the recirculation bubble did not spread along the whole shock train, but was instead located under the leading shock, which coincided with the highest wall pressure growth rate region. Notably, two opposing pairs of counter-rotating vortices formed in the streamwise-normal plane

in between each successive shock. These vortices were located under the shock fronts, and progressively decreased in amplitude along the pseudoshock.

2. It was found that wall heat losses decreased the size and strength of the turbulent boundary layer vortices. It also considerably reduced the size of the recirculation bubble. This resulted in a smaller detachment and a larger sonic core region. Hence, the shock structure was larger, particularly the normal-like portion of the lambda-shock. In agreement with the previous observations on the effect of confinement on cold pseudoshocks, this also resulted in a higher pressure growth rate along the pseudoshock. Therefore, the pseudoshock was smaller in the isothermal wall case.

3. By comparing the solutions obtained from the equilibrium and nonequilibrium thermodynamic models, several important results were found. First, the presence of compression waves introduces cold nonequilibrium. O_2 relaxes sufficiently fast such that it has reached thermal equilibrium by the shock train tail. Interestingly, the alternating compression and expansion waves in each diamond cell create subsequent regions of vibrationally cold and hot O_2, respectively. N_2 remains vibrationally cold throughout the whole pseudoshock and does not reach equilibrium even at the isolator outflow. Hence, the thermodynamic state of the airflow entering the combustor is altered due to this noequilibrium phenomenon. Specifically, the nonequilibrium airflow possesses a temperature 90 K higher, and a 9.4 g.m^{-3} smaller density.

4. The rate of conversion of kinetic into internal enthalpy is lowered by the presence of vibrationally cold gas, just as in a simple normal shock configuration. Coincidentally, the pressure growth rate was reduced throughout the shock train. This caused the shock train to move upstream to allow for a longer pseudoshock length in order to reach the prescribed isolator exit pressure.

5. The vibrationally cold N_2 causes a pressure-defect at the isolator outflow. This pressure will be recovered further downstream once N_2 equilibrates. In this sense, the N_2

population can be viewed as a thermal time-bomb.

6. It was estimated that these effects become important for flight speed beyond Mach 3.6 for a 35 km flight altitude. Decreasing the altitude would also lower this limit.

7. Last, a direct correlation was found between the size of the shock train sonic core (defined as the distance between the leading shock and the most downstream sonic location) and the first shock train diamond cell size (defined as the centerline distance between the first and second shocks).

Simulation of DMSJ combustors: Simulation of DMSJ combustors operating in both ramjet and scramjet modes were performed to analyze the impact of vibrational nonequilibrium on the ignition process. The ramjet-mode simulations simply consisted of an extension of the hot isolator configuration with a H_2-injector placed at the center of the bottom wall. The scramjet-mode simulations replicated the HyShot-II geometry for a 35 km Mach 9.0 flight.

1. *Ab initio* reaction rates derived from a QCT approach were used to quantify the effect of vibrational nonequilibrium on key chain-branching reaction rates. It was shown that some reactions were less sensitive than others to their reactants vibrational temperatures. As a result, reactions can even be counter-intuitively fastened under particular vibrationally cold conditions. For instance, at constant internal energy, it is preferable to under-excite the vibrational energy of the diluter and transfer this energy into the gas translational mode: it would increase the reaction rates of $H_2 + O \rightarrow H + OH$.

2. The scramjet simulations revealed a complex ignition region. A bow-shock formed in front of the cold impinging fuel stream, and the resulting adverse pressure gradient created a horseshoe structure. Intermittent radical-rich pockets convected through the mixing layer of the lifted supersonic flame.

3. The ramjet and scramjet modes simulations revealed that the reactants species interacted at nonequilibrium, mostly due to the upstream compression waves and by the mixing between the cold fuel and hot airflow. The rates of the chain reactions governing the ignition process were affected. This results highlights the importance of resolving nonequilibrium throughout the isolator in order to properly estimate the combustor's inflow T_{v,O_2} and T_{v,N_2}.

4. In both cases, the incoming O_2-stream was vibrationally hot, which increased the formation of radicals O. However, in ramjet mode, the absence of a region of vibrationally hot H_2 and OH decreased the rate of the other chain reactions. The scramjet mode presented two major differences. First, at the bow-shock foot, the temperature becomes higher than 3000 K while T_{v,N_2} is less than 1500 K. This considerably enhanced the production of radicals H and OH in this low-speed area which coincides with the origin of the mixing layer. Second, an expansion wave crossed the mixing layer which created a vibrationally hot ignition region. This considerably increased the production rates of radicals H, O and OH. As a result, the flame lift-off distance was reduced compared to the equilibrium case by a distance of approximately 4 channel heights.

5. DNS of the experiment of Hannemann *et al.* (also based on the HyShot-II geometry) were also carried out. A comparison of the wall pressure profiles between the two DNS and the experiment showed that the nonequilibrium matched the experiment better considering both the mean squared error and correlation coefficients.

6. Based on these results, it can be concluded that vibrational nonequilibrium does appreciably affect the ignition process, especially in scramjet mode. Given the understanding developed in the present study, several guidelines to DMSJ designs are suggested. First, it is preferable to keep the vibrational energy of the diluter N_2 as low as possible to over-excite the other modes. For instance, strong shocks located right upstream of the combustor and an isolator as short as possible would both ensure that $T_{v,\mathrm{N}_2} < T$ in the

mixing region. Second, it is counter-intuitively interesting to generate an expansion wave inside the ignition region. Perhaps a convecting/diverging duct could be used in ramjet/scramjet modes. Third, the injector scheme could be placed against the flow stream to generate a locally supersonic relative velocity even in ramjet mode, resulting in the appearance of a bow-shock.

State-specific simulations: Two DNS computations of a N_2 turbulent planar jet were carried out using both the multi-temperature approach and a state-specific method. This latter method consists in transporting the vibrational energy states populations instead of assuming it to always remain as a Boltzmann distribution with a prescribed vibrational temperature. Since the maximum temperature is 4000 K, 10 energy states are sufficient to adequately resolve the distribution. The state-specific relaxation rates are derived using a QCT approach.

1. Vibrational nonequilibrium appeared due to the flow compressibility. When the flow accelerated, T decreased triggering hot nonequilibrium. Conversely, when the flow decelerated, T increased triggering cold nonequilibrium.

2. The turbulent mixing of the bulk vibrational energy was similarly resolved by the multi-temperature and the state-specific methods.

3. The distribution of the vibrational energy states deviates from a Boltzmann distribution. Notably, the highest energy states are considerably over-populated as they reach local equilibrium fast. On the other hand, the population in the slowly-relaxing lowest energy states were lower than their local Boltzmann numbers. An intermediate state level presented both over/under-population on each side of the mixing layer.

4. This suggests that chemical reaction rates computed using a multi-temperature approach would be underestimated, since reactions are driven by the most energized

molecules. Hence, state-specific reaction and relaxation rates would permit a higher-order description of the effect of vibrational nonequilibrium on ignition. This demonstrates the interest of the use of state-specific rates for DMSJ calculations and motivates further research.

To conclude, this research work has provided novel and critical insights into the functioning of a dual-mode scramjet engine. By combining supercomputing resources with state-of-the-art modeling, an unprecedented level of detail could be simulated. These insights have guided the derivation of a new reduced-order model for pseudoshocks, the accuracy of which has been demonstrated over a wide range of flight conditions. The main finding of these highly-resolved numerical simulations is the demonstration of the importance of vibrational nonequilibrium for supersonic air-breathing engines. Failure to resolve the relaxation process of the vibrational energies can lead to misprediction of both the pseudoshock length, the combustor airflow thermodynamic state, and of the ignition process. As a result, engine unstart would become less predictable and occur more easily if equilibrium models were used to design the engine. Conversely, by gaining a sufficient understanding of these effects, it becomes possible to use vibrational nonequilibrium to improve the efficiency of scramjet engines. Last, this work motivates further research into state-specific approaches in order to improve the accuracy of nonequilibrium simulations in the context of DMSJ. These studies, results, and models contribute to the design and development of stable and robust hypersonic vehicles.

Several issues, follow-up questions and potential improvements were highlighted throughout these studies, which would require the following additional work:

1. The dynamic reduced-order model for pseudoshock still needs closure. To this end, the pseudoshock's local stiffness ξ and characteristic pulsation ω_0 have to be derived as a function of values obtained from the static profile (such as pressure and Mach number). It is suggested that an inverse power law would serve as a good starting point. However, more data is needed to derive a robust function.

2. The pseudoshock DNS could use a less diffusive numerical scheme in the shock-less regions. Namely, the implementation of continuous hybrid schemes would be a valuable addition to UTCOMP.

3. Due to a lack of available potential energy surfaces, many reactions did not use QCT-derived efficiency functions, but relied on the CVCV model designed for dissociating reentry flows, not for internal reacting flows. Hence, the use of QCT rates for all reactions would improve the model accuracy. It would be interesting to see how it affects the chain-terminating reactions rates and the distribution of HO_2 inside the combustor.

4. Likewise, the lack of PES for many sorts of molecular collisions prevented the derivation of state-specific relaxation rates for all the species involved in H_2-O_2 combustion. It is estimated that a state-specific approach will require the transport of ≈ 100 scalars (≈ 10 states' population densities are needed per species to appropriately define the distribution at temperatures below 3000 K). Furthermore, it would even be possible to use state-specific reaction rates and better resolve the effect of nonequilibrium on ignition.

5. Another kind of engine which relies on shock-based compression is the rotating detonation engine (RDE). In an RDE, a traveling detonation wave burns the fuel-air mixture: the ignition zone is located right behind the shock front. Hence, the reactant species are vibrationally under-excited. Interestingly, Taylor *et al.* [123] found that detonation cell sizes for H_2-O_2-Ar mixtures (mono-atomic diluter) were bigger than for H_2-O_2-N_2 mixtures (diatomic diluter), and attributed this difference to the slow vibrational relaxation process of the diluter N_2 through the reaction layer.

List of related peer-reviewed publications

- Fiévet, R., Koo, H., Raman, V., Auslender, A., Numerical investigation of shock train response to inflow boundary layer variations, AIAA Journal, Vol. 55, No. 9, 2017.
- Fiévet, R., Voelkel, S., Koo, H., Raman, V. and Varghese, P., Effect of Thermal Nonequilibrium on Ignition in Scramjet Combustors, Proceeding of the Combustion Institute, Vol.36, No. 2, 2017.
- Fiévet, R., Voelkel, S., Varghese, P. and Raman, V., Numerical investigation of vibrational relaxation coupling with turbulent mixing, Journal of Computational Physics *(in review)*.
- Fiévet, R., Raman, V. and Auslender, A., Data-driven one-dimensional modeling of pseudoshocks, AIAA Journal *(in review)*.
- Fiévet, R. and Raman, V., Effect of vibrational nonequilibrium on isolator shock structure, Journal of Propulsion and Power *(in review)*.

List of related conference proceedings

- Fiévet, R., Voelkel, S., Varghese, P. and Raman, V., Numerical investigation of vibrational relaxation coupling with turbulent mixing, 55th AIAA Aerospace Sciences Meeting, AIAA 2017-0663, 2017.
- Reising, H., Haller, T., Clemens, N., Varghese, P., Fiévet, R. and Raman, V., Spontaneous Raman Scattering Temperature Measurements and Large Eddy Simulations of Vibrational Non-equilibrium in High-Speed Jet Flames, AIAA AVIATION Forum, AIAA 2016-3550, 2016.
- Fiévet, R., Raman, V. and Auslender, A., Direct Numerical Simulation of a normal shock train with vibrational nonequilibrium, 69th Annual Meeting of the APS Division of Fluid Dynamics, 2016.
- Fiévet, R., Koo, H., Raman, V., Auslender, A., Numerical simulation of shock trains in a 3D channel, 54th AIAA Aerospace Sciences Meeting, AIAA 2016-1018, 2016.
- Raman, V., Fiévet, R., Clarke, P. and Varghese, P., A Mesoscopic Model for the Description of Small-scale Inhomogeneity in Turbulent Flows with Thermal Nonequilibrium, 68th Annual Meeting of the APS Division of Fluid Dynamics, Volume 59, Number 20, 2015.
- Fiévet, R., Voelkel, S., Koo, H., Varghese, P. and Raman, V., Direct Numerical Simulation of a supersonic reacting jet with thermochemical nonequilibrium, 68th Annual Meeting of the APS Division of Fluid Dynamics, Volume 60, Number 21, 2015.

- Fiévet, R., Koo, H. and Raman, V., Numerical simulation of a scramjet isolator with thermodynamic nonequilibrium, 22nd AIAA Computational Fluid Dynamics Conference, AIAA 2015-3418, 2015.
- Fiévet, R., Voelkel, S., Koo, H., Varghese, P. and Raman, V., Numerical Simulation Study of Thermochemical Nonequilibrium Effect on Mixing and Combustion, 67th Annual Meeting of the APS Division of Fluid Dynamics, Volume 59, Number 20, 2014.
- Koo, H., Fiévet, R., Raman, V., Voelkel, S. and Varghese, P., Direct Numerical Simulation Study of Thermochemical Nonequilibrium Effect on Mixing and Combustion, 67th Annual Meeting of the APS Division of Fluid Dynamics, Volume 59, Number 20, 2014.

Recognition

- Rachkam Predoctoral Fellowship recipient
- Rachkam's Towner Prize nominee
- Invitation into NASA's supercomputing division team at the Supercomputing Conference 2016

APPENDICES

APPENDIX A

Turbulent mixing of vibrational energy states populations - Reversed configuration

The reversed configuration presented in Sec. 2.2.4.3 (case 2, see Tab. 2.1) with a jet hotter than the coflow was also simulated. Spatial resolution was not verified in this case as the jet possesses a lower Reynolds number due to its higher viscosity and lower density than for case 1. Hence, its Kolmogorov lengthscales are larger such that the grid is relatively finer. A comparison of the mixing of various states populations are shown in Figs. A.1 A.2 and A.3. Case 2 presents larger vortical structures compared to case 1 due to its lower Reynolds number, and a logically reversed mixing process. The radial profiles of all states populations are simply inverted as seen in Fig. A.2, notably for state level i = 2.

The error between the local bulk vibrational energy e_v and its equilibrated values e_v^* (as was shown in Fig. 2.13) is plotted in Fig. A.4. The flow is dominantly vibrationally under-excited as observed in case 1. However, the volume entrainment ratio is now close to 1.0. Hence the compressibility is evenly distributed throughout the mixing layer as seen in Fig. A.5, with occurrences of both flow compression and expansion. This suggests that there should be more vibrationally hot areas, yet this is not the case.

Realizations of e_v-e_v^* relative errors shown in Fig. A.6 (analogous to Fig. 2.14). The left figure simply mirrors case 1. The right figure shows that a flow fraction greater than case

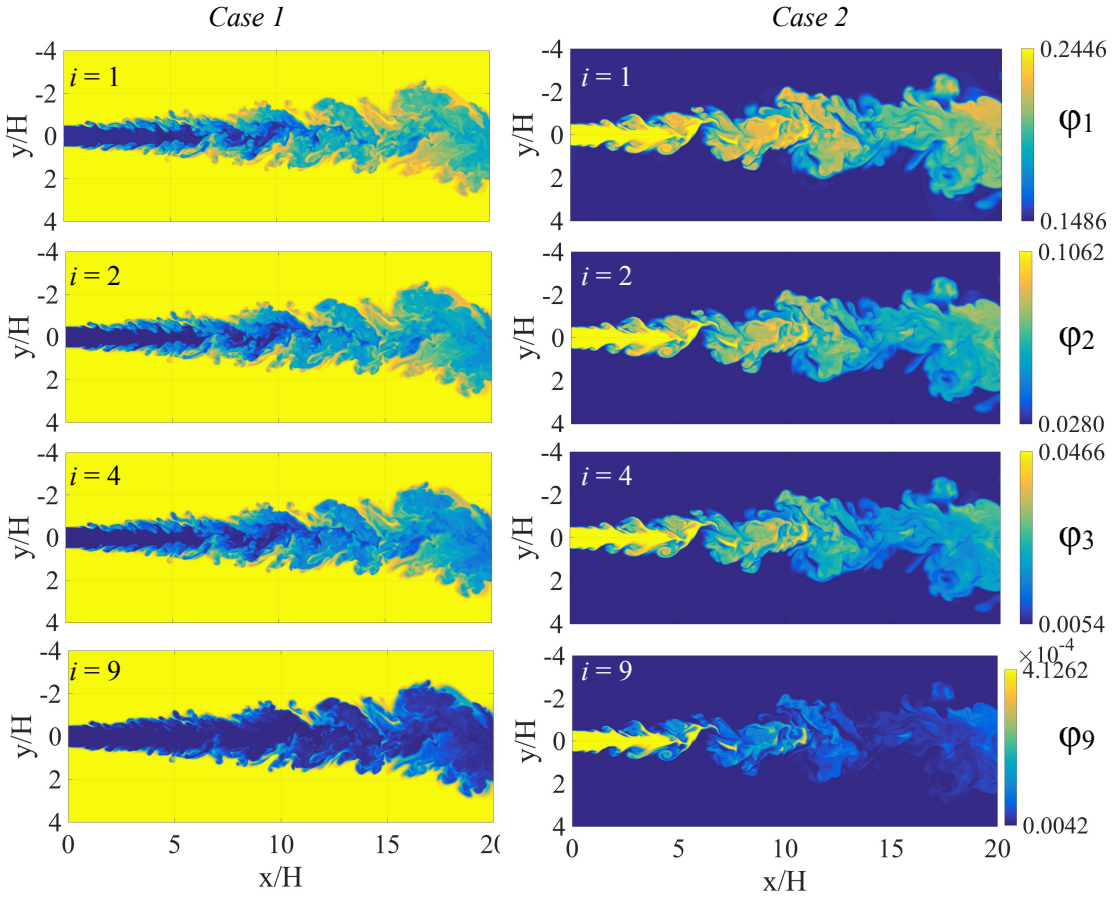

Figure A.1: Snapshots of vibrational state population number densities ϕ_i for levels $i \in [1\ 2\ 4\ 9]$ from top to bottom for the (left) cold jet and (right) hot jet.

1 has a negative compressibility as observed in Fig. A.5. However, the correlation between compressibility and e_v-e_v^* relative errors reveals that, contrary to case 1, the realizations are skewed towards the bottom quadrants (cold nonequilibrium). As can be observed in the zoomed zones, wherever the compressibility factor is neutral the flow is still in cold nonequilibrium. This suggests that another process triggering nonequilibrium through the mixing layer happens in case 2, but was absent from case 1. As the mass entrainment ratio increased from 1.0 to 2.1 from case 1 to case 2, the mixing theory of Reising *et. al* now predicts a predominantly cold nonequilibrium instead of a neutral mixing. It is postulated that the combination of both compressibility effects and Reising *et. al*'s theory explain the current results. Note that in order to solely investigate Reising *et. al*'s turbulent

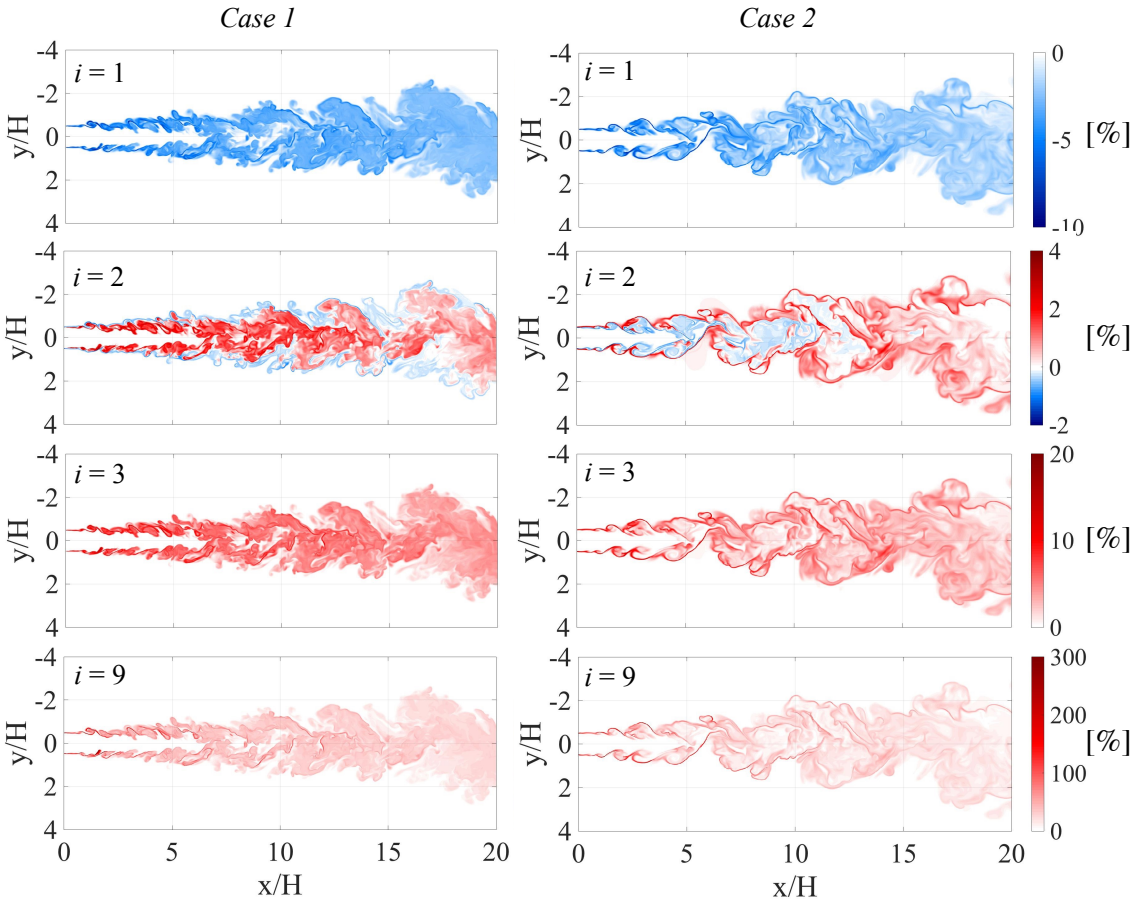

Figure A.2: Snapshots of $\mathcal{E}_i$ [%] for levels $i \in [1\ 2\ 4\ 9]$ from top to bottom for the (left) cold jet and (right) hot jet.

mixing theory, any compressibility-triggered nonequilibrium should be canceled. A uniform inflow velocity should therefore be used across the inlet plane. Unfortunately, we found that Rayleigh-Taylor instabilities were not sufficient to create turbulence, and were unable to study such configuration.

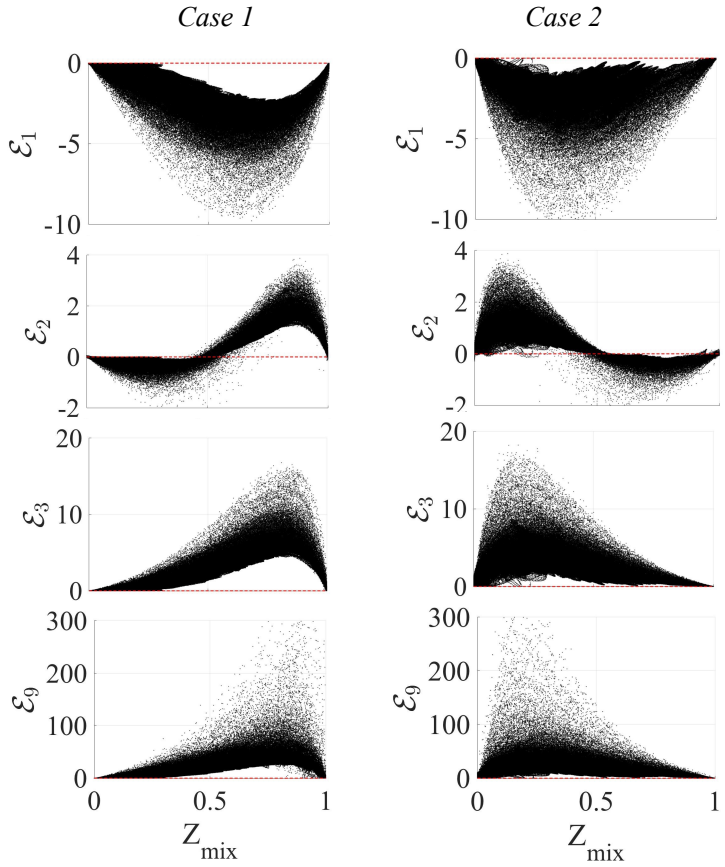

Figure A.3: Realizations of $\mathcal{E}_i$ [%] for $i \in [1\ 2\ 4\ 9]$ from top to bottom with Z_{mix} for the (left) cold jet and (right) hot jet.

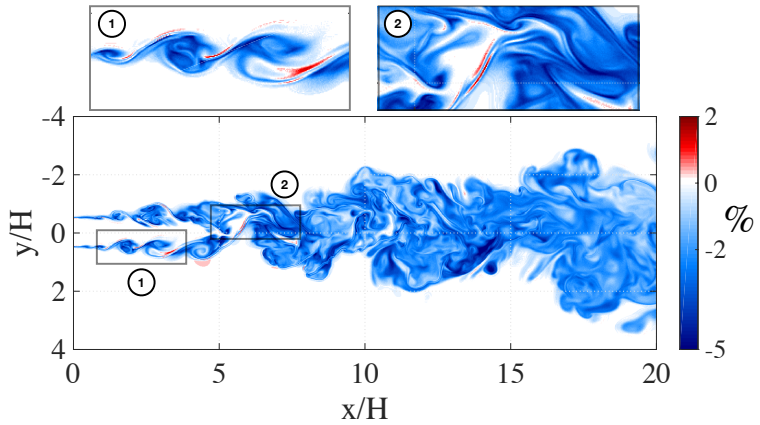

Figure A.4: Snapshots of error between e_v and $e_v{}^*$ [%] for case 2. Red/blue indicate a locally vibrationally over/under-excited population.

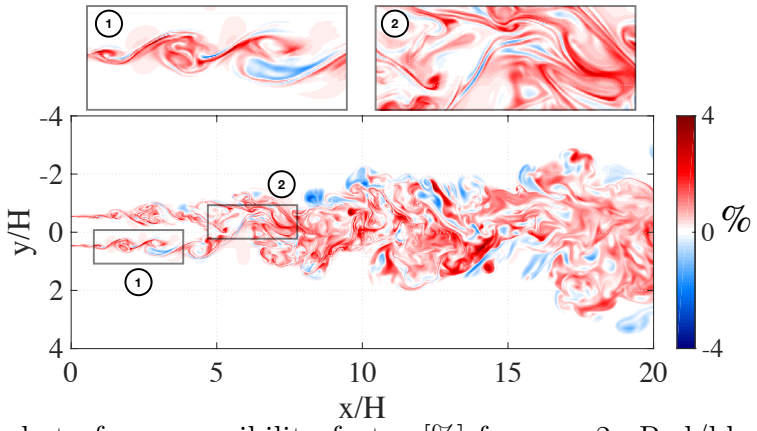

Figure A.5: Snapshot of compressibility factor [%] for case 2. Red/blue indicate a locally compressed/expanded flow.

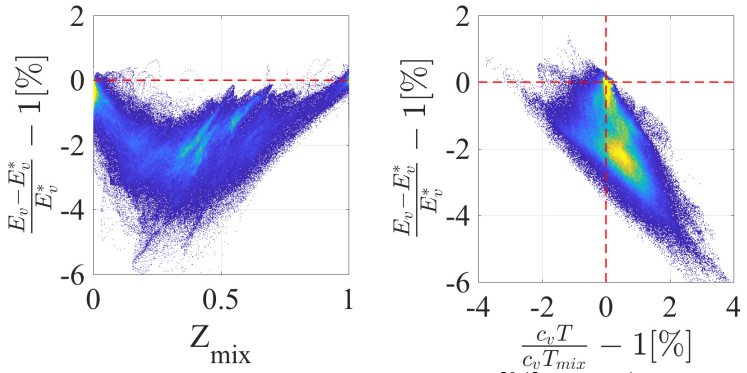

Figure A.6: Realizations of error between e_v and $e_v{}^*$ [%]. Red/blue indicate a locally vibrationally over/under-excited population.

APPENDIX B

1D model Matlab script

A functional implementation of the 1D model derived in Chap. IV is presented in the Matlab script below. It is calibrated to match case 4 (see Tab. 4.1) and is compared with the DNS wall pressure profile.

```
clear all;close all;clc;format long
% DNS data
xDNS = [0.0700    0.5356    1.0011    1.4667    1.9322    2.3978    ...
    2.8634    3.3289    3.7945    4.2600    4.7256    5.1912    5.6567 ...
       6.1223 6.5878    7.0534    7.5190    7.9845    8.4501 8.9157];
yDNS = 1.0e+04*[1.6706    2.2949    2.9484    3.1253    3.4122    ...
    3.5160    3.6412    3.7776    3.8377    3.8935    3.9519    4.0137 ...
       4.0588    4.1091 4.1480    4.1730    4.1995    4.2251    4.2475 ...
    4.268];

% Model parameters
parameters = 1.0e+02 *[ 0.0347   0.0000170   0.0151   0.259   1.355   ...
    0.0164  0.0176  0.01428   0.0106];
Cfr = parameters(1);
Cfr_cst = parameters(2);
```

```
slope = parameters(3);
refMach1 = parameters(4);
kref = parameters(5);
scalar1 = parameters(6);
power2 = parameters(7);
Mref = parameters(8);
power5 = parameters(9);

% Case parameters
M0 = 1.906;
Dh = 2*0.0572*0.0698/(0.0572+0.0698);% Hydraulic diameter
gam = 1.4;
BackPressure = 42561;
P0 = 1.7314e4;
Cf0 = 1.05e-3;
P1 = 16000;
M1 = 1.721056629837177;
recoveryEfficiency_ =   0.769520803266958;% Computed from McLafferty ...
    model (see Fig. 4.2)

% Vectors initialization
Nx = 2500;
Lx = 10*Dh;
dx = Lx/Nx;
xx = linspace(0,Lx,Nx)';
Aratio = ones(length(xx),1);
Mach2 = ones(length(xx),1)*M1^2;
dPP = zeros(length(xx),1);
p = ones(length(xx),1)*P1;
q1 = gam*M1^2*P1/2;
q = ones(length(xx),1)*q1;

% 1D model
```

```
k0 = kref*recoveryEfficiency_^power2;
Cf1 = Cfr_cst+Cfr*Cf0;
powerQ = refMach1*(1-tanh(slope*(M1-Mref)));
for i=1:length(xx)-1
    q(i) = gam*Mach2(i)*p(i)/2;
    kq = k0*[(scalar1 + q(i)/q1)^(powerQ)] / [ ( ...
        (scalar1+1)^(powerQ+1)-scalar1^(powerQ+1) )/(1*(powerQ+1)) ];
    dPP(i)= kq/Dh*Cf0^power5*gam*Mach2(i)*dx/2;
    Mach2(i+1) = Mach2(i) - Mach2(i)*[(1+(gam-1)/2 * Mach2(i)) * ...
        [(2/gam/Mach2(i)/Aratio(i)) * dPP(i)] + 4*Cf1/Dh*dx/Aratio(i) ];
    Aratio(i+1) = Aratio(i) +  ...
        Aratio(i)*([1-Mach2(i)*(1-gam*(1-Aratio(i)))]...
         /(gam*Mach2(i)*Aratio(i))* dPP(i) + ...
         (1+(gam-1)*Mach2(i))/2/Aratio(i)*4*Cf1/Dh*dx);
    p(i+1) = p(i) + dPP(i)*p(i);
end
% Cut solution where reattachment occurs
Aratio = min(1.0,Aratio);iA1 = find(Aratio(2:end)==1, 1, 'first');
p(iA1:end) = p(iA1);Mach2(iA1:end) = Mach2(iA1);

% Plotting some of the DNS data wall pressure profile on top of 1D ...
    model profile
p1=plot(xx/Dh,p/P1,'LineWidth',1,'Color',[0 0 0]);hold on;
plot(xDNS,yDNS/P1,'LineStyle','none','LineWidth',2,'Marker','+',...
    'Color','r','MarkerSize',10,'MarkerFaceColor',[1 1 1]);
legend('1D model','DNS','Location','SouthEast');
set(gca,'YLim',[1 3]); set(gca,'XLim',[0 10]);
set(gca,'Xtick',[0:2:12]);set(gca,'Ytick',[0:4]);
set(gca, 'fontsize', 18, 'fontname', 'times');
grid on;
set(get(gca,'Xlabel'),'String','x/D_h')
set(get(gca,'Ylabel'),'String','P/P_1')
```

BIBLIOGRAPHY

BIBLIOGRAPHY

[1] L. Agostini, L. Larcheveque, and P. Dupont. Mechanism of shock unsteadiness in separated shock/boundary-layer interactions. *Physics of Fluids*, 27(12), Dec 2015.

[2] I. V. Arsentiev, B. I. Loukhovitski, and A. M. Starik. Application of state-to-state approach in estimation of thermally nonequilibrium reaction rate constants in mode approximation. *Chemical Physics*, 398:73–80, 2012.

[3] E. Baumann, J. W. Pahle, M. C. Davis, and J. T. White. X-43A Flush Airdata Sensing System Flight-Test Results. *Journal of Spacecraft and Rockets*, 47(1):48–61, Jan-Feb 2010.

[4] A. Ben-Yakar, M. Mungal, and R. Hanson. Time evolution and mixing characteristics of hydrogen and ethylene transverse jets in supersonic crossflows. *Physics of Fluids*, 18(2), Feb 2006.

[5] J. Bender, I. Nompelis, P. Valentini, S. Doraiswamy, T. Schwartzentruber, G. Candler, Y. Paukk, K. Yang, Z. Varga, and D. Truhlar. Quasiclassical trajectory analysis of the n2 + n2 reaction using a new ab initio potential energy surface. In *11th AIAA/ASME Joint Thermophysics and Heat Transfer Conference, 16-20 June 2014, Atlanta, GA, USA*, number AIAA 2014-2964, 2014.

[6] J. D. Bender, P. Valentini, I. Nompelis, Y. Paukku, Z. Varga, D. G. Truhlar, T. Schwartzentruber, and G. V. Candler. An improved potential energy surface and multi-temperature quasiclassical trajectory calculations of $N_2 + N_2$ dissociation reactions. *The Journal of Chemical Physics*, 143(5):054304, 2015.

[7] M. Berglund, E. Fedina, C. Fureby, J. Tegnér, and V. Sabel'nikov. Finite rate chemistry large-eddy simulation of self-ignition in a supersonic combustion ramjet. *AIAA Journal*, 48(3):540–550, 2010.

[8] I. Bermejo-Moreno, L. Campo, J. Larsson, J. Bodart, D. Helmer, and J. K. Eaton. Confinement effects in shock wave/turbulent boundary layer interactions through wall-modelled large-eddy simulations. *Journal of Fluid Mechanics*, 758:5–62, Nov 2014.

[9] M. Bernardini, I. Asproulias, J. Larsson, S. Pirozzoli, and F. Grasso. Heat transfer and wall temperature effects in shock wave turbulent boundary layer interactions. *Physical Review Fluids*, 1:084403, Dec 2016.

[10] F. S. Billig. Research on Supersonic Combustion. *Journal of Propulsion and Power*, 9(4):499–514, Jul 1993.

[11] I. D. Boyd. Computation of Hypersonic Flows Using the Direct Simulation Monte Carlo Method. *Journal of Spacecraft and Rockets*, 52(1):38–53, Jan-Feb 2015.

[12] I. D. Boyd and E. Josyula. Detailed analysis of vibrational nonequilibrium of molecular oxygen in shock-heated flow. *Physical Review Fluids*, 2(12), Dec 18 2017.

[13] P. J. K. Bruce and H. Babinsky. Unsteady shock wave dynamics. *Journal of Fluid Mechanics*, 603:463–473, May 2008.

[14] G. V. Candler and R. W. MacCormack. Computation of weakly ionized hypersonic flows in thermochemical nonequilibrium. *Journal of Thermophysics and Heat Transfer*, 5(3):266–273, 1991.

[15] C. Cao, T. Ye, and M. Zhao. Large eddy simulation of hydrogen/air scramjet combustion using tabulated thermo-chemistry approach. *Chinese Journal of Aeronautics*, 28(5):1316–1327, Oct 2015.

[16] B. Carrol and J. Dutton. Characteristics of Multiple Shock-wave Turbulent Boundary-layer Interactions in Rectangular Ducts. *Journal of Propulsion and Power*, 6(2):186–193, Mar-Apr 1990.

[17] B. Carrol and J. Dutton. Multiple Normal Shock-wave Turbulent Boundary-layer Interactions. *Journal of Propulsion and Power*, 8(2):441–448, Mar-Apr 1992.

[18] B. Carrol, P. Lopezfernandez, and J. Dutton. Computations and Experiments for a Multiple Normal-shock Boundary-layer Interaction. *Journal of Propulsion and Power*, 9(3):405–411, May-Jun 1993.

[19] M. Chapuis, E. Fedina, C. Fureby, K. Hannemann, S. Karl, and J. M. Schramm. A computational study of the HyShot II combustor performance. *Proceedings of the Combustion Institute*, 34:2101–2109, 2013.

[20] N. T. Clemens and V. Narayanaswamy. Low-frequency unsteadiness of shock wave/-turbulent boundary layer interactions. *Annual Review of Fluid Mechanics*, 46:469–492, 2013.

[21] P. A. T. Cocks, C. Bruno, J. M. Donohue, and M. Haas. Iddes of a dual-mode ethylene fueled cavity flameholder with an isolator shock train. In *51st AIAA Aerospace Sciences Meeting*, number AIAA-2013-0116, 2013.

[22] A. W. Cook and W. H. Cabot. A high-wavenumber viscosity for high-resolution numerical methods. *Journal of Computational Physics*, 195:594–601, 2004.

[23] A. W. Cook and W. H. Cabot. Hyperviscosity for shock-turbulence interactions. *Journal of Computational Physics*, 203:379–385, 2005.

[24] B. Costa and W. S. Don. High order Hybrid central - WENO finite difference scheme for conservation laws. *Journal of Computational and Applied Mathematics*, 204(2):209–218, JUL 15 2007. 7th International Conference on Mathematical and Numerical Aspects of Waves, Brown Univ, Providence, RI, June 20-24, 2005.

[25] A. D. Cutler, L. M. L. Cantu, E. C. A. Gallo, R. Baurle, P. M. Danehy, R. Rockwell, C. Goyne, and J. McDaniel. Nonequilibrium Supersonic Freestream Studied Using Coherent Anti-Stokes Raman Spectroscopy. *AIAA Journal*, 53(9):2762–2770, Sep 2015.

[26] A. D. Cutler, G. Magnotti, L. Cantu, E. Gallo, R. Rockwell, and C. Goyne. Dual-Pump Coherent Anti-Stokes Raman Spectroscopy Measurements in a Dual-Mode Scramjet. *Journal of Propulsion and Power*, 30(3):539–549, May-Jun 2014.

[27] S. Desai, V. Kulkarni, and H. Gadgil. Delusive Influence of Nondimensional Numbers in Canonical Hypersonic Nonequilibrium Flows. *Journal of Aerospace Engineering*, 29(5), Sep 2016.

[28] P. Dimotakis. Two-Dimensional Shear-layer Entrainment. *AIAA Journal*, 24(11):1791–1796, Nov 1986.

[29] H. Do, S.-k. Im, M. G. Mungal, and M. A. Cappelli. The influence of boundary layers on supersonic inlet flow unstart induced by mass injection. *Experiments in Fluids*, 51(3):679–691, Sep 2011.

[30] P. Donde, H. Koo, and V. Raman. A multivariate quadrature based moment method for LES based modeling of supersonic combustion. *Journal of Computational Physics*, 231(17):5805–5821, 2012.

[31] J. R. Edwards and J. E. Fulton. Development of a RANS and LES/RANS Flow Solver for High-Speed Engine Flowpath Simulations. In *20th AIAA International Space Planes and Hypersonic Systems and Technologies Conference Glasgow, Scotland*, number AIAA 2007-115, 2015.

[32] A. F. El-Sayed. *Fundamentals of Aircraft and Rocket Propulsion*. Springer, 2007.

[33] R. Fiévet, , H. Koo, A. H. Auslender, and V. Raman. Numerical investigation of shock train response to inflow boundary layer variations. *AIAA Journal*, 55(9):2888–2901, May 2017.

[34] R. Fiévet, H. Koo, and V. Raman. Numerical simulation of a scramjet isolator with thermodynamic nonequilibrium. In *22nd AIAA Computational Fluid Dynamics Conference, 22-26th June 2015, Dallas, TX, USA*, number AIAA-2015-3418, 2015.

[35] R. Fiévet and V. Raman. Effect of vibrational nonequilibrium on isolator shock structure. *Jounal of Propulsion and Power*. In review.

[36] R. Fiévet and V. Raman. Direct Numerical Simulation of a normal shock train with thermal nonequilibrium. In *APS Division of Fluid Dynamics Meeting Abstracts*, page L5.003, Nov. 2016.

[37] R. Fiévet, V. Raman, and A. H. Auslender. Data-driven one-dimensional modeling of pseudoshocks. *AIAA Journal*. In review.

[38] R. Fiévet, S. Voelkel, H. Koo, V. Raman, and P. L. Varghese. Numerical investigation of vibrational relaxation coupling with turbulent mixing. *Physics of Fluids*. In review.

[39] R. Fiévet, S. Voelkel, H. Koo, V. Raman, and P. L. Varghese. Effect of thermal nonequilibrium on ignition in scramjet combustors. *Proceedings of the Combustion Institute*, 36(2):2901 – 2910, 2017.

[40] R. Fiévet, S. Voelkel, H. Koo, V. Raman, and P. L. Varghese. Numerical investigation of vibrational relaxation coupling with turbulent mixing. In *55th AIAA Aerospace Sciences Meeting Grapevine, TX, USA*, number AIAA 2017-0663, 2017.

[41] M. L. Fotia and J. F. Driscoll. Isolator-Combustor Interactions in a Direct-Connect Ramjet-Scramjet Experiment. *Journal of Propulsion and Power*, 28(1):83–95, Jan-Feb 2012.

[42] M. L. Fotia and J. F. Driscoll. Ram-Scram Transition and Flame/Shock-Train Interactions in a Model Scramjet Experiment. *Journal of Propulsion and Power*, 29(1):261–273, Jan-Feb 2013.

[43] D. C. Freeman, D. E. Reubush, C. R. McClinton, V. L. Rausch, and J. L. Crawford. Nasa hyper-x program. Technical Report NASA-TM-1997-207243, NASA Lewis Research Center, 1997.

[44] J. A. Fulton, J. R. Edwards, H. A. Hassan, J. C. McDaniel, C. P. Goyne, R. D. Rockwell, A. D. Cutler, C. T. Johansen, and P. M. Danehy. Large-Eddy/Reynolds-Averaged Navier-Stokes Simulations of Reactive Flow in Dual-Mode Scramjet Combustor. *Journal of Propulsion and Power*, 30(3):558–575, May-Jun 2014.

[45] M. Gamba and M. G. Mungal. Ignition, flame structure and near-wall burning in transverse hydrogen jets in supersonic crossflow. *Journal of Fluid Mechanics*, 780:226–273, Oct 2015.

[46] J. S. Geerts and K. H. Yu. Shock Train/Boundary-Layer Interaction in Rectangular Isolators. *AIAA Journal*, 54(11):3450–3464, May 2016.

[47] J. Goodman and J. Weare. Ensemble Samplers with Affine Invariance. *Communications in Applied Mathematics and Computational Science*, 5(1):65–80, 2010.

[48] K. Hannemann, S. Karl, J. Martinez Schramm, and J. Steelant. Methodology of a combined ground based testing and numerical modelling analysis of supersonic combustion flow paths. *Shock Waves*, 20(5):353–366, Oct 2010.

[49] R. Hanson. Shock-tube study of vibrational relaxation in carbon monoxide using pressure measurements. *AIAA Journal*, 9(9):1811–&, 1971.

[50] D. W. Hogg. emcee: The MCMC Hammer. *Publications of the Astronomical Society of the Pacific*, 125(925):306–312, 2013.

[51] R. L. Hunt, J. F. Driscoll, and M. Gamba. Periodic forcing of a shock train in mach 2.0 flow. In *55th AIAA Aerospace Sciences Meeting*, number AIAA-2017-0088, 2017.

[52] R. L. Hunt, J. F. Driscoll, and M. Gamba. Unsteadiness characteristics and three-dimensional leading shock structure of a mach 2.0 shock train. In *55th AIAA Aerospace Sciences Meeting*, number AIAA-2017-0087, 2017.

[53] K. E. Hutchins, M. R. Akella, N. T. Clemens, J. M. Donbar, and S. Gogineni. Experimental Identification of Transient Dynamics for Supersonic Inlet Unstart. *Journal of Propulsion and Power*, 30(6):1605–1612, Nov-Dec 2014.

[54] T. Ikui, K. Matsuo, and M. Nagai. The mechanism of pseudo-shock waves. *Bulletin of the JSME-Japan Society of Mechanical Engineers*, 17(108):731–739, 1974.

[55] A. Ingenito, C. Bruno, and D. Cecere. LES of the hyshot scramjet combustor. In *48th AIAA Aerospace Sciences Meeting*, number AIAA-2010-758, 2010.

[56] G.-S. Jiang and C.-W. Shu. Efficient implementation of weighted eno schemes. *Journal of Computational Physics*, 126:202–228, 1996.

[57] E. Johnsen and T. Colonius. Implementation of WENO schemes in compressible multicomponent flow problems. *Journal of Computational Physics*, 219(2):715–732, Dec 2006.

[58] E. Johnsen, J. Larsson, A. V. Bhagatwala, W. H. Cabot, P. Moin, B. J. Olson, P. S. Rawat, S. K. Shankar, B. Sjoegreen, H. C. Yee, X. Zhong, and S. K. Lele. Assessment of high-resolution methods for numerical simulations of compressible turbulence with shock waves. *Journal of Computational Physics*, 229(4):1213–1237, Feb 2010.

[59] R. Kamali, S. M. Mousavi, and A. R. Binesh. Three dimensional CFD investigation of shock train structure in a supersonic nozzle. *Acta Astonautica*, 116:56–67, Nov-Dec 2015.

[60] S. Karl, K. Hannemann, J. Streelant, and A. Mack. Cfd analysis of the HyShot II supersonic combustion flight experiment configuration. In *14th AIAA Space Planes and Hypersonic Systems and Technologies Conference*, number AIAA-2006-8041, 2006.

[61] S. Kawai and S. K. Lele. Large-Eddy Simulation of Jet Mixing in Supersonic Crossflows. *AIAA Journal*, 48(9):2063–2083, Sep 2010.

[62] R. L. Klomparens, J. F. Driscoll, and M. Gamba. Unsteadiness characteristics and pressure distribution of an oblique shock train. In *53rd AIAA Aerospace Sciences Meeting*, number AIAA-2015-1519, 2015.

[63] R. L. Klomparens, J. F. Driscoll, and M. Gamba. Response of a shock train to downstream back pressure forcing. In *54th AIAA Aerospace Sciences Meeting*, number AIAA-2016-0078, 2016.

[64] O. Knab, H. H. Fruhauf, and E. W. Messerschmid. Theory and validation of the physically consistent coupled vibration-chemistry-vibration model. *Journal of Thermophysics and Heat Transfer*, 9(2):219–226, 1995.

[65] O. Knab, T. H. Gogel, H. H. Fruhauf, and E. W. Messerschmid. CVCV-model validation by means of radiative heating calculations. In *33rd AIAA Aerospace Science Meeting and Exhibit*, number AIAA-95-0623, 1995.

[66] M. Kodera, T. Sunami, and K. Itoh. Numerical simulation of a scramjet engine for jaxas flight experiment using hyshot. In *AIAA/CIRA 13th International Space Planes and Hypersonics Systems and Technologies*, number AIAA-2005-3355, 2005.

[67] V. Kolar. Vortex identification: New requirements and limitations. *International Journal of Heat and Fluid Flow*, 28(4, SI):638–652, Aug 2007. International Conference on Modelling Fluid Flow (CMFF 06), Budapest Univ Technol & Econ, Budapest, Hungary, Sep 06-09, 2006.

[68] H. Koo. *Large-eddy simulations of scramjet engines*. PhD thesis, The University of Texas at Austin, 2011.

[69] H. Koo, P. Donde, and V. Raman. A quadrature-based les/transported probability density function approach for modeling supersonic combustion. *Proceedings of the Combustion Institute*, 33:2203–2210, 2011.

[70] H. Koo, P. Donde, and V. Raman. Les-based eulerian pdf approach for the simulation of scramjet combustors. *Proceedings of the Combustion Institute*, 34(2):2093–2100, 2013.

[71] H. Koo and V. Raman. Large-eddy simulation of a supersonic inlet-isolator. *AIAA Journal*, 50(7):1596–1613, 2012.

[72] H. Koo, V. Raman, and P. Varghese. Direct numerical simulation of supersonic combustion with thermal nonequilibrium. *Proceedings of the Combustion Institute*, 35(2):2145–2153, 2015.

[73] S. kyun Im and H. Do. Unstart phenomena induced by flow choking in scramjet inlet-isolators. *Progress in Aerospace Sciences*, 2018.

[74] L. D. Landau and E. Teller. Theory of sound dispersion. *Phys. Z. Sowjetunion*, 10, 1936.

[75] J. Larsson, S. Laurence, I. Bermejo-Moreno, J. Bodart, S. Karl, and R. the. Incipient thermal choking and stable shock-train formation in the heat-release region of a scramjet combustor. Part II: Large eddy simulations. *Combustion and Flame*, 162(4):907–920, Apr 2015.

[76] S. Laurence, D. Lieber, J. M. Schramm, K. Hannemann, and J. Larsson. Incipient thermal choking and stable shock-train formation in the heat-release region of a scramjet combustor. part i: Shock-tunnel experiments. *Combustion and Flame*, 162(4):921 – 931, 2015.

[77] S. J. Laurence, S. Karl, J. M. Schramm, and K. Hannemann. Transient fluid-combustion phenomena in a model scramjet. *Journal of Fluid Mechanics*, 722:85–120, May 2013.

[78] B. P. Leonard. A stable and accurate convective modelling procedure based on quadratic upstream interpolation. *Computational Methods in Applied Mechanics*, 19:59–98, 1979.

[79] R. J. Leveque. *Finite volume methods for hyperbolic problems*. Cambridge University press, 2002.

[80] K.-C. Lin, C.-J. Tam, and K. Jackson. Characterization of shock train structures inside constant-area isolators of model scramjet combustors. In *44th AIAA/ASME/SAE/ASEE Joint Propulsion Conference & Exhibit*, number AIAA 2006-816, 2006.

[81] P. Lin, G. Rao, and G. O'Connor. Numerical analysis of normal shock train in a constant area isolator. In *27th Joint Propulsion Conference*, number AIAA 1991-2162, 1991.

[82] C. D. Lindstrom, D. Davis, S. Williams, and C.-J. Tam. Shock-Train Structure Resolved with Absorption Spectroscopy Part 2: Analysis and CFD Comparison. *AIAA Journal*, 47(10):2379–2390, Oct 2009.

[83] F. Lordet, J. G. Méolans, A. Chauvin, and R. Brun. Nonequilibrium vibration-dissociation phenomena behind a propagating shock wave: vibrational population calculation. *Shock Waves*, 4:299–312, 1995.

[84] M. P. Martin. Direct numerical simulation of hypersonic turbulent boundary layers. Part 1. Initialization and comparison with experiments. *Journal of Fluid Mechanics*, 570:347–364, Jan 2007.

[85] K. Matsuo, Y. Miyazato, and H.-D. Kim. Shock train and pseudo-shock phenomena in internal gas flows. *Progres in Aerospace Sciences*, 35:33–100, 1999.

[86] G. S. Mcbride, B. and M. Reno. Coefficients for calculating thermodynamic and transport properties of individual species. Technical Report NASA-TM-4513, NASA Lewis Research Center, 1993.

[87] C. McClinton, A. Roudakov, V. Semenov, and V. Kopehenov. Comparative flow path analysis and design assessment of an axisymmetric hydrogen fueled scramjet flight test engine at a mach number of 6.5. In *7th AIAA International Space Planes and Hypersonic Systems and Technologies Conference, Norfolk, VA, USA*, number AIAA 1996-4571, 1996.

[88] G. McLafferty. Theoretical Pressure Recovery Through a Normal Shock in a Duct with Initial Boundary Layer. *Journal of the Aeronautical Sciences*, 20(3):169–174, Dec 1953.

[89] P. E. Merkli. Pressure recovery in rectangular constant area supersonic diffusers. *AIAA Journal*, 14(2):168–172, 1976.

[90] R. C. Millikan and D. R. White. Systematics of vibrational relaxation. *Journal of Chemical Physics*, 39:3209, 1963.

[91] B. Morgan, K. Duraisamy, and S. K. Lele. Large-eddy simulations of a normal shock train in a constant-area isolator. *AIAA Journal*, 52(3):539–558, 2014.

[92] B. Morgan, K. Duraisamy, N. Nguyen, S. Kawai, and S. K. Lele. Flow physics and RANS modelling of oblique shock/turbulent boundary layer interaction. *Journal of Fluid Mechanics*, 729:231–284, Aug 2013.

[93] Y. Moule, V. Sabel'nikov, A. Mura, and M. Smart. Computational Fluid Dynamics Investigation of a Mach 12 Scramjet Engine. *Journal of Propulsion and Power*, 30(2):461–473, Mar-Apr 2014.

[94] M. Mueller, T. Kim, R. Yetter, and F. Dryer. Flow reactor studies and kinetic modeling of the h-2/o-2 reaction. *International Journal of Chemical Kinetics*, 31:113–125, 1999.

[95] D. Musielak. Year in review: High-speed air-breathing propulsion. Technical report, AIAA High Speed Air Breathing Propulsion Technical Committee, 2011.

[96] T. Oka, D. Ono, and Y. Miyazato. Study of shock trains and pseudo-shock waves in constant area ducts. In *52nd Aerospace Sciences Meeting, 13-17 January 2014, National Harbor, MD, USA*, number AIAA 2014-049, 2014.

[97] T. A. Oliver. Favre-averaged navier-stokes and turbulence model equation documentation. Technical report, Institute for Computational Engineering and Sciences, 2009.

[98] D. Om and M. E. Childs. Multiple transonic shock-wave turbulent boundary-layer interaction in a circular duct. *AIAA Journal*, 23(10):1506–1511, 1985.

[99] P. J. Ortwerth. Scramjet vehicle integration. In *Scramjet Propulsion Progresse in Astronautics and Aeronautics, AIAA, Reston, VA, USA*, 2001.

[100] C. Park. Assessment of a two-temperature kinetic model for dissociating and weakly ionizing nitrogen. *Journal of Thermophysics and Heat Transfer*, 2(1):8–16, 1988.

[101] C. Park. Review of chemical-kinetic problems of future NASA missions. 1 - earth entries. *Journal of Thermophysics and Heat Transfer*, 7(3):385–398, 1994.

[102] C. Park. The limits of two-temperature kinetic model in air. *48th AIAA Aerospace Sciences Meeting Including the New Horizons Forum and Aerospace Exposition*, Jan 2010.

[103] A. Pauli, H. Alesi, and S. Anderson. *The development of the HyShot flight program*, pages 31–48. Springer Berlin Heidelberg, Berlin, Heidelberg, 2005.

[104] R. Pecnik, V. E. Terrapon, F. Ham, G. Iaccarino, and H. Pitsch. Reynolds-Averaged Navier-Stokes Simulations of the HyShot II Scramjet. *AIAA Journal*, 50(8):1717–1732, Aug 2012.

[105] S. Pirozzoli. Conservative hybrid compact-WENO schemes for shock-turbulence interaction. *Journal of Computational Physics*, 178(1):81–117, May 2002.

[106] S. Pirozzoli, M. Bernardini, and F. Grasso. Direct numerical simulation of transonic shock/boundary layer interaction under conditions of incipient separation. *Journal of Fluid Mechanics*, 657:361–393, Aug 2010.

[107] M. Pizzella, S. Warning, M. Jennerjohn, M. McQuilling, A. Purkey, R. Scharnhorst, and M. Mani. Numerical investigation of a normal shock wave boundary layer interaction in a 4.3 aspect ratio test section. In *54th AIAA Aerospace Sciences Meeting, 4-8 January 2016, San Diego, CA, USA*, number AIAA 2016-0614, 2016.

[108] T. J. Poinsot and S. K. Lele. Boundary conditions for direct simulations of compressible viscous flows. *Journal of Computational Physics*, 101:104–129, 1992.

[109] S. B. Pope. Turbulent flows. *Measurement Science and Technology*, 12(11):2020, 2001.

[110] A. Ramprakash and T. M. Murganandam. Experimental study on start/unstart behavior of two dimensional mixed compression inlet by cowl actuation. In *52nd AIAA/SAE/ASEE Joint Propulsion Conference, 25-27 July 2016, Salt Lake City, UT, USA*, number AIAA 2016-5072, 2016.

[111] H. Reising, T. Haller, N. Clemens, P. Varghese, R. Fiévet, and V. Raman. Spontaneous raman scattering temperature measurements and large eddy simulations of vibrational non-equilibrium in high-speed jet flames. In *32nd AIAA Aerodynamic Measurement Technology and Ground Testing Conference, 13-17 June 2016, Washington, D.C.*, number AIAA 2016-3144, 2016.

[112] H. H. Reising, U. KC, N. T. Clemens, and P. L. Varghese. Measurement of mixing-induced thermal non-equilibrium in a supersonic shear layer using spontaneous raman scattering. *Physics of Fluids*, 29(7):076101, 2017.

[113] L. P. Riley, M. A. Hagenmaier, J. M. Donbar, and D. V. Gaitonde. A computational investigation of unstart in a dual-mode scramjet. In *54th AIAA Aerospace Sciences Meeting, 4-8 January 2016, San Diego, CA, USA*, number AIAA 2016-1901, 2015.

[114] C. Roussel, F. Alizard, and F. Grasso. Turbulence generation and sensitivity to mean inflow conditions for a supersonic flow in a rectangular duct at m = 1.61. In *22nd AIAA Computational Fluid Dynamics Conference, 22-26 June 2015, Dallas, TX, USA*, number AIAA 2015-2618, 2015.

[115] C. W. Shu. High order finite difference and finite volume WENO schemes and discontinuous galerkin methods for CFD. Technical Report 2001-11, ICASE, 2001.

[116] M. K. Smart. Flow Modeling of Pseudoshocks in Backpressured Ducts. *AIAA Journal*, 53(12):3577–3588, Dec 2015.

[117] M. K. Smart, N. E. Hass, and A. Paull. Flight data analysis of the HyShot 2 scramjet flight experiment. *AIAA Journal*, 44(10):2366–2375, Oct 2006.

[118] W.-Y. Su, Y.-X. Ji, and Y. Chen. Effects of Dynamic Backpressure on Pseudoshock Oscillations in Scramjet Inlet-Isolator. *Journal of Propulsion and Power*, Jan 2016. Article in advance.

[119] H. Sugiyama, Y. Tsujiguchi, and T. Honma. Structure and oscillation phenomena of pseudo-shock waves in a straight square duct at mach 2 and 4. In *15th AIAA International Space Planes and Hypersonic Systems and Technologies Conference*, number AIAA 2014-0231, 2008.

[120] G. Sullins and G. Mclafferty. Experimental results of shock trains in rectangular ducts. In *AIAA Paper 92-5104*, 1992.

[121] H. J. Tan, S. Sun, and H. X. Huang. Behavior of shock trains in a hypersonic inlet/isolator model with complex background waves. *Experiments in Fluids*, 53(6):1647–1661, Dec 2012.

[122] H. j. Tan, S. Sun, and Z.-l. Yin. Oscillatory Flows of Rectangular Hypersonic Inlet Unstart Caused by Downstream Mass-Flow Choking. *Journal of Propulsion and Power*, 25(1):138–147, Jan-Feb 2009.

[123] B. D. Taylor, D. A. Kessler, V. N. Gamezo, and E. S. Oran. Numerical simulations of hydrogen detonations with detailed chemical kinetics. *Proceedings of the Combustion Institute*, 34(2):2009–2016, 2013.

[124] F. Tong, Z. Tang, C. Yu, X. Zhu, and X. Li. Numerical analysis of shock wave and supersonic turbulent boundary interaction between adiabatic and cold walls. *Journal of Turbulence*, 18(6):569–588, 2017.

[125] A. Valdivia, K. B. Yuceil, J. L. Wagner, N. T. Clemens, and D. S. Dolling. Control of Supersonic Inlet-Isolator Unstart Using Active and Passive Vortex Generators. *AIAA Journal*, 52(6):1207–1218, Jun 2014.

[126] Z. Vane, I. Bermejo-Moreno, and S. K. Lele. Simulations of a Normal Shock Train in a Constant Area Duct Using Wall-Modeled LES. In *43rd Fluid Dynamics Conference, 24-27 June 2013, San Diego, CA*, number AIAA 2013-3204, 2013.

[127] W. G. Vincenti and C. H. Kruger. *Introduction to Physical Gas Dynamics*. Krieger Pub. Co., 1975.

[128] A. Viviani and G. Pezzella. Nonequilibrium Aerothermodynamics for a Capsule Reentry Vehicle. *Engineering Applications of Computational Fluid Mechanics*, 3(4):543–561, 2009.

[129] S. Voelkel. *Thermal Nonequilibrium Models for High-Temperature Reactive Processes*. PhD thesis, The University of Texas at Austin, 2017.

[130] S. Voelkel, V. Raman, and P. L. Varghese. Effect of thermal nonequilibrium on reactions in hydrogen combustion. *Shock Waves*, pages 1–11, 2016.

[131] S. Voelkel, P. L. Varghese, and V. Raman. Quasi-state-specific qct method for calculating the dissociation rate of nitrogen in thermal non-equilibrium. In *54th AIAA Aerospace Sciences Meeting, 4-8 January 2016, San Diego, California, USA*, number AIAA 2016-0449, 2016.

[132] P. Volpiani, J. Larsson, and M. Bernardini. Investigating the effects of non-adiabatic walls on shock/boundary-layer interaction at low reynolds number using direct numerical simulations. In *AIAA Aerospace Sciences Meeting, 812 January 2018, Kissimmee, Fl, USA*, number AIAA 2018-1806, 2018.

[133] C. Wagner, T. Huttl, and P. Sagaut. *Large-Eddy Simulation for Acoustics*. Cambridge University Press, 2007.

[134] J. L. Wagner, K. B. Yuceil, and N. T. Clemens. Velocimetry measurements of unstart of an inlet/isolator model in a mach 5 flow. *AIAA Journal*, 48(9):1875–1888, 2010.

[135] P. J. Waltrup and F. S. Billig. Prediction of precombustion wall pressure distributions in scramjet engines. *Journal of Spacecraft and Rockets*, 10(9):620–622, 1973.

[136] P. J. Waltrup and F. S. Billig. Structure of shock waves in cylindrical ducts. *AIAA Journal*, 11(10):1404–1408, 1973.

[137] J. Watanabe, T. Kouchi, K. Takita, and G. Masuya. Characteristics of hydrogen jets in supersonic crossflow: Large-eddy simulation study. *Journal of Propulsion and Power*, 29(3):661–674, May 2013.

[138] A. Weiss and H. Olivier. Behaviour of a shock train under the influence of boundary-layer suction by a normal slot. *Experiments in Fluids*, 52(2):273–287, Feb 2012.

[139] M. Werman and D. Keren. A Bayesian method for fitting parametric and nonparametric models to noisy data. *IEEE Transactions on Pattern Analysis and Machine Intelligence*, 23(5):528–534, May 2001.

[140] F. A. White. *Viscous Fluid Flow, 3e*. McGraw-Hill Education (India) Pvt Limited, 1974.

[141] M. Wu and M. P. Martin. Direct numerical simulation of supersonic turbulent boundary layer over a compression ramp. *AIAA Journal*, 45(4):879–889, 2007.

[142] X.-K. Zhu, C.-P. Yu, F.-L. Tong, and X.-L. Li. Numerical Study on Wall Temperature Effects on Shock Wave/Turbulent Boundary-Layer Interaction. *AIAA Journal*, 55(1):131–140, Jan 2017.